ADVANCEMENTS IN COUPLING AMBIENT PLASMA IONIZATION AND DRIFT TUBE ION MOBILITY SPECTROMETRY WITH MASS SPECTROMETRY

A Ph.D. Dissertation
Presented to
The Academic Faculty

by

Joel D. Keelor

In Partial Fulfillment
of the Requirements for the Degree
Doctorate of Philosophy in the
School of Chemistry and Biochemistry

Georgia Institute of Technology
August 2016

ADANCEMENTS IN COUPLING AMBIENT PLASMA IONIZATION AND DRIFT TUBE ION MOBILITY SPECTROMETRY WITH MASS SPECTROMETRY

Approved by:

Dr. Facundo M. Fernández, Advisor
School of Chemistry and Biochemistry
Georgia Institute of Technology

Dr. Ronghu Wu
School of Chemistry and Biochemistry
Georgia Institute of Technology

Dr. Lawrence A. Bottomley
School of Chemistry and Biochemistry
Georgia Institute of Technology

Dr. Matthew P. Torres
School of Biology
Georgia Institute of Technology

Dr. M. Cameron Sullards
School of Chemistry and Biochemistry
Georgia Institute of Technology

Date Approved: July 14, 2016

Science is made up of so many things that appear obvious after they are explained.

-Pardot Kynes, Frank Herbert's *DUNE*

ACKNOWLEDGEMENTS

This section *should* be the longest of my dissertation, as there are myriad family, friends, and colleagues I am indebted to who have made this enterprise possible. Firstly, I wish to thank my adviser and friend, Dr. Facundo M. Fernández, for his patience, guidance, and encouragement. Under his mentorship during the past 6 years, I have become a more capable scientist, and I hope to keep growing our relationship throughout my career. I also want to thank all active members of my thesis committee, the gatekeepers to my degree: Dr. Lawrence A. Bottomley, Dr. Cameron Sullards, Dr. Ronghu Wu, and Dr. Matthew Torres, as well as those who served temporarily including Dr. L. Andrew Lyon, Dr. Charles Eckert, and Dr. Amanda M. Stockton. Your insights will continue to shape my perspective in science.

So how did I end up here? Going back to my days at Battle Ground Academy, I was lucky to have teachers like Mrs. McElroy and Mrs. Davis who believed in me and fostered my creativity and desire to learn. At the College of Wooster, I had exceptional instruction from my advisers Dr. Paul Bonvallet and Dr. Paul Edmiston, who provided me with early research opportunities and through a collaboration, lead me to my job after college working for Georgia Tech Research Institute. There, I benefited from working for kind and colorful bosses like Ken Johnson and Dan Campbell, who helped me adjust to a new job in a new city, until I parted ways to pursue my doctorate.

I am grateful to those faculty and staff in the School of Chemistry and Biochemistry at Georgia Tech who have contributed to my professional development. Thanks to Richard Bedell for long talks troubleshooting equipment, Arian Padron for the

relentless technical support, and Christine Conwell, Sue Winters, and Shantel Floyd for moral boosts and the best administrative assistance. Much of my success is shared with all the past and present group members of the Fernández cohort, such good people, who gave their knowledge and friendship on a daily basis. A few distinguished mentions are owed to Glenn A. Harris and Prabha Dwivedi for their good tutelage when I began, Ken Laszlo, Rachel Bennett and Christina Jones for keeping hope and laughter alive in the early years, Jennifer Pittman and María Eugenia-Monge who looked after me and were always smiling and supplying chocolate or jelly beans, and now of course my "Rat Pack" lab mates Jay Forsythe, Martin Paine, Matthew Bernier, and perspicacious protégé Stephen Zambrzycki. I wish to thank my professional collaborators, within the Center for Chemical Evolution, and elsewhere, who worked together closely with me on pieces of this dissertation research, particularly Dr. Paul B. Farnsworth and Dr. Matthew Curtis. And also I must thank NSF and NASA government funding agencies for sponsoring this work.

I'd like to pay special thanks to the friends I found in the graduate school program. To survive this ordeal, I needed every "Cupcakes & Cocktails," that blessed tradition, with Tim and Alicia Lenz., "ladies night" at MJQ or Star Bar with Brian Cafferty and friends, good times with my first year classmates who were part of the funky bunch (Kim Clarke), and even that heavy drinking crew I tangoed with when I started. I cannot convey enough appreciation for my oldest and most stalwart comrades here in Atlanta who I connected with through GTRI: Eric Rader, Danielle Wright, Ryan O'Neill, Briana Dams, and Brian Parese, whose generosity and friendship know no bounds and whom I truly cherish. I'm blessed to have a boyhood friend like Michael Schmidt, a co-

conspirator from college like Nick Weida, and my best roommate ever, Patrick Christensen. Between summers practicing speech at UNTIF in Austin, TX, and Wooster college nights living in the service dog house, there are simply too many more friends and experiences to recollect here, but they have all left an impression on me that has brought me to this moment.

Finally, I have the deepest love and gratitude for the most permanent fixtures in my life, my family. I need to thank my mom and dad, whose constant love, financial support, and reassurance has seen me through this crucible and enabled me to do something, everything great. I want to thank my amazing, beautiful, and more talented younger sister Amanda, who will one day soon achieve more than I dream to. And in the same breadth, I am so very grateful to all my relatives, Grandpa Keelor, Barbara, and the rest of the Keelor Tribe, Aunt Kiki and Aunt Stephie, Grandpa Swartz, Grandma Ruth, Grandma Bette and Phil, you share in this milestone with me. Thank You.

TABLE OF CONTENTS

Page

ACKNOWLEDGEMENTS iv

LIST OF TABLES AND SCHEMES xii

LIST OF FIGURES xiii

LIST OF SYMBOLS xxiii

LIST OF ABBREVIATIONS xxvi

SUMMARY xxix

CHAPTERS

1. INTRODUCTION 1

    1.1. Abstract 1

    1.2. Ambient Desorption Ionization 1

        1.2.1. An Overview of Plasma-based Ion Sources 4

        1.2.2. Plasma Discharge Ionization: Principles and Mechanisms 5

        1.2.3. Plasma Source Sampling Practice and Multimode Configurations 8

    1.3. Ion Mobility Spectrometry: Separation and Detection 10

        1.3.1. Drift Tube Ion Mobility Spectrometry: Principles and Theory 11

        1.3.2. Alternative Ion Mobility Techniques 16

    1.4. Multidimensional Analysis Using Ion Mobility-Mass Spectrometry 18

2. SCHLIEREN VISUALIZATION OF THE FLUID DYNAMICS EFFECTS IN DIRECT ANALYSIS IN REAL TIME MASS SPECTROMETRY 23

    2.1. Abstract 23

    2.2. Introduction 24

    2.3. Experimental 25

2.3.1. Schlieren Apparatus 25
2.3.2. Instrumentation 26
2.3.3. Sample Probes and Modes of Analysis 27
2.4. Results and Discussion 28
2.4.1. Schlieren Imaging: Principles of Experimental Design 28
2.4.2. General Gas Flow Characterization of DART-MS 29
2.4.3. Sample Probes and Sampling Strategies 32
2.4.4. GIST Adapter and Vapur® Pump Effects 35
2.4.5. Transmission Mode (TM) DART-MS 38
2.5. Conclusion 41
3. A MUTLIMODAL VACUUM-ASSISTED PLASMA IONIZATION (VAPI) SOURCE WITH LASER ABLATION AND TRANSMISSION MODE SAMPLING CAPABILITIES 43
3.1. Abstract 43
3.2. Introduction 43
3.3. Experimental 45
3.3.1. Materials and Sample Preparation 45
3.3.2. VaPI Ion Source Design and Operation 47
3.3.3. Instrumentation and Sampling Methods 48
3.4. Results and Discussion 50
3.4.1. TM-VaPI Characterization 50
3.4.2. Comparison of AC and DC VaPI Operation Modes 57
3.4.3. TM-VaPI Analysis of Solids 60
3.4.4. LA-VaPI Characterization 63
3.4.5. Application of LA-VaPI to Reaction Product Screening 68
3.5. Conclusion 70

4. AN EFFECTIVE APPROACH FOR COUPLING DIRECT ANALYSIS IN REAL TIME WITH ATMOSPHERIC PRESSURE DRIFT TUBE ION MOBILITY SPECTROMETRY 72

4.1. Abstract 72

4.2. Introduction 73

4.3. Experimental 74

4.3.1. Materials and Reagents 74

4.3.2. Instrumentation and Methods 75

4.4. Results and Discussion 77

4.4.1. Ion Source and System Characterization 77

4.4.2. Fluid Dynamics and Electric Field Considerations 86

4.4.3. Solid Sample Analysis 88

4.5. Conclusion 93

5. HIGH-RESOLUTION ATMOSPHERIC PRESSURE DRIFT TUBE ION MOBILITY SPECTROMETRY COUPLED WITH ACCURATE MASS ORBITRAP MASS SPECTROMETRY 94

5.1. Abstract 94

5.2. Introduction 94

5.3. Experimental 97

5.3.1. Chemicals and Materials 97

5.3.2. Instrumentation and System Parameters 97

5.3.3. DTIMS Ion Gating Schemes 100

5.4. Results and Discussion 102

5.4.1. AP-DTIMS Characterization: General Physical Parameters 102

5.4.2. AP-DTIMS-Orbitrap MS Characterization: Sensitivity and Resolving Power 110

5.4.3. AP-DTIMS-Orbitrap MS: Benchmark Applications 119

5.5. Conclusion....123

6. CONLCUSION....125

6.1. Abstract....125

6.2. Progress with Plasma-based Ambient Sampling Strategies: Understanding and Implementation....125

6.2.1. Physiochemical Variables Determining Plasma Discharge Source Performance....126

6.2.2. Development of New Ambient Plasma Sources for Mass Spectrometry: Versatility and Portability....128

6.2.3. Coupling Plasma Ion Sources with Ion Mobility Spectrometry....130

6.3. Development of a High-Resolution Ion Mobility-Mass Spectrometry Platform for Multidimensional Analysis....131

6.4. Proposed Future Directions....133

6.4.1. Hybrid Ambient Source Development and Enhanced Sampling Approaches....133

6.4.2. Digitally Multiplexed AP-DTIMS-FT-MS and Alternative DTIMS Architectures....135

APPENDIX A: Absolute Number Densities of Metastable Helium Atoms Determined by Atomic Absorption Spectroscopy in Helium Plasma-based Discharges Used as Ambient Desorption/ Ionization Sources for Mass Spectrometry....137

A.1. Abstract....137

A.2. Introduction....138

A.3. Experimental....139

A.3.1. Helium Plasma-discharge Sources....139

A.3.2. Atomic Absorbance Spectroscopy....143

A.4. Results and Discussion....146

A.4.1. Time-averaged Density Measurements....146

A.4.2. Time-Resolved Density Measurement....150

A.4.3. Limiting Reagent Determination 153

A.5. Conclusion 154

APPENDIX B: Microplasma Ionization of Volatile Organics for Air/Water Contaminant Analysis Aboard the International Space Station 156

B.1. Abstract 156

B.2. Introduction 156

B.3. Experimental 158

B.3.1. MHCD Microplasma 158

B.3.2. Direct Analysis in Real Time 159

B.3.3. TOF MS Instrumentation 160

B.4. Results and Discussion 160

B.4.1. General MHCD Performance and Comparison with DART 160

B.4.2. Effect of Gas Composition and Flow Rate 163

B.4.3. Device Power and Lifetime 167

B.5. Conclusion 168

APPENDIX C: Design and Construction of a Dual-gate AP-DTIMS Prototype 170

C.1. Abstract 170

C.2. Introduction 170

C.3. Experimental 171

C.4. Preliminary Results 174

C.5. Conclusion 178

REFERENCES 179

LIST OF PUBLICATIONS 199

VITA 200

LIST OF TABLES AND SCHEMES

Page

Table 3.1: Comparison of DC and AC VaPI discharges.....58

Table 5.1: Key AP-DTIMS and Orbitrap MS parameters 99

Table 5.2: DTIMS ion gating schemes 102

Table A.1: Time-averaged number densities of He_m for four plasma sources 148

Scheme 5.1: Modes of Mobility Analysis.....102

LIST OF FIGURES

Page

Figure 1.1: Illustration of common ambient desorption/ionization approaches 2

Figure 1.2: Simplified schematic representations of 4 main IMS formats: DTIMS, TWIMS, DMS, and TIMS. The electric field profiles employed (orange traces) are illustrated below the device architectures. Carrier/buffer gas flow directions are indicated with grey arrows. Ions are depicted as colored circles.....16

Figure 2.1: Diagram of single mirror or double-pass Schlieren configuration used for DART gas flow visualization in the AP interface 28

Figure 2.2: Schematic of system 1, where solid bold lines indicate visible silhouettes of the DART-SVP source and AccuTOF skimmer cone, and red dotted lines demarcate the test region visualized. Panels **A-D** show the metastable helium stream (default 3.5 L min^{-1}) over different AP interface distances when the AccuTOF cavity was properly covered (**A** and **C**) and left exposed (**B** and **D**). The interface distance was ~6 cm in **A** and **B** and ~1.5 cm in **C** and **D**. The helium stream remained collimated as in **A** for DART heater temperatures up to 500 °C.....31

Figure 2.3: Helium flow profiles upon introduction of common sample probes used for DART-MS analyses. Panels **A-B** show a glass melting point capillary, **C-D** a cotton swab, and **E-F** a tablet in tweezers. Probes were inserted at two stream locations, one close to the exit of the DART-SVP (*top images*) and another close to the AP interface of the AccuTOF (*bottom image*s). The sample gap distance was maintained at ~6 cm and the default DART source helium flow rate (3.5 L min^{-1}) was used.....33

Figure 2.4: Schematic of system 2, where solid bold lines indicate visible silhouettes of the DART-100 source and Bruker micrO-TOF I mount, and red dotted lines demarcate the test region visualized. The top panels show the DART helium stream (1 L min^{-1}) across the AP interface for Vapur® pumping rates set to yellow (**A**), green (**B**), and gray (**C**). Panels **D-F** show the effect on those same settings with the N_2 drying gas on (1.4 L min^{-1}). The sample gap length was ~3 cm for all panels.....36

Figure 2.5: Probe sampling performed on the Bruker micrO-TOF I coupled to the DART-100 source with the Vapur® pump and N_2 drying gas active. The top panels show the helium flow patterns (gas flowing left to right) with the pump set to either yellow or gray for a flat face tablet (**A**), a rounded tablet edge (**B**), and a glass capillary (**C**). The bottom panels show the effect on the same samples and settings with the N_2 drying gas switched on (**D**-**F**). AP interface length was ~3 cm and helium flow rate was set to 1 L min^{-1} 38

Figure 2.6: Schematic of system 3, where solid bold lines indicate visible silhouettes of the DART-SVP source and GIST adapter on the Bruker micrO-TOF II, and red dotted lines demarcate the test region visualized. The Vapur® pump was set to gray and N_2 drying gas was turned off. Panels show the DART helium flow (2 L min^{-1}) through a hollow screen holder (**A**), a 60x60 mesh (**B**), and a 100x100 mesh (**C**) over a short interface distance (~2 cm). Helium flow through a 60x60 mesh shown for a larger interface distance (~4 cm) and a more centralized screen position removed from the DART nozzle (**D)** 39

Figure 2.7: Single frames collected over the span of 3 seconds showing the impact of GIST pump pulsations on TM-DART gas flow profiles for gray pump setting (~26 L min^{-1}) and N_2 drying gas at 3.0 L min^{-1} (TOP PANELS **A-E**) and the more stable flow profile achieved with the yellow pump setting (~22 L min^{-1}) and N_2 drying gas at 3.0 L min^{-1} (BOTTOM PANELS **F-J**). The pulsation is evident comparing panels **C** and **H**. Sample gap was ~4 cm and DART helium flow rate was 2 L min^{-1} through a 60x60 mesh, with DART gas flowing left to right 40

Figure 3.1: Schematic of vacuum-assisted plasma ionization (VaPI) source assembly. Configuration used for transmission mode (TM)-VaPI sampling (**A**). Configuration used for laser ablation (LA)-VaPI sampling (**B**). Open atmospheric pressure interface arrangement with plasma source (**C**). Pictures of source assemblies for TM-VaPI (**D**) and LA-VaPI (**E**) 50

Figure 3.2: Extracted ion peak traces measured using TM-VaPI with a 20W DC discharge and 1.6 LPM helium flow rate. Consecutive extracted TIC peaks in the full concentration series for 2,4-lutidine analyte in aqueous solution (**A**) and selected TIC peaks for DMMP at 50 μM (**B**). Droplet volumes sampled were 3 μL delivered to mesh by micropipette tip. Cross union was not heated 52

Figure 3.3: Signal intensities as a function of source gas flow rate for 2,4-lutidine and DMMP using TM-VaPI with a 20 W DC discharge. Data points and standard deviation error bars represent the average extracted TIC areas for 3 consecutive peak traces per point 54

Figure 3.4: Signal intensities as a function of volatile concentration for 2,4-lutidine and DMMP using TM-VaPI with a 20 W DC discharge. Data points and standard deviation error bars represent the average extracted TIC areas for 5 consecutive peak traces 55

Figure 3.5: Extracted ion peak traces for 1 mM DMMP at 1.6 LPM helium flow rate with (red) and without (blue) the cross union heated to 275 °C. Baseline/ time axis for superimposed consecutive red traces were altered to fit blue trace 56

Figure 3.6: Thermal images of the VaPI cell (wrapped in heat rope) for 20 W AC and DC discharges ramping the helium flow rate from 1.0-2.0 LPM.....59

Figure 3.7: Mass spectra for acetaminophen (**A-B**), Doralgine **(C-D)**, and Coartem (**E-F**) drug tablet fragments collected by TM-VaPI using 20 W DC discharge and 1.6 LPM helium with (*right*) and without (*left*) cross union heated to 275 °C and/or organic solvent addition. All spectra were derived from 30 second averages of the TIC signal for each tablet 62

Figure 3.8: Mass spectra of 2.5 mM amino acid standard in 0.1 N HCl sampled by laser ablation and plasma ionization using either the LA-VaPI scheme from Figure 3.1B (A) or a traditional open AP interface arrangement shown in Figure 3.1C (**B**). Standard mixture was ablated from 10 μL droplet on Omni slide substrate. Spectra are an average of full time until droplets were consumed (~20 seconds each). Laser wavelength, frequency, and effective energy were 2940 nm, 10 Hz, and ~1 mJ. Optimal helium flow rate for (**A**) was 1.6 LPM and 1.3 LPM for (**B**) with the cross union heated to ~200 °C.....64

Figure 3.9: Investigation of solvent matrix effects using LA-VaPI with 20 W DC discharge and 1.6 LPM helium. Mass spectra for ~4 mg mL^{-1} PEG standard (M_n ~ 400) in 100% aqueous solution (black trace) and 50:50 methanol/water (red trace). Unless otherwise specified, ablation was performed from 200 μL solution in capillary ampoule held by vacuum in the cross union heated to ~200 °C. Laser wavelength, frequency, and effective energy were 2940 nm, 10 Hz, and ~1 mJ. Spectra and bar graph intensities were extracted from 1 minute average of stable TIC signal 66

Figure 3.10: Investigation of salt matrix effects using LA-VaPI with 20 W DC discharge and 1.6 LPM helium. Mass spectrum of 2.5 mM TAP in deionized water sampled from 200 μL of solution in ampoule (black trace) or 10 μL droplet on glass substrate (dotted gray trace). Table includes signal intensity of ions detected for 2.5 mM TAP in aqueous solution as a function of KCl molar concentration ablating from ampoule. Unless otherwise specified, ablation was performed from 200 μL solution in capillary ampoule held by vacuum in the cross union heated to ~200 °C. Laser wavelength, frequency, and effective energy were 2940 nm, 10 Hz, and ~1 mJ. Spectra and bar graph intensities were extracted from 1 minute average of stable TIC signal.....67

Figure 3.11: Mass spectra for model prebiotic synthetic reactions monitored by LA-VaPI using 20 W DC discharge and 1.6 LPM helium with cross union heated to 200 °C. Formamide reaction nucleobase products measured at 72 h and 120 h time points (**A**) and reaction side products from pyrazine reaction after 24 h and workup (**B**). Aqueous solutions were filtered for particulates and sampled in 200 μL from ampoule. Laser wavelength, frequency, and effective energy were 2940 nm, 10 Hz, and ~1 mJ. Spectra represent 1 minute average of TIC trace 69

Figure 4.1: Schematic of the resistive glass DTIMS inlet showing the standard starting configuration for the repeller electrode and DART-SVP ion source. The repeller potential and position (x, z) and the DART (φ_{xz}, ψ_{xy}) and repeller angles (θ_{xz}) were varied as described within the characterization studies.....78

Figure 4.2: SIMION 8.1 scaled models of the resistive glass IMS desolvation cell (l = 11 cm, *i.d.* = 3 cm, *o.d.* = 4 cm) without the repeller, panel **A,** and with the repeller (*dia.* = 1 mm) point electrode 1.5 kV above the inlet potential, panel **B**. Models are built from a cylindrical potential array mirrored in the y-plane (*# grid units (gu) after symmetry*: x = 1099 gu, y = 199*2 gu, z = 199*2 gu, *xyz gu length* = 0.125 mm). The entrance and exit electrodes of the cell (x = 40 gu, y = 1 gu, inter-electrode distance x = 880 gu) were defined at 12,000 V and 10,300 V, respectively. Ground was included as a solid plate (x = 1 *gu*, y = 199 *gu*) marked ~27.5 mm (x = 220 gu) away from the entrance electrode to approximate field strength diminishing as (1/r). The repeller electrode potential was defined at 13,500 V drawn normal and on-axis with the IMS, 40 gu inside the inlet electrode (x = 220 gu, y = 4 gu) 79

Figure 4.3: Ion mobility spectra observed during system characterization showing background and $[M+H]^+$ signal peaks for 2,6-dtBP vapor bubbled from methanol. Spectrum baseline with repeller electrode <13,500 V and DART plasma off (**A**). Background spectrum of reactant ions with repeller at 13,500 V and DART plasma on (**B**). DART signal for 2,6-dtBP with repeller at 13,500 V (**C**) and corona discharge signal for 2,6-dtBP with electrode at 14,500 V and DART plasma off (**D**). The repeller point was coaxial in all cases and at a fixed depth of 5 mm inside the cell. Spectra were collected using a DTIMS gate pulse width of 100 μs and total scan time of 102.4 ms over 128 averages 81

Figure 4.4: DART-generated signal for 2,6-dtBP vapor as a function of the repeller depth inside the DTIMS inlet (*z*) for increasing repeller electrode potentials. Initially, the repeller was placed coaxial and normal to the DTIMS entrance with the DART exit capillary placed orthogonal to the repeller and flush with the DTIMS face plane 83

Figure 4.5: Signal for 2,6-dtBP vapor at DART ϕ_{xz} angles between 0 and 60 degrees (0 degrees being orthogonal to repeller) with *red*) the repeller electrode centered and coaxial, *orange*) the repeller electrode coaxial and offset x=6 mm away from the DART capillary, and *yellow*) the repeller centered and coaxial but with the rod partially shielded. The repeller at was set at 13,300 V and fixed z=7 mm inside the DTIMS opening. When the DART capillary was rotated along ϕ_{xz} a distance of ~1 cm was kept constant between the capillary exit and point *A* (Figure 4.1) 84

Figure 4.6: Signal for 2,6-dtBP vapor with the repeller initially placed coaxially (θ_{xz}=90°) and then moved across θ_{xz} angles in the 60 to 120 degree range. This experiment was done for both DART and corona regimes. In these experiments, the repeller electrode point was fixed at z=7 mm inside and kept stationary; the DART capillary was kept orthogonal (ϕ_{xz}=0°) to the DTIMS face 85

Figure 4.7: Schematic of Foucault single mirror apparatus for Schlieren experiments (**A**). Visualization of the N_2 (200 °C) flow from the DART nozzle glass capillary, with the DART stream passing through a plume of ethanol solvent vapor (~0.3 L min^{-1}) and showing no observable perturbation across a ~3.5 cm distance (**B)**. DART stream with capillary set orthogonal to DTIMS using 2 L min^{-1} N_2 drift gas, indicating only minor turbulence after passing over the repeller rod (**C**) 86

Figure 4.8: Image of an orthogonal DART DTIMS sampling configuration employed for solid tablet analysis. The arrangement shows the DART source angled 45° over a tablet situated between the coaxial repeller electrode and inner lip of the DTIMS inlet 88

Figure 4.9: Signal observed for an acetaminophen tablet as a function of the repeller electrode potential at a fixed depth (*z*=7 mm). The repeller was centered coaxially with the spectrometer axis and normal to the IMS entrance plane, held at 12,000 V with a drift gas flow of N_2 at 1 L min^{-1}. The DART source was oriented orthogonal to the repeller and operated with a N_2 gas flow of 2 L min^{-1}. **A**) Repeller potential at 13,500 V with DART (300 °C) plasma off. **B**) Repeller potential at 13,500 V with DART (300 °C) plasma on. **C**) Repeller potential at 14,500 V with DART (300 °C) plasma on. **D**) Repeller potential at 14,500 V with DART (300 °C) plasma off. **E**) Repeller potential at 14,500 V with DART (450 °C) plasma off. **F**) Repeller potential at 14,500 V with DART (450 °C) plasma on 90

Figure 4.10: Mass spectra of acetaminophen (**A**) and reactant ion population (**B**) observed for N_2 DART collected on a JEOL AccuTOF mass spectrometer. The DART heater temperature was 350 °C and the grid voltage was 500 V. (AccuTOF settings: orifice 1, 10 V; orifice 2, 2 V; ring lens, 8 V; sweep voltage, 120-280 V; pusher bias, 29 V). To assist in species identification, single-point drift correction was performed using a 2,6-dtBP as a reference 91

Figure 4.11: Mass spectra of acetaminophen (**A**) and reactant ion population (**B**) observed for a corona discharge (+3500 V) collected on a JEOL AccuTOF mass spectrometer. DART (plasma off) heater temperature was 350 °C. (AccuTOF settings: orifice 1, 10 V; orifice 2, 2 V; ring lens, 8 V; sweep voltage, 120-280 V; pusher bias, 29 V). To assist in species identification, single-point drift correction was performed using a 2,6-dtBP as a reference 91

Figure 5.1: Schematic of the EXCELLIMS MA3100 atmospheric pressure drift tube ion mobility unit coupled with the Thermo Q Exactive Orbitrap mass spectrometer 99

Figure 5.2: DTIMS Faraday responses for a standard solution of nicotinamide (NIC), 2,6-dtBP (dtBP), and trihexylamine (THA) 25 ppm w/v in 50:50 methanol/water as a function of drift gas (air) flow rate and exhaust pump rate. Drift gas flow rates were 1.0 L min^{-1} (A), 2.0 L min^{-1} (B), and 3.0 L min^{-1} (C). DTIMS operation potential was set to +8,500 V and drift gas temperature was held at 180℃ 104

Figure 5.3: DTIMS Faraday responses for a standard solution of nicotinamide (NIC), 2,6-dtBP (dtBP), and trihexylamine (THA) 25 ppm w/v in 50:50 methanol/water as a function of drift gas temperature. DTIMS operation potential was set to +8,500 V, and drift gas flow rate and exhaust pump rate were 2.0 L min^{-1} and 0.5 L min^{-1}, respectively 107

Figure 5.4: DTIMS Faraday responses for a standard solution of nicotinamide (NIC), 2,6-dtBP (dtBP), and trihexylamine (THA) 25 ppm w/v in 50:50 methanol/water as a function of DTIMS operation potential. Drift gas temperature was set to 180 ˚C, and drift gas flow rate and exhaust pump rate were 2.0 L min^{-1} and 0.5 L min^{-1}, respectively 109

Figure 5.5: Comparison of the peak intensity distribution in mass spectra acquired for a 25 ppm w/v solution of mobility standards setting both DTIMS gates open (A) or fixing BNG #2 open for 12 ms (B). The inset in (B) shows the Faraday image for the gated-mode acquisition 111

Figure 5.6: Faraday response (A), "scan mode" MS TIC (B), and total mass spectrum (C) acquired for a 25 ppm w/v solution of mobility standards scanning BNG #2 between 4-16 ms in the drift window using a 100 µs gate pulse width and a 25 µs scan step.....112

Figure 5.7: Faraday signal response for 4 ppm w/v citric acid in 80:20 methanol/ water using increasing DTIMS BNG #1 pulse widths. DTIMS operation potential was -7000 V, drift gas temperature was 200 ˚C, and drift gas flow rate and exhaust pump rate were 2.0 L min-1 and 0.5 L min-1, respectively.....113

Figure 5.8: MS TIC signal for 10 ppm w/v citric acid in 80:20 methanol/water using increasing DTIMS BNG #2 pulse widths over a 2.5 ms scan window. The BNG #1 pulse width was 100 µs and the scan step was 25 µs. DTIMS operation potential was -7000 V, drift gas temperature was 200 ˚C, and drift gas flow rate and exhaust pump rate were 2.0 L min^{-1} and 0.5 L min^{-1}, respectively 114

Figure 5.9: MS TIC signal for 10 ppm w/v citric acid in 80:20 methanol/water using increasing DTIMS BNG #2 scan step ratios over a 2.5 ms scan window. BNG #1 and #2 pulse widths were set equal at 100 µs. DTIMS operation potential was -7000 V, drift gas temperature was 200 ˚C, and drift gas flow rate and exhaust pump rate were 2.0 L min^{-1} and 0.5 L min^{-1}, respectively 116

Figure 5.10: Citric acid concentration curve for dual-gate AP-DTIMS-Orbitrap MS as a function of Orbitrap maximum injection time (IT). DTIMS BNG #1 pulse width was set to 100 µs and BNG #2 was fixed open from 8.5-11 ms (2.5 ms window). MS automatic gain control was held at 5.0E+06. A trend-line is drawn for the linear dynamic range (0.1-10 ppm). The inset shows a similar curve trend for a scanned-gate acquisition over the 2.5 ms window (BNG #1 and #2: 100 µs, scan step: 25 µs).....118

Figure 5.11: Scan mode analysis signal for 25 ppm w/v citric acid using high AGC (5.0E+06) and low AGC (2.0E+04) and a maximum injection time set to 1000 ms. (BNG #1 & #2: 100 µs, scan step: 25 µs).....119

Figure 5.12: Mass spectrum and Faraday response (*inset*) for 100 ppm w/v of mixture of [Ser-Asp-Gly-Arg-Gly] and [Gly-Arg-Gly-Asp-Ser] peptide isomers in 50:50 acetonitrile/water with 0.1% formic acid (A). All ion fragmentation HCD using a normalized collision energy of 20 V of the independent peptide isomers separated by ion mobility (B and C). (DTIMS operation potential: 10,000 V, drift gas temperature: 220 ˚C, drift gas flow rate: 3.0 L min^{-1}, exhaust pump rate: 1.5 L min^{-1}). Asterisks (*) denote identified sidechain fragments of serine, aspartic acid, and arginine.....120

Figure 5.13: AP-DTIMS-Orbitrap MS analysis for 100 ppm solution (w/v in 50:50 methanol/water) of 3 saccharides: D-(+)-melebiose, D-(+)-melezitose, and D-(+)-raffinose. Panels show the extracted mass spectra for each mixture component (A), the corresponding Faraday response (B), a map of the chemical space with m/z plotted as a function of drift time (C), and the extracted MS total ion chronograms (D). (BNG#1 & #2: 200 µs, can step: 50 µs; AGC: 5.0e+06, IT: 1000 ms, Resolution: 35,000). 122

Figure A.1: Schematic (**a**) and photograph (**b**) of active HF-DBD 140

Figure A.2: Schematic (**a**) and photograph (**b**) of active LTP.....141

Figure A.3: Schematic (**a**) and photographs of active glow discharge using DC excitation (**b**) and AC excitation (**c**).....142

Figure A.4: Schematic of low-pressure reference discharge cell 143

Figure A.5: Diagrammatic illustration of the atomic absorption instrument. The low-pressure discharge cell was only in place during wavelength calibration measurements 144

Figure A.6: Absorbance spectra for low-pressure reference discharge (gray trace) and HF-DBD (bold trace).....147

Figure A.7: Absolute number densities of He_m in the HF-DBD as a function position in the luminous plasma plume downstream from the capillary exit. The error bars represent the standard deviation of 24 replicate determinations made in rapid succession.....148

Figure A.8: Time-resolved absorbance measured in the HF-DBD afterglow 0.5 mm downstream from the capillary exit. The dashed trace is the applied voltage waveform from the power supply and the bold signal trace is the HF-DBD absorbance.....151

Figure A.9: Time-resolved absorbance measured for the LTP plasma plume 0.5 mm downstream from the capillary exit. The dashed trace is the applied voltage waveform from the power supply and the bold signal trace is the LTP absorbance.....152

Figure A.10: Time-resolved absorbance measured for the AC-excited glow discharge midway between electrodes. The dashed trace is the applied voltage waveform from the power supply and the bold signal trace is the plasma absorbance 153

Figure B.1: Schematics and images of the metal-insulator-metal (MIM) microhollow cathode discharge (MHCD) microplasma device. Detailed component breakdown of the MHCD assembly (**a**). Side-view (**b**) and front-view (**c**) of the source showing an active discharge plasma in operation using 0.3 L min^{-1} nitrogen gas 159

Figure B.2: Mass spectra of target ISS test analytes acquired using DART and MHCD microplasma ion sources with nitrogen source gas at 2.2 L min^{-1} and 0.5 L min^{-1}, respectively. Spectra for DART (left column) and MHCD (right column) are shown for background ions (**a**), methanol (**b**), ethanol w/ 0.5% IPA (**c**), isopropanol (**d**), and acetone (**e**) 161

Figure B.3: Microplasma mass spectra for volatile analytes methanol (**a**), ethanol (**b**), isopropanol (**c**), and acetone (**d**). Spectra were acquired using nitrogen (green), Ar (purple), and He (orange) discharge gases at optimized flow rates of 1.0, 0.3, and 0.5 L min^{-1}, respectively, and plasma currents of 0.050 mA for all gases. Identified species are indicated by markers, showing $[M+H]^+$ (black triangles), $[M+NH_4]^+$ (black stars), and $[2M+H]^+$ (black circles). Spectra are an average of three trials collected from one total ion chronogram taken over multiple insertions of capillary probes carrying volatile sample 164

Figure B.4: Peak areas of the $[2M+H]^+$ species detected for methanol (**a**), ethanol (**b**), isopropanol (**c**), and acetone (**d**) using argon (purple), helium (orange), and nitrogen (green) gases with the MHCD (left) and DART (right) source. Flow rates were 0.05, 0.15, 0.3, 0.5, and 1.0 L min^{-1} for the MHCD and 0.15, 0.3, 0.5, 1.0, 1.4, 1.8, and 2.2 L min^{-1} for DART. Error bars were derived from the standard deviation of three trials 165

Figure B.5: MHCD microplasma power consumption as a function of plasma gas type for a constant gas flow rate (0.100 L min^{-1}) using nitrogen highlighted in green (diamonds), argon highlighted in purple (squares), and helium highlighted in orange (triangles) 168

Figure C.1: Showcase of newly machined parts for dual-gate resistive glass AP-DTIMS 172

Figure C.2: Photograph (top) and cartoon schematic (bottom) of assembled dual-gate resistive glass AP-DTIMS prototype 174

Figure C.3: Corona discharge RIP signal transmission with different fixed voltages applied to the second BNG. Faraday response observed without drift gas or heating 175

Figure C.4: Example of periodic noise and the Faraday response induced by the second gate trigger pulse. No ion source or aperture grid present 176

Figure C.5: Faraday signal for corona discharge of neat DMMP vapor and the residual trigger pulse response at the fringes of the 80 ms drift time window using a low grid density aperture.....177

LIST OF SYMBOLS

V (kV)	Voltage (kilovolts)
A (*mA*, *μA*)	Ampere (microampere, milliampere)
W	Watt
Hz (*kHz*, *MHz*)	Hertz (kilohertz, megahertz)
$M_{(s,g)}$	Analyte Molecule (solid or gaseous)
$M^{+\cdot}$	Molecular Ion
$[M+H]^+$	Protonated Ion
S_n	Solvent Molecules
$S^{+\cdot}$	Solvent Molecular Ion
$[nS+H]^+$	Protonated Solvent Cluster Ion
*He**	Helium Metastable Atom
N_2*	Nitrogen Metastable Molecule
$2s\ ^3S_1$	Helium Excited/Metastable State
$A^3\Sigma_u^+$	Nitrogen Excited/Metastable State
K	Ion Mobility *or* Temperature Kelvin
m	Mass
D	Diffusion Coefficient
k_B	Boltzmann Constant
T	Temperature
q	Ion Charge State
E	Electric Field

L	Length
v_d	Drift Velocity
t_d	Drift Time
μ	Reduced Mass (ion and gas molecule)
N	Gas Number Density *or* Theoretical Plate Number
Ω	Collision Cross-Section
K_0	Reduced Ion Mobility
P	Pressure
R_p	Resolving Power
w_h	Peak Width at Half Height
w	Peak Width
t_g	Time Width of Ion Gate Pulse
t_{diff}	Diffusion Broadening Time Term
R_{pp}	Peak-to-Peak Resolution
α	Separation Factor
R_g	Ion Gate Pulse Width Contribution to Resolving Power
R_{diff}	Diffusion-based Contribution to Resolving Power
$Å$	Angstrom
A_v	Transition Dependent Absorbance
$\Delta\lambda$	Spectral Free Range
S_v	Spectral Line Function
o.d.	Outer Diameter
i.d.	Inner Diameter
M (μM, mM)	Molar Concentration (micromolar, millimolar)

ppm	Parts-per-Million
w/v	Weight-by-Volume

LIST OF ABBREVIATIONS

ADI	Ambient Desorption Ionization
AC	Alternating Current
AP	Atmospheric Pressure
APCI	Atmospheric Pressure Chemical Ionization
APPI	Atmospheric Pressure Photoionization
CCS	Collision Cross-Section
DAPPI	Desorption Atmospheric Pressure Photoionization
DART	Direct Analysis in Real Time
DBDI	Dielectric Barrier Discharge Ionization
DC	Direct Current
DESI	Desorption Electrospray Ionization
DMMP	Dimethyl methylphosphonate
DMS	Differential Ion Mobility Spectrometry
DTIMS	Drift Tube Ion Mobility Spectrometry
ESI	Electrospray Ionization
ETV	Electrothermal Vaporization
FAIMS	Field Asymmetric Ion Mobility Spectrometry
FAPA	Flowing Atmospheric Pressure Afterglow
FT	Fourier Transform
FT-ICR	Fourier Transform-Ion Cyclotron Resonance
FWHM	Full Width Half Maximum
GD	Glow Discharge

GIST	Gas Ion Separator Tube
HF-DBD	High Frequency-Dielectric Barrier Discharge
ICP	Inductively Coupled Plasma
IP	Ionization Potential
IMS	Ion Mobility Spectrometry
IM-MS	Ion Mobility-Mass Spectrometry
IR-LAMICI	Infrared-Laser Ablation Metastable Induced Chemical Ionization
LA	Laser Ablation
LD	Laser Desorption
LOD	Limit of Detection
LTP	Low Temperature Plasma
MALDI	Matrix Assisted Laser Desorption Ionization
MIM	Metal-Insulator-Metal
MHCD	Microhollow Cathode Discharge
MS	Mass Spectrometry
MSI	Mass Spectrometry Imaging
NIC	Nicotinamide
OES	Optical Emission Spectroscopy
PA	Proton Affinity
PADI	Plasma Assisted Desorption Ionization
RASTIR	Remote Analyte Sampling and Transport Ionization Relay
RF	Radio Frequency
SIMS	Secondary Ionization Mass Spectrometry
SNR	Signal-to-Noise Ratio
SVP	Simplified Voltage and Pressure

THA	Trihexylamine
TIMS	Trapped Ion Mobility Spectrometry
ToF	Time-of-Flight
TLC	Thin Layer Chromatography
TM	Transmission Mode
TWIMS	Traveling Wave Ion Mobility Spectrometry
VaPI	Vacuum-assisted Plasma Ionization
2,6-dtBP	2,6-ditertbutyl pyridine

SUMMARY

Mass spectrometry (MS), a technique for measuring and identifying charged molecules based on their intrinsic masses, is an essential analytical tool. The technique has matured drastically since its conception in 1912, where J. J. Thomson and F.W. Aston first demonstrated the modest yet remarkable detection of discrete neon isotopes while studying canal rays. MS is now routinely used in applications ranging from forensic screening and clinical diagnostics to environmental monitoring and manufacturing quality control. To satisfy the growing number and diversity of applications, modern instruments are equipped with several modular ion source options and often feature multiple analytical stages for ion filtering, activation, or tandem ion selection/separation prior to detection. The field of mass spectrometry has progressed so rapidly, in fact, that many of the current MS analyzer technologies are reaching their theoretical limits for accuracy and resolving power. Likewise, the advanced data-processing tools being developed for MS-based chemical imaging and "-omics" fields have expanded spectral discrimination and compound identification capabilities through use of machine learning and predictive modeling. A consistently active area of research, meanwhile, is still focused on improving sampling efficiency and maximizing throughput to enhance instrument sensitivity, dynamic range, and peak capacity. A detailed introduction to modern MS instrumentation and the emergent role of ambient ion sources for these analytical platforms is provided in **Chapter 1**.

As a longstanding member of the Center for Chemical Evolution at Georgia Tech, an overarching motivation for this body of work has been the development of MS instrumentation and methods suitable for analysis of the often intractable mixtures produced in model prebiotic reactions. Along this vein, the bulk of initial research presented has sought to understand and control the variables affecting sampling

efficiency with a new generation of plasma ion sources. Firstly, in **Chapter 2**, the operational mechanics of a commercial glow discharge source were evaluated to inform proper sampling strategies based on real-time visualization of source gas fluid dynamics. A parallel investigation involving absorption spectroscopy of the active metastable populations generated in plasma discharges was also carried out to elucidate potential differences in ionization efficiency between typical plasma device architectures (summarized in **Appendix A**). Findings from these studies inspired the development of a versatile hybrid plasma source, described in **Chapter 3**, which incorporated two interchangeable sampling modes to enhance compatibility with various sample formats while also improving sensitivity and sampling reproducibility. Although tangent to the work in Chapter 3, the incentive to engineer ultraportable ambient ion sources for environmental monitoring applications also prompted the design and characterization of a miniaturized, low-resource microplasma discharge source for operation aboard the International Space Station (reported in **Appendix B**).

The final undertaking along this research track is discussed in **Chapter 4**, where the ion source described in Chapter 2 was inventively coupled with standalone atmospheric pressure drift tube ion mobility spectrometry (AP-DTIMS). Using a new plasma source configuration, the electric field of the prototype ion mobility detector inlet was favorably shaped to restore sampling capacity for rapid compound screening. Concepts and instrumentation from Chapter 4 lay the foundation for the last research theme in this dissertation. Transitioning beyond optimization and development of the source-instrument interface, the next objective was to integrate high-resolution AP-DTIMS with ultra-high resolution, accurate mass Orbitrap mass spectrometry. The project described in **Chapter 5** entails parameter space characterization and a brief suite of benchmark applications for this unprecedented combination of techniques, which used together, promised superior separation power over contemporary systems featuring reduced-pressure mobility stages as well as higher mass accuracy and sensitivity than

traditional time-of-flight mass analyzers. The DTIMS prototype from Chapter 4 was additionally modified with dual ion shutters, approximating a higher resolution alternative to the commercial ion mobility counterpart featured in Chapter 5, and was primed for experiments ultimately involving a digitally-multiplexed ion gating approach to improve duty cycle and sensitivity with MS (highlighted in **Appendix C**). At last, concluding remarks in **Chapter 6** offer the final perspectives learned from these efforts in the context of ongoing research in the field, and suggest future paths forward for ambient ion source and ion mobility development for MS.

CHAPTER 1: INTRODUCTION

1.1. Abstract

This chapter provides a thorough survey of new and applied technologies in the field of mass spectrometry involving ambient ion sources and ion mobility instrumentation developed for multi-dimensional analytical platforms. An overview of ambient/desorption ionization is presented, and the device design, principles of operation, sampling methodology, and target applications for a subset of plasma-based ambient ion sources are discussed in detail. Strategies for coupling these ambient sources with different detector formats are also described. Finally, the attributes and capabilities of several ion mobility techniques are reviewed as well regarding their evolving roles for ion separation and filtering when integrated with different types of mass analyzers.

1.2. Ambient Desorption/Ionization

The term “ambient,” as it pertains to MS analysis, delimits probing of samples in the immediate or open environment surrounding the spectrometer inlet in the absence of ion source enclosures. In this way, it is distinct from traditional atmospheric pressure ionization methods, like electrospray ionization (ESI), atmospheric pressure chemical ionization (APCI), atmospheric pressure photoionization (APPI), and atmospheric pressure matrix-assisted laser desorption ionization (AP-MALDI), but encompasses adaptation of these techniques for the purpose of direct analysis of substrates and samples in their native form. The criterion for ambient analysis typically involves analyte desorption and ion generation in successive order without extraneous and protracted sample preparation, pretreatment, concentration, or chromatography. Some of the most widely recognized and routinely implemented ambient desorption/ionization source schemes are shown in Figure 1.1.

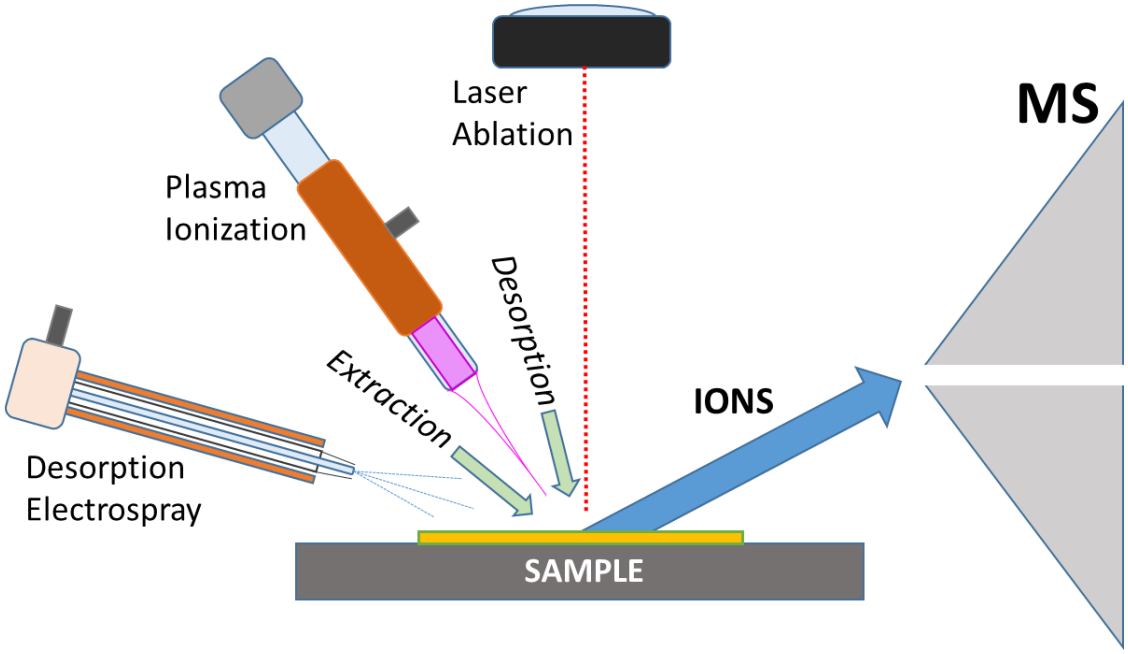

Figure 1.1: Illustration of common ambient desorption/ionization approaches.

The advent of desorption electrospray ionization (DESI)[1] in 2004 and direct-analysis-in-real-time (DART) in 2005[2] ushered in the modern era of ambient desorption/ionization (ADI) source development and application with MS. DESI employs a highly-pressurized electrospray to wet planar sample surfaces, inciting a dynamic solid/liquid extraction process, followed by ejection of charged droplets that undergo evaporation and Coulombic fission, where after ionization ensues by standard ESI ion evaporation or charge deposition model mechanisms. DART, conversely, is less restricted to 2D substrates, and uses a glow discharge to generate excited-state species in a heated gas stream that thermally desorbs and ionizes volatilized sample material. Once the exclusive domain of MALDI-MS and secondary ionization mass spectrometry (SIMS)[3], the power and utility of ambient sampling approaches like DESI were realized when used to chemically map surface areas by mass spectrometry, correlating analyte signal to specific locations across a sample[4]. DESI provides spatial resolutions averaging 100-400 µm, for which spot size is limited by solvent spread. Even higher spatial resolutions can be achieved with laser desorption by AP-MALDI in the range of

50-200 µm, or new scanning nanoprobe desorption techniques[5] that claim resolutions ≤1 µm. Mass spectrometry imaging (MSI) of biological tissue specimens (*e.g.* mouse brain cross-sections) for clinical analysis of lipids and proteins as disease biomarkers is at the forefront of MS research and is becoming a new niche for ADI sources[6].

Since DESI and DART emerged simultaneously, ADI sources have become far more diverse in form and function over the past decade. Most ambient ionization sources can be categorized based on their desorption format, including solvent spray-based, photoacoustic (laser) ablation-based, and plasma discharge and/or thermal desorption-based. Decoupled from the ionization process for a singular technique, these desorption motifs are constantly rearranged in new permutations to enable different multimode source constructs. Some of the most recognizable forms of these hybrid techniques include desorption atmospheric pressure photoionization (DAPPI)[7], laser ablation electrospray ionization (LA-ESI)[8], and laser desorption paired with APCI (LD-APCI)[9] and different plasma discharge ion sources to be mentioned later. The advantage of these composite ADI approaches is the ability to tailor desorption chemistry, energy, and spatial resolution while refining ionization efficiency and selectivity. For instance, DAPPI uses toluene for desorption, and although a poor ESI solvent, for photoionization the toluene doubles as a dopant to facilitate charge transfer. LA-ESI is another good example. Where the surface extraction process of DESI may be too inefficient for particular analytes or larger molecules, laser ablation can offer superior spatial resolution with more rapid raster scans and produce an abundance of neutral species without theoretical size/chemical restrictions to be accumulated and effectively ionized by ESI mechanisms. The list of ADI sources using variations on a theme of desorption or ionization method continues to be populated, with now over 50 combinations to suite different applications[10].

1.2.1. An Overview of Plasma-based Ion Sources

In the field of ambient desorption/ionization, plasma-discharge ionization continues to be a burgeoning source genre. The origins of these devices can be partly traced back to glow discharge (GD) sources used in optical emission spectroscopy (GD-OES) and mass spectrometry (GDMS), and metastable beam sources used for lithography and surface analysis[11, 12]. Ambient plasma discharges operate at scaled-down powers and temperatures to enable chemically "soft" molecular ionization rather than elemental analysis.

Plasma sources for ADI-MS have garnered wide acceptance and demonstrated utility for rapid, routine detection of small molecules in homeland security and forensic applications[13, 14], environmental[15, 16] and reaction monitoring[17], food[15, 18] and drug quality analysis[19-21], and more recently in metabolic fingerprinting for diagnostic applications[22, 23]. Such devices advantageously enable direct probing of sample objects introduced into the discharge afterglow or plasma gas stream at the spectrometer inlet, thus serving as attractive alternatives to electrospray or laser desorption ionization where minimal sample preparation and matrix-free chemical ionization are desired. Since direct-analysis-in-real-time (DART) was first reported by Cody *et al.*[2], a variety of different plasma ionization technologies have been developed, the most notable examples including low temperature plasma (LTP)[24], dielectric barrier discharge ionization (DBDI)[25], plasma-assisted desorption ionization (PADI)[26, 27], and flowing atmospheric pressure afterglow (FAPA)[28, 29]. Performance has been shown to be comparable between different source constructs, with unique plasma traits principally dictated by device dimensions, *I/V* characteristics and power regime (AC or DC), and the discharge gases used, mainly helium[30, 31]. LTP and DBDI share a common architecture, and employ an AC excitation of 2-5 kV_{p-p} with low kHz frequencies or to induce a plasma discharge between a metal pin electrode enclosed in quartz capillary dielectric and an external ring counter-electrode. Similar in design, PADI discharges are sustained using a lower V_{p-p}

with an RF (Mhz) frequency. DART and FAPA glow discharges are generated by continuous DC excitation between a point electrode and a disk electrode (DART) or capillary electrode (FAPA). While DART employs a ceramic heating element to facilitate thermal desorption, FAPA currents are high enough (~25 mA) to produce a "hot" plasma. For the typical helium discharge support gas used, standard plasma powers range from 1-5 W for LTP and DART to 5-30 W for FAPA and DBDI. The currently understood glow discharge mechanisms for positive ionization mode and the physiochemical variables influencing ionization efficiency are summarized in the next section.

1.2.2. Plasma Discharge Ionization: Principles and Mechanisms

Ionization pathways for the plasma device architectures mentioned are theorized to proceed similarly to those for atmospheric pressure chemical ionization (APCI) sources. But it is important to briefly distinguish APCI from plasma discharges or "metastable" ionization sources like DART or LTP, focusing on the mechanisms involved for the more commonly employed positive ionization mode. APCI features a corona discharge, an electrical breakdown in the Townsend regime induced by cosmic radiation (*e.g.* photons) that is not merely dictated by Paschen's law, as is truer for ambient plasma source discharges. And unlike these sources, the current density of a corona discharge (μA) is much lower than a DC glow discharge (mA) or AC plasma, and the Townsend breakdown is not self-sustained at the electrode. The APCI corona ionization cascade initiates with atmospheric reactant ions. Molecules excited by the high electric field protruding from the point electrode (+2-3kV) experience electron dissociation stimulated by photon collision. Electrons accelerated toward the positive point electrode collide energetically other excited molecules, triggering an avalanche of charge dissociation forming the "discharge." Reactions occurring in the plasma ionization region near the APCI corona tip are outlined below for atmospheric reagents and nebulized analyte molecule, $M_{(g)}$[32].

$$N_{2(g)} + e \rightarrow {N_2}^{+}{}_{(g)} + 2e \quad (1)$$

$${N_2}^{+}{}_{(g)} + 2N_{2(g)} \rightarrow {N_4}^{+}{}_{(g)} + N_{2(g)} \quad (2)$$

$${N_4}^{+}{}_{(g)} + H_2O_{(g)} \rightarrow {H_2O}^{+}{}_{(g)} + 2N_{2(g)} \quad (3)$$

$${H_2O}^{+}{}_{(g)} + H_2O_{(g)} \rightarrow {H_3O}^{+}{}_{(g)} + {OH}^{\cdot}{}_{(g)} \quad (4)$$

$${H_3O}^{+}{}_{(g)} + nH_2O_{(g)} + nN_{2(g)} \rightarrow (H_2O)_{n+1}{H^+}_{(g)} + nN_{2(g)} \quad (5)$$

$$M_{(g)} \xrightarrow{(H_2O)_{n+1}{H^+}_{(g)}} M(H_2O)_n{H^+}_{(g)} + H_2O_{(g)} \xrightarrow{-n(H_2O)_{(g)}} [M+H]^{+}{}_{(g)} \quad (6)$$

Ionization with ambient plasma sources ensues, instead, via highly energetic neutral excited-state species called metastables. A negatively biased DC glow discharge (≤5 kV) or similarly excited AC plasma, most often sustained using He or N_2 gas in these ADI devices, produces metastable species through ion-electron recombination events (He*, 2s $^3S_1$, 19.8 eV; N_2*, $A^3\Sigma_u^+$, 9.8 eV). The metastable-enriched gas is delivered to the sample, and either through direct exposure to the plasma afterglow or high temperature discharge gas, induces (thermal) desorption of sample molecules. (With DART, this stream is heated during transport the AP interface and passes through a secondary grid electrode for the purpose of filtering residual primary ions.) These volatilized molecules concomitantly undergo ionization either directly by Penning ionization or, more often indirectly by proton transfer with other protonated reactant ions. One suspected ionization pathway for generating protonated ions $[M+H]^+$ from He* is expressed below, which relies on ambient water cluster population as the primary proton vectors.

$${He^*}_{(g)} + nH_2O_{(g)} \rightarrow He_{(g)} + (H_2O)_{n-1}{H^+}_{(g)} + {OH^-}_{(g)} \quad (7)$$

$$M_{(s)} \xrightarrow{heat} M_{(g)} \quad (8)$$

$$M_{(g)} \xrightarrow{(H_2O)_{n-1}H^+{}_{(g)}} M(H_2O)_{m-1}H^+{}_{(g)} + H_2O_{(g)} \xrightarrow{-(m-1)H_2O_{(g)}} [M+H]^+{}_{(g)} \quad (9)$$

Although, spectroscopic measurements for a plasma source have identified many of the same reactant ions produced by APCI, so there is expected overlap with that ionization pathway[33]. The net reactant ion density generated by these metastables is presumably higher than for APCI corona discharge, but the key similarity between both APCI and "hotter" plasma based mechanisms is the formation of protonated water clusters that engage in proton exchange with gaseous analyte molecules. The ionization processes shown above have been simplified, when in reality, ambient sampling occurs from matrices of varying complexity. When considering analyte dispersed in organic solvent microenvironments, where the solvent molecules far outnumber ambient water clusters, the Penning ionization step is likely to proceed via the solvent molecules[34].

$$He^*{}_{(g)} + S_{(g)} \rightarrow He_{(g)} + S^{+\cdot}{}_{(g)} \quad (10)$$

$$S^{+\cdot}{}_{(g)} + S_{n(g)} \rightarrow [S-H]^{\cdot}{}_{(g)} + [S_n+H]^+{}_{(g)} \quad (11)$$

If the solvent or matrix molecules possess a higher proton affinity (PA) than water, the solvent is able to acquire a proton from water clusters and engage in proton transfer directly with a target analyte, again assuming the PA of the analyte is greater than that of the solvent.

$$[(H_2O)_m+H]^+{}_{(g)} + S_{n(g)} \rightarrow (H_2O)_{m(g)} + [S_n+H]^+{}_{(g)} \quad (12)$$

$$[S_n+H]^+{}_{(g)} + M_{(g)} \rightarrow S_{n(g)} + [M+H]^+{}_{(g)} \quad (13)$$

While steps 10-13 are presumed to dominate, it is also possible that a solvent molecular ion generated by Penning ionization can donate a proton to an analyte with a higher PA, or participate in direct charge transfer with an analyte having a low PA.

$$S^{+\cdot}{}_{(g)} + M_{(g)} \rightarrow [S-H]^{\cdot}{}_{(g)} + [M+H]^+{}_{(g)} \quad (14)$$

$$S^{+\cdot}_{(g)} + M_{(g)} \rightarrow S_{(g)} + M^{+\cdot}_{(g)} \quad (15)$$

It is believed the efficiency of these metastable-activated ionization pathways ultimately depends on the energy and number density of metastables produced, and this understanding is the subject of ongoing investigations under different plasma source conditions. Since discharge sources were only used to study positive ions in this dissertation, the mechanisms delineated here were exclusively for positive ionization mode. But, it is worthy to note these sources are also used for negative mode analysis, where O_2^-, NO_2^-, and NO_3^- are observed as some of the main reactant ions that lead to generation of deprotonated species.

1.2.3. Plasma Source Sampling Practice and Multimode Configurations

The simplest and most common sampling strategy for ADI sources like DART-MS involves inserting a sample-coated probe (e.g. glass capillary, cotton swab, or mesh) into the heated metastable gas stream, or plasma afterglow for LTP-type sources, between the ion source exit and the spectrometer inlet. Ionization efficiency with plasma discharge sources is determined by a number of factors[16, 35] including: the relative reactant ion population abundance, the effective temperature of the activated plasma gas, the proton affinity and volatility of the target analyte(s), the sample matrix concentration and composition, residence time of reactants in the sample region, and the fluid dynamics at the AP interface during sampling. Importantly, fluid dynamic effects play a critical role in the overall success of plasma discharge ionization by dictating analyte desorption and mass transport across gas boundary layers and directing the flux of ions to the spectrometer inlet.

Understandably, the main limitation with ambient MS analyses remains related to ion transmission efficiency, since fluid dynamics across the AP interface can be difficult to control. Reproducible sampling and quantitation with plasma discharge sources has proven quite complicated, necessitating the use of internal standards[36, 37] and automated

sampling approaches[35]. Much effort has been dedicated to improving the sensitivity and sampling efficiency of these ionization techniques with the aid of simulations that model gas flow patterns[38, 39] and real-time visualization of source gas flow profiles using the Schlieren technique[40, 41], like those described within this work. The most successful attempts at enhancing the quantitative capability of ambient plasma-based analysis have been realized primarily with DART-MS systems incorporating a Vapur® interface, rail-mounted sampling probes, and auxiliary pumping, all of which help entrain divergent gas flows toward the mass spectrometer inlet and reduce variability[42]. Likewise, implementation of sample templates with uniform geometries and properties assisting with even sample deposition or analyte absorption/extraction have helped increase quantitative consistency, and include permeable sample-coated screens or solid phase microextraction probes. More recently, continuous quantitative surface scanning with DART has been accomplished using planar substrates in place of capillary holders[43].

ADI sources continue to draw appeal for MS imaging applications, but the path forward using plasma discharge sources for this intent has required multimode sampling strategies. When used to directly probe large area substrates, the spatial resolution of plasma discharge sources is compromised by gas flow dispersal across the surface and/or diffusive coupling of the plasma afterglow streamer upon contact with the sample. With very acute source dimensions, reasonable lateral resolutions comparable to DESI were achieved[44]. A seemingly ideal complement to these plasma sources then, given the typically high discharge currents and gas temperatures employed, has been laser desorption. In addition to high spatial resolution, the laser component is able to surpass the upper mass limits of conventional thermal desorption while generating an abundance of neutral species for ionization, thus providing a usefulness beyond MSI applications for sensitive and controlled sampling. The combination of laser ablation and metastable-induced chemical or plasma ionization has been presented in several iterations, such as LA-FAPA, LA-DART, and LA-DBD, with relative success. However, these approaches

are affected by the same ablation plume dynamics influencing mass transport and the matrix suppression difficulties that have been a persistent pariah for AP-MALDI sampling schemes. Many of the reported hybrid AP laser desorption/plasma ionization setups, if not relying on an appropriate sample matrix, have necessitated secondary enclosures for sample containment and aerosol transport[45], have defaulted to targeting analytes that absorb strongly for the laser excitation wavelength (UV-Vis spectrum)[46], or have used excessive laser fluences in order to energize/eject sufficient analyte which can incite undesired fragmentation. Therefore, optimization of such a multimode source continues to be a matter of active research in this dissertation.

1.3. Ion Mobility Spectrometry: Separation and Detection

The underlying principle of ion mobility spectrometry holds that the rate at which an ion propagates through a pressurized atmosphere along an electric field gradient is contingent upon the extent of its interactions with the surrounding gas molecules; this rate factor, expressed as "mobility" (*K*), varies uniquely for an ion in proportion with its reduced mass, charge, and collisional cross-section. Thus, by tuning the physical properties of the buffer gas (*i.e.* composition, temperature, and pressure), as well as the magnitude of the electric field, discrete ions become temporally and/or spatially differentiated. Salient examples of different mobility motifs include classic drift tube ion mobility spectrometry (DTIMS), traveling wave ion mobility spectrometry (TWIMS), field-asymmetric or differential ion mobility spectrometry (FAIMS and DMS), and trapping ion mobility spectrometry (TIMS). Each of the various ion mobility methods use different metrics to translate resolving power, all resembling the expression ($m/\Delta m$) for MS analyzers, but correlate a dependence on time ($t_d/\Delta t_d$), collisional cross-section ($CCS/\Delta CCS$), or electric field strength ($E_c/\Delta E_c$)[47].

1.3.1. Drift Tube Ion Mobility Spectrometry: Principles and Theory

As the only format of IMS applied in this dissertation research, a more thorough description of DTIMS theory is provided here. Drift tube ion mobility spectrometry has been employed in the past few decades as a standalone detector for chemical warfare agents[48], explosives[49] and narcotics[50], environmental contaminants[51], foods[52], and pharmaceuticals[53, 54]. DTIMS offers good sensitivity with short (ms) analysis times, and resolving powers typically comparable to classic liquid chromatography systems, while also enabling the detection of optically non-active species. Spectrometer design is fairly straightforward, similar in concept and construction to time-of-flight MS detectors, the core element comprising a (most often linear) compartment with segmented electrodes that establish a time-invariant electric field gradient along the drift axis.

DTIMS is based on the gas phase electrophoretic separation of ions migrating through a weak electric field. As pulsed ion packets traverse this drift region in the presence of a pressurized gas, the collisional interactions cause dissimilar ions to separate from one another due to changes in velocity based on their unique size/shape and charge state[55, 56]. Assuming the traditional hard-sphere approximation for a molecule, ion diffusion D through a fluid is simply expressed with the Einstein relation

$$D = \frac{k_B T K}{q} \tag{16}$$

where k_B is the Botlzmann constant, T is temperature, q is the ion charge, and K is the ion mobility proportionality term. For ions diffusing in an electric field, the ion mobility can be redefined as the ratio between ion drift velocity v_d and the electric field E (V/cm^{-1}).

$$K = \frac{v_d}{E} = \frac{L^2}{V t_d} \tag{17}$$

The ratio in equation (17) is expanded to show the relation between the drift tube length L, the applied potential V, and the ion drift time t_d. A more comprehensive empirical description is given with the Mason-Schamp equation, which accounts for the ion mobility dependence on charge state e, and significantly, the properties that define collision gas interactions – the number density N of the gas, the reduced mass μ of the ion and neutral gas molecule, and the ion collision cross-section. (The α term, often neglected, is a small correction factor <0.02 for ions with masses larger than the buffer gas mass).

$$K = \frac{3q}{16N}\sqrt{\frac{2\pi}{\mu k_B T}}\frac{1+\alpha}{\Omega} \tag{18}$$

Of worthy note from equation (18) is the linear inverse proportionality of ion mobility with collision cross-section, the property correlated with ion shape and conformation. The Mason-Schamp equality holds true for standard DTIMS operation in the low electric field regime, where the thermal energy imparted to an ion is larger than the energy obtained from the electric field. Under these conditions (E/N<2 Td), the ion diffusion process is dominant and the drift velocity scales linearly with the electric field. At higher electric field strengths, like those typically implemented with FAIMS or DMS, ions gain excess internal energy and collisions with gas molecules become inelastic, causing the mobility to deviate from linearity as $(E/N)^2$. Only the low field limit behavior and applications relevant to DTIMS are discussed here.

Lastly, on account of the lack of standard IMS instrumentation and settings, mobility comparisons are tabulated using a reduced mobility value K_0. The below equation normalizes the mobility of a given ion measured over different system pressures and temperatures.

$$K_0 = K \times \frac{P}{760\ Torr} \times \frac{273\ K}{T} \tag{19}$$

DTIMS performance is evaluated by two essential parameters, resolving power and peak resolution. Much effort in DTIMS development has been devoted to enhancing sensitivity and resolving power. Optimization of the physicochemical parameters that govern resolving power and the corresponding theory have been extensively reviewed in the literature [57-61]. Classically, the resolving power (R_p) of a single Gaussian peak is expressed as

$$R_p = \frac{t_d}{w_h} \tag{20}$$

where t_d is ion drift time and w_h is peak width at half the maximal intensity measured on the detector. The peak width is the collective sum of several band-broadening terms, the most important of which are the initial pulse width, t_g and the width due to broadening of an infinitely narrow pulse by diffusion, t_{diff}. For shorter drift times, the gate pulse width term becomes increasingly more important.

$$w^2 = {t_g}^2 + {t_{diff}}^2 \tag{21}$$

The temporal duration measured at the anode, shown as t_{diff} above, can be expanded from the spatial standard deviation of the diffusion coefficient D (not shown) to yield

$$w^2 = {t_g}^2 + \left(\frac{16 k_B T \ln 2}{qV}\right) {t_d}^2 \tag{22}$$

From equations (20)-(22), it is deduced that the peak width, and ultimately the resolving power, are weighted by contributions from gate pulse width-limited and diffusion-limited regimes.

$${R_p}^{-2} = {R_g}^{-2} + {R_{diff}}^{-2} \tag{23}$$

The smaller of the two terms, R_g or R_{diff}, will dominate the overall resolving power. The quotient t_g^2 in equation (22) can be expanded with terms borrowed from Hill *et al.* so that equation (23) may be rewritten and as

$$R_p = \frac{1}{\sqrt{\frac{t_g{}^2 K^2 V^2}{L^4} + \frac{16 k_B T ln(2)}{qV}}} \tag{24}$$

In cases where $R_{diff} << R_g$ and diffusion dominates, optimal resolving power is achieved with the maximum applied voltage potential and lowest allowable temperatures (slower rate of diffusion). While if $R_g << R_{\text{diff}}$ is true, resolving power changes proportionately with V^{-1}, T^{-1}, L^2, and K^{-1}. Hence, improved separation efficiency occurs with elongated drift times for R_g, achieved by decreasing potential V, reducing initial gate pulse width t_g, and increasing drift length L. Standard operation relies on contributions from both quotients R_g and R_{diff} to balance sensitivity and resolution. In practice, however, the resolving power deviates negatively from prediction. The reduced separation efficiencies are attributed to Coulombic repulsions in the ion swarm and electric field inhomogeneities, which need to be accounted for empirically using correction factors.

Viewing IMS as a chromatographic technique, it is useful to quantify resolving power in terms of the number of theoretical plates, N.

$$N = 5.55\left(\frac{t_d}{w_h}\right)^2 \tag{25}$$

Like LC, the greater the number of theoretical plates, the greater the peak capacity and the better the resolving power. Relating equations (21) and (23), Hill and coworkers observed that separation efficiency in theoretical plates is contingent on initial gate pulse width, voltage potential, and temperature. The theoretical plate count increases with

smaller initial pulse widths and with lower temperatures due to longer separation drift times. The trend with electric potential is not as simple. Higher voltage potentials initially compensate for diffusional broadening, but eventually the number of theoretical plates decreases past a maximum potential as the drift time substantially decreases (meaning fewer effective plates). Typical high-resolution IMS systems are capable of averaging between 40,000-80,000 theoretical plates, corresponding to resolving powers of R_p~80-120.

The number of theoretical plates N, and by relation the resolving power (t_d/w_h), is linked to a second crucial measure of IMS performance, the peak-to-peak resolution R_{pp}.

$$R_{pp} = \frac{\sqrt{N}}{4}\left(\frac{\alpha - 1}{\alpha}\right) \tag{26}$$

Peak-to-peak resolution is a useful determination of the separation selectivity. The term α, or the separation factor, is a simple ratio of drift times for two separate peaks (t_{d2}/t_{d1}). As a function of drift time, the separation factor is sensitive to physical parameters including temperature and drift gas composition, but is independent of pressure. Reducing the pressure shifts the drift times equally for t_{d1} and t_{d2}, so the separation factor is unaltered. But, different drift times do not shift equally with changes in temperature. In studies by Tabrizchi *et al* [62, 63], the effects of temperature on drift time at sub-ambient pressures were correlated with the degree of ion-neutral clustering. Drift time varies linearly with pressure in accordance with the approximated Mason-Schamp derivation,

$$K \propto \frac{1}{t_d} \propto \frac{T}{P} \tag{27}$$

while changes with temperature deviate from expectation for certain ions. It is postulated that temperature affects the clustering equilibrium rate constant, which is exponentially expressed by the Arrhenius relation, and therefore the drift time variation is not always

linear. Conversely, pressure directly disturbs the extent of ion solvation by clustering neutrals, but not the rate constant, and is observed to scale linearly with drift time. So to improve the R_{pp}, temperature effects must be considered as the rate of ion-neutral clustering can change separation selectivity.

Like most chromatography, it should be apparent from this discussion that controlling resolution and resolving power in DTIMS *can* be a highly variable and complex procedure. But that variability ultimately imparts function and power to the technique.

1.3.2. Alternative Ion Mobility Techniques

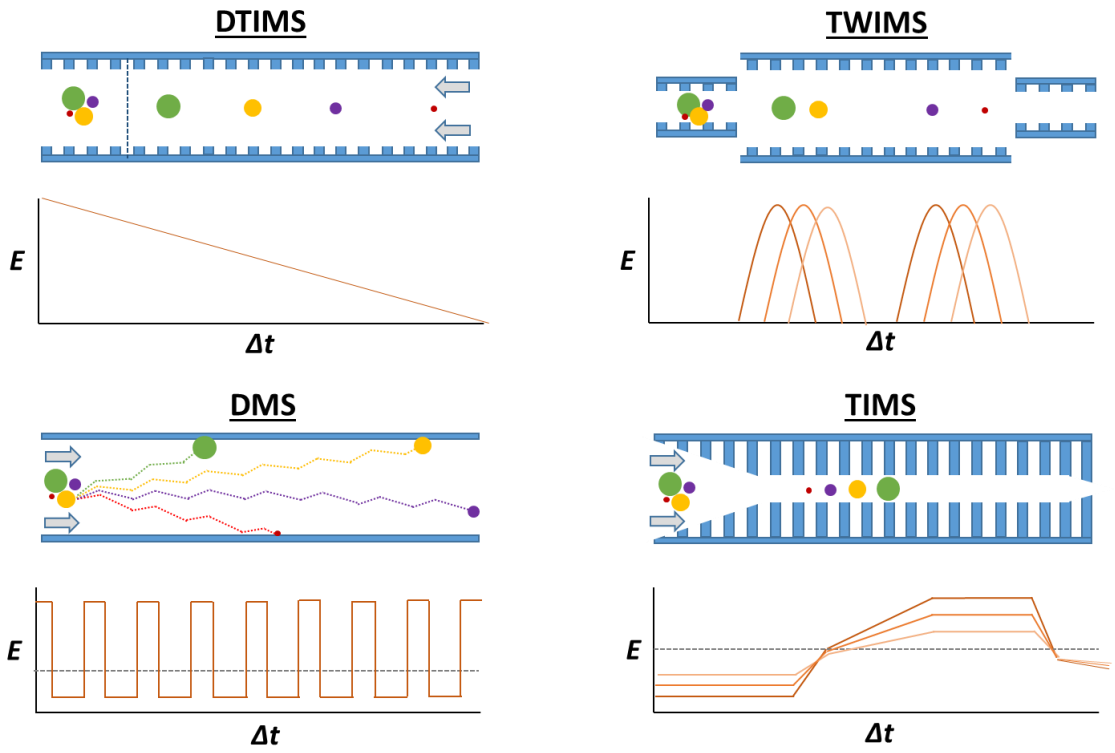

Figure 1.2: Simplified schematic representations of 4 main IMS formats: DTIMS, TWIMS, DMS, and TIMS. The electric field profiles employed (orange traces) are illustrated below the device architectures. Carrier/buffer gas flow directions are indicated with grey arrows. Ions are depicted as colored circles.

Together with DTIMS, a select subset of other IMS techniques are shown in Figure 1.2. Traveling wave ion mobility spectrometry (TWIMS) is a newer time-dispersive mobility motif unique from the classic DTIMS archetype. TWIMS employs an RF guiding potential to the stacked-ring drift cell electrodes for radial confinement. Superimposed on this RF waveform are symmetric DC potentials, applied to adjacent pairs of electrodes spaced five electrode segments apart, forming "waves" with adjustable amplitudes and velocities. As these DC waves propagate in sequence along the guide electrodes, they reinforce the electric field gradient. Smaller ions are propelled toward the detector riding the front edge of the waves, heavier ions bob as the potential waves roll over them, and those ions in between sizes are able to "surf" on the waves toward the detector[64]. Like atmospheric pressure DTIMS, TWIMS allows simultaneous acquisition of all ions being separated, but unlike DTIMS, does not provide absolute mobility values (without extra calibration steps) and, importantly, is strictly operated at reduced pressures (~3 Torr) and so offers relatively limited resolving powers (R_p<40). Although not discussed due to lack of commercial application, other important time-dispersive methods related to DTIMS include pulsed cyclotron[65, 66] and overtone ion mobility spectrometry[67-69].

Differential ion mobility spectrometry (DMS) and field-asymmetric ion mobility spectrometry (FAIMS) are spatially-dispersive IM techniques. They are intrinsically related to DTIMS, separating ions based on collision cross-section, but do so using variable electric field strengths to influence mobility K[70]. DMS and FAIMS operate on this same principle, but feature different geometries, with DMS employing a planar electrode arrangement and FAIMS utilizing a concentric cylindrical electrode configuration (the latter perhaps offering a small field focusing enhancement before transmission to a detector). Mechanistically with these devices, an atmospheric pressure carrier gas transports ions through an orthogonal electric field as a periodically oscillating asymmetric waveform cycles electrode potential between low- and high-electric field

regimes[71]. As ions migrate, their mobilities shift in relation to changes in ion-neutral clustering dynamics at different periods in the cycle due to the fluctuating electric field strengths, and thus ions experience uneven displacement in their trajectory toward one electrode according to their "differential" mobility. In order for an ion to pass to the detector without being eliminated on an electrode, the net or transverse velocity between electrodes must approach zero. A constant low potential compensation voltage (CV) is applied to one electrode in order to balance the asymmetric dispersion voltage (DV) and correct or restore transmission for selected ion mobilites. This CV can either be scanned or held constant to afford a full sweep of ion mobilities or filter selected mobilities, respectively. DMS has been successfully employed for aerosol particle analysis[72, 73] and in microfabricated nano-sensor units for explosives[74], but in practice now, they have found greater utility paired with higher specificity detectors.

Trapped ion mobility spectrometry (TIMS) is a method developed more recently than FAIMS or TWIMS, but borrows concepts from each. Explicit in the name, ions are "trapped" in an RF guide by the competitive fluid dynamic and electrostatic forces. Inverse to DTIMS, ions moving down a pressure gradient in a concurrent gas flow are separated and held stationary against an energy potential barrier. Gradually relaxing the fixed opposing electric field bias allows elution of different ions based on their mobility K over a tunable timeframe (10 ms to 1 s). Gas velocity and the magnitude of the ion guide entry bias have the greatest impact on separation efficiency, but resolving powers that rival high-resolution DTIMS can be achieved (R_p=100-250) and collision cross-section values can be derived[75, 76]. TIMS technology is still quite new, and the fundamentals continue to be explored.

1.4. Multidimensional Analysis Using Ion Mobility-Mass Spectrometry

The power and utility of IMS has been realized when coupled with modern mass spectrometry (MS), where it is being developed as a versatile tool for discriminating

compounds obscured in more complex environmental and biological sample matrices, such as crude oil or blood serum. A newfound practicality of IM-MS exists in differentiation of structural isomers, including peptides and polysaccharides, used to further validate or altogether replace isomer identification by tandem MS/MS fragment pattern correlation. Moreover, particularly relevant to the clinical "-omics" fields, IMS continues to aide structural elucidation of biopolymer conformations based on collisional cross-section measurements. A brief synopsis of IMS implementation strategies with MS is provided here to highlight the advantages and capabilities for different system configurations.

The oldest embodiment of ion mobility, DTIMS, was also the first commercial example of the technique coupled with MS using a quadrupole analyzer[77]. In later IM-MS arrangements, drift tube mobility separations became paired with time-of-flight ion detection. These configurations are ideally suited for time-nested analysis, where the mass spectrometer's faster microsecond scan speed enabled acquisition of several data points for each mobility peak eluted on the millisecond timescale. Significantly, these instruments generate data from which mobility/mass correlations may be derived, augmenting peak capacity and redistributing signal-to-noise across two dimensions. Plotting these correlations produces "trend-lines" for groups of ions based on mass and charge as a function of drift time (or collision cross-section) and vice versa[78, 79]. Interpretation of the trend-line slope and density confers information about the class of compound, ion charge state, and ion conformation. Accordingly, these IM-MS systems have become invaluable for studying structural biology.

In addition to accurate collision cross-section information, drift tube ion mobility separations carried out at atmospheric pressure have demonstrated much higher resolving powers than the other mobility techniques. Yet, few effective examples of atmospheric pressure (AP)-DTIMS coupled with MS have been reported[80] or have become commercially viable account of the inherently low throughput. The main disadvantage of

the DTIMS-(ToF) MS motif stems from the nature of time-dispersive ion mobility[47], as the conventional pulsed ion mobility scans, compounded by the requisite signal averaging, result in low duty cycles (≤0.01%) that compromise system sensitivity. Some instruments have alleviated this symptom by substituting the ToF detector with dedicated quadrupole/linear ion trap analyzers, which are able to compensate for losses in sensitivity, but at a sacrifice to scan speed, mass accuracy, and total peak capacity.

Modern IM-MS arrangements incorporating a time-dispersive mobility have instead repaired functionality by flanking the mobility cell with quadrupole or ion trap stages for ion selection, accumulation, and injection prior to subsequent ToF detection. These compartmentalized systems offer an additional advantage, enabling some combination of IM and MS/MS analysis for fragmentation studies. The Waters Synapt G2 HDMS represents the industry standard of this platform design, and the TWIMS component has been essential in generating a collision cross-section calibration database[81], creating a framework for studying charge state dependent molecular dynamics of protein complexes[82-84], and accomplishing energy-resolved separations of carbohydrate isomers[85]. However, since such system configurations have resorted to embedding the mobility cell inside of the instrument, where operation at reduced pressures (~1-10 Torr) is required, the achievable resolving powers are ultimately limited when equated to AP-DTIMS-MS configurations.

Ongoing efforts to recover sensitivity losses in AP-DTIMS-MS systems involve spatial and temporal multiplexing strategies. Spatial multiplexing, in short, envisions amplifying throughput by using a coordinated array of multiple ion mobility modules coupled to a single mass spectrometer. The more frequently demonstrated approach is temporal multiplexing, in which time-binned ion pulses are executed in specific sequences (*e.g.* up to 50% duty cycle per scan) and the oversampled composite spectra are deconvoluted post-acquisition by Fourier transform (FT) algorithms[86-89]. The latter approach has been shown to improve signal-to-noise by several-fold, and is an intended

feature of the instrumentation described in this work. Multiplexing approaches will also be necessary for coupling DTIMS more efficiently with ultra-high resolution FT ion trap analyzers, like Orbitrap-MS and FT ion cyclotron resonance (ICR)-MS, in order to reduce the total analysis times affected by the slow detection events. With these types of detectors, single spectral acquisition times based on image current collection or oscillating ion frequency scans can last several seconds or longer as the analyzer attempts to maximize intensity gain and peak resolution.

Matching the appropriate mobility format to the type of detector becomes an essential consideration. The throughput and sensitivity issues encountered with pulsed mobility techniques may be largely circumvented when using spatially dispersive or trapping IMS motifs. FAIMS/DMS has found success coupled to a variety of mass analyzers, including quadrupole, ToF, and FT-ICR MS for applications related to protein discovery[90] and oligosaccharide[91], lipid[92], and peptide[93] isomer discrimination. In constant CV bias mode, AP-FAIMS provides continuous sample throughput, and the sensitivity decline if scanning CV is not as severe as it is for DTIMS ion binning. But by comparison, FAIMS/DMS lacks the information simplicity and separation power of its time-dispersive IMS counterparts, and has worked best as a mobility filter that serves to minimize rather than enrich spectral density, for instance, helping to dramatically improve signal-to-noise with DESI-MS imaging of biological tissues[94]. The differential mobility aspect of DMS also exhibits greater orthogonality to MS than time-dispersive techniques, and so when integrated together in tiered DMS-IMS-MS configurations, peak capacity and signal-to-noise can be even further enhanced in three dimensions. In this way, DMS has been valuable for probing protein structure by using collisional heating to activate unfolding[95].

Distinct from DTIMS and FAIMS, TIMS offers many favorable attributes, simultaneously operating as an RF funnel for ion focusing, a trap for ion concentration, and a pseudo-classical drift mobility method to afford higher power separations based on

absolute collisional cross-section. Analytical throughput can be increased using selected or parallel accumulation strategies as well, making it advantageous for screening complex mixtures[96] important in metabolomics. TIMS duty cycle can also be tuned to suit the analyzer or to reach the desired R_p by executing multi-step or single-step elution gradient profiles for ToF or FT-ICR, respectively[97]. TWIMS, DMS, TIMS and more alternative ion mobility separation techniques are becoming competitive with traditional DTIMS as they are adopted into the mainstream. Yet until these methods mature, DTIMS continues to be preferred for its ease of use, higher resolving powers at sustainable pressures, and accurate collision cross-section information without additional calibration steps.

CHAPTER 2: SCHLIEREN VISUALIZATION OF THE FLUID DYNAMICS EFFECTS IN DIRECT ANALYSIS IN REAL TIME MASS SPECTROMETRY

Adapted from

Curtis, M.; Keelor, J. D.; Jones, C. M.; Pittman, J. J.; Jones, P. R.; Sparkman, O. D.; Fernández, F. M. *Rapid Commun. Mass Spectrom.* **2015**, *29*(5), 431-439.

2.1 Abstract

The success of ambient analysis using plasma-based ion sources depends heavily on fluid dynamics and mass transport efficiency in the sampling region. To help characterize the influence of these determining factors, visualization of the gas flow profile for a Direct Analysis in Real Time (DART) ion source at the mass spectrometer atmospheric pressure (AP) interface was performed using the Schlieren technique. The DART helium flow pattern was imaged in model systems incorporating different interface designs, i.e. skimmer or capillary inlet, and for sampling strategies using several types of traditional DART sample probes including a glass capillary, swab, and drug tablet. Notably, Schlieren experiments were conducted on instruments equipped with the gas-ion separator tube (GIST) adapter and Vapur® pump, and on setups featuring the transmission mode (TM)-DART module used in standard practice. DART sources were seen to produce a collimated, highly-laminar helium stream across interface distances up to ~8 cm. The helium stream was robust to the influence of gas temperature (50-500 °C) and flow rate ($\leq$ 3.5 L min^{-1}), but considerable DART gas deflection or full disruption was observed in each sampling scenario. The severity of the flow disturbance depended on probe size and placement, the GIST/Vapur® settings, or counter-current gas movements present at the interface. The real-time Schlieren visualizations introduced

here provide new insight on the fluid dynamics within the DART-MS sample gap while also helping to identify those experimental parameters requiring optimization for improved transmission.

2.2 Introduction

Thus far, DART has mainly been used for qualitative or semi-quantitative analysis, as quantification in ambient sampling with plasma sources is often plagued by poor reproducibility owing to the somewhat turbulent mass/fluid transport at the AP interface. DART-MS setups that implement automated sampling approaches for precise control have been demonstrated to improve consistency[42]. Even assuming consistent sample preparation and sampling procedure, accurate quantification with acceptable error typically requires addition of internal standards[36, 98, 99]. Although the reliance on standards ensures good precision, it does not guarantee maximum sensitivity, a fault which can often be credited to mishandled fluid dynamics in the sample gap.

Initial attempts at understanding the effect of fluid dynamic forces in DART-MS were undertaken by Harris *et al.* It was found that positioning the sample probe centrally within the DART gas stream served to maximize desorption efficiency, but could potentially disturb the gas flow and ion current stability. Both computational modeling and sensitivity experiments performed for capillary-deposited and drug tablet samples showed that introduction of solids, unlike volatiles, can drastically disturb, divert, or even completely obstruct the metastable DART gas stream away from the AP interface depending on placement[38, 39, 100]. Despite the usefulness of these previous finite element simulations, no results have been reported to date on the direct visualization of flow dynamics specifically within the DART-instrument sample gap with the aim of improving ion transfer efficiency and reproducibility in quantitative applications.

In seminal works by Pfeuffer *et al.*, the gas flow profile in the sample gap between a FAPA source and mock MS orifice was studied using the Schlieren

technique[41]. This technique is a clever means of visualizing gas flow patterns based on the "Schlieren effect," wherein gases can be distinguished by gradients in light intensity proportional to the change in density or refraction between media, and rendered "visible" using traditional optics[101, 102]. The images recorded by Pfeuffer *et al.* revealed useful information on the formation of gas boundary layers on top of sample substrates and the appearance of laminar and turbulent flow regimes affected by gas flow rate, source dimensions, and sample probe position. This work was recently expanded upon to include valuable MS sensitivity correlations for probe, mesh, and planar substrates[40]. The FAPA source, however, still remains largely confined to a single laboratory unlike the commercially popularized DART source.

The work herein has sought to complement earlier DART simulation studies and previous work with FAPA, and offer new insight on the fluid dynamics observed in the sample gap of a DART source. Schlieren imaging experiments were conducted to visualize gas flow patterns using typical source parameters and sampling modes with the DART coupled to several instruments bearing different inlet configurations, including those featuring the Vapor® gas-ion separator tube (GIST) pump and transmission mode (TM)-DART sampling geometry. The collection of Schlieren photographs and videos acquired helps rationalize common experimental difficulties with DART-MS attributed to fluid dynamic effects.

2.3 Experimental

2.3.1. Schlieren Apparatus

Schlieren imaging experiments were conducted using a single-mirror "double-pass" or coincident configuration[103]. Essential components included a parabolic mirror, a point light source, and a camera with a magnifying lens. A 75 mm diameter commercial grade spherical mirror (*f.l.* 750 mm) acquired from Anchor Optics (Barrington, NJ, USA) was secured on an adjustable lens mount in close proximity (~5 cm) to the visualization

zone at the DART-MS interface. The camera was positioned directly across from the mirror at exactly twice the focal length, oriented perpendicular to the mirror face along the axis of the mirror's center of curvature, see Figure 1. A light source fashioned from a 10-mm, 20 mA white light diode (Radioshack®, Fort Worth, TX, USA) was fixed above and back (~2 cm) from the edge of the camera lens. The diode was converted to a point source by cutting off the plastic bulb tip and covering the flat base with a foil cap bearing a pin-hole perforation. Mirror alignment was optimized by reflecting a laser beam, originating in place of the diode, off of the mirror and back into the camera lens. Thin plastic orange or blue colored filters were placed over the camera lens to improve image contrast. No knife edge beam stop was used. Images were captured as high definition videos (1920 x 1080, 24 fps), and individual frames selected for figures using one of two cameras, a Cannon EOS Rebel T3i with a 75-250 mm lens or a Cannon EOS 5D Mark II with a 400 mm lens (Cannon U.S.A., Inc., Melville, NY, USA).

2.3.2. Instrumentation

Three system combinations were investigated using the Schlieren technique for two DART ion source models interfaced to time-of-flight mass analyzers with either skimmer or capillary inlet designs. These configurations are representative of the common mass spectrometer inlet types and DART ion sources available. In system 1, a DART-SVP (simplified voltage and pressure) ion source (IonSense, Saugus, MA, USA) was paired with a JEOL JMS-T100LC AccuTOF^{TM} mass spectrometer (JEOL, Peabody, MA, USA) featuring a standard pin-hole (*i.d.* = 250 μm) skimmer orifice. In system 2, a Bruker micrOTOF-Q I mass spectrometer (Bruker, Bremen, Germany) equipped with a capillary inlet (*i.d.* = 400 μm) was interfaced with a first generation DART-100 source. For system 3, a DART-SVP source was coupled to a Bruker micrOTOF-Q II mass spectrometer.

Systems utilizing Bruker mass spectrometers were fitted with a gas-ion separator tube (GIST) flange connected to a Vapur® diaphragm pump (IonSense). The net volume of the GIST adapter was ~37-40 cm^3 depending on the positioning of the transfer tube (*l.* = 4 cm, *i.d.* = 0.65 cm) in proximity to the spectrometer capillary. Bruker micrOTOF instruments required use of the GIST and Vapur® pump to alleviate the DART helium gas load on the vacuum system turbo pumps. The JEOL AccuTOF system was capable of handing the helium load and was operated with no modifications to the atmospheric pressure interface. Vapur® pump flow rates were regulated using the supplied color-coded needle valve, corresponding to flow rates of 0-27 L min^{-1} measured with an Aalborg XFM mass flow controller (Aalborg, Orangeburg, NY, USA) when disconnected from the instrument vacuum. Nitrogen drying gas flow rates for the micrOTOF systems were adjusted between 1.4 and 2.0 L min^{-1} at 150 °C with the Vapur® pump active.

DART ion sources were operated with the helium gas at ambient temperature (~25 °C) and the discharge turned off unless otherwise specified, in which cases, the DART ceramic heater was set to temperatures up to 500 °C. Helium flow rates were set to 1-2 L min^{-1} using the bundled DART-100 software (parameters: flow factor = 0.3, regulator intake value pressure = 55 psi) or, where software control was not possible with the DART-SVP, regulated using an Aalborg GFC17 flow meter in-line with the ion source. DART nozzle exit diameters measured 3.5 mm and 2 mm for the DART-100 and DART-SVP, respectively.

2.3.3. Sample Probes and Modes of Analysis

A collection of traditional sample probes was surveyed on the different DART-MS setups. Probes sampled by the DART-SVP on the JEOL AccuTOF, system 1, included a glass melting point capillary, cotton swab, and drug tablet. The probes were manually inserted into the DART gas stream at positions close (1-2 cm) to the DART exit nozzle and the spectrometer inlet. The sample gap for system 1 was kept sufficiently

large (≤ 8 cm) to accommodate bulky probes while still affording clear visualization of the gas flow patterns. Fluid dynamics on system 2 between the DART-100 and Bruker micrOTOF-Q I were evaluated independently of sample probes to show the isolated effect of the GIST and drying gas variables on gas flow. System 3, also incorporating the GIST adapter, was selected to test TM DART-MS. Stainless steel mesh screens (1.1 cm diameter; ~30% void space) used for transmission mode analysis were mounted in a custom thin-sleeve plastic aperture and sampled by the DART-SVP on the Bruker micrOTOF-Q II. As in standard practice, the mesh was spaced 1-2 mm from the DART exit nozzle and less than 2 cm from the spectrometer inlet for most experiments.

2.4 Results and Discussion

2.4.1. Schlieren Imaging: Principles of Experimental Design

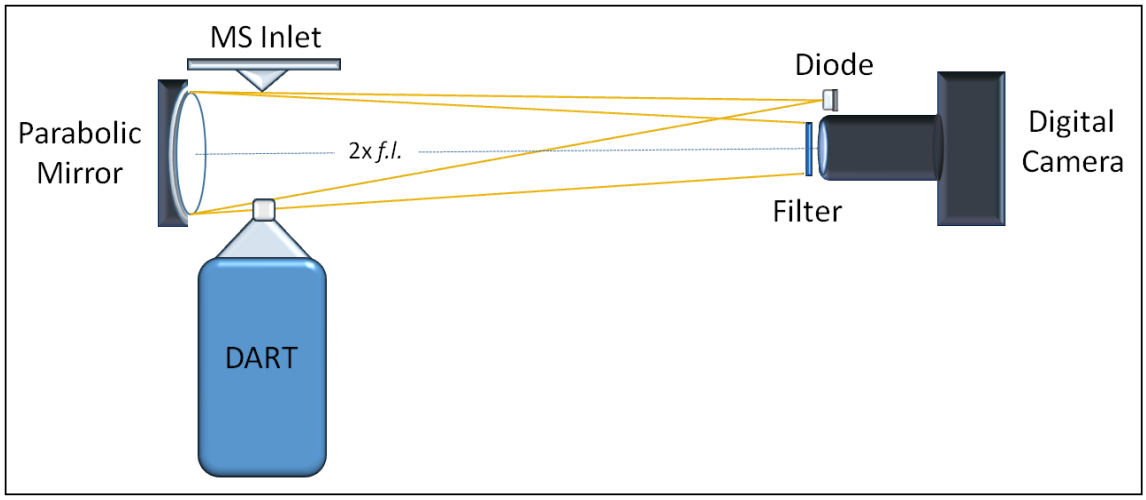

Figure 2.1: Diagram of single mirror or double-pass Schlieren configuration used for DART gas flow visualization in the AP interface.

Schlieren photography fundamentals and modern applications have been extensively reviewed by Settles[103], but the specific design and operation of the configuration used in this study are briefly described here. The single-mirror Schlieren apparatus for DART-MS gas flow visualization is depicted in Figure 2.1. When white diode light passes from air through the less dense helium DART stream, the velocity and

direction of the light rays are altered according to the angle of incidence and change in refractive index between the gaseous media. Light traversing between air and helium deviates upon refraction to generate bright and dark zones, as can be readily distinguished in a shadowgraph projection. This refraction occurs a second time in the Schlieren arrangement following reflection off the mirror. Cumulative light rays that are subsequently refocused and coincident along the vector being visualized then illuminate the helium stream to appear brighter than the surrounding air. Thus, the DART gas stream is optically differentiated from background air by the resulting gradients in light intensity that are recorded with the high-speed digital camera.

The light intensity varies proportionally in relation to the first spatial derivative of the refractive index gradient, and better contrast sensitivity is achieved for longer focal lengths as the degree of light refraction increases. Optionally, depending on the precision of component alignment, a portion of the deflected light may be obstructed by a beam cut-off at the projection point to further enhance contrast in the resulting gray scale image. Since color is more readily discernible than gray-scale tone, the typical knife-edge beam block was substituted in our setup for a blue filter at the camera lens. The Schlieren single-mirror configuration in this study affords improved sensitivity over the more common two mirror Z-type assembly on account of the doubled interaction of light with the subject area using a parabolic mirror. In addition, the setup is also relatively easy to align. However, a slightly off-axis arrangement between the light source and camera lens can produce a shadowing effect in images, which causes shadow borders to outline the helium stream and, for some cases, the sample probes in the test area appear duplicated.

2.4.2. General Gas Flow Characterization of DART-MS

Initial Schlieren experiments aimed at examining general DART gas flow mechanics were performed with the DART-SVP coupled to the JEOL AccuTOF mass spectrometer. A common misconception is that DART gas exiting past the secondary grid

electrode becomes instantaneously turbulent and dispersed, which in the absence of predictive simulations or direct visualization, helps to explain the rapid signal degradation over extended interface distances. Such a putative diffuse metastable plume would lead a user to position the sampling probe near the DART nozzle for maximal exposure to the activated helium and would suggest a substantially limited sample space, thereby making the device unusable for large-area sample substrates and diminishing the achievable spatial resolution in chemical mapping applications. In actuality, this Schlieren study shows the helium is expelled from the DART source as a highly-collimated, laminar gas stream. These findings are congruent with the Schlieren visualizations done for FAPA[40, 41].

Figure 2.2A shows the illuminated helium stream traveling right to left from the silhouette of the DART-SVP nozzle to the spectrometer skimmer. Looking closer at the DART helium column, the stream appears brighter where pure helium exits the DART nozzle and dimmer closer to the skimmer cone as the gas diffuses and the narrow beam broadens slightly. Upon arriving at the spectrometer inlet, the bulk of the incident stream is seen to follow the contour of the skimmer and spreads uniformly in all directions. The orange discoloration of the mixed helium plume blanketing the skimmer plate is an artifact of the blue contrast filter used and light scattering out of the viewing plane. The collimated jet stream was seen to persist across the entire span of the sample gap (~6 cm), remaining laminar for volumetric helium flow rates between 1 L min^{-1} and the ~3.5 L min^{-1} default rate, and for DART heater temperatures set up to 450 °C (not shown). It is suggested from these preliminary flow diagnostics that, unlike FAPA, the linear velocity of helium with DART is sufficiently low when exiting the relatively wide-diameter (*i.d.* 2 cm) of the DART-SVP nozzle to avoid early onset turbulence in the sample gap. Furthermore, similar to FAPA, the stream profile remains preserved at higher temperatures likely due to a favorable increase in gas viscosity correlated with a low Reynolds number (R_e<1000), as argued by Pfeuffer *et al.*[41].

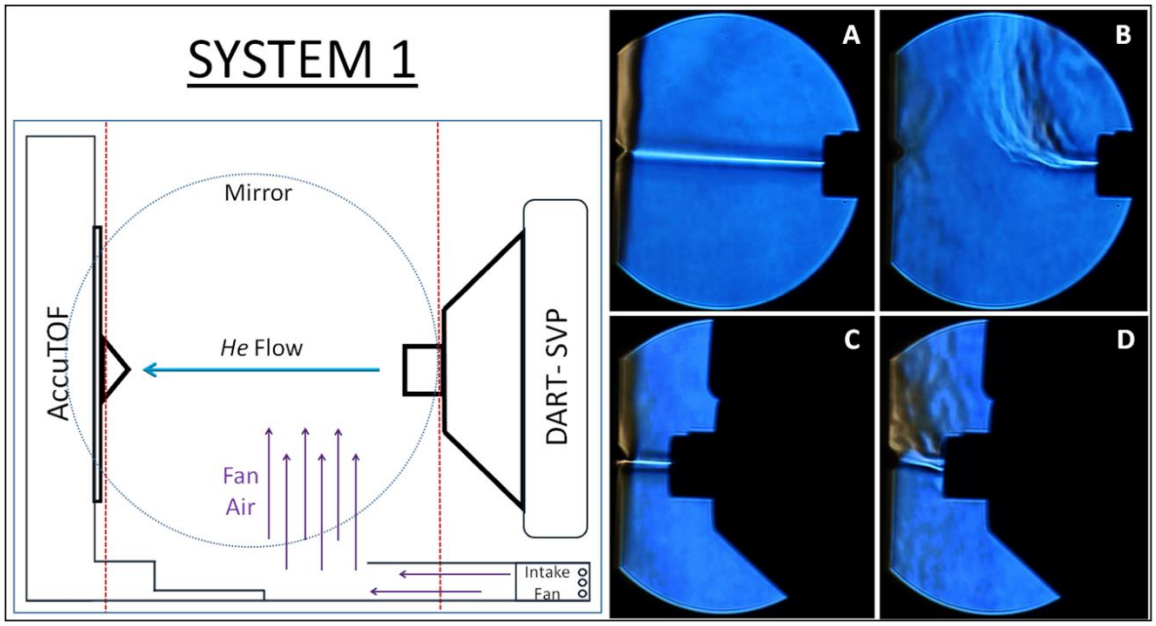

Figure 2.2: Schematic of system 1, where **solid bold lines** indicate visible silhouettes of the DART-SVP source and AccuTOF skimmer cone, and red dotted lines demarcate the test region visualized. Panels **A-D** show the metastable helium stream (default 3.5 L min^{-1}) over different AP interface distances when the AccuTOF cavity was properly covered (**A** and **C**) and left exposed (**B** and **D**). The interface distance was ~6 cm in **A** and **B** and ~1.5 cm in **C** and **D**. The helium stream remained collimated as in **A** for DART heater temperatures up to 500 °C.

DART-MS interface spacing is a critical factor impacting sampling efficiency. The distance is principally decided by the helium metastable longevity and DART stream stability under "dynamic" ambient conditions. Despite the rigid appearance of the DART stream in Figure 2.2A, the flow continuity is highly susceptible to disruption by cross-flowing air currents, as shown in Figure 2.2B. When the DART linear rail mount was removed, an open cavity situated several centimeters below the AccuTOF skimmer cone was exposed. Airflow from the instrument's front intake fan was blown upward through this opening and into the AP interface with enough force to upset the helium stream shortly past the DART-SVP nozzle. (Without the DART rail mount in place, a practical fix was to simply block the opening.) While the interface lengths shown in Figures 2.2A-B were increased for clear visualization, in practice the sampling distance is much shorter ($\leq$ 2 cm) in order to minimize metastable depletion and cooling of the helium desorption

gas. Figure 2.2C shows the strong DART stream for this reduced sample gap distance with the cavity covered, in which the collimated flow remains undisturbed. Turbulence was again present for the reduced interface distance in Figure 2.2D when the cavity was left unshielded exposing the intake fan exhaust, although the turbulence was less severe owing to a more enclosed spacing at the AP interface. As seen in the next section, contrary to an imagined disperse plume of helium, the linear DART gas profile observed here dictates the proper sampling technique for effective analyte desorption and the fluid dynamics favoring ion transmission.

2.4.3. Sample Probes and Sampling Strategies

Ideal DART-MS sample probes are adsorbent to concentrate analytes, thermally insulating to reduce heat dissipation hindering efficient desorption, and compact to minimize obstruction of the DART gas flow. Three standard types of hand-held sample probes exemplifying such traits were tested on system 1: a glass melting point capillary, a cotton swab, and a solid drug tablet held by tweezers. Probes were immersed in the DART stream at different depths and positions, either proximate to the DART-SVP nozzle or to the AccuTOF mass spectrometer skimmer. The sample gap spacing used was wider than in standard practice (~6 cm) for a clear view of the fluid dynamics. It should be noted that the MS ion signal was diminished or undetectable when using the extended AP interface distance, precluding signal correlation with these Schlieren flow diagnostics. The type of probe and the sampling approach used affected gas flow fidelity across the AP interface differently, and even the most compact probe (i.e. melting point capillary *dia.* 1.60 mm) was seen to have a dramatic impact on gas flow behavior. When a glass capillary was introduced ~1-2 cm downstream from the DART exit, the helium jet diverged abruptly upon contact. The split stream transiently re-converged further past the probe, but ultimately dispersed into turbulent eddies before reaching the spectrometer inlet (Figure 2.3A). The DART stream was better preserved when the capillary was

moved ~2 cm from the skimmer cone (Figure 2.3B). At this position in the interface, the path length for the scattered helium beam past the probe was small. In addition, it is likely that a combination of a lower helium velocity and the reduced pressure draw into the skimmer helped minimize spreading of the helium stream at the spectrometer inlet.

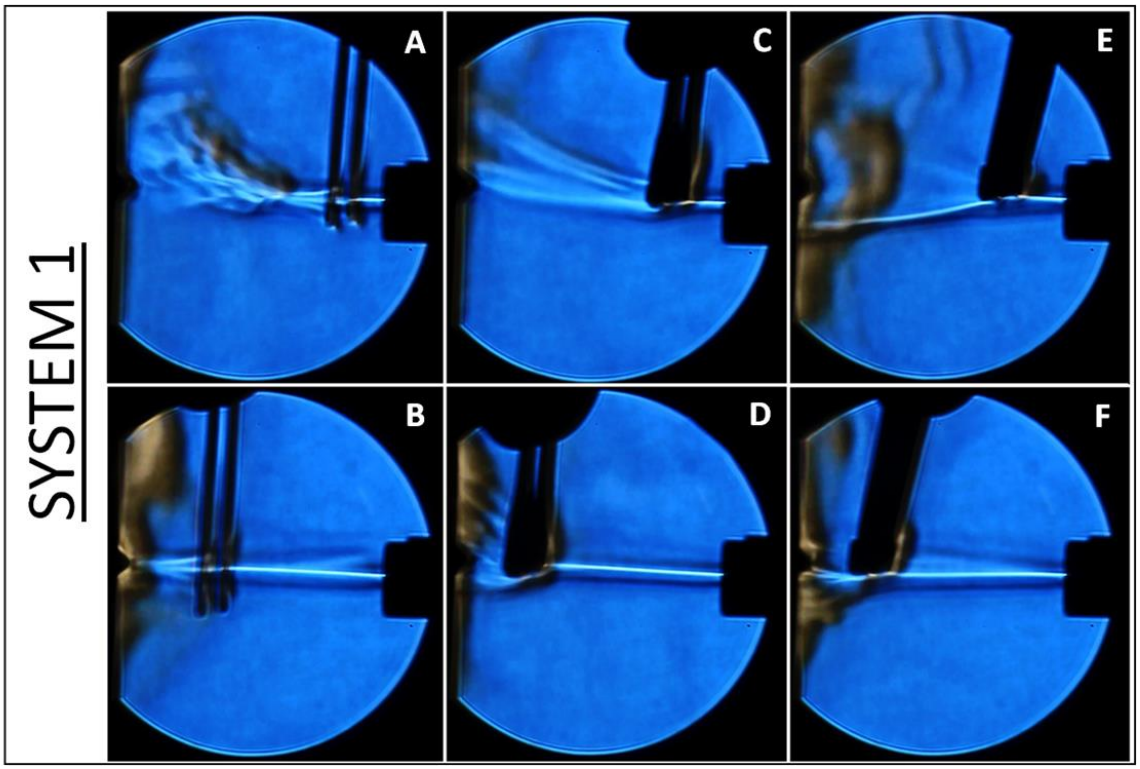

Figure 2.3: Helium flow profiles upon introduction of common sample probes used for DART-MS analyses. Panels **A**-**B** show a glass melting point capillary, **C**-**D** a cotton swab, and **E**-**F** a tablet in tweezers. Probes were inserted at two stream locations, one close to the exit of the DART-SVP (*top images*) and another close to the AP interface of the AccuTOF (*bottom image*s). The sample gap distance was maintained at ~6 cm and the default DART source helium flow rate (3.5 L min^{-1}) was used.

A bulkier probe, a cotton swab, was inserted into the stream next. Placing the swab close to the DART nozzle (Figure 2.3C), a portion of the helium stream followed the contour of the probe via the Coandă effect, as evidenced by the vertical orange-colored boundary layer. The remainder of the helium stream was bent vertically by the tip of the swab, fanning out toward and above the skimmer orifice. With the swab positioned nearer to the skimmer, the orange boundary layer remained present and the helium flow

past the probe was observably more dispersed (Figure 2.3D). The turbulence is attributed in part to the slightly more diffuse helium gas at this distance in the AP interface, and to the increased probe depth in the DART stream. Unlike with the narrow-body glass capillary, the DART gas interacts more extensively with the swab's larger surface area. This increased interaction possibly benefits desorption but clearly disrupts flow continuity, and full insertion of sample probes this size into the stream was seen to entirely obstruct gas flow. Similar effects were observed for the third type of probe examined, an open-face half drug tablet secured in tweezers. The tablet face was oriented toward the DART source and positioned along the stream border. As with the cotton swab, some of the helium spread over the tablet in a vertically extending boundary layer seen in orange, while part of the stream was redirected downward off the tablet edge (Figure 2.3E). If the tablet was dipped into the body of the stream, the gas beam was even more sharply deflected over the tablet corner than seen before with the rounded tip of the cotton swab. The stream missed the orifice even when the tablet was moved next to the skimmer, and acute turbulence was observed as in the case of the swab (Figure 2.3F).

Probe size, shape, and position in the sample gap must be considered carefully when developing the proper sampling method. As expected, bulkier probes interfere with the helium flow more severely. Stream disruption can be mitigated by sampling along the periphery of the helium beam. Increasing probe exposure time and surface area potentially improve desorption efficiency at the expense of a cohesive flow. In all cases, it is reasonable to assume gas dispersion losses during sampling could be minimized and spectrometer collection efficiency improved for a realistically reduced AP interface distance. Similar flow behavior was observed for some of these probes using DART gas heated to 450 °C, in which the stream appeared to exhibit subtly enhanced stability as a result of the increased gas viscosity and average linear momentum. Although not shown here, brief visualization of the DART source angled over a planar TLC substrate further demonstrated the tendency of helium DART gas to conform to rather than rebound from

the surface, but more informative images of the gas spread can be found in another study[40].

2.4.4. GIST Adapter and Vapur® Pump Effects

DART sources can be operated on all mass spectrometers that feature an AP interface. However, modern instruments that function using ultra low-vacuum pressures require an auxiliary pump at the AP interface to alleviate the strain of the DART helium gas load delivered to the turbo pumps. The Vapur® pump and GIST interface adapter commercially offered to suit this purpose were installed on a Bruker micrOTOF-Q I coupled to the DART-100 source. The first-generation DART-100 is a bulkier, more versatile version of the DART-SVP model used in the previous experiments, but the core device construction and operation are nearly identical. It has been proposed that the Vapur® and GIST elements may afford increased sample collection efficiency at the spectrometer inlet due to the assisting vacuum draw. However, this benefit is highly contingent on the interface design and Vapur®/GIST parameters, as well as the sampling method implemented and described in the next section. The effect of different Vapur® pumping volumes on DART gas flow stability was evaluated in combination with the instrument "drying gas" introduced at the AP interface of some instruments.

The large DART-100 mount for the Bruker instruments obscures the view of the GIST flange, but the assembly is illustrated in the Figure 2.4 schematic. Vapur® pumping volumes are regulated with a color-coded needle valve that scales purple-blue-yellow-green-gray. The colors correspond to approximate (±10%) ambient air pumping rates of 9 L min^{-1} (purple), 15 L min^{-1} (blue), 22 L min^{-1} (yellow), 26 L min^{-1} (green and gray), where for the fully opened valve, the 0.25" *i.d.* PTFE tubing connecting the Vapur® to the GIST adapter restricted the maximum achievable pumping volume. As surmised from flow effects in Figure 2.2B, the DART gas flow profile proved to be very sensitive to the Vapur® pump settings above a certain pump volume threshold. For color

dial settings below yellow (<20 L min^{-1}), the helium stream at 1 L min^{-1} remained steady and passed uninterrupted left to right from the DART to the GIST (Figure 2.4A). At or above the yellow dial setting, the helium stream became disrupted by regular pulsations caused by the diaphragm pump, with the turbulence becoming more extreme at the highest valve settings (Figure 2.4B-C). Interestingly, although the effective pumping rate was limited to ~26 L min^{-1} above the green dial marker, the perturbation was noticeably worse for the gray dial setting, Figure 2.4C. It is likely that the relief gas flow to the Vapur® pump was severely restricted at the highest pump rates by the narrow diameter junction (*i.d.* ~0.3 cm) to the Vapur® line on the GIST adapter, causing the choking effect. This observation may also be attributed to the added complications of the differential pressures at the interface, whereby the helium influx within the GIST chamber could be throttling the Vapur® pull volume and worsening the pulsations.

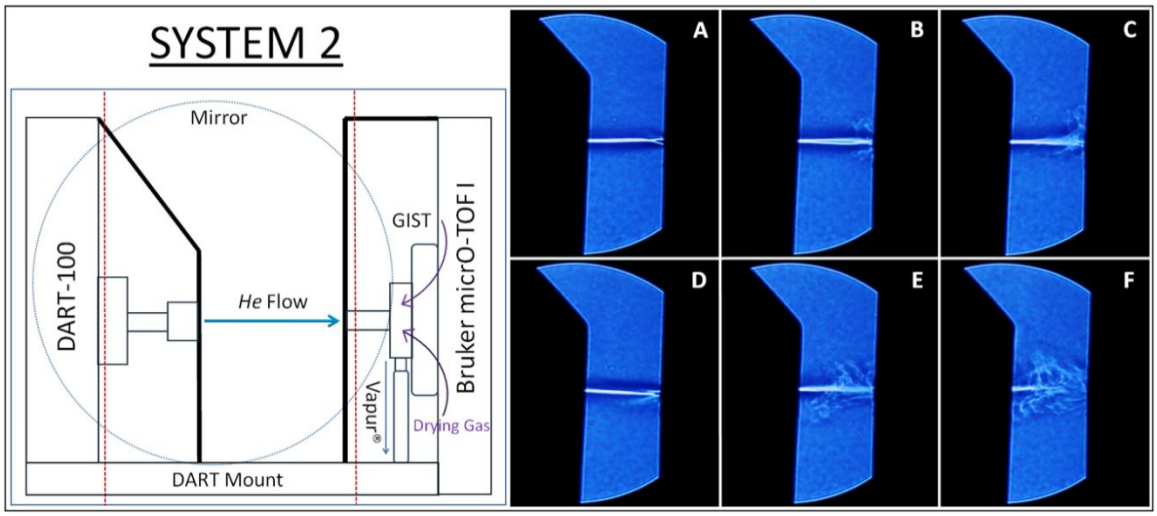

Figure 2.4: Schematic of system 2, where **solid bold lines** indicate visible silhouettes of the DART-100 source and Bruker micrO-TOF I mount, and red dotted lines demarcate the test region visualized. The top panels show the DART helium stream (1 L min^{-1}) across the AP interface for Vapur® pumping rates set to yellow (**A**), green (**B**), and gray (**C**). Panels **D-F** show the effect on those same settings with the N_2 drying gas on (1.4 L min^{-1}). The sample gap length was ~3 cm for all panels.

The potentially deleterious effect of the Vapur® pump on the stable flow profile was exacerbated when nitrogen drying gas flooded the AP interface. The counter-flow of dry N_2 (1.4 L min^{-1}) into the GIST chamber from the spectrometer inlet did not visibly corrupt the helium stream for the blue dial setting (Figure 2.4D) or lower Vapur® pump volumes. But again, for the higher settings exceeding pumping rates of 20 L min^{-1}, Vapur® pump line-choking resulted in even more dramatic pulsations across the full length of the interface (Figure 2.4E-F). The GIST adapter volume and the diameter of the Vapur® pump connection hose should be adjusted to accommodate the pumping requirements on different systems, or the impact on sampling efficiency is more likely to be negative as witnessed here. It is significant to note that the pulsations observed will help explain possible erratic and fluctuating signal intensities seen on some systems and we anticipate these pulsations can be eliminated by the use of larger volume GIST flanges and larger diameter Vapur® gas lines. Additional frame capture photos for select sample probes introduced on the Bruker system with the GIST and Vapur® pump components are shown below (Figure 2.5), each depicting similar disruptive gas flow trends as seen for system 1.

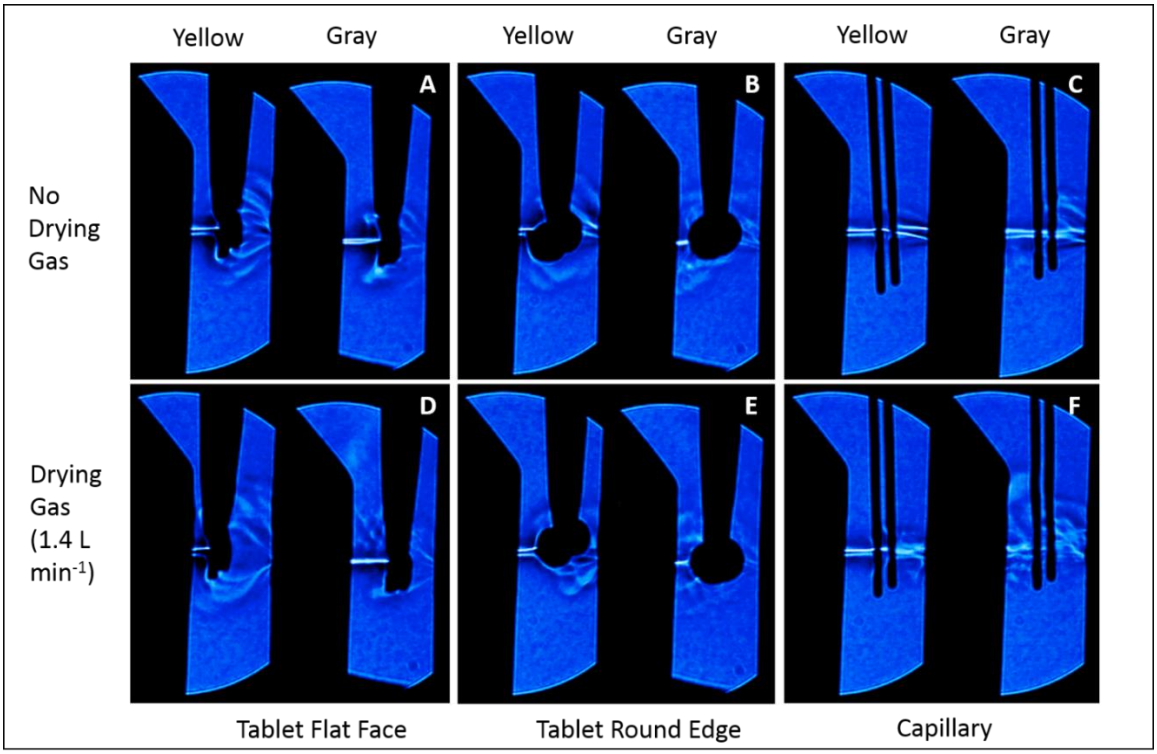

Figure 2.5: Probe sampling performed on the Bruker micrO-TOF I coupled to the DART-100 source with the Vapur® pump and N_2 drying gas active. The top panels show the helium flow patterns (gas flowing left to right) with the pump set to either yellow or gray for a flat face tablet (**A**), a rounded tablet edge (**B**), and a glass capillary (**C**). The bottom panels show the effect on the same samples and settings with the N_2 drying gas switched on (**D**-**F**). AP interface length was ~3 cm and helium flow rate was set to 1 L min^{-1}.

2.4.5. Transmission Mode (TM) DART-MS

Transmission mode analysis features a mesh screen spotted with sample solution that is situated between the DART ion source and spectrometer inlet, where the heated DART afterglow passes through the mesh, desorbing and ionizing analytes. This technique was developed with the aim of improving both ambient sampling efficiency and reproducibility[104]. Aside from sample volatility, concentration, and mesh coverage, success depends on component parameters such as the screen wire density, DART helium flow rate, and position of the sample screen relative to the DART nozzle and spectrometer inlet. A TM DART-MS assembly was configured using a new generation

DART-SVP source and a Bruker microOTOF-Q II mass spectrometer equipped with the Vapur® pump and GIST module. The DART source selected for this investigation is the source model routinely employed with transmission mode analysis. Schlieren visualization of this setup was performed to reveal the gas flow profile in the AP interface for TM DART-MS and to advise proper execution of the technique.

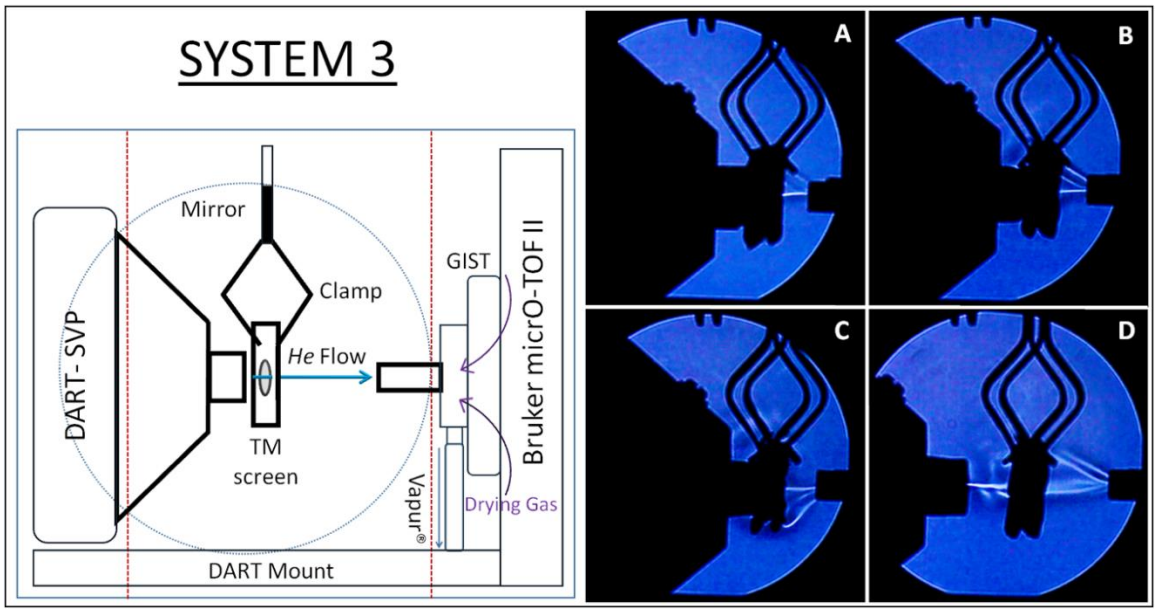

Figure 2.6: Schematic of system 3, where **solid bold lines** indicate visible silhouettes of the DART-SVP source and GIST adapter on the Bruker micrO-TOF II, and red dotted lines demarcate the test region visualized. The Vapur® pump was set to gray and N_2 drying gas was turned off. Panels show the DART helium flow (2 L min^{-1}) through a hollow screen holder (**A**), a 60x60 mesh (**B**), and a 100x100 mesh (**C**) over a short interface distance (~2 cm). Helium flow through a 60x60 mesh shown for a larger interface distance (~4 cm) and a more centralized screen position removed from the DART nozzle (**D**).

Using the typical DART source parameters and a slightly protracted AP interface distance (~2 cm) for clear visualization, the helium flow pattern observed for transmission mode was counter-intuitive. Helium exiting the DART-SVP nozzle (*i.d.* 2 mm) at 2 L min^{-1} largely circumvented the mesh rather than penetrating it. Two standard meshes with different grid densities were tested, 60x60 (wire *dia.* 0.19 mm) and 100x100 (wire *dia.* 0.23 mm), each having approximately equivalent void space areas of ~30.5%

to permit equal helium throughput. For reference, Figure 2.6A shows the helium stream passing unimpeded into the GIST adapter through a hollow custom screen holder (*i.d.* 1.1 cm) adjacent to the DART nozzle.

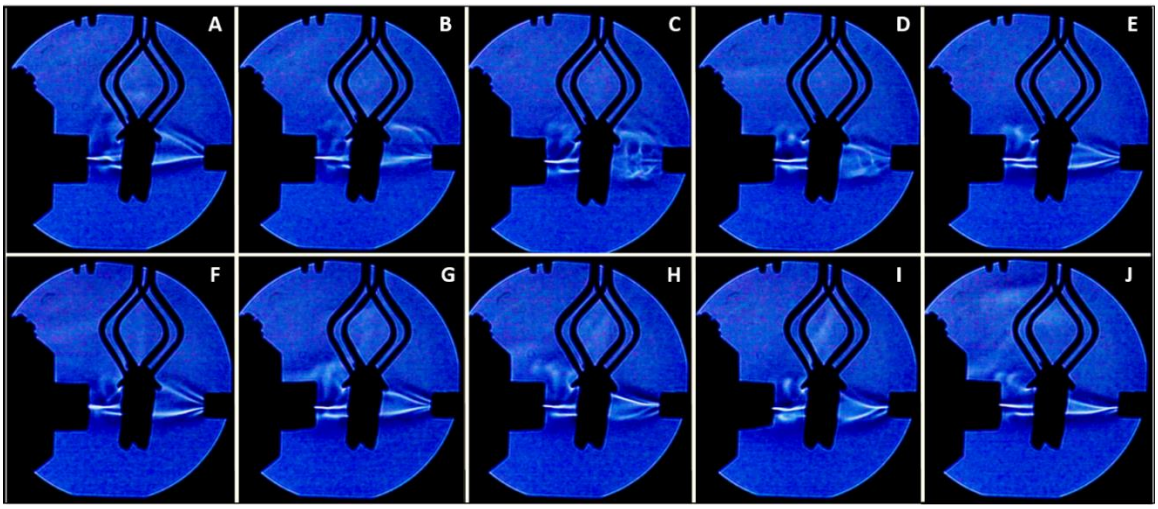

Figure 2.7: Single frames collected over the span of 3 seconds showing the impact of GIST pump pulsations on TM-DART gas flow profiles for gray pump setting (~26 L min^{-1}) and N_2 drying gas at 3.0 L min^{-1} (TOP PANELS **A**-**E**) and the more stable flow profile achieved with the yellow pump setting (~22 L min^{-1}) and N_2 drying gas at 3.0 L min^{-1} (BOTTOM PANELS **F**-**J**). The pulsation is evident comparing panels **C** and **H**. Sample gap was ~4 cm and DART helium flow rate was 2 L min^{-1} through a 60x60 mesh, with DART gas flowing left to right.

Although not evident from the still frame image, Vapur® pump pulsations were again present using the maximum "gray" setting, which momentarily disturbed the jet stream at ~1s regular intervals. In Figure 2.6B, helium passed not just through the 60x60 mesh, but also around the top of the holder as the helium contoured to the surface of the planar screen mount. The effect was the same for the 100x100 mesh in Figure 2.6C, but with a significant portion of the helium accumulated between the DART nozzle and screen wrapping below the holder before being drawn into the GIST. The last panel, Figure 2.6D, shows the gas flow profile for a sample gap expanded to ~4 cm and the 60x60 mesh repositioned midstream from the DART nozzle. The outcome is similar, and helium continued to partially penetrate the mesh while being pulled by the GIST vacuum

in an undercurrent both through the screen and over top of the holder. The flow aberrations induced with the drying gas on were also observed for TM DART-MS across the ~4 cm sample gap with the Vapur® tuned above the yellow dial setting (>20 L min^{-1}), as depicted in supporting information (Figure 2.7), but flow remained noticeably more stable at lower Vapur® pumping rates.

Despite the complications with flow stability that may arise from using a poorly configured Vapur® and GIST setup, the large diameter transfer tube on the GIST adapter in tandem with the assisting vacuum draw of the Vapur® are arguably essential for this mode of analysis, helping to collect the ensuing helium spread from insufficient mesh penetration. Signal intensity is expected to suffer on smaller diameter skimmer-type mass spectrometer orifices like on the AccuTOF where much of the helium that was redirected around the holder would be lost unless the AP interface spacing is substantially reduced. Adjusting the helium flow rate ±1 L min^{-1} did not observably change mesh transmission or gas behavior, although better throughput and signal intensity are anticipated for higher flow rates (~3.5 L min^{-1} default on DART-SVP) if the spectrometer can handle the increased helium load and tighter interface spacing. In addition to a higher linear gas velocity, a lower density mesh (40x40 or 20x20) should allow more helium penetration at some compromise to sample absorption over the screen. Alternatively, the angle or shape of the sample mesh could be altered to better guide flow and afford better transmission by taking advantage of the helium stream tendency to contour to surfaces.

2.5 Conclusion

The collection of Schlieren images presented in this work serves to demystify gas transport phenomena at the DART-MS AP interface, identifying the system dependent variables that impact flow fidelity and instructing the proper technique for efficient sampling using different types of sample probes. Contrary to conventional wisdom, helium gas was seen to propagate from the DART sources as a collimated, highly-laminar

stream across interface expanses of several centimeters. It was observed that flow disturbances may be minimized by skillfully positioning sample probes along the edge of the DART stream rather than fully inserting probes into the DART sample gap. Additionally, transmission losses that ensue from turbulence during sampling should be mitigated by reducing the AP interface distance. The GIST/Vapur® apparatus was found useful for entraining the dispersive source gas when performing transmission mode analysis, but the pumping rate must be carefully adjusted to balance gas ingress to the mass spectrometer and avoid pressure pulsations that disrupt flow. While the fluid dynamics investigated in this study were specific to helium as the DART source gas, it is anticipated that most of the sampling strategies developed from these visualizations remain applicable for alternative nitrogen or argon source gases, notwithstanding potentially different flow characteristics.

CHAPTER 3: A MULTIMODAL VACUUM-ASSISTED PLASMA IONIZATION (VAPI) SOURCE WITH LASER ABLATION AND TRANSMISSION MODE SAMPLING CAPABILITIES

Adapted from

Keelor, J. D.; Farnsworth, P. B.; Weber, A.; Abott-Lyon, H.; Fernández, F. M. *J. Am. Soc. Mass Spectrom.* **2016**, *27*(5), 897-907.

3.1 Abstract

A multimodal ion source was developed for on the fly configuration using various analysis modes, designed for more efficient and reproducible sampling at the mass spectrometer atmospheric pressure (AP) interface in a number of different applications. This vacuum-assisted plasma ionization (VaPI) source features interchangeable transmission mode and laser ablation sampling geometries. Operating in both AC and DC power regimes with similar results, the ion source was optimized for parameters including helium flow rate and gas temperature using transmission mode to analyze volatile standards and drug tablets. Using laser ablation, matrix effects were studied, and the source was used to monitor the products of model prebiotic synthetic reactions.

3.2 Introduction

Ambient fluid dynamics at the mass spectrometer inlet significantly impact ion transmission and can be difficult to control. Some of the most successful attempts at stabilizing gas flow patterns to enhance the quantitative capability of ambient plasma-based analysis have been realized with DART-MS systems incorporating a Vapur® interface, rail-mounted sampling probes, and auxiliary pumping, all of which help entrain divergent gas flows toward the mass spectrometer inlet and reduce variability[42]. More

recently, continuous quantitative surface scanning with DART in such arrangements has been accomplished using planar substrates in place of capillary holders and transmission sample meshes[43].

As mass spectrometer AP interfaces become increasingly accessible, they continue to enable new sample introduction modes that alleviate ion losses related to mass transport. For example, other vacuum-assisted sampling strategies have been devised with RF plasma discharges enclosed within or directly connected to the inlet transfer capillary[25, 105, 106]. Such sampling approaches function as aerodynamic remote sampling stages similar to the remote analyte sampling, transport, and ionization relay (RASTIR)[107] idea implemented with extractive electrospray ionization (EESI). These types of sampling constructs can benefit hybrid ion source arrangements, where the analyte desorption and ionization events are decoupled from one another to afford more control during sampling and better spatial resolution in chemical mapping applications.

Spatial resolution for plasma ion sources is affected by sample substrate size and shape, and is typically limited by dispersive gas-flow dynamics. One effective strategy used to improve precision with surface sampling has been combining plasma ionization with laser ablation, wherein continuous high-energy laser pulses desorb neutral material with micron spatial resolution, also serving to regulate the analyte supply available for ionization. For example, laser ablation has been paired successfully with dielectric-barrier-discharges (DBD)[108] to examine non-volatile explosives, and used with DART[109] and FAPA[45] for imaging mass spectrometry of biological tissues, dyes, and drugs. In these approaches, the substrate radiation absorption efficiency and ablation plume expansion remain the limiting factors determining the abundance of aerosolized sample available for ionization, while the plasma discharge current and source gas-flow fidelity dictate the ion generation and transmission efficiencies, respectively.

Drawing inspiration from these AP sampling techniques and several methodologies established in the same vein, including electrothermal vaporization

(ETV)-DART[110] or Drop-on-Demand FAPA[111], a multimodal plasma ion source named vacuum-assisted plasma ionization (VaPI) is presented. Uniquely, the source design integrates laser ablation and transmission mode sampling motifs with AC/DC plasma ionization mass spectrometry. The core component of this new ion source architecture is a central cross union bridging a plasma discharge cell to the mass spectrometer transfer capillary in a coaxial orientation. Open cross bridge joints are interchangeably adapted with either a mesh sample screen for transmission mode analysis (TM-VaPI) or sealed with a sapphire window permitting focused laser throughput for ablation experiments (LA-VaPI). The suction of the mass spectrometer is partially maintained within the cross union when using helium discharge gas, thereby allowing material to be drawn into the source, improving sampling consistency. With increasing plasma power and concomitant rising cell temperature, the union serves as an incubated vessel facilitating analyte desolvation and mixing, as well as efficient ionization and transmission. Optimal settings for co-dependent variables affecting ionization efficiency and transmission, namely helium gas flow rate, cell temperature, and plasma power, have been determined. Effects of matrix composition were also investigated, showcasing VaPI's robust tolerance to sample complexity. The best sample delivery practices to ensure sampling reproducibility are also discussed.

3.3 Experimental

3.3.1. Materials and Sample Preparation

Reagent grade dimethyl methylphosphonate [DMMP] and 2,4-lutidine were purchased from Sigma-Aldrich (St. Louis, MO, USA) and prepared as aqueous solutions by serial dilution in concentrations of 6.25 μM, 12.5 μM, 25 μM, 50 μM, 100 μM, and 200 μM from a 1 mM stock solution. An analytical grade standard mixture of amino acids was also procured from Sigma-Aldrich and used without further preparation. The mixture concentration was 2.5 μmol mL^{-1} in 0.1 N HCl for all components unless

otherwise specified, and consisted of L-alanine, ammonium chloride, L-asparagine, L-aspartic acid, L-cystine (1.25 μmol mL^{-1}), L-glutamic acid, glycine, L-histidine, L-isoleucine, L-leucine, L-lysine, L-methionine, L-phenylalanine, L-proline, L-serine, L-threonine, L-tyrosine, and L-valine. Triaminopyrimidine [TAP] (Acros Organics, part of Thermo Fisher Scientific Inc., NJ, USA) was made into 2.5 mM aqueous solutions mixed with potassium chloride (J.T. Baker® brand from Avantor Performance Materials, Center Valley, PA, USA) using salt concentrations of 5 mM, 10 mM, 20 mM, and 40 mM KCl. Poly(ethylene) glycol [M_n 395, M_w 430] from American Polymer Standards Corporation (Mentor, OH, USA) was dissolved into ~4 mg mL^{-1} aqueous solutions with solvent compositions of 0%, 20%, 50%, and 90% volume methanol (LC-MS grade, Sigma-Aldrich).

Drug tablet samples included acetaminophen [500 mg] sold by Target, Inc. (Minneapolis, MN, USA), Doralgine [25/500 mg caffeine/noramidopyrine] made by Medical Supply Company, LTD. (Phnom Penh, Cambodia), and Coartem [20/120 mg artemether/lumefantrine] from Novartis AG Pharmaceutical Company (Sufferen, NY, USA).

Synthetic nucleobase mixtures were produced from two separate model prebiotic reactions. Purine and pyrimidine compounds were synthesized in the formamide reaction. A ~5 mL volume of formamide (reagent grade, Sigma-Aldrich) was heated in an oven at 160 ˚C for up to 120 hours in a 20-mL scintillation vial covered with foil. Fractions of the reaction mixture were collected at 72 h and 120 h time points and stored at 8 C for 24 h before workup. Reacted formamide mixture aliquots of 100 μL or ~120 mg were dissolved in 10 mL of deionized water and filtered through a 0.45 μm PTFE membrane before analysis. Pyrazine derivatives were synthesized from a one-pot reaction, in which 1,3-dihydroxyacetone, glycolaldehyde, and 2-aminoacetamidine-dihydrobromide (0.10 M 1:1:1 ratio) were mixed in aqueous solution with sodium phosphate (0.25 M) at pH 7.4 by addition of NaOH, then heated to 85 °C for 24 hours. In a 2-mL microvial, reaction

contents were deaerated and purged with nitrogen before being sealed under vacuum. A 1.0 mL aliquot of the product mixture was diluted with 8 mL of water, and a 5 mL portion was then desalted on a 20 mL Discovery DSC-18 column (Supelco, Bellefonte, PA, USA). Material was eluted with 36 mL water and 44 mL 50% methanol/water, collected in 20 separate fractions. Salt-free fractions #10-20 (from 37-80 mL eluent) were combined and concentrated to 0.5 mL syrup using a CentriVap centrifuge. After storage at -20 °C, the mixture was suspended in 200 μL water, and 50 μL aliquots were further diluted in 300 μL water for adequate ampoule sampling volume.

Deionized water was generated with a Barnstead Nanopure Diamond™ laboratory water system (Thermo Fisher Scientific, Inc.) and ultrapure (99.999%) helium source gas was supplied by Airgas (Atlanta, GA, USA).

3.3.2. VaPI Plasma Ion Source Design and Operation

The custom plasma discharge source was fashioned from a quarter-inch PFA Swagelok (Solon, OH, USA) T-junction securing a quartz tube (*l* = 50 mm, *o.d.* = 6.25 mm, *i.d.* = 3.95 mm) that enclosed a tungsten needle electrode (*l* = 120 mm, *dia.* = 1 mm) at one joint opening. The point electrode was center-mounted in a perforated ceramic piece (*dia.* = 3.95 mm) inserted at the base of the quartz tube, and the electrode rod extended within the T-junction body through a Teflon plug capping the opposite joint. A gas feed line was fitted in the top opening. The quartz tube terminated at an eighth-inch metal ferrule (grounded counter-electrode) in a stainless steel quarter-inch Swagelok cross union, which was connected on-axis with the mass spectrometer via a truncated glass transfer capillary (*l* = 40 mm, *o.d.* = 6.35 mm, *i.d.* = 500 μm) from Bruker (Billerica, MA, USA). The Swagelok cross union body was wrapped in 1 ft. high-temperature heating cord (22 W) with a J-type thermocouple, allowing temperature to be regulated using an SDC digital temperature controller (Briskheat, Columbus, OH, USA). High-temperature quarter-inch 60%/40% vespel/graphite ferrules (Restek, Bellefonte,

PA, USA) were used at all Swagelok joint connections. Thermal images of the plasma source and cross unit were collected with a FLIR T300 IR camera (FLIR Systems AB, Danderyd, Sweden).

The electric discharge was operated at powers of ~20 ±1 W in both AC and DC regimes using helium source gas. In DC mode, a negative potential bias of ~2500 V was applied to the tungsten needle in series with 50 kΩ ballast resistor using a Bertan Associates 205A-50R HV power supply (Bertan Associates Inc., Hicksville, NY, USA). The effective DC electrode potential and current measured with a HV probe were ~1850 V and ~11 mA, respectively. For AC mode, power was applied to the tungsten needle from a T&C Power Conversion AG-0201A RF power supply (T&C Power Conversion Inc., Rochester, NY, USA). Plasma power was estimated from the difference between effective load powers ($P_{Load} = P_{Forward} - P_{Reverse}$) with the discharge on and off. AC electrode potentials of ~1240-1460 V_{rms} were measured on an oscilloscope (Tektronix, Beaverton, OR, USA), with I_{rms} estimated between 13-16 mA for a 20 W AC discharge. Helium flow rates were controlled between 1.0-2.0 LPM using an analog rotameter (Aalborg, Orangeburg, NY, USA) in-line with an M series digital flow meter (Alicat Scientific, Tuscon, AZ, USA). Vacuum pressure within the cross union was estimated with a DM8320 digital manometer (General® Tools, Secaucus, NJ, USA) fastened on one open joint while keeping the others sealed.

3.3.3. Instrumentation and Sampling Methods

For transmission mode geometry sampling, a 40x40 stainless steel mesh screen (*dia.* = 9.35 mm) was fastened in the top cross union opening of the VaPI ion source and the lower union opening was kept sealed. During ion source characterization, volatile compounds were sampled from a strictly aqueous matrix to reduce spectral complexity. The droplet water introduced during sampling would only contribute to the $(H_2O)_nH^+$ reactant ion population, thereby preventing the possibility of ion competition with an

organic solvent. Solutions were spotted onto the mesh in 3 μL aliquots using a micropipette. For solids analysis, drug tablet fragments were placed atop the mesh with tweezers for approximately 1 minute, and then removed. If needed, methanol solvent or water were spotted in aliquots of 10-100 μL to rinse the mesh.

When sampling by laser ablation, the bottom union inlet was left open and a sapphire window (*h* = 1 mm, *dia.* = 9.35 mm) was fastened in the top joint. Laser ablation was performed using an IR Opolette™ OPO laser model 2731 (Opotek, Inc., Carlsbad, CA, USA). Laser wavelength and frequency were tuned to 2940 nm and 10 Hz, respectively. Laser energy was tuned to 88.1%, equating to an output energy of ~1.55 mJ measured with an ES111C pyroelectric sensor (Thorlabs, Inc., Newton, New Jersey, USA), focused by a MgF_2 plano-convex lens (*f.l.* 5 cm) through the Swagelok cross union. Ablation of sample solution was conducted from 10 μL droplets deposited on an Omni Slide™ glass substrate with Teflon-coated spot arrays (Prosolia, Indianapolis, IN, USA), or from a 200 μL reservoir of solution contained in a quarter-inch quartz ampoule. Unless otherwise specified, all ablation was performed from aqueous solutions. Laser ablation was also performed using an open AP interface arrangement during a comparison study. In place of the cross union bridge unit, the discharge source was capped with a ¼" Swagelok end fitting as the grounded counter electrode and positioned ~0.5 cm away from the spectrometer capillary inlet. The planar Omni slide substrate was mounted on a guide arm extending from a *xyz* stage, and centered below the spectrometer inlet in the interface flush underneath the plasma endcap electrode.

All experiments were conducted on a JEOL JMS-T100LC AccuTOF™ mass spectrometer (JEOL USA, Inc., Peabody, MA, USA) using the following positive mode tune parameters optimized for the low mass range – orifice #1: 25 V, orifice #2: 5V, ring lens: 10 V, orifice temperature: 100 ˚C; ion guide RF voltage: 100-400 V, sweep time: 80%; guide bias voltage: 29V, pusher bias voltage: -0.28 V, MCP detector: 2650 V. In most cases, nominal masses are reported for known compound peaks, but for unknown

species, assigned ion formulas were deduced from the accurate masses provided in the text.

3.4 Results and Discussion

3.4.1. TM-VaPI Characterization

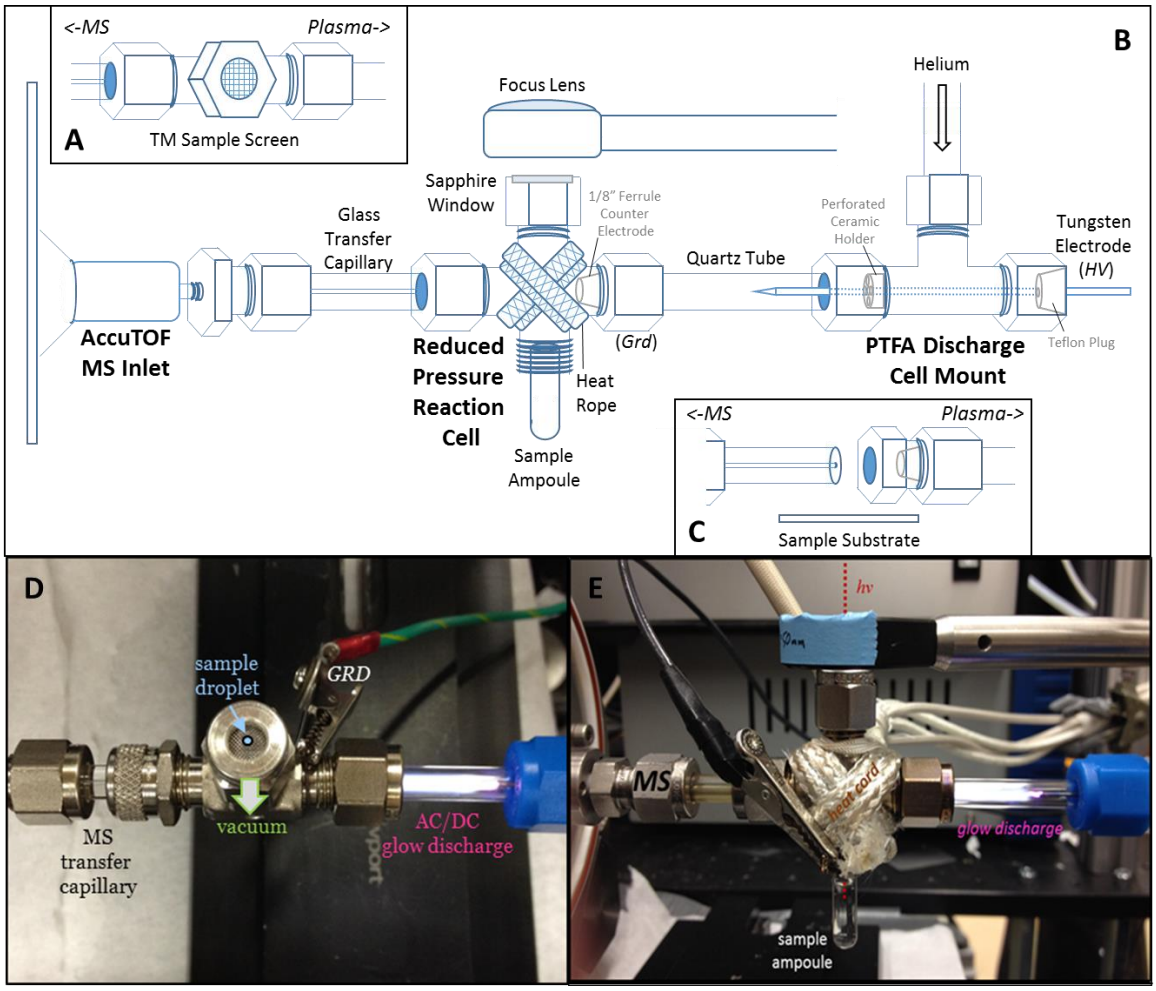

Figure 3.1: Schematic of vacuum-assisted plasma ionization (VaPI) source assembly. Configuration used for transmission mode (TM)-VaPI sampling (**A**). Configuration used for laser ablation (LA)-VaPI sampling (**B**). Open atmospheric pressure interface arrangement with plasma source (**C**). Pictures of source assemblies for TM-VaPI (**D**) and LA-VaPI (**E**).

A schematic illustration of the VaPI source assembly is depicted in Figure 3.1 with corresponding pictures. The source configuration in Figure 3.1A and 3.1D, intended for transmission mode analysis, features a mesh sample screen on the top cross union joint. A steady draw of air flows into the cross union through the sample mesh, driven by the suction from the spectrometer inlet and modulated by helium flow rate and cell temperature. This source design mitigates the unfavorable fluid dynamics of open format (ambient) plasma ion sources, with the focused vacuum draw through the mesh improving sensitivity by affording more complete entrainment of volatilized sample into the plasma gas. With this setup, an elevated plasma gas temperature was necessary not only to initiate analyte thermal desorption, but also to enhance analyte cluster desolvation and minimize condensation on the interior cell surface. Accordingly, glow discharges were operated at target powers of ~20 W, where helium gas temperatures measured with a thermocouple reached 200˚C in the cross union without the addition of extra heating elements.

Aqueous solutions of 2,4-lutidine and DMMP were sampled first to determine general performance and dynamic range while optimizing for helium gas flow rate and cell temperature. When microliter aliquots of solution were spotted onto the screen, the droplet was slowly aspirated into the cross union, mixing in the afterglow helium stream. Volatile analytes were initially chosen for characterization experiments to avoid carryover that might skew trends. Figure 3.2A shows the highly repeatable extracted ion chronograms for the protonated monomer of 2,4-lutidine in a concentration series, and Figure 3.2B displays a select subset of extracted ion chronograms for the DMMP protonated monomer and dimer detected from a 50 μM solution.

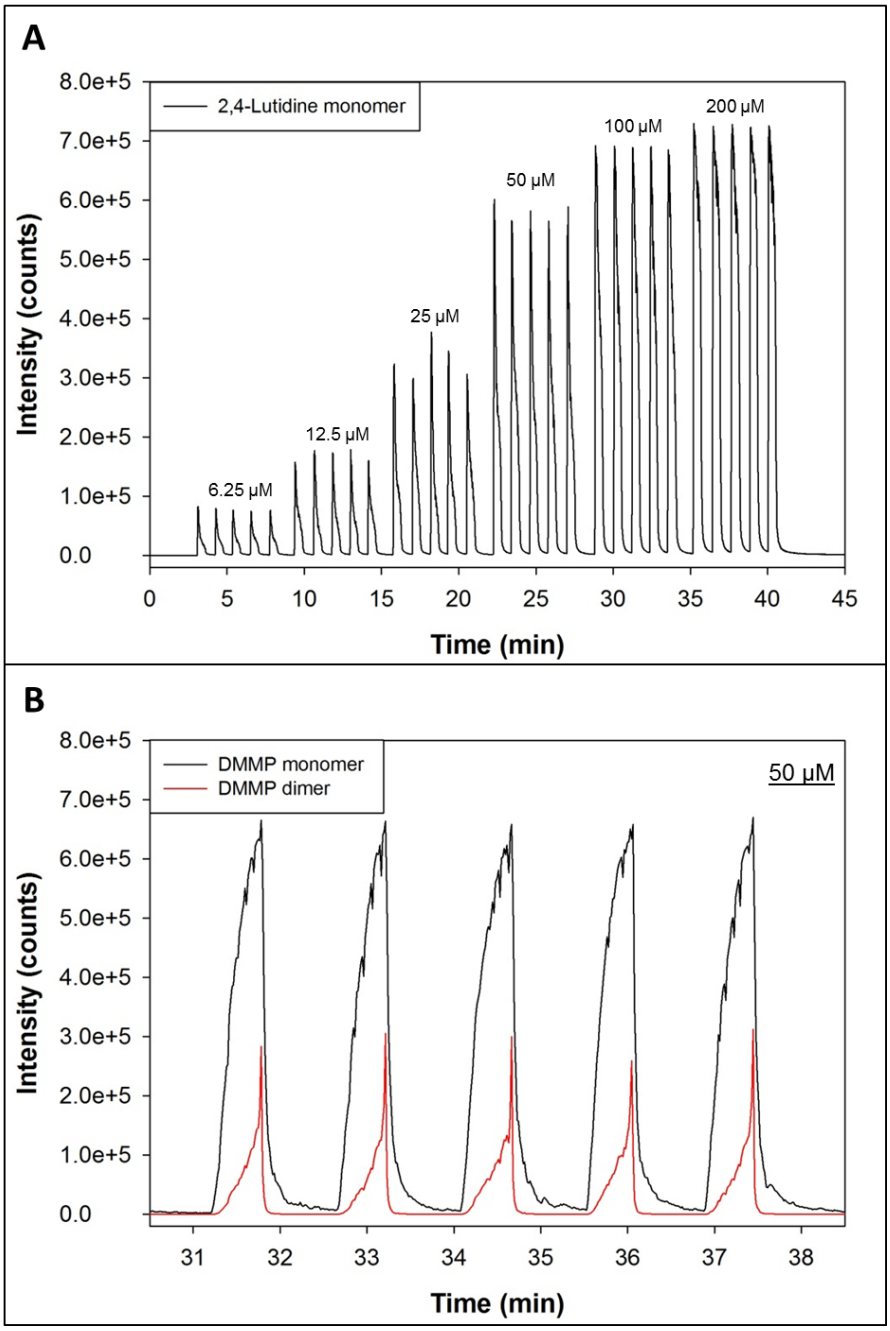

Figure 3.2: Extracted ion peak traces measured using TM-VaPI with a 20W DC discharge and 1.6 LPM helium flow rate. Consecutive extracted TIC peaks in the full concentration series for 2,4-lutidine analyte in aqueous solution (**A**) and selected TIC peaks for DMMP at 50 µM (**B**). Droplet volumes sampled were 3 µL delivered to mesh by micropipette tip. Cross union was not heated.

Differences in desorption profile shapes were observed based on analyte volatility. For instance, the desorption profile for DMMP suggested a lower volatility from the droplet surface, indicated by the gradual rise to a maximum and subsequently sharp decrease to baseline upon depletion of the droplet, compared to the more volatile 2,4-lutidine whose peak profile showed an inverse trend. Furthermore, as it is apparent in Figure 3.2B, the DMMP dimer peak emerged later than the monomer, appearing only after concentration by the shrinking droplet. These observations were compatible with DMMP's slightly higher enthalpy of vaporization and boiling point. Meanwhile no dimer ion was observed for the more rapidly volatilized 2,4-lutdine even at 1 mM solution concentrations. However, a minor ion suspected to form through a pyridine N-oxide intermediate did appear at higher 2,4-lutidine concentrations, with the formula $[C_7H_8NO]^+$ assigned by accurate mass (m/z=122.0628). The origin of this and other product ions is discussed in following sections.

The cross union pressure and vacuum draw were largely influenced by the plasma helium flow rate and cell union temperature, which in turn impacted sampling reproducibility and sensitivity for TM-VaPI. Figure 3.3 shows the signal intensity as a function of helium flow rate for aliquots of DMMP and 2,4-lutidine spotted on the mesh. When the glow discharge was active, the cross union vacuum pressure measured between -116 mmHg at 1.0 LPM helium to -13 mmHg at 1.8 LPM helium. A plot of the VaPI cross union pressure as a function of helium flow rate showed the trend was linear with the discharge on or off, and that the vacuum pressure decline was steeper for active plasma. Signal was seen to increase for each analyte with helium flow rates up to ~1.6 LPM (cell pressure: -40 mmHg) due to a higher flux of plasma species into the VaPI cross joint available to sustain ionization reactions. The high intensity of reactant protonated water clusters persisted for helium flow rates over 2.0 LPM, but measured analyte signal rapidly disappeared with flow rates beyond 1.8 LPM helium. This result was the consequence of a now positive pressure at the mesh (≥15 mmHg), which

effectively negated suction through the cross joint and suppressed transmission of desorbed neutrals. Additionally, the flood of hot gas into the cross union when using these higher helium flow rates also heated the mesh, likely accelerating some sample evaporation into the environment, thereby contributing to signal loss. Newer, more sensitive mass analyzers with vacuum systems less robust to high helium gas loads could potentially operate VaPI at far lower flow rates or use reduced cell assembly dimensions, thereby maximizing vacuum draw for improved sample uptake and ion transmission without much compromise to ionization efficiency.

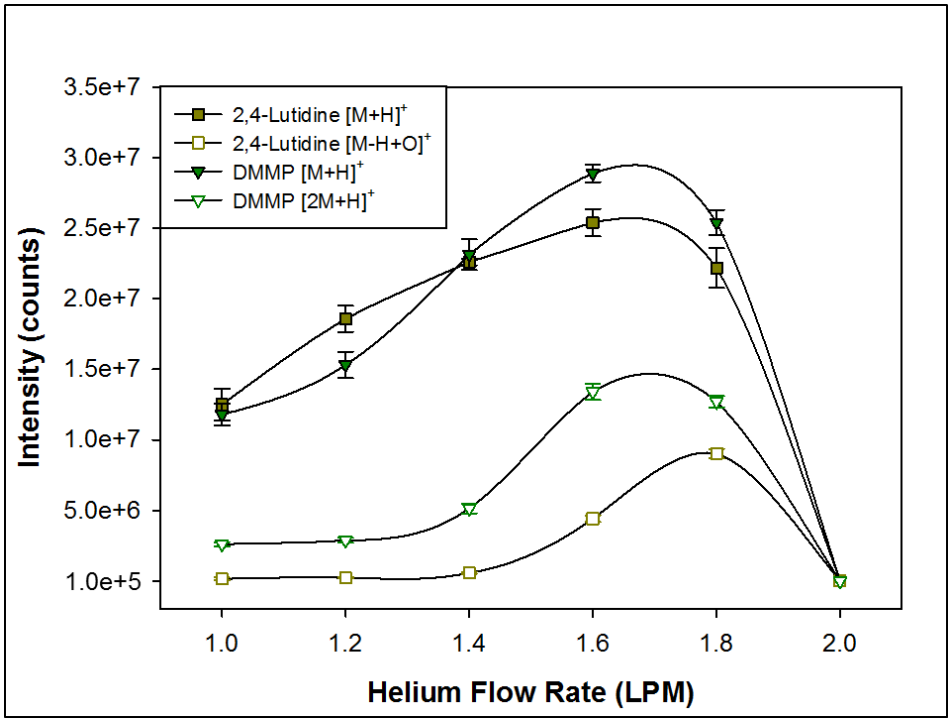

Figure 3.3: Signal intensities as a function of source gas flow rate for 2,4-lutidine and DMMP using TM-VaPI with a 20 W DC discharge. Data points and standard deviation error bars represent the average extracted TIC areas for 3 consecutive peak traces per point.

The VaPI linear range was also examined via concentration series for each standard, Figure 3.4. The increasing signal intensity deviated from linearity after the concentration range spanned three orders of magnitude, with the protonated ion signals beginning to plateau at around 100 µM. (The same trend was forecast when plotting the

total ion signal of each analyte for both AC & DC plasmas.) Interestingly, the protonated water population was not fully consumed even at higher analyte concentrations, an observation suggesting that fluid dynamics and ionization reaction kinetics rather than reactant ion depletion are likely the limiting factors. It is reasoned that evaporative losses from the slowly aspirating micro-droplets are more significant at higher volatile concentrations, and dynamic range linearity may be restored by either amplifying VaPI vacuum pressure or sealing off the sample mesh after spotting. The %RSD for volatile standards in Figure 3.4 still never exceeded ± 8%, and was under ± 2% for the majority of data points.

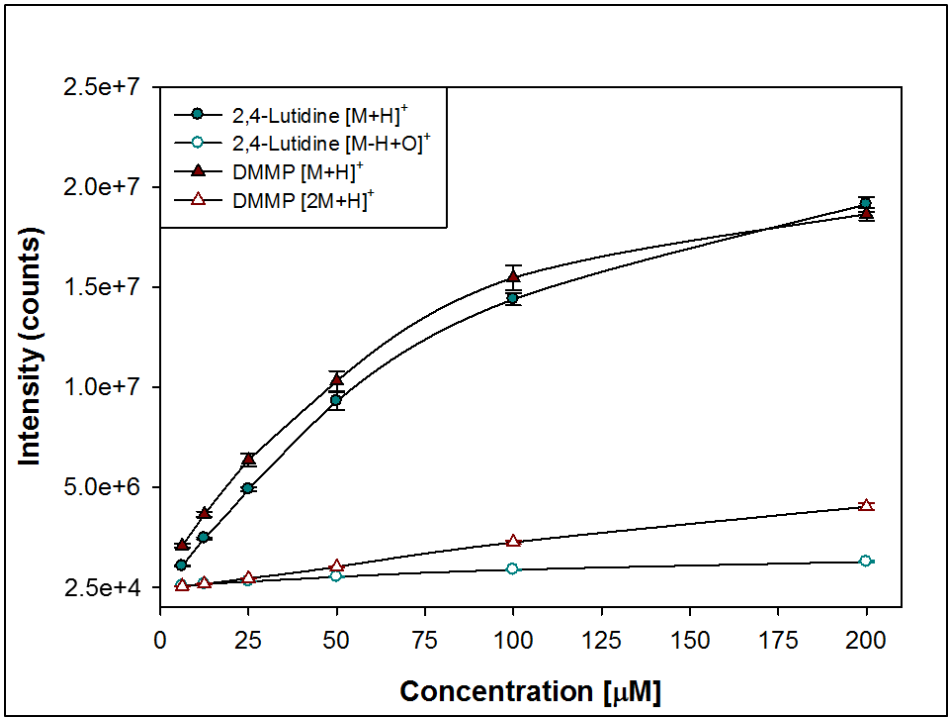

Figure 3.4: Signal intensities as a function of volatile concentration for 2,4-lutidine and DMMP using TM-VaPI with a 20 W DC discharge. Data points and standard deviation error bars represent the average extracted TIC areas for 5 consecutive peak traces.

Where sensitivity was not an issue, that sampling reproducibility could be further improved by controlling cell temperature. Material aspirated through the sample mesh partially cools the afterglow gas while mixing in the cross union, disrupting the gas flow profile and vacuum equilibrium to cause temporary fluctuations in the total ion

chronogram. With heating rope wrapped around the cross union and programmed to 275°C, the extracted ion chronogram shapes for each standard appeared more smooth and narrow (Figure 3.5) when compared to TIC peaks at lower temperatures, with the standard deviation decreasing more than 2-fold. However, this improvement came at the expense of lower sensitivity for the volatile analyte, with the average integrated signal intensity for DMMP being reduced by almost half.

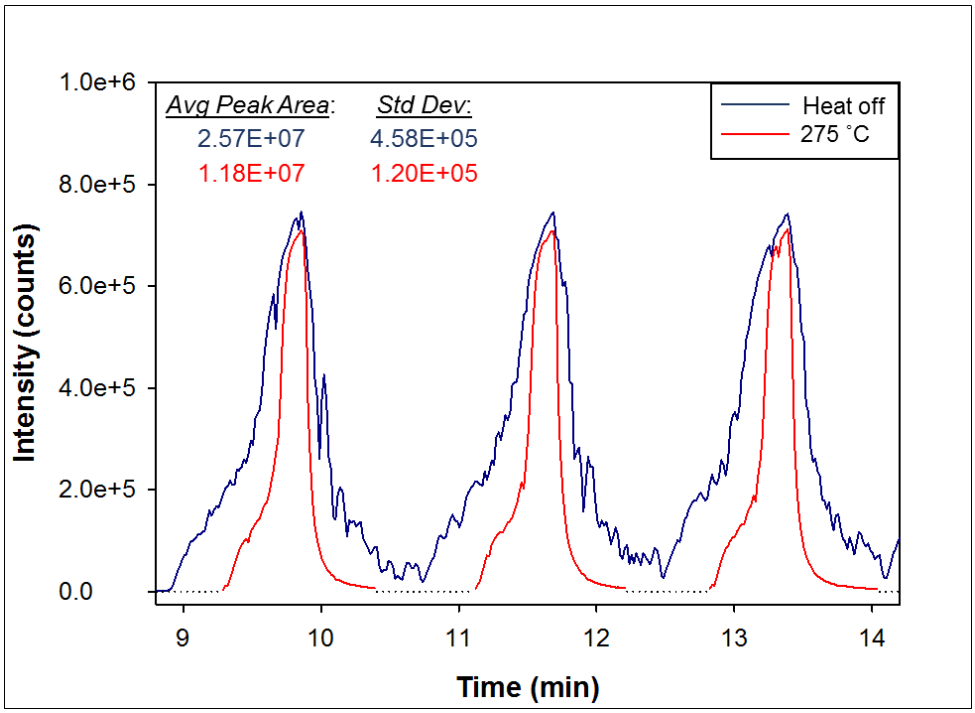

Figure 3.5: Extracted ion peak traces for 1 mM DMMP at 1.6 LPM helium flow rate with (red) and without (blue) the cross union heated to 275 °C. Baseline/time axis for superimposed consecutive red traces were altered to fit blue trace.

The signal decrease in response to excessively heating the cell is easily rationalized. Higher temperatures accelerated sample desorption from the mesh while simultaneously reducing the net vacuum pull. A near total loss of cross union vacuum pressure (-2 mmHg) was actually measured at 1.6 LPM and 275 ˚C, indicating signal under these conditions may have depended almost solely on analyte diffusion into the cell. As will be seen in the next section, such temperature effects also manifest themselves as differences in performance between AC and DC plasma power regimes.

Since setting the cross union temperature to match the temperature of the discharge gas minimizes hysteresis during sampling, the cross union temperature was set to 200 ˚C where vacuum draw was preserved.

3.4.2. Comparison of AC and DC VaPI Operation Modes

A recent study (see Appendix B) involving high-frequency DBD plasmas and point-to-plane glow discharges presented spectroscopic evidence suggesting the abundance of helium metastables varies considerably for different plasma ion source geometries and between AC or DC operation modes[112]. Metastable atom concentration within a plasma was seen to scale proportionally with plasma power, with lower wattage (10-15 W) DBDs generating He* populations up to an order of magnitude larger than those observed for higher power FAPA-type DC discharges. In principle, a greater number of plasma metastable species should be followed by a higher population of reactant ions in the AP interface and possibly higher ionization efficiency. Given the reproducible, semi-quantitative capabilities of TM-VaPI, AC and DC discharges were tested in order to investigate the downstream implications of the spectroscopic findings, and to determine any performance advantage.

At first glance, the plasma discharges appeared visually distinct for a given mode; the AC discharge existing as a pink, focused plasma and the DC discharge as a more diffuse, white glow. Signal trends observed as a function of helium flow rate and concentration were almost identical between both power regimes, with plots closely imitating Figures 3.3 and 3.4. For comparison, analyte ion intensity ratios for the discharge modes (DC/AC) are presented in Table 3.1. Signal intensity gradually shifted in favor of the DC discharge from ≥0.75x to over 1.5x the total AC ion count as the helium flow rate was increased. Additionally, the signal gain for the DC discharge slowly diminished from around 2x to 1.3x the AC ion intensity as analyte concentration increased.

Table 3.1: Comparison of DC and AC VaPI discharges

Helium Flow Rate (LPM)	Ratio of Ion Signal Intensity (DC:AC)	
	2,4-Lutidine	*DMMP*
1.0	0.74	0.90
1.2	0.98	0.93
1.4	1.09	1.03
1.6	1.18	1.30
1.8	1.54	1.85
2.0	-	-
Sample Concentration (µM)	**Ratio of Ion Signal Intensity (DC:AC)**	
	2,4-Lutidine	*DMMP*
6.25	2.10	1.76
12.5	1.96	1.56
25.0	1.68	1.50
50.0	1.58	1.39
100	1.46	1.42
200	1.28	1.29

The overall lower signal for the AC plasma in most cases is difficult to rationalize based on the previously measured metastable densities. Apart from plasma visual appearance, the major observable difference between the two discharges was the VaPI cell temperature. Thermal images of the source recorded using different helium flow rates showed temperatures approximately 20 °C higher for AC versus DC operation, as might be expected due to the 2-3 mA larger plasma current calculated for the AC discharge, see Figure 3.6. Recalling the effect of raised gas and cross union temperatures on signal described previously using this configuration, it is likely this small temperature disparity between power modes that was predominantly responsible for decreased ion transmission and lower volatile signal intensity in AC mode.

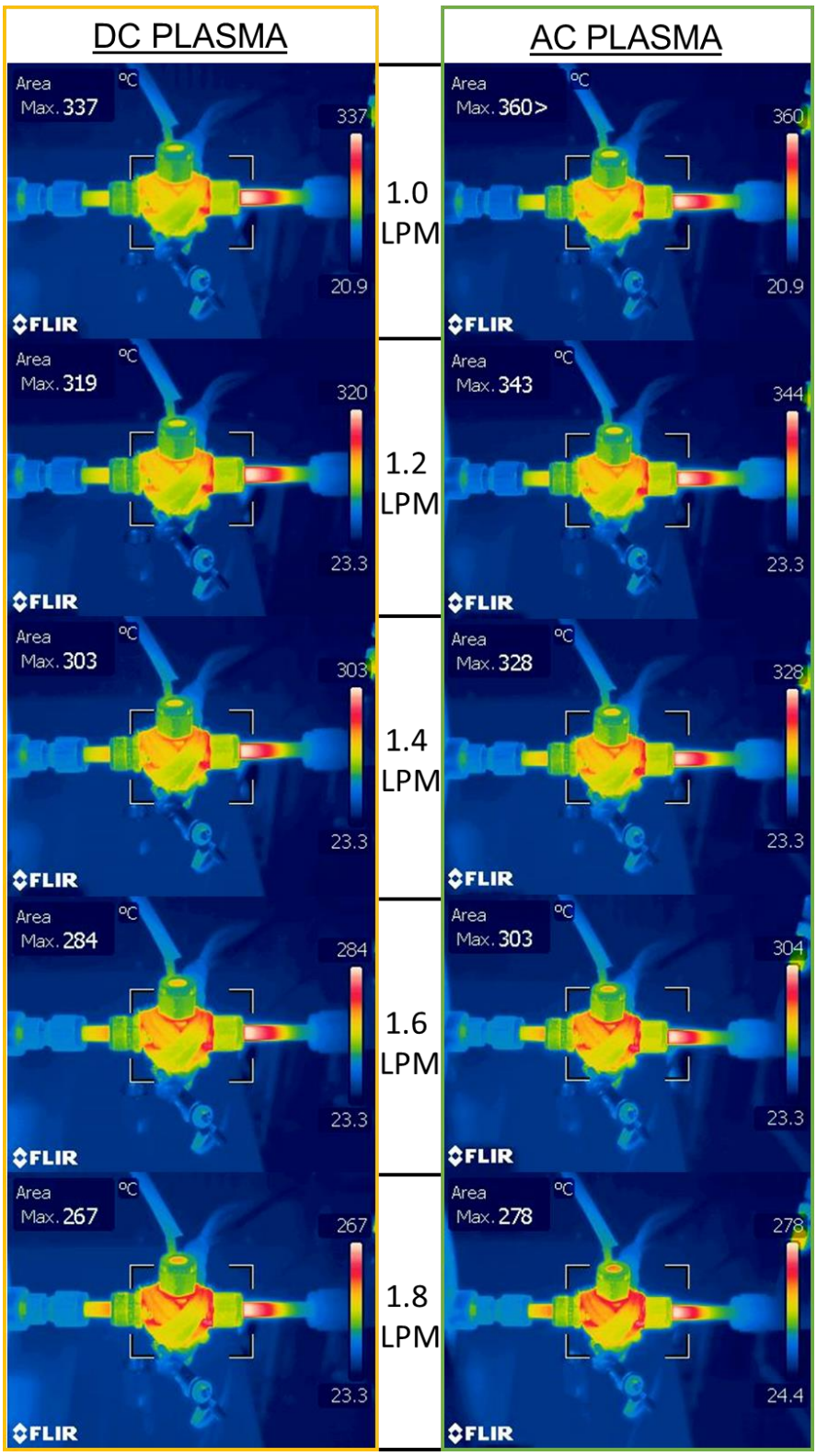

Figure 3.6: Thermal images of the VaPI cell (wrapped in heat rope) for 20 W AC and DC discharges ramping the helium flow rate from 1.0-2.0 LPM.

On average, the protonated water cluster population detected for the AC plasma was comparable to that of the DC mode discharge, with the net water ion signal consistently equal or only marginally higher. Even with VaPI parameters optimized, the largest $(H_2O_nH)^+$ signal advantage witnessed for AC mode was <2.5-fold intensity over DC mode, still significantly less than the order of magnitude higher concentration that could be expected from metastable atom spectroscopy. Interestingly, protonated water clusters were observed even when all cross union openings of the VaPI ion source were sealed off from the atmosphere. This finding suggests reactant ions were formed in the discharge from plasma gas impurities and not just He* Penning ionization of ambient air molecules. More substantive conclusions may be reached by comparing plasmas in AC/DC power regimes using even higher quality gases while controlling system temperature. Ultimately, since the DC discharge offered more stable operation and simpler *I/V* control, it was selected over AC mode for continued experiments.

3.4.3. TM-VaPI Analysis of Solids

Based on the characterization experiments with volatile standards, the TM-VaPI ion source is potentially well-suited to MS applications that require rapid qualitative and semi-quantitative analysis, such as composition screening, reaction monitoring, and molecular profiling. Using the default transmission mode geometry, the ion source was amenable to sampling solids without protracted analyte extraction/dissolution steps. Fragment pieces from a variety of pharmaceutical tablets were placed on the cross union sample mesh and a stable signal TIC trace could be achieved. Absolute ion intensity and relative distribution for tablet active ingredients was again found to depend on both helium flow rate and plasma temperature, with less detriment than when sampling volatiles. Desorption and ionization could be effectively tuned to favor different target analytes by raising the cross union temperature. Cross union temperature was maintained at approximately 275 °C, where thermal desorption for heavier compounds from a solid

matrix was efficient, but below the temperature limit where poor fluid dynamics and vacuum loss occurred. For a few select cases, it was found that higher sensitivity was obtained when organic solvent was spotted on the mesh immediately after removing the larger tablet fragments.

The spectrum for a single component drug tablet containing acetaminophen (500 mg) is shown in supporting information, Figure 3.7A. Interestingly, both the molecular ion and protonated species were detected. The afterglow of the 20 W DC plasma (~200 ℃) was sufficient to thermally desorb the compound and provide ample signal, but a noticeable 20-25% increase in total acetaminophen ion intensity was observed when heating the cross union to 275 ℃, Figure 3.7B. As expected, the elevated cross union temperature served to enhance desorption off the mesh and cross union interior walls, resulting in a stable $[M+H]^+$ intensity but now a more abundant $[2M+H]^+$ species. A similar effect was seen for Doralgine tablets containing both caffeine (25 mg) and noramidopyrine (120 mg). Without external heating the spectrum featured primarily the $[M+H]^+$ ions of both ingredients, with caffeine being the most abundant, Figure 3.7C. Again, $M^{+\cdot}$ molecular ions of both compounds were also observed. Raising the cross union temperature to 275 ˚C had a dramatic effect, where the signal for caffeine was quickly dwarfed and the protonated monomer and dimer peaks of the more concentrated noramidopyrine ingredient dominated the spectrum with an ~4-fold signal increase, Figure 3.7D. The smaller peaks neighboring the noramidopyrine signals suggest the inclusion of dipyrone and/or methamizole analogues as lesser tablet constituents, having formulas matching a methamizole protonated fragment ion $[C_{13}H_{17}N_3O+H]^+$ (m/z = 232.1427) and noramidopyrine/dipyrone fragment dimer complex $[(C_{13}H_{16}N_3O)(C_{12}H_{15}N_3O)]^+$ (m/z = 447.2500). For both tablets, the increased abundance of dimer species is attributed to both a rise in the overall analyte vapor pressure with higher VaPI cell temperatures, and also partial cooling/clustering of the volatilized analyte in the transfer capillary.

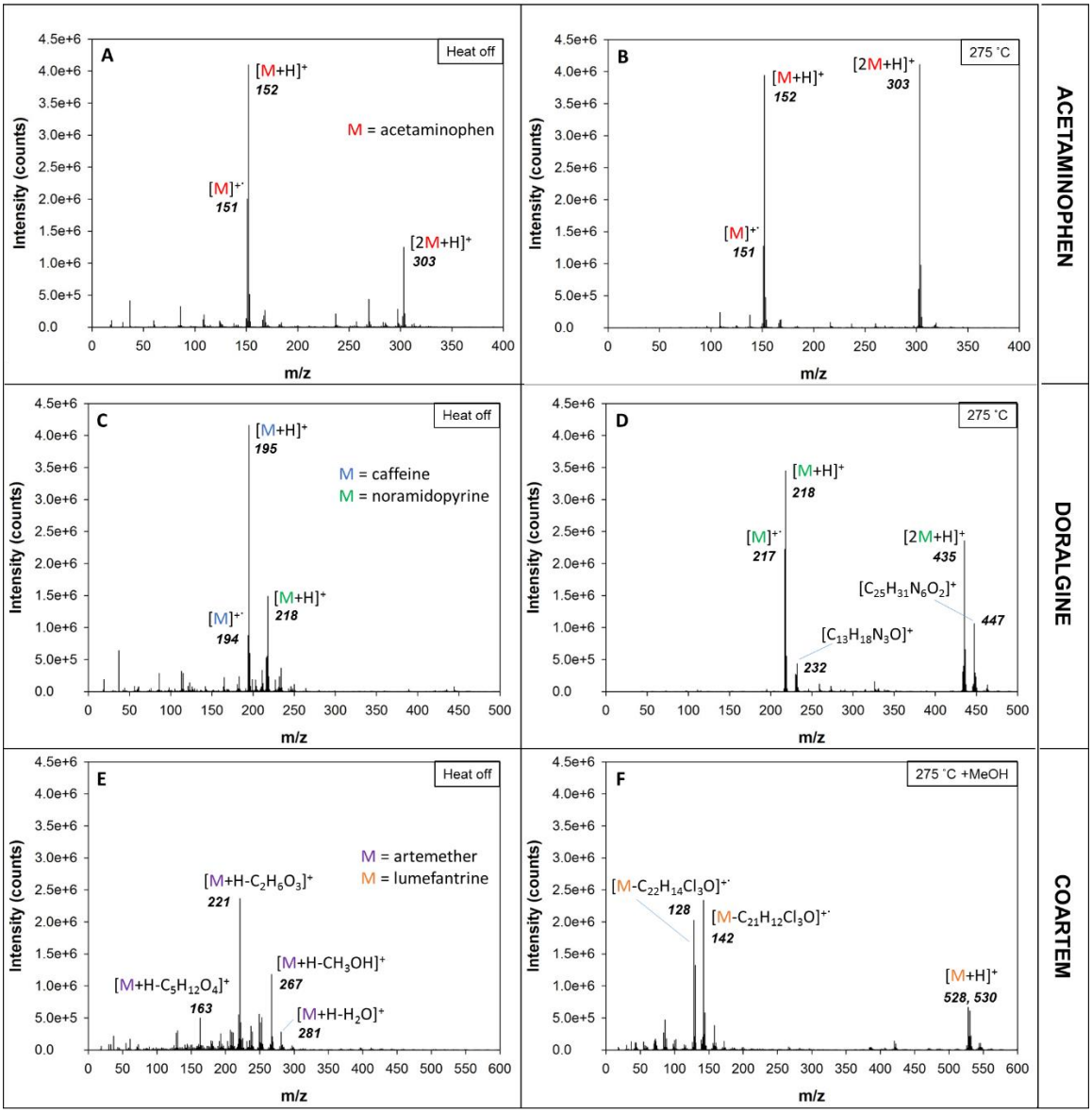

Figure 3.7: Mass spectra for acetaminophen (**A-B**), Doralgine **(C-D)**, and Coartem (**E-F**) drug tablet fragments collected by TM-VaPI using 20 W DC discharge and 1.6 LPM helium with (*right*) and without (*left*) cross union heated to 275 °C and/or organic solvent addition. All spectra were derived from 30 second averages of the TIC signal for each tablet.

Antimalarial Coartem tablets containing higher mass artemether (20 mg) and lumefantrine (80 mg) ingredients were sampled as well, employing additional sample treatment to improve analysis. Compounds in the artemisinin family are prone to fragmentation during both electrospray and plasma ionization. In Figure 3.7E, the

characteristic ion fragments for artemether are readily seen at m/z = 163, m/z = 221, m/z = 267, and m/z = 281 as previously identified in the literature[113]. Heating the cross union to 275 ˚C only shifted the relative intensities of the observed species in greater favor of fragments at m/z = 221 and a lesser fragment at m/z = 253 (spectrum not shown), but otherwise did not alter the total ion signal distribution. Detection of the heavier lumefantrine ingredient required addition of organic solvent to the mesh, Figure 3.7F. It is speculated that the solvent vapor acted as a sort of extractant, similar to a codistillation process, where the boiled solvent wetted tablet residue and freed material condensate adhering to the mesh or cross union walls. Upon removal of the tablet pieces and addition of methanol in microliter aliquots to the mesh screen, the protonated lumefantrine monomer with its chlorine isotopes appeared at m/z = 528 and m/z = 530, accompanied by more intense peaks in the low mass range. These peaks are associated with $M^{+\cdot}$ fragments of lumefantrine formed by cleavage of the amine moiety and are identified based on accurate mass as $[C_8H_{18}N]^+$ (m/z = 128.1449) and $[C_9H_{20}N]^+$ (m/z = 142.1604). The observation of $M^{+\cdot}$ ions in addition to $[nM+H]^+$ is not entirely unexpected, considering the analyte direct exposure to the highly energetic afterglow reactive species.

3.4.4. LA-VaPI Characterization

Typical LA-plasma ion source configurations reported in the literature make use of an open format where fluid dynamic effects at the mass spectrometer inlet result in significant ion transmission losses. To investigate if the more controlled sampling capabilities of VaPI could further enhance LA-plasma ionization approaches, we tested a LA-VaPI configuration, as depicted in Figure 3.1B and 3.1F.

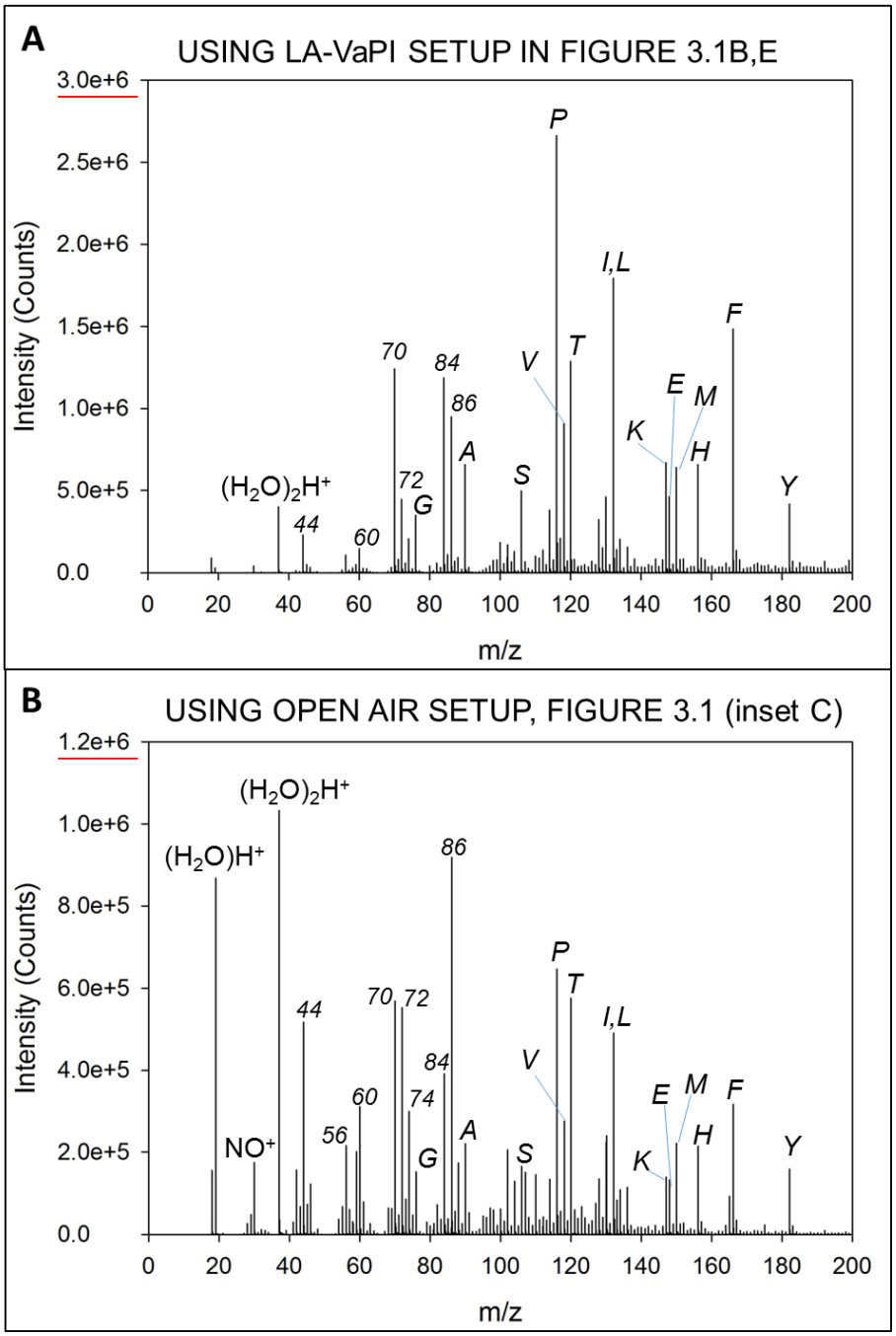

Figure 3.8: Mass spectra of 2.5 mM amino acid standard in 0.1 N HCl sampled by laser ablation and plasma ionization using either the LA-VaPI scheme from Figure 3.1B (A) or a traditional open AP interface arrangement shown in Figure 3.1C (**B**). Standard mixture was ablated from 10 µL droplet on Omni slide substrate. Spectra are an average of full time until droplets were consumed (~20 seconds each). Laser wavelength, frequency, and effective energy were 2940 nm, 10 Hz, and ~1 mJ. Optimal helium flow rate for (**A**) was 1.6 LPM and 1.3 LPM for (**B**) with the cross union heated to ~200 °C.

Performance of the vacuum-assisted LA-VaPI source design compared with an optimized open air configuration (Figure 3.1C) is presented in Figure 3.8. An amino acid standard mixture was analyzed by laser ablation of microliter droplets deposited between Teflon spots on a glass Omni Slide™. Tentative peak assignments were made for 14 of the 17 mixture components. Judging by the spectral distribution, ionization appeared to be decided by compound hydrophobicity and enthalpy of vaporization rather than gas phase basicity, favoring amino acids with higher surface activity and evaporation rates over those with the greatest side chain proton affinity. The exception relative to the other undetected basic and hydrophilic amino acids was proline, primed to dominate the spectrum owing to a higher predicted volatility over species like histidine and a rigid structure better able to withstand the energy of glow discharge ionization without fragmentation or rearrangement[114]. The amino acid ion populations observed were very similar across spectra for both source configurations, but signal intensities were superior using the LA-VaPI scheme shown in Figure 3.1B. Total signal intensity was ≥2.5x higher for all amino acids detected (Figure 3.8A) and the protonated reactant water clusters were almost completely consumed. In contrast, many of the reactant ions were seen to survive in the spectrum for the open interface LA-plasma source arrangement, Figure 3.8B. As observed previously using a VaPI configuration, ambient air suctioned through the inlet partly cooled the plasma gas. This effect in combination with the enclosed nature of the VaPI ion source also helped reduce spectral complexity in the low mass range, signified by fewer amino acid fragment ions appearing under 100 Da (Figure 3.8B).

Following these LA-VaPI experiments, an alternative sampling approach was tested with the goal of further increasing ablation plume collection and/or controlling evaporative loss. The Omni slide planar substrate was substituted with a ¼" glass capillary ampoule filled with several hundred microliters of sample solution. Keeping the cross union temperature below 250 ˚C, the sample-loaded ampoule was inserted at the bottom cross union joint and held in place by system vacuum. With this sampling

strategy, uptake of aerosols generated in the ablation plume was maximized, allowing heavier ejecta to be recycled upon recapture in the capillary reservoir.

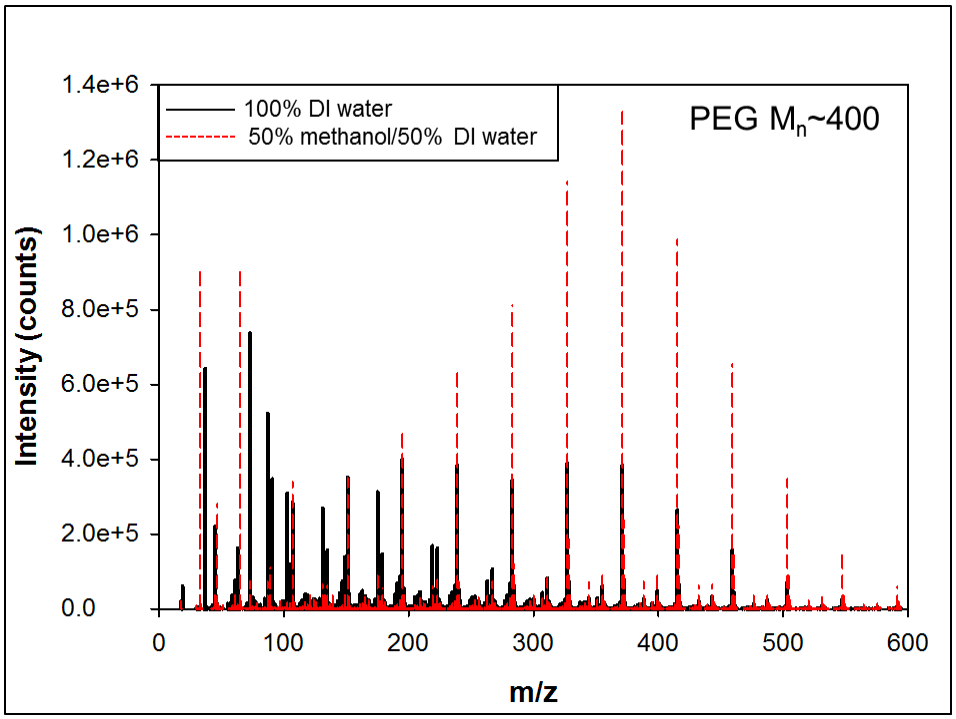

Figure 3.9: Investigation of solvent matrix effects using LA-VaPI with 20 W DC discharge and 1.6 LPM helium. Mass spectra for 4 mg mL^{-1} (~10 nmol μL^{-1}) PEG standard (M_n ~400) in 100% aqueous solution (**black trace**) and 50:50 methanol/water (red trace). Unless otherwise specified, ablation was performed from 200 µL solution in capillary ampoule held by vacuum in the cross union heated to ~200 °C. Laser wavelength, frequency, and effective energy were 2940 nm, 10 Hz, and ~1 mJ. Spectra and bar graph intensities were extracted from 1 minute average of stable TIC signal.

Figure 3.9 depicts the LA-VaPI spectrum obtained from an aqueous PEG solution, showing uniform ion intensity and polymer unit spacing. Interestingly, both analyte signal intensity and peak distribution were enhanced by addition of organic solvent to the aqueous matrix solution (red dotted trace). Not only was the net signal significantly higher for polymer analytes ablated from the mixed solvent system, but the $[M+H]^+$ peak distribution more accurately reflected the PEG polydispersity (M_n = 395-410). It is conjectured that the higher organic solvent content facilitated aerosol plume formation by changing the droplet size distribution[115] and the degree of analyte

enrichment, which in turn promoted more facile desolvation/ionization in the afterglow region. Experiments with methanol concentrations in the 20-90% range showed largely similar results.

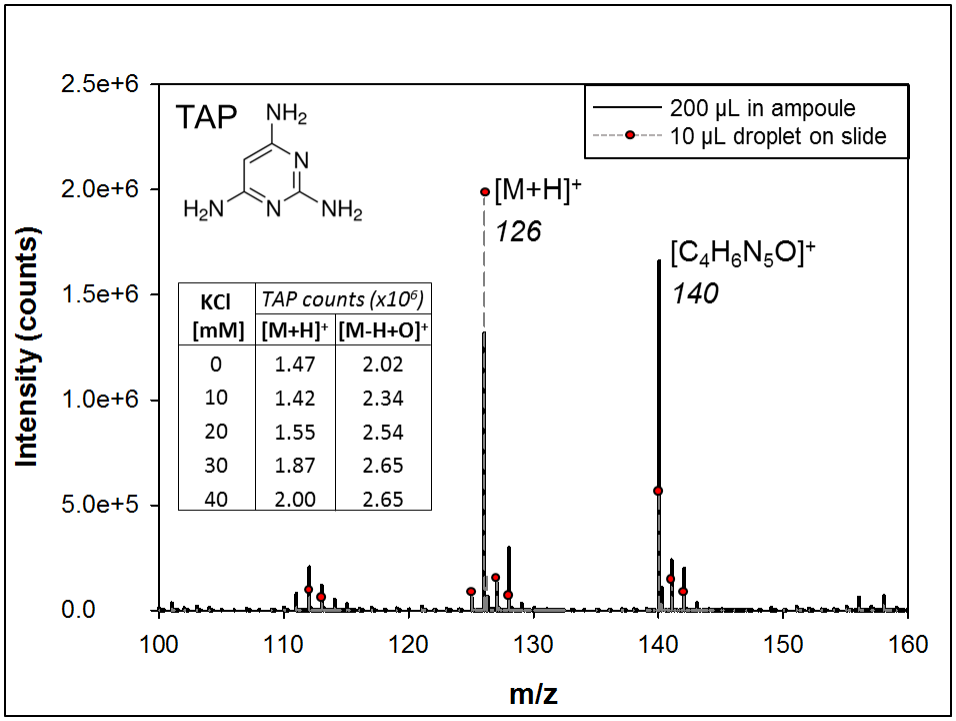

KCl [mM]	TAP counts (x10⁶) [M+H]⁺	[M-H+O]⁺
0	1.47	2.02
10	1.42	2.34
20	1.55	2.54
30	1.87	2.65
40	2.00	2.65

Figure 3.10: Investigation of salt matrix effects using LA-VaPI with 20 W DC discharge and 1.6 LPM helium. Mass spectrum of 2.5 mM TAP in deionized water sampled from 200 µL of solution in ampoule (**black trace**) or 10 µL droplet on glass substrate (dotted gray trace). Table includes signal intensity of ions detected for 2.5 mM TAP in aqueous solution as a function of KCl molar concentration ablating from ampoule. Unless otherwise specified, ablation was performed from 200 µL solution in capillary ampoule held by vacuum in the cross union heated to ~200 °C. Laser wavelength, frequency, and effective energy were 2940 nm, 10 Hz, and ~1 mJ. Spectra and bar graph intensities were extracted from 1 minute average of stable TIC signal.

LA-VaPI also proved relatively resistant to the negative effects associated with high salt concentrations in the sample medium. For example, LA-VaPI was used to analyze solutions containing both potassium chloride and 2,4,6-triamidopyrimidine (TAP), a nucleobase analogue involved in non-covalent self-assembly structures with cyanuric acid that are stabilized by cationic salts in aqueous solution [116]. For KCl concentrations up to 40 mM, the average TAP signal was relatively unaffected (inset

table, Figure 3.10), with a moderate signal enhancement as salt concentrations increased. Similar to the effect of organic solvent on PEG signal, concentrated salt ions in the aqueous matrix may influence analyte solubility and droplet distribution to promote volatilization.

Mass spectra showing the two TAP analytes detected using the different LA-VaPI sampling approaches are overlaid in Figure 3.10. The protonated TAP monomer and an additional TAP derivative with accurate mass m/z = 140.0583 and formula $[C_4H_6N_5O]^+$ (alternatively denoted as $[TAP\text{-}H+O]^+$) are present in varying proportions. Reactant ions including N_2^+, O^+/O_2^+, and NO^+ have been commonly reported for ambient helium discharge sources like FAPA[29] and PADI[31]. Although far less abundant than the reactant $(H_2O)_nH^+$ series, the peak intensity for NO^+ was observed to increase (more than double) in the background spectrum using the enclosed ampoule sampling method due to enhanced diffusion of atmospheric N_2 and O_2 into the discharge. This same exposure to the plasma corresponded to an increase of the TAP byproduct ion (m/z = 140) relative to the protonated monomer (m/z = 126). Again, this effect was not an anomaly. As witnessed previously for 2,4-lutidine, a minor byproduct identified as $[M\text{-}H+O]^+$ was seen at m/z = 122 using TM-VaPI, and an NO^+ adduct of 2,4-lutidine was also detected at m/z = 137 (not shown) when sampling from the LA-VaPI ampoule. It appears conjugated cyclic amines of the pyridine/pyrimidine structure are prone to byproduct formation when sampling with VaPI via plasma oxidation.

3.4.5. Application of LA-VaPI to Reaction Product Screening

Model prebiotic reactions studied in origins of life chemistry, such as the Miller-Urey experiment[117, 118] or the formamide reaction[119], generate highly complex, seemingly intractable mixtures[120]. In these systems, the products of interest are often not the most abundant and product loss can propagate during sample cleanup with chromatography or extraction steps. Successful MS analysis of such mixtures necessitates

sensitive instrumentation and efficient sampling measures that are robust to matrix effects.

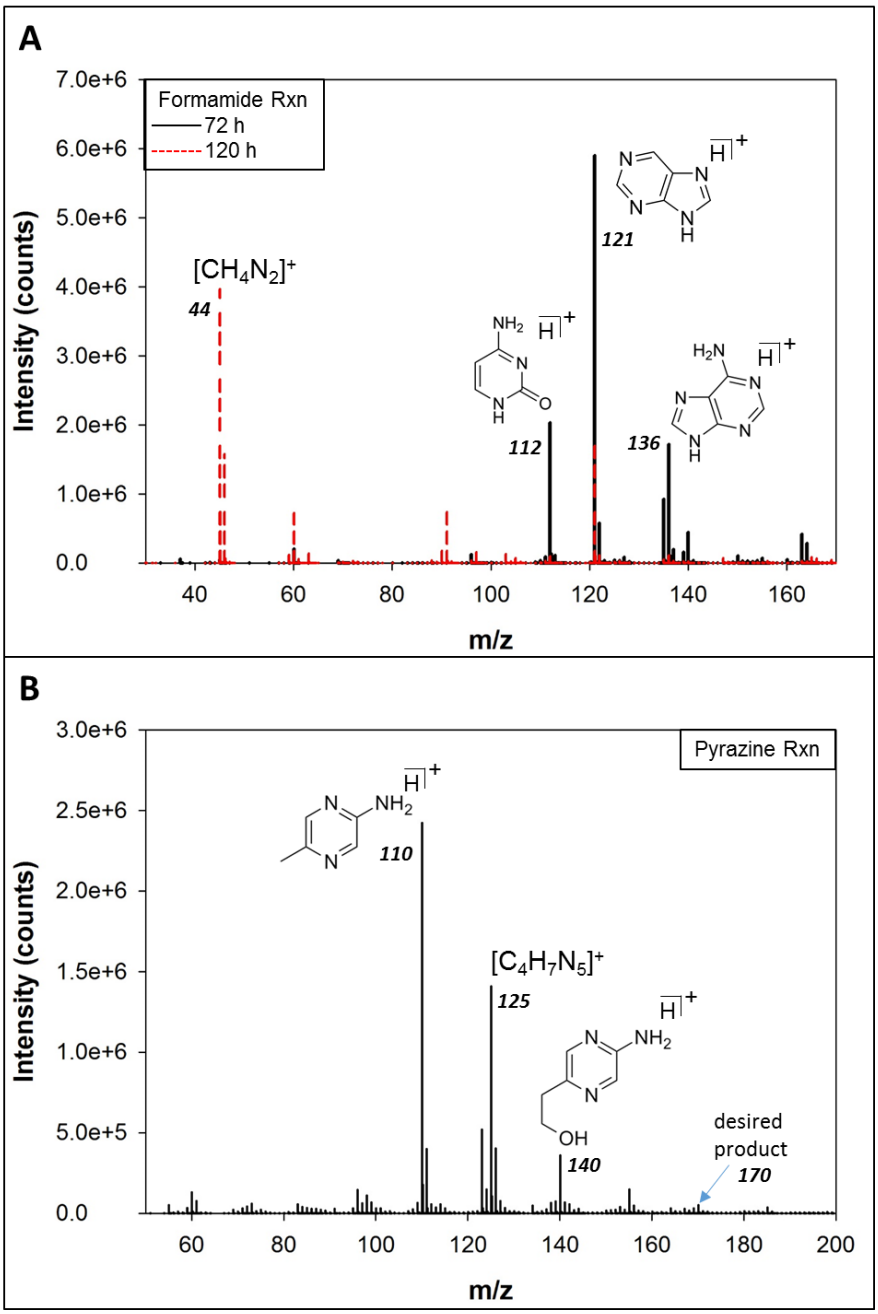

Figure 3.11: Mass spectra for model prebiotic synthetic reactions monitored by LA-VaPI using 20 W DC discharge and 1.6 LPM helium with cross union heated to 200 °C. Formamide reaction nucleobase products measured at 72 h and 120 h time points (**A**) and reaction side products from pyrazine reaction after 24 h and workup (**B**). Aqueous solutions were filtered for particulates and sampled in 200 µL from ampoule. Laser wavelength, frequency, and effective energy were 2940 nm, 10 Hz, and ~1 mJ. Spectra represent 1 minute average of TIC trace.

LA-VaPI was used to monitor natural and alternative nucleobase products formed in formamide and pyrazine model prebiotic reactions. The synthetic pathways postulated for the formamide reaction have been reviewed in the literature[119, 121, 122], and the reaction pathway for the predicted pyrazine products proceeds similarly to schemes reported for the sugar-based formation of pyrazinones[123]. Basic sample preparation involved collecting portions of the crude product or fractions of the desalted mixture (see experimental section for details), followed by resuspension in DI water and filtration to remove large particulates prior to laser ablation from the sample ampoule. In Figure 3.11A, the nucleobases predicted to form in the formamide reaction, including purine, adenine, and cytosine, were all identified for a reaction run to completion (120 hours at 160 ˚C). Analyzing the same reaction after only 72 hours, purine was still seen as the prevailing nucleobase, but the spectrum was also dominated by low mass species involving the volatile formamidine precursor, and adenine and cytosine were far less abundant. Figure 3.11B shows a spectrum for a reaction mixture containing 2-aminopyrazine products. The desired 5(6)-dinydroxypropyl-2-aminopyridine compound at m/z = 170 was barely observable above the noise threshold, but appreciable amounts of other pyrazine products were detected, including the protonated monomers of 5-methyl-2-pyrazinamine and 5-amino-2-pyrazineethanol at m/z = 110 and m/z = 140, respectively. A possible reaction byproduct of the glycine amidine reagent was also copiously present and identified with the formula $[C_4H_7N_5]^+$ based on accurate mass (m/z = 125.0702).

3.5 Conclusion

The VaPI source is a highly modular design featuring complementary sampling techniques, readily adaptable to a number of sampling scenarios and directly compatible with modern instrument inlets incorporating glass transfer capillaries. Acquiring reproducible, quantitative signals with TM-VaPI or LA-VaPI depends on a balance between source gas temperature and helium flow rate, which ultimately govern the

vacuum pressure dynamics within the cross union and determine the available reactant ion population. To this effect, differences in analyte signal intensity observed between equivalent power AC and DC discharges were linked to subtle variations in temperature between power regimes rather than differences in active metastable concentration. As demonstrated, the VaPI source is amenable to analyzing both solutions and solids, but both transmission and laser ablation modes can benefit from addition of more volatile organic solvent during sampling to facilitate aerosol extraction and expedite evaporation. This initial investigation of VaPI has promised to inspire additional source modalities in future work, such as TM-VaPI combined with solid phase micro-extraction sample meshes, LA-VaPI from thin-layer chromatography substrates, direct infusion extractive spray (ES)-VaPI for online reaction monitoring, and microchip surface acoustic wave nebulization (SAWN)-VaPI.

CHAPTER 4: AN EFFECTIVE APPROACH FOR COUPLING DIRECT ANALYSIS IN REAL TIME WITH ATMOSPHERIC PRESSURE DRIFT TUBE ION MOBILITY SPECTROMETRY

Adapted from

Keelor, J. D.; Dwivedi, P.; Fernández, F. M. *J. Am. Soc. Mass Spectrom.* **2014**, *25*(9), 1538-48.

4.1 Abstract

Drift tube ion mobility spectrometry (DTIMS) has evolved as a robust analytical platform routinely used for screening small molecules across a broad suite of chemistries ranging from food and pharmaceuticals to explosives and environmental toxins. Most modern atmospheric pressure IM detectors employ corona discharge, photoionization, radioactive or electrospray ion sources for efficient ion production. Coupling standalone DTIMS with ambient plasma-based techniques, however, has proven an exceptional challenge. Device sensitivity with near-ground ambient plasma sources is hindered by poor ion transmission at the source-instrument interface, where ion repulsion is caused by the strong electric field barrier of the high potential IMS inlet. To overcome this shortfall, we introduce a new ion source design incorporating a repeller point electrode used to shape the electric field profile and enable ion transmission from a direct analysis in real time (DART) plasma ion source. Parameter space characterization studies of the DART DTIMS setup were performed to ascertain the optimal configuration for the source assembly favoring ion transport. Preliminary system capabilities for the direct screening of solid pharmaceuticals are briefly demonstrated.

4.2 Introduction

Standard atmospheric pressure (AP)-DTIMS instruments offer much greater resolving power than their reduced pressure counterparts for equivalent drift lengths, but require relatively large electric fields (300-450 $V \cdot cm^{-1}$) to effectively propel ions through the pressurized buffer gas[63, 124]. Such high electric potentials and field strengths at the drift tube entrance complicate transmission from ion sources that operate at a nearer-to-ground potential. In some modern DTIMS detectors, outdated beta-emission sources have been replaced by corona discharge, electrospray, or photoionization ion sources which can easily be biased to potentials higher than the instrument inlet[125]. Sensitivity losses arising from poor ion transmission are far reduced in these cases because ion formation occurs either within the instrument desolvation/reaction region or in the confines of a favorable electric field gradient.

Newer desorption-based "ambient" ionization techniques developed for MS, like DART, AP-MALDI, and DESI, have garnered attention as attractive alternatives to contemporary APCI and electrospray ion sources[10]. These methods have grown increasingly popular for probing surfaces while affording soft, chemically-selective ionization. Yet successful implementation of these ambient techniques with DTIMS has proven difficult, since the ionization process using these sources takes place at or near ground potentials. DESI has primarily been coupled with IMS on reduced-pressure IM-MS platforms where ion transport is vacuum-assisted[126, 127], and was only recently adapted for atmospheric pressure IM-MS[128]. Likewise, pairing of DTIMS with laser ablation has required hybrid ion source setups employing corona discharge or electrospray elements to assist ionization and transmission, as with LAESI/LADESI DTIMS[129]. LTP[130] and dielectric barrier microplasma[131] sources have been coupled with DTIMS, but used restricted arrangements with the source partially embedded in the instrument or the sample region confined within the electric field gradient, both limiting accessibility for ambient sample introduction. Our group recently reported on a

transmission mode (TM)-DART DTIMS interface featuring a sample mesh mounted at the DTIMS inlet and biased at the same electric potential[132]. Although volatiles or solutions could be easily deposited on the mesh for analysis, direct sampling of solids proved difficult and the high potential on the mesh prevented safe sampling. Additionally, the chances for evaporative loss and diffusion of analytes prior to ionization, as well as the turbulent introduction of high flow rate plasma gas into the DTIMS cell during sampling, both contributed to some reduced instrument resolving power and sensitivity.

Here, a new DART DTIMS approach intended to address TM-DART DTIMS limitations stemming from poor ion transmission at the plasma ion source-instrument interface is introduced. In this development, a DART-SVP (simplified voltage and pressure) model ion source is coupled to a resistive-glass DTIMS with the use of a repeller electrode. Our investigations suggest that ion transport into the DTIMS was facilitated by this electrode, which functioned to favorably shape the electric field lines and enable DART-generated ion transmission through the high potential barrier. Preliminary evidence also indicates the strong field near the point electrode possibly works to promote APCI mechanisms involving DART excited N_2 species. As briefly showcased, this source scheme incorporating DART is also amenable to the direct analysis of solids or non-volatile samples, and may advantageously serve as an alternative to traditional corona discharge ionization. We believe that this DART DTIMS methodology holds promise for interfacing DTIMS not only to DART, but also to other plasma-based ambient ionization sources such as FAPA, LTP, and microplasma devices.

4.3 Experimental

4.3.1. Materials and Reagents

All chemicals were analytical grade (Sigma-Aldrich, St. Louis, MO) and used without further purification. Solutions of 2,6-di-*tert*-butylpyridine (2,6-dtBP, ≥97%) were

prepared in methanol (HPLC grade) or ultra-pure water (18.2 MΩ cm, Barnstead Nanopure Diamond, Van Nuys, CA) in concentrations ranging from 5 to 50 mM. Over-the-counter tablets of acetaminophen (500 mg) used were Target Brand, Inc. (Minneapolis, MN). Nitrogen (99.995%, Airgas, Atlanta, GA) was used as the DTIMS buffer and DART source gas. Tungsten (2% Thoriated) and Mo-doped M2/M7 steel rods (0.400 mm *dia.*) were procured from McMaster-Carr and precision ground to points (1/10000" tolerance) for their use as repeller electrodes.

4.3.2. Instrumentation and Methods

The drift tube ion mobility spectrometer used in this study has been described in detail in previous publications[133, 134]. Briefly, the DTIM spectrometer was constructed of two monolithic resistive glass tubes (PHOTONIS USA, Sturbridge, MA) with a resistance of 0.45 GΩ·cm^{-1}. The desolvation and drift regions measured 11 cm and 25 cm, respectively, with 3 cm *i.d.* and 4 cm *o.d.* dimensions. The two tubes were separated by a Bradbury-Nielsen-style ion gate (TOFWERK AG, Thun Switzerland) centered in a PEEK bridging unit with 0.5 cm net gap between cells (0.25 cm on either side of the gate). When the gate is closed, a potential of ±35 V is applied across the adjacent sets of wires in addition to the drift tube entrance potential. An iridited aluminum Faraday plate detector (2.6 cm *dia.*), spaced 0.3 cm apart from an aperture grid, was fixed at the end of the drift cell and connected to a custom-built amplifier (TOFWERK AG). The amplifer input resistance was 1 kΩ and the gain setting was 0.1 pA·mV^{-1} for a rise time of 250 μs (10-90%). Voltage provided to the instrument via a high-voltage power supply (FUG HCL 14-2000, Magnavolt Technologies, Plattsburgh, NY) was passed through a voltage divider to four electrode contacts connected at the entrance and exit of each glass cell. With a DTIMS entrance potential of 12,000 V, the approximate electric fields were 155 V cm^{-1} for the desolvation cell and 385 V cm^{-1} for the drift cell. Dry nitrogen buffer gas entered the drift cell behind the Faraday plate and the gas flow rate was controlled using a

precision flow analog manometer (PMR 1, Del-ART/Scienceware, Pequannock, NJ). Drift gas and DTIMS cell temperatures were kept ambient for all measurements to afford optimal resolving power on our instrument. Ion gate timing was software-triggered and performed synchronously with data acquisition using a NI 5411 arbitrary waveform generator and a NI 6111 ADC with in-house custom software developed on Labview 7.1 (National Instruments, Austin, TX).

The ion source scheme featured a DART-SVP unit (IonSense, Inc. Saugus, MA) positioned orthogonally to the IMS inlet. A glass capillary (L = 4.0 cm, 0.15 cm *i.d.*, 0.30 cm *o.d.*) extended from the DART outlet approximately 2 mm past the inner lip of the IMS opening. The repeller electrode (L = 3.5 cm, 0.400 mm *dia.*) was connected to a high-voltage power supply (Bertan Associates, Inc. Series 205B, Hicksville, NY) independently from the DTIMS power supply and coaxially centered normal to the face of the DTIMS entrance, spaced 1 cm away from the DART capillary. The standard IMS calibrant 2,6-dtBP was selected for characterization experiments because of the compound's low clustering tendency across a broad range of temperatures and pressures, giving a single, reproducible reduced mobility value ($K_0 = 1.42 \pm 0.02$ cm$^2 \cdot$V^{-1} s^{-1})[135].

A Schlieren linear single-mirror double pass configuration was used to visualize gas flow patterns at the DTIMS interface. All optical equipment was purchased from Anchor Optics (Barrington, NJ). The key component of the setup was a commercial grade 75 mm diameter spherical mirror (f.l. 750 mm). The mirror was placed securely in a kinematic lens mount on a linear rail in immediate proximity (2-5 cm) to the DART source outlet and test area. A camera lens was positioned in plane and opposite to the mirror at approximately twice the focal length. The mirror and camera lens were set as close to perpendicular with one another as possible to attain the best contrast. Image capture was accomplished using a Cannon EOS 5D Mark II (Cannon U.S.A., Inc., Melville, NY) with a Sigma 210 mm zoom lens (Sigma Co. of America, Ronkonkoma, NY). The Cannon EOS 5D Mark II was fixed on custom stilts to an optics bench with

the lens ~3 cm behind a 50/50 planar beam splitter (50x50 mm) held in a prism mount. A 10-mm white light-emitting diode (RadioShack®, Fort Worth, TX) with the clear plastic lens cut flat and polished was used as the point light source, situated perpendicular to the camera and aligned with the beam splitter. The diode was powered using a constant 20 mA current on B&K Precision 1623A 60V/1.5A power supply (B&K Precision, Yorba Linda, CA). Light was focused through a pin-hole in an aluminum foil cap covering the diode cavity. Image contrast was improved by placing a blue color filter in front of the camera lens. Optimal mirror/lens alignment was estimated by manipulating the mirror to reflect a laser beam fired at the mirror center through the beam splitter back to the camera lens. All Schlieren images were recorded using high-definition video (1920x1080, 24 fps) and individual frames were selected for figures. Infrared thermography measurements of sample surfaces heated by the DART gas stream at the DTIMS interface were recorded using a FLIR TC300 IR digital camera (FLIR Systems AB, Danderyd, Sweden).

All DART-SVP mass spectra were collected on a JEOL JMS-T100 LC AccuTOF time-of-flight mass spectrometer (Peabody, MA). The MS skimmer desolvation gas and heater temperature were kept off. The orifice voltages were tuned to maximize ion transmission and minimize in-source fragmentation – orifice 1: 10 V, ring lens: 8 V, orifice 2: 2 V. Ion guide peaks voltage was swept (120-280 V) for optimal sensitivity in the low mass range using a bias voltage of 29 V. Pusher bias was -0.28 V and MCP detector voltage was 2650 V. Sample was introduced into the DART sample gap (~1 cm) via a solution-coated capillary probe or as the raw drug tablet.

4.4 Results and Discussion

4.4.1. Ion Source and System Characterization

The repeller-assisted DART ion source concept originates from the point-to-plane corona ionization schemes routinely employed with DTIMS and MS [136, 137]. The standard configuration of the experimental setup is depicted in Figure 4.1. A high voltage

point electrode generates intensely focused electric field lines near its tip and, when appropriately biased above the DTIMS inlet potential, a potential energy gradient between the electrode tip and the DTIMS inlet is created.

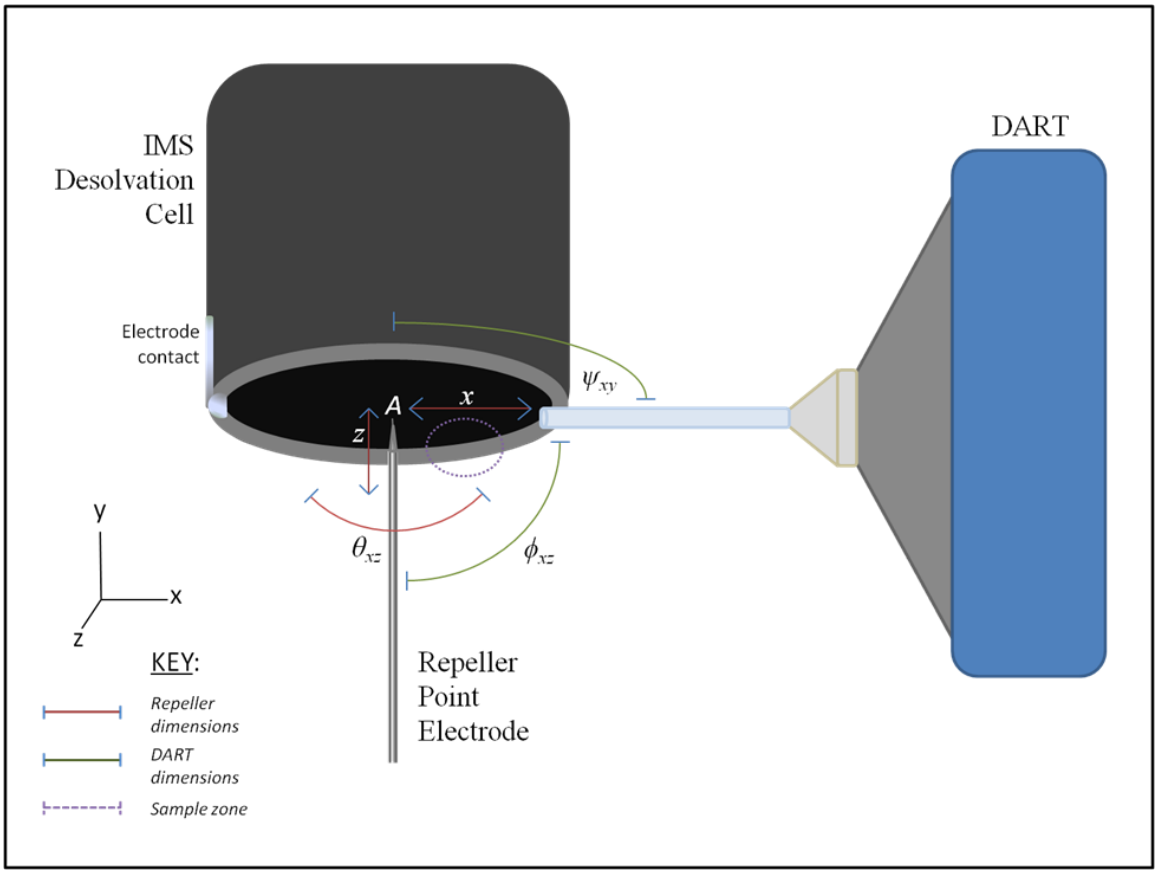

Figure 4.1: Schematic of the resistive glass DTIMS inlet showing the standard starting configuration for the repeller electrode and DART-SVP ion source. The repeller potential and position (x, z) and the DART (φ_{xz}, ψ_{xy}) and repeller angles (θ_{xz}) were varied as described within the characterization studies.

This gradient facilitates ion transfer into the DTIMS cell for ions generated by the DART source at electrode potentials below the Townsend breakdown threshold. The envisaged effect was modeled in SIMION 8.1. Potential energy contours for the DTIMS desolvation cell (*length* = 11 cm, *i.d.* = 3 cm, *o.d.* = 4 cm) are shown for the standard IMS inlet at 12,000 V (Figure 4.2A) and for the DTIMS cell with the repeller point electrode at 13,500 V inserted 5 mm inside the cell (Figure 4.2B). Ground (0 V) is defined ~3 cm away and the electric field gradient inside the desolvation cell is

approximately 155 V·cm^{-1}. The aim was to utilize the favorable potential slope created by the electric field lines near the repeller (Figure 4.2B) to guide ions originating from an orthogonal plasma source at ground potential into the DTIMS cell held at an elevated potential.

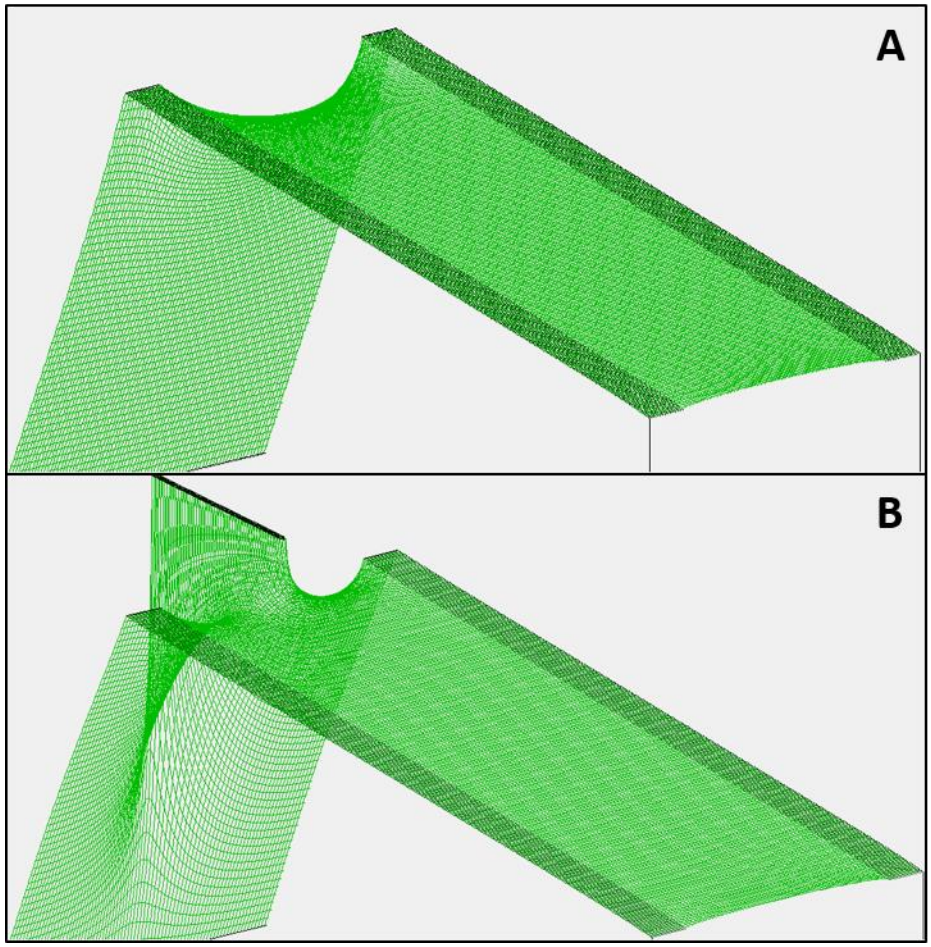

Figure 4.2: SIMION 8.1 scaled models of the resistive glass IMS desolvation cell (*l* = 11 cm, *i.d.* = 3 cm, *o.d.* = 4 cm) without the repeller, panel **A,** and with the repeller (*dia.* = 1 mm) point electrode 1.5 kV above the inlet potential, panel **B**. Models are built from a cylindrical potential array mirrored in the y-plane (*# grid units (gu) after symmetry*: x = 1099 gu, y = 199*2 gu, z = 199*2 gu, *xyz gu length* = 0.125 mm). The entrance and exit electrodes of the cell (x = 40 gu, y = 1 gu, inter-electrode distance x = 880 gu) were defined at 12,000 V and 10,300 V, respectively. Ground was included as a solid plate (x = 1 *gu*, y = 199 *gu*) marked ~27.5 mm (x = 220 gu) away from the entrance electrode to approximate field strength diminishing as (1/r). The repeller electrode potential was defined at 13,500 V drawn normal and on-axis with the IMS, 40 gu inside the inlet electrode (x = 220 gu, y = 4 gu).

Thus, when interfaced with DTIMS, this point electrode could function as a repeller enhancing the electric field profile at the inlet to facilitate ion transmission from plasma ion sources. A preliminary proof of this concept is demonstrated in Figure 4.3, where the mobility peak for a volatile analyte was observed only under certain source conditions. To prevent ion generation by a corona ionization mechanism, the electrode was biased above the IMS cell inlet potential but below the corona discharge threshold when operating the DART plasma source. Figure 4.3A shows the ion mobility spectrum baseline with the DART source off and the repeller at a potential of 13,500 V. A low intensity background reactant ion signal only appeared at this repeller potential when the DART source was activated, shown in Figure 4.3B. Introducing 2,6-dtBP vapors with the DART on and repeller potential at 13,500 V (still below threshold for corona discharge), a solitary peak for the volatile analyte appeared, seen in Figure 4.3C. With the repeller potential then increased to 14,500 V (above the corona discharge threshold) and the DART turned off, the 2,6-dtBP signal was retained, if not slightly increased, in the mobility spectrum shown in Figure 4.3D. The peak response detected for 2,6-dtBP was identified as that of the protonated monomer ion with a calculated reduced mobility (K_0) value of 1.44 ± 0.02 $cm^2\ V^{-1}\ s^{-1}$, which is in accordance with literature values[135]. With a measured drift time of 39.5 ms, the resolving power (*Rp*) for the 2,6-dtBP peak was 82. As shown, both background and analyte ions were not detected when the potential on the repeller was raised to ~13,000 V. This suggests that the field contour shaped by the potential gradient between the electrode tip and the DTIMS inlet was not sufficient to aid in transferring ions generated by the plasma source over the inlet potential barrier. However, increasing the repeller potential to 13,500 V resulted in a large detected ion intensity.

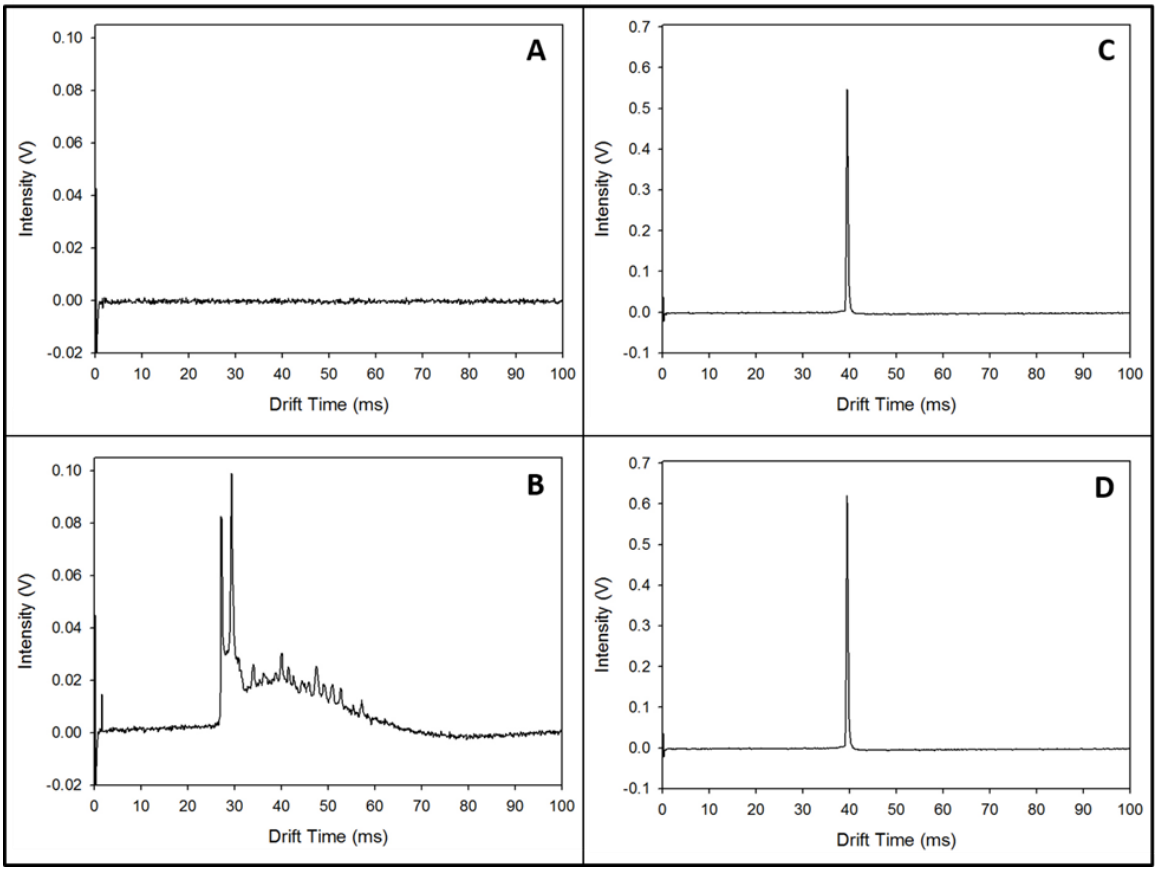

Figure 4.3: Ion mobility spectra observed during system characterization showing background and the $[M+H]^+$ signal peak for 2,6-dtBP bubbled from methanol. Spectrum baseline with repeller electrode <13,500 V and DART plasma off (**A**). Background spectrum of reactant ions with repeller at 13,500 V and DART plasma on (**B**). DART signal for 2,6-DtBP with repeller at 13,500 V (**C**) and corona discharge signal for 2,6-dtBP with electrode at 14,500 V and DART plasma off (**D**). The repeller point was coaxial in all cases and at a fixed depth of 5 mm inside the cell. Spectra were collected using a DTIMS gate pulse width of 100 μs and total scan time of 102.4 ms over 128 averages.

Since the repeller potential was below the typical corona discharge threshold, the ions detected could not have been formed by Townsend corona discharge chemical ionization mechanisms; detection of ions at 13,500 V suggested that the observed ions originated from DART ionization of neutrals, perhaps following previously proposed mechanisms [34], later transported along the potential slope into the DTIMS. As shown, the relative potential difference between the repeller electrode and the DTIMS inlet

impacts both transmission and sensitivity when coupling an ion source near ground potential.

The system described in Figure 4.1 can be optimized across several geometric variables (x, z, ϕ_{xz}, θ_{xz}, $\Psi_{x,y}$). Signal intensity as a function of both repeller potential magnitude and electrode depth (z) inside the DTIMS entrance was first examined. Figure 4.4 shows the influence of this parameter on the measured signal intensity for the 2,6-dtBP response peak. At a given electrode potential, it was observed that as the repeller was placed deeper into the first DTIMS tube (from z=0 mm at the plane of the IMS inlet up to z=12 mm inside), signal for 2,6-dtBP increased and plateaued before abruptly declining. Peak height directly scaled with increasing repeller potential between 12,900 V and 13,300 V, starkly rising to higher intensities at higher potentials, with the maximum signals reached at depths of 5-10 mm. With increasing repeller depth, the potential energy slope between the electrode tip and as the DTIMS cell is augmented, better favoring ion injection.

It can be reasoned that at higher potentials, the electric field lines emanating from the repeller are denser, better shaping the electrical field contour for more efficient transfer of ions generated by the plasma ion source. Furthermore, it is speculated that the signal drop off observed past tip depths of approximately 10 mm is likely attributed to the encounter of a net repulsive potential energy surface by the plasma ions generated in the ionization region, where the now fully "buried" repeller point, but protruding repeller rod, effectively result in a potential barrier that cannot be overcome by the fluid dynamic forces carrying ions with the plasma gas flow. The ion intensity plotted for 2,6-dtBP as a function of repeller potential at z=7 mm was seen to fit a quadratic curve and not the typical exponential growth curve expected for an AP corona discharge process[136], suggesting that saturation of the observed signal may result from a finite DART-generated reactant ion population and/or incomplete transmission.

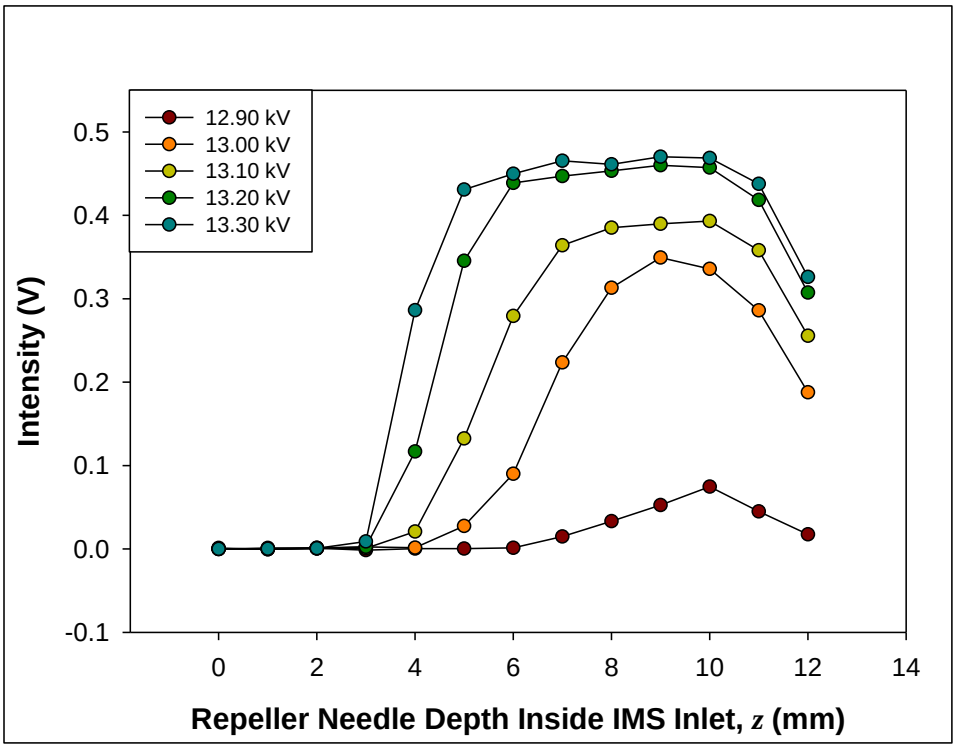

Figure 4.4: DART-generated signal for 2,6-dtBP vapor as a function of the repeller depth inside the DTIMS inlet (*z*) for increasing repeller electrode potentials. Initially, the repeller was placed coaxial and normal to the DTIMS entrance with the DART exit capillary placed orthogonal to the repeller and flush with the DTIMS face plane.

The next set of studies was aimed at determining how the angle between the DART plasma nozzle and the repeller electrode (ϕ_{xz}) impacted signal intensity (Figure 4.5). For these experiments, the repeller needle was set at a fixed distance inside the DTIMS inlet (z=7 mm) where previous experiments had shown efficient ion transmission. Rotating the plasma nozzle from the orthogonal position (ϕ_{xz}=0º) up to a ϕ_{xz}=60º angle nearing contact with the bare repeller electrode, signal was observed to quickly vanish past ϕ_{xz}=20º. When laterally-translating the coaxial repeller 5-6 mm off-center and away from the plasma nozzle, signal was restored for an angle approaching 50°. Conversely, increasing the lateral proximity of the coaxial repeller to the orthogonal plasma nozzle by 5-6 mm resulted in no ion signal at any nozzle angle. These results suggested that under certain configurations the repeller electric field disrupted ion formation and/or transport, perhaps through charging of the DART plasma nozzle or

repulsion of reactant ion species, such as protonated water clusters [$(H_2O)_nH^+$], away from a favorable trajectory conducive for adequate ion transmission/formation. These distortive effects were mitigated by shielding the coaxial repeller electrode using generic coaxial shielding stripped from a copper wire and slipped over the repeller electrode, but with the electrode point left exposed. Under these conditions, signal intensity was regained across the full ϕ_{xz}=0º-60º range.

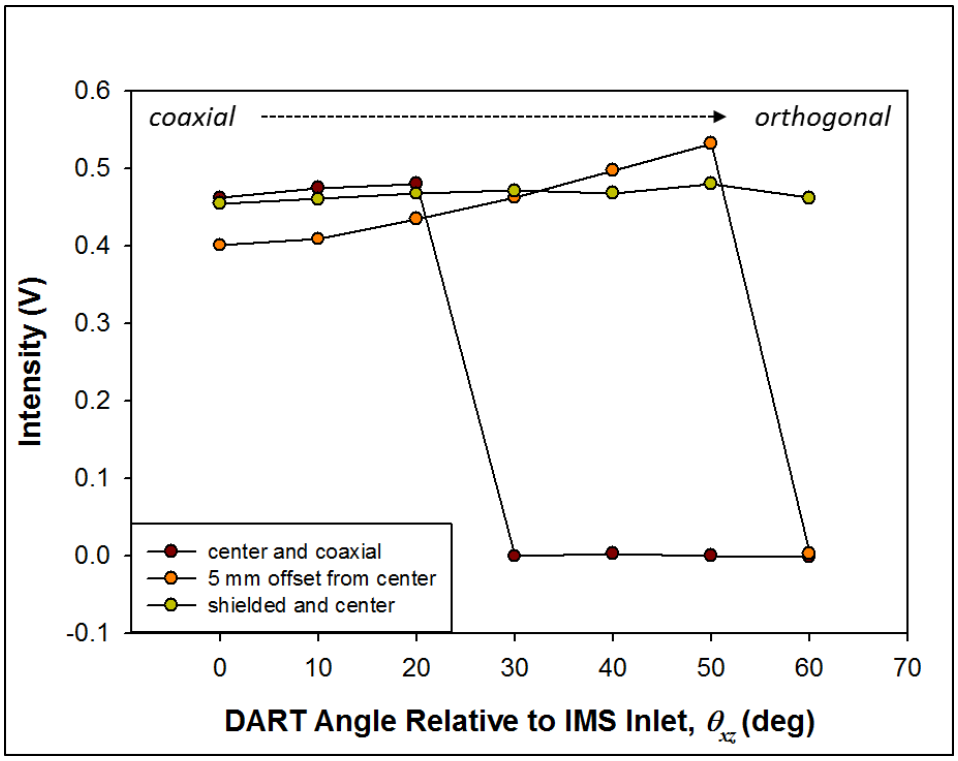

Figure 4.5: Signal for 2,6-dtBP vapor at DART ϕ_{xz} angles between 0 and 60 degrees (0 degrees being orthogonal to repeller) with *red*) the repeller electrode centered and coaxial, *orange*) the repeller electrode coaxial and offset *x*=6 mm away from the DART capillary, and *yellow*) the repeller centered and coaxial but with the rod partially shielded. The repeller at was set at 13,300 V and fixed *z*=7 mm inside the DTIMS opening. When the DART capillary was rotated along ϕ_{xz} a distance of ~1 cm was kept constant between the capillary exit and point *A* (Figure 4.1).

Similarly, signal dependence on repeller electrode angle with respect to the DTIMS entrance (θ_{xz}) was investigated (Figure 4.6). With the plasma nozzle placed orthogonally with respect to the DTIMS entrance plane (ϕ_{xz}=0º), maximum peak heights

were observed with the repeller electrode positioned coaxially (θ_{xz}=90°) with respect of the DTIMS axis. Signal dropped off sharply as the repeller electrode was angled towards the plasma nozzle at acute angles ($\theta_{xz} \leq 70^{o}$), but degraded at a much slower rate over more obtuse angles ($\geq 100^{o}$), stemming from intermittent ion transmission. Greater peak intensity was observed at higher potentials for which denser field lines help dampen ion transmission losses at wider angles. As expected, signal appeared stable across all electrode angles when the potential on the repeller electrode was increased to a corona discharge threshold of 14,000 V (2 kV above the DTIMS inlet potential). For corona discharge, localized ionization on the plasma tip inside the DTIMS inlet was less susceptible to ion transport changes arising from configuration-dependent electric field effects at the ion source-spectrometer interface.

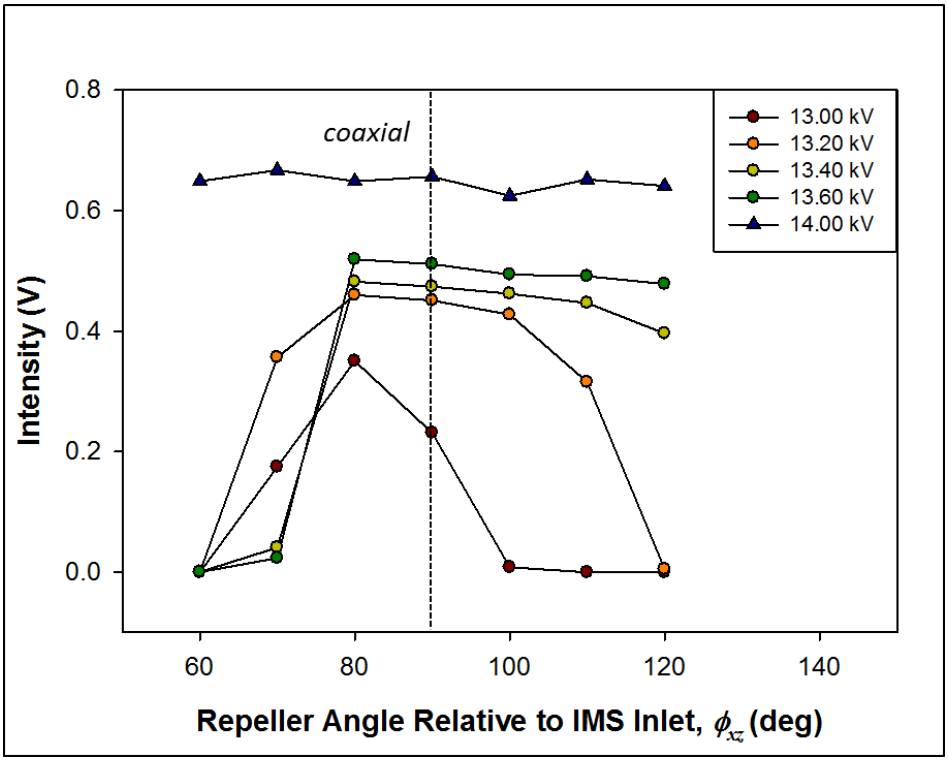

Figure 4.6: Signal for 2,6-dtBP vapor with the repeller initially placed coaxially (θ_{xz}=90°) and then moved across θ_{xz} angles in the 60 to 120 degree range. This experiment was done for both DART and corona regimes. In these experiments, the repeller electrode point was fixed at z=7 mm inside and kept stationary; the DART capillary was kept orthogonal (ϕ_{xz}=0°) to the DTIMS face.

4.4.2. Fluid Dynamics and Electric Field Considerations

The results depicted in Figures 4.4-4.6 suggest that when coupling a DART plasma ion source to DTIMS, signal abundance depends on a confluence of physical forces, the balance of which determines the extent of ion transmission. Most notably, these forces include those arising from the electric field shape defined between the ion source, repeller electrode, and DTIMS inlet; and also the fluid dynamic forces resulting from the mixing of the drift and DART gas flows at the ion source-spectrometer interface. To better understand the fluid dynamic effects in the proposed interface, the interaction between the DTIMS drift gas, the DART plasma working gas, and the sample carrier gas in the orthogonal DART DTIMS configuration was examined. Gas flows were visualized using the Schlieren imaging technique, which is capable of optically distinguishing gases based on a change in refractive index[102, 138].

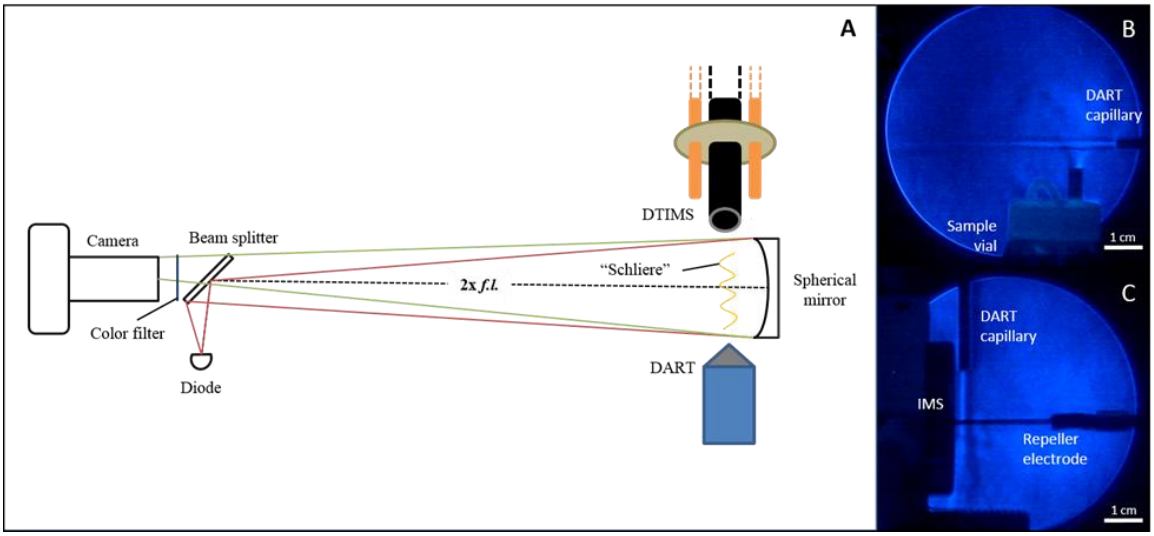

Figure 4.7: Schematic of Foucault single mirror apparatus for Schlieren experiments (**A**). Visualization of the N_2 (200 °C) flow from the DART nozzle glass capillary, with the DART stream passing through a plume of ethanol solvent vapor (~0.3 L min^{-1}) and showing no observable perturbation across a ~3.5 cm distance (**B**). DART stream with capillary set orthogonal to DTIMS using 2 L min^{-1} N_2 drift gas, indicating only minor turbulence after passing over the repeller rod (**C**).

Figure 4.7A illustrates the schematic of the Foucault single mirror setup employed for Schlieren experiments. The Schlieren image in Figure 4.7B shows a highly-collimated, consistently-laminar DART N_2 gas stream (2 L min^{-1} at 200 °C) near the IMS inlet that was not significantly disrupted by bubbling sample vapor (~0.3 L min^{-1}). With the DART source set orthogonal to the DTIMS and in plane with the repeller electrode (Figure 4.7C), the plasma jet stream experienced only minor turbulence when passing over the repeller rod. No additional distortion of the plasma stream was observed with DTIMS N_2 drift gas flowing up to 2 L min^{-1}. It should be noted that 1) the highly collimated nature of the DART gas stream depicted in Schlieren images was due to the extension of the DART nozzle with a ~4 cm *i.d.* glass capillary, 2) some gas along the DART stream periphery would be prone to diffuse and cool, and thus not be readily visualized by Schlieren imaging, and 3) due to the limitations of the setup, the lateral dispersion (out of the picture plane) of cross-flowing sample gas and DART gas may be more extreme than the vertical displacement shown.

From the observable DART flow profiles, it can be concluded that mixing of drift gas and plasma gas at the interface does not seem to significantly disrupt ion transmission, and that ions formed by DART processes within its plasma plume may be transported to the vicinity of the repeller region by purely mechanical forces. It is within this region of sharp electric fields that ions may be redirected into the drift tube. Because flow fidelity is expected to change with the introduction of sample probes or solid surfaces, the redirection of gas flows under these scenarios may require a re-optimization of the repeller-nozzle geometry. The point electrode seems to function as a field focusing element that effectively steers positive ions born within the DART plasma afterglow into the DTIMS desolvation cell against the spectrometer's high potential inlet barrier.

4.4.3. Solid Sample Analysis

A photograph depicting one working arrangement for solid sampling using repeller-assisted DART DTIMS is presented in Figure 4.8. Results for the direct analysis of a drug tablet containing acetaminophen using this configuration are provided in Figure 4.9, also showcasing the effects for different plasma source and repeller electrode conditions.

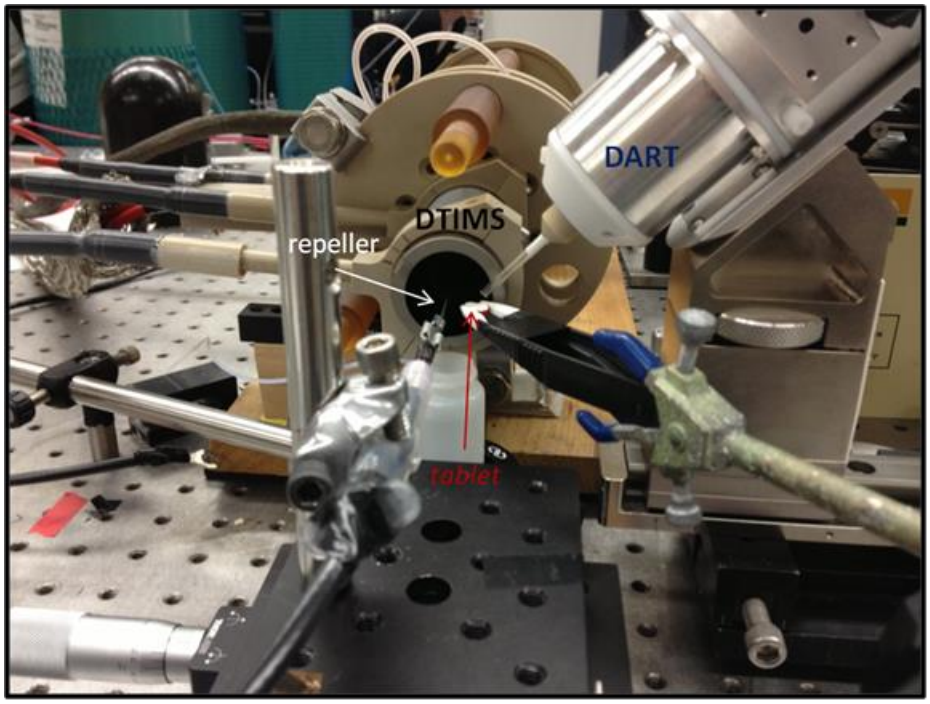

Figure 4.8: Image of an orthogonal DART DTIMS sampling configuration employed for solid tablet analysis. The arrangement shows the DART source angled 45° over a tablet situated between the coaxial repeller electrode and inner lip of the DTIMS inlet.

Figure 4.9A shows, as expected, that in the absence of a plasma discharge and hot plasma plume, no ion signal was detected even when the repeller electrode was biased to 1,500 V above the inlet potential (12,000 V). Once the plasma discharge and DART heater were turned on, a mobility spectrum was readily obtained for a repeller potential of 13,500 V, Figure 4.9B. A high intensity mobility peak for acetaminophen was observed at a drift time of 49.5 ms and reduced mobility (K_0) value of 1.15 $cm^2 \cdot V^{-1} \cdot s^{-1}$. The peak most likely represents a proton-bearing acetaminophen dimer or trimer clustered with

ambient water or ammonia. In Figure 4.9C, signal intensity for this same peak was shown to increase as the repeller electrode potential was raised from 13,500 V to 14,500 V. The spectrum is characteristically similar to Figure 4.9B, with smaller peaks appearing more clearly at lower drift times of t = 43.2 ms and t = 37.0 ms. These two peaks very tentatively correlate with the reduced mobility values for ions pertaining to the acetaminophen dimer (*calculated* K_0 = 1.32 $cm^2 \cdot V^{-1}\ s^{-1}$, *literature* K_0 = 1.36 $cm^2 \cdot V^{-1}\ s^{-1}$) and monomer (*calculated* K_0 = 1.54 $cm^2\ V^{-1}\ s^{-1}$, *literature* K_0 = 1.56 $cm^2\ V^{-1}\ s^{-1}$), respectively[53]. Alternatively, it is also possible these peaks are residual clusters of atmospheric reactant ion adducts dissociated from the broader low mobility peak at the higher DART gas temperatures used.

The signals in Figures 4.9B and 4.9C are both subtly specific to DART over corona discharge, as can be confirmed from looking at Figure 4.9D. When the DART glow discharge was turned off and a corona breakdown was incited on the electrode, the signal dissolved into a broad series of reactant ion peaks observed in the background. The DART gas temperature in this instance was not sufficient to desorb acetaminophen without the DART plasma active. The effective tablet surface temperature recorded with an IR camera measured around 80 °C with the plasma discharge off and DART heater set to 300 °C, approximately 50 °C lower than with the plasma discharge on and much lower than the set DART heater temperature. Increasing the DART heater temperature to 450 °C with the plasma off resulted in an effective temperature on the tablet surface of 120 °C, restoring the acetaminophen signal produced by the corona discharge in Figure 4.9E. The relative peak intensity distribution was somewhat different for the corona discharge spectrum, with the tallest signal shown at t = 48.1 ms, likely corresponding to a less clustered or partially fragmented acetaminophen species formed within the more energetic corona. In Figure 4.9F, with both DART and corona active at a higher gas temperature, the tallest peak is shifted back to t = 49.5 ms with new spectral peak ratios showing enhanced signal for the higher mobility ions.

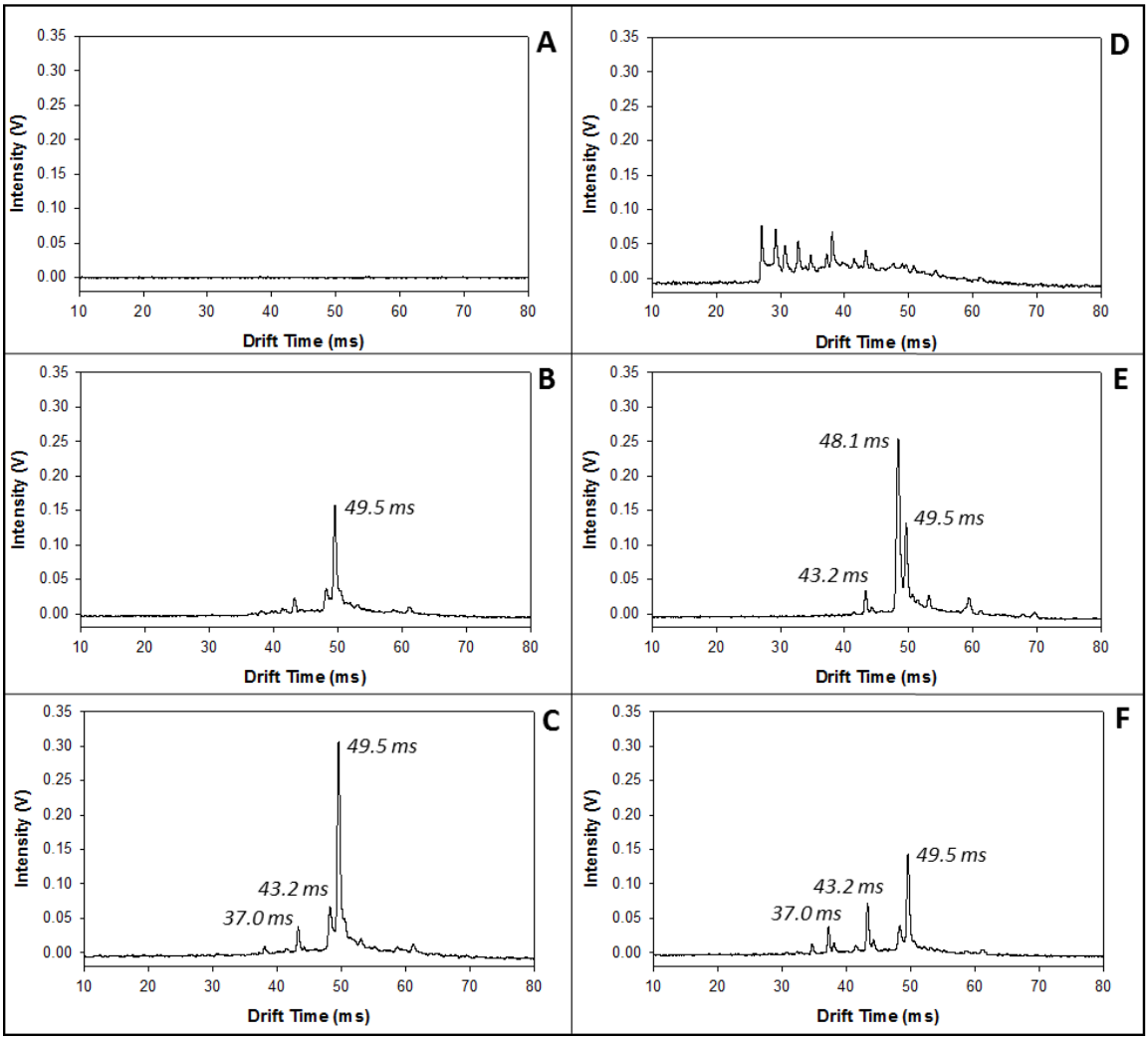

Figure 4.9: Signal observed for an acetaminophen tablet as a function of the repeller electrode potential at a fixed depth (*z*=7 mm). The repeller was centered coaxially with the spectrometer axis and normal to the IMS entrance plane, held at 12,000 V with a drift gas flow of N_2 at 1 L min^{-1}. The DART source was oriented orthogonal to the repeller and operated with a N_2 gas flow of 2 L min^{-1}. **A**) Repeller potential at 13,500 V with DART (300 °C) plasma off. **B**) Repeller potential at 13,500 V with DART (300 °C) plasma on. **C**) Repeller potential at 14,500 V with DART (300 °C) plasma on. **D**) Repeller potential at 14,500 V with DART (300 °C) plasma off. **E**) Repeller potential at 14,500 V with DART (450 °C) plasma off. **F**) Repeller potential at 14,500 V with DART (450 °C) plasma on.

MS data were collected for acetaminophen with the same DART parameters used in DTIMS experiments. With the mass spectrometer skimmer settings optimized to minimize in-source fragmentation, the spectrum showed a variety of acetaminophen ions

were formed, comprising not simply the protonated monomer and dimer, but also ammonium adducts (Figure 4.10A). The DART source reactant ion population observed under these conditions also corroborated the distribution of acetaminophen species detected (Figure 4.10B).

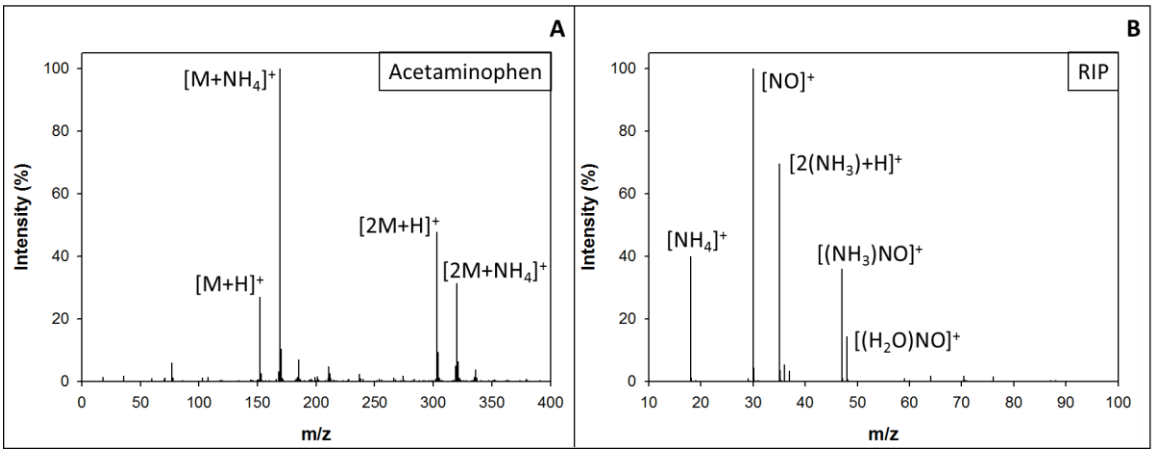

Figure 4.10: Mass spectra of acetaminophen (**A**) and reactant ion population (**B**) observed for N_2 DART collected on a JEOL AccuTOF mass spectrometer. The DART heater temperature was 350 °C and the grid voltage was 500 V. (AccuTOF settings: orifice 1, 10 V; orifice 2, 2 V; ring lens, 8 V; sweep voltage, 120-280 V; pusher bias, 29 V). To assist in species identification, single-point drift correction was performed using a 2,6-dtBP as a reference.

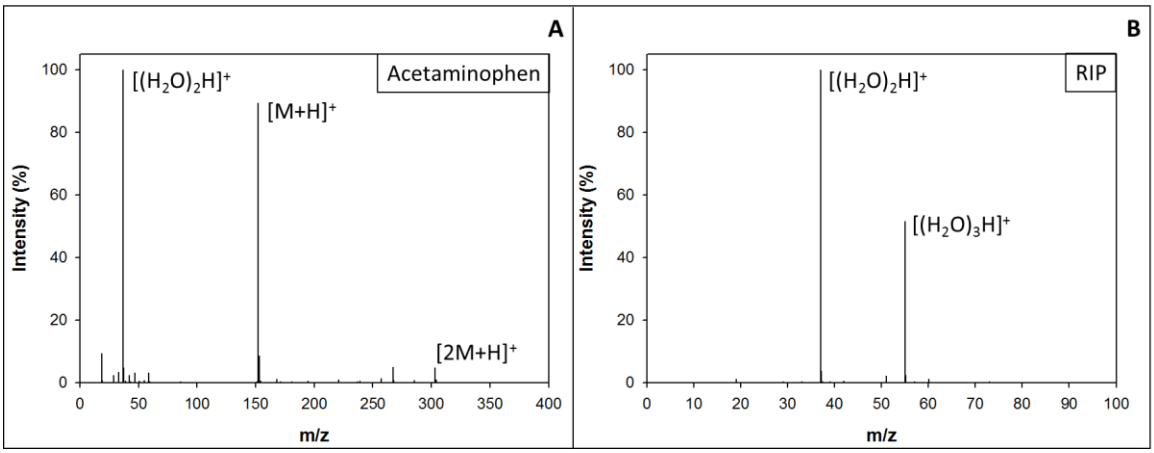

Figure 4.11: Mass spectra of acetaminophen (**A**) and reactant ion population (**B**) observed for a corona discharge (+3500 V) collected on a JEOL AccuTOF mass spectrometer. DART (plasma off) heater temperature was 350 °C. (AccuTOF settings: orifice 1, 10 V; orifice 2, 2 V; ring lens, 8 V; sweep voltage, 120-280 V; pusher bias, 29 V). To assist in species identification, single-point drift correction was performed using a 2,6-dtBP as a reference.

The peaks identified by MS may help explain the multiple ion mobility responses observed for acetaminophen under atmospheric pressure conditions. Moreover, the shift in mobility peaks around t = 49 ms when operating in corona discharge versus DART ionization regimes appeared to agree with the changes observed between mass spectra for either source, where the protonated adducts dominated with corona (Figure 4.11A-B) versus DART. Similar spectral shifts have also been reported for caffeine in mobility experiments where an ammonium dopant was used [139].

The reduced degree of clustering observed for the acetaminophen corona discharge mass spectrum is attributed to the effectively higher potential (+1 kV above mass spectrometer inlet) and lower DART gas temperature without the plasma active, resulting in less analyte material being desorbed before exposure to the corona tip adjacent to the MS skimmer. Infrared thermometry experiments showed that the DART source was only capable of heating a tablet surface up to 200 °C at maximum heater settings using nitrogen as the plasma working gas rather than helium. Excessive discharges and arcing at the DTIMS interface precluded the use of a higher thermal conductivity gas such as helium for DART. Depending on tablet packing density and tablet weight, these temperatures may not be adequate to desorb less volatile analytes, and facilitate declustering.

The abundance of NO^+ and NH_4^+ adducts in the heated DART reactant ion spectrum, and the fact that the highest reported excited state N_2* energy is relatively low (<11.6 eV for the second positive system and 6.2-9.8 eV for the longer-lived first positive system) compared to He* (19.8-20.6 eV)[140-144], suggest alternative ionization processes may be prevalent when operating DART with N_2 versus He. The abundance of NO^+ is consistent with observations in electron-rich He plasma afterglows with some degree of air mixing[145], pulsed discharges[146, 147], and ^{63}Ni β-emitters ion sources in N_2[148]. Induced secondary electron emission, and/or secondary ion formation at the metal repeller electrode surface[149], and/or field ionization of DART gas excited states in the

electrode point vicinity are other ionization mechanisms that could be occurring in this experiment, individually or concurrently. Preliminary evidence for a secondary ionization mechanism was suggested by observation of a small induced current on the repeller electrode (~0.3 μA) with the potential at 13,500 V and the DART plasma active. This current was slightly variable depending on electrode position, potential, and DART volumetric gas flow, but current levels up to 3.5 μA did not alter the signal intensity or spectral appearance and may therefore have merely been a symptom. In addition, a faint glow was only intermittently seen on the electrode surface under certain conditions. These phenomena are likely correlated with the hypothesized effect of the point electrode on DART DTIMS ionization/transmission and are the subjects of ongoing investigation.

4.5 Conclusion

The orthogonal DART DTIMS system described here is well-suited for analysis of volatiles and offers potential for compound identification based on thermal desorption profiles and peak pattern recognition. Based on our suite of characterization studies, we believe that when coupling the repeller-assisted orthogonal DART scheme with DTIMS, increased sensitivity is a consequence of the refined electric field profile governing ion transmission at the electrode-DTIMS interface. Evidenced by the subtle shifts in spectral peak distribution between DART and corona regimes during solid analysis, ions formed appear DART specific, with identities dependent on the composition of the DART plasma afterglow. The use of N_2 DART resulted in the generation and detection of more clustered mobility species than those typically observed for AP-DTIMS with other ion sources. In addition to a heated DTIMS buffer gas, the repeller motif might be coupled more effectively with laser ablation, photoionization, or a higher energy plasma to afford superior desorption, ionization and transmission efficiencies. The exact mechanisms involved in ion formation under these conditions continue to be the matter of active research.

CHAPTER 5: HIGH-RESOLUTION ATMOSPHERIC PRESSURE DRIFT TUBE ION MOBILITY SPECTROMETRY COUPLED WITH ULTRA-HIGH RESOLUTION ORBITRAP MASS SPECTROMETRY

5.1. Abstract

Ion mobility spectrometry has become increasingly associated with mass spectrometry, as these ion separation and mass-to-charge detection techniques are now routinely integrated for high-resolution multidimensional analysis. While spatially-dispersive and trap-based ion separation methods paired with MS are on the rise, the more heavily developed and applied iterations of ion mobility continue to be time-dispersive formats typified by drift tube and traveling wave ion mobility. Most multiplatform instruments employing these mobility techniques have been designed to maximize sensitivity at a cost to resolution. In an effort to circumvent the drawbacks related to modern IM-MS configurations, and increase separation power while maintaining sensitivity and improving mass accuracy, atmospheric pressure drift tube ion mobility spectrometry (AP-DTIMS) was coupled with Fourier transform (Orbitrap) mass spectrometry. The performance capabilities of this facile new arrangement were demonstrated for different DTIMS ion gating operations and the Orbitrap analyzer scan speed functions in regard to sensitivity and resolving power.

5.2. Introduction

In past decades, the separation method most commonly interfaced with ambient MS has been liquid chromatography (LC). This chemical partitioning of analytes between mobile and stationary phases according to hydrophilic/hydrophobic interactions offers good orthogonality to MS, thereby enhancing spectral coverage in two dimensions (elution time and *m/z*) and minimizing ion suppression. Similar to LC-MS, integrating

IMS with MS affords an extra analytical dimension for separation as well as the ability for ion selection/filtering based on size-to-charge, ultimately serving to increase instrument specificity, peak capacity, and dynamic range. Since size-to-charge is only pseudo-orthogonal to mass-to-charge, *K* has been found to vary in some cases almost co-linearly with *m/z*, meaning somewhat diminished gains in peak capacity for IMS relative to LC[79]. One remedy for this small deficiency has been augmentation of the mobility/mass multi-dimensional platform into time-nested LC-IM-MS or tiered IM-IM-MS systems[150] capable of providing greater information density all the while reducing spectral complexity without a cost to analysis time. Yet another strategy for improving peak capacity, pursued here, is to further increase resolving power in both the mobility and m/z dimensions.

Currently, the most successful commercial implementations of IMS paired with MS exist in systems featuring embedded mobility cells that are restricted to operation at reduced pressures by the vacuum constraints of the mass analyzer[83]. These configurations, often employing additional ion trapping and transfer stages, have been necessary to in order to alleviate the inherently low duty cycles (≤0.1%) of conventional pulsed time-dispersive mobility techniques that diminish throughput and compromise sensitivity. As all IMS separations rely on ion/gas interactions that scale with pressure, these arrangements inevitably limit the achievable mobility resolving power. Mostly small enhancements have been made in such systems by modifying gas polarizability[151] or applying additional electrodynamic RF field focusing[152] through use of custom components to reduce diffusional broadening. But a more desirable advancement involves IMS operation at higher, ideally atmospheric pressures, where for instance, the resolving power of classic drift tube ion mobility is comparable to and often surpasses LC separation efficiencies (R_p = 60-200).

More modern MS technologies have afforded large improvements in sensitivity owing to higher transmission efficiencies through the AP inlet and primary ion guiding

stages, in addition with faster detector scanning electronics for newer time-of-flight and FT-MS (Orbitrap) analyzers. In addition, spatial and temporal multiplexing approaches for DTIMS-MS continue to progress and have enabled significant increases in signal-to-noise ratio and sensitivity[47, 80]. Together these developments have enhanced MS compatibility with lower-throughput but higher resolving power AP-IMS systems. The next step forward, alternative to amplifying total IM-MS peak capacity through separation power in the mobility dimension, involves increasing resolution in the mass dimension. This can be readily accomplished by replacing traditional linear ion trap and time-of-flight (ToF) detectors with Fourier transform ion cyclotron resonance (FT-ICR), or as proposed here, new Orbitrap mass analyzers, since these instruments can offer R_p up to 140,000 and retain much of the same functionality of multistage ToF systems for MS^n analysis.

Presented in this work is the first combination of AP-DTIMS-MS, promising to restore separation power, improve mass accuracy and peak capacity, and maintain sensitivity. An EXCELLIMS MA3100 atmospheric pressure drift tube ion mobility spectrometer was coupled with a Thermo Q-Exactive Orbitrap mass spectrometer. The DTIMS module is designed with dual ion gates, which not only serve to define the boundaries of the drift region, but enable several different modes of mobility analysis for ion selection and filtering. General DTIMS performance was optimized for key mobility parameters, including drift tube temperature, drift gas flow rate, and the electric field strength in both positive and negative ion modes. The effect of DTIMS gate pulse width on IM-MS resolving power, together with the impact of fixed-gate versus scanned-gate acquisition modes on system sensitivity, was also explored. Primary consideration was given to understanding Orbitrap variables that determine maximum detector scan rate, injection times (IT) and automatic gain control settings (AGC), while investigating system limits of detection.

5.3. Experimental

5.3.1. Chemicals and Materials

Positive mode ion mobility calibration standards including 2,6-ditertbutyl pyridine (≥97%), nicotinamide (≥99.5%), trihexylamine (≥96%), and negative mode standard citric acid (≥99.5%) were purchased from Sigma Aldrich (St. Louis, MO). Positive mode standards were mixed in a 1:1:1 ratio in 50:50 methanol/water at 25 ppm w/v (*i.e.* 130 pmol/µL, 204 pmol/µL, and 93 pmol/µL of 2,6-ditertbutyl pyridine, nicotinamide, and trihexylamine, respectively). A concentration series of negative mode citric acid standard, ranging from 100 ppb to 100 ppm w/v (~0.52–520 pmol/µL), was prepared by serial dilution of a 1000 ppm w/v stock solution dissolved in 80:20 methanol/water. Solutions containing isomeric Gly-Asp-Gly-Arg-Ser and Ser-Arg-Gly-Asp-Gly peptide sequences were prepared in 50:50 acetonitrile/water with 0.1% formic acid to 1 mg/mL following the protocol provided with the Waters reverse peptide kit (P#700005089), obtained from Waters Corporation (Milford, MA), and then mixed and diluted to 100 ppm w/v (204 pmol/µL). Sugar analytes D-(+)-raffinose pentahydrate (≥98%), D-(+)-melezitose hydrate (≥99%), and D-(+)-melebiose (≥98%) were also procured from Sigma Aldrich, and dissolved in 80:20 methanol/water as a 100 ppm w/v mixture (~168 pmol/µL for D-(+)-raffinose and D-(+)-melezitose hydrates, and 292 pmol/µL for D-(+)-melebiose) with ≥10 molar excess of NaCl. HPLC grade methanol or acetonitrile organic solvents (Sigma Aldrich) and ultra-pure 18.2 MΩ cm deionized water (Barnstead Nanopure Diamond, Van Nuys, Ca) were used for all analyte solutions. High-purity nitrogen (99.998%) and ultra zero grade compressed air (99.998%) were acquired from Airgas Inc. (Atlanta, GA) and used as DTIMS buffer gases.

5.3.2. Instrumentation and System Parameters

The EXCELLIMS model MA3100 drift tube ion mobility spectrometer uses a traditional stacked-ring motif divided into desolvation and drift segments 6.25 cm and

10.55 cm long, respectively, all encased in a temperature-regulated (≤250 ℃) ceramic block. For reference, the electrodes consist of conductive bands (*width:* ~4.5 mm), all resistively-coupled to one another via printed circuit board connections, spaced apart (~1 mm) on a rectangular insulating ceramic support (50 cm x 25 cm). Potentials up to ±10,000 V can be applied to the desolvation cell inlet, resulting in a maximum linear electric field gradient of ~570 V/cm across the entire drift space. Attached in front of the desolvation chamber is a source enclosure housing an electrostatic capillary (50 µm *i.d.*) ion spray tip, without nebulizing gas assistance, with a maximum potential ±5000 V above the IMS inlet. The MA3100 features two Bradbury-Nielsen ion shutters, situated at the entrance and the exit of the drift cell. The first and second gates are floated at ~62.9% and ~7.7% of the operation potential, respectively. Gate #1 is pulsed with a symmetric potential of ±70 V during conventional drift mode operation. Positioned directly behind the second ion gate (or aperture grid) at the end of the drift region is a Faraday disk anode with ~1 cm diameter opening permitting partial ion transmission to the Orbitrap capillary inlet. Compressed air or nitrogen drift gas (≤3.0 L/min) is delivered through a heated input line at the drift cell terminus, passed as an symmetric sheath-flow across the anode, and diaphragmatically pumped (≤3.5 L/min) out through an exhaust port located at the front of the desolvation cell. Gas feed lines, high voltage electronics, and DAQ hardware are contained in the MA3100 peripheral controller box connected to the DTIMS and Orbitrap computer system. Controller box commands were issued using the EXCELLIMS VisIon software (version 1.2.0.31). Known drift tube dimensions and empirically-determined optimal settings for key mobility parameters in positive and negative ion mode are outlined in Table 5.1.

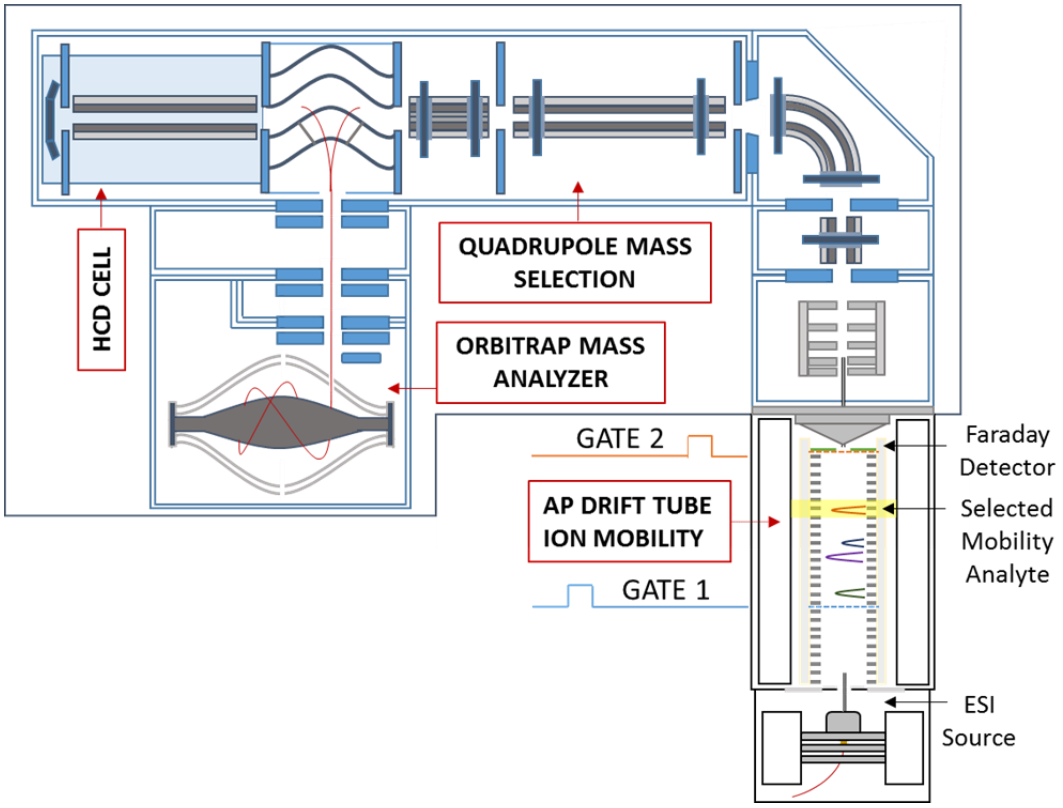

Figure 5.1: Schematic of the EXCELLIMS MA3100 atmospheric pressure drift tube ion mobility unit coupled with the Thermo Q Exactive Orbitrap mass spectrometer.

Table 5.1: Key AP-DTIMS and Orbitrap MS parameters

ESI Source		Q Exactive MS	
Electrospray Potential (kV) *above IMS inlet*	2000-3500 (-2200, +2600 std.)	Mass Range (Da)	50-500
Flow Rate (µL/min)	2-3	Resolution	17,500
MA3100 DTIMS		Scan Rate (Hz)	12
Drift Length (cm)	~10.5	Automatic Gain Control (AGC)	2E+04, 5E+06
Drift Tube/Gas Inlet Temperature (˚C)	60-240 (200 std.)	Microscans	1
Ambient Pressure (Torr)	730-750	Maximum Injection Time (ms)	100-2000 (1000 std.)
Air/N_2 Drift Gas Flow Rate (L/min)	1.0-3.5 (2.0 std.)	Inlet Capillary Temperature (˚C)	60-240 (200 std.)
Exhaust Pump Rate (L/min)	0.1-3.5 (0.5 std.)	S-Lens RF Level (V)	50
DTIMS Operation Potential (kV)	5000-10000 (-7000, +8500 std.)	HCD Normalized Collison Energy (V)	20-45
Ion Gate #1 Pulsing Potential (V)	±70	All Ion Fragmentation Range Center (m/z)	400

The EXCELLIMS MA3100 module was mounted to the atmospheric pressure interface of a Thermo Fisher Orbitrap Q-Exactive mass spectrometer. A schematic of the instrument configuration is depicted in Figure 5.1. Ion transport past the Faraday detector relied mainly on mechanical (vacuum) forces in the interstitial space preceding intake at the mass spectrometer inlet. The Q-Exactive transfer capillary temperature was set to match the drift tube temperature (60-240℃), Orbitrap MS Tune source voltages and sheath gas flows were assigned "0" values (switched off), and the S-Lens RF Level was held at 50 V. Parameter space experiments focused on the Orbitrap detector automatic gain control (AGC), injection time (IT), and resolution settings which influenced the effective detector scan speed. For the fastest possible scan speeds (~12 Hz), resolution was set at 17,500 unless otherwise specified. During IM-MS analysis, AGC was tuned to a minimum 2.0E+04 ion counts or maximum 5.0E+06 ion counts threshold, while IT was varied from 100-2000 ms. The number of microscans was left at 1, and the mass range was typically designated between 50-500 Da. For fragmentation studies with peptides using the high energy collision dissociation (HCD) cell, the normalized collision energy (NCE) was 20-45 V for an all ion fragmentation (AIF) range centered at m/z = 400 Da. Orbitrap analysis was conducted using Thermo Xcalibur 2.6 software. Most relevant MS settings are summarized in Table 5.1.

5.3.3. DTIMS Ion Gating Schemes

There are several analysis modes the MA3100 is equipped to perform based on programming of the dual ion gates. The DTIMS can be operated passively as an ion guide when floating both ion gates at the respective drift cell potentials ("open mode") or function as a conventional standalone IMS by pulsing only the first ion gate open/closed while floating the second gate and detecting ion current at the anode ("Faraday mode"). For increased functionality when coupled with a mass analyzer, the second ion gate may be utilized to select/filter target ions by either pulsing at fixed ion drift times ("gated

mode") or scanning the gate pulses in sequence bins across the entire drift period ("scan mode") in order to generate a full mobility spectrum. Adjustable gate pulse durations ranged from 30 μs to the full time period allowed per mobility acquisition (≤ 50 ms). Unless operating in open mode, the gate #1 pulse width in all our experiments was varied between 50-600 μs, precluding total loss of signal resolution with larger gate pulse widths. Using gated mode, ion gate #2 was typically pulsed open for 1-2 ms over the drift time region or mobility peak of interest. Scan mode function required definition of the drift zone or scan duration, gate #2 pulse width, and gate #2 scan step ratio. Unless otherwise specified, the scan time window was set within a boundary of 4-16 ms over the standard 20.3 ms acquisition period, following a short delay (≤1 ms) from the gate #1 trigger pulse. (The period was defined as an uneven value to reduce periodic anode noise.) Scan dwell time was set to 1015 ms, which equated to 50 spectral acquisitions per gate scan step for the set 20.3 ms scan period. Except during specific characterization experiments, gate #1 and gate #2 pulse widths were set equal to one another. The second gate was stepped at time intervals ½ to ¼ the gate pulse width over the defined scan window to effectively oversample using scan-step-to-pulse-width ratios of 2:1 or 4:1. VisIon Faraday spectra were generated from 20 s summations of conventional full-period scans, and mass spectra were produced from total scan time averages of the Orbitrap TIC spectra. DTIMS gate analysis modes are visualized in Scheme 5.1 and ion gate parameters are summarized in Table 5.2.

Scheme 5.1: Modes of Mobility Analysis

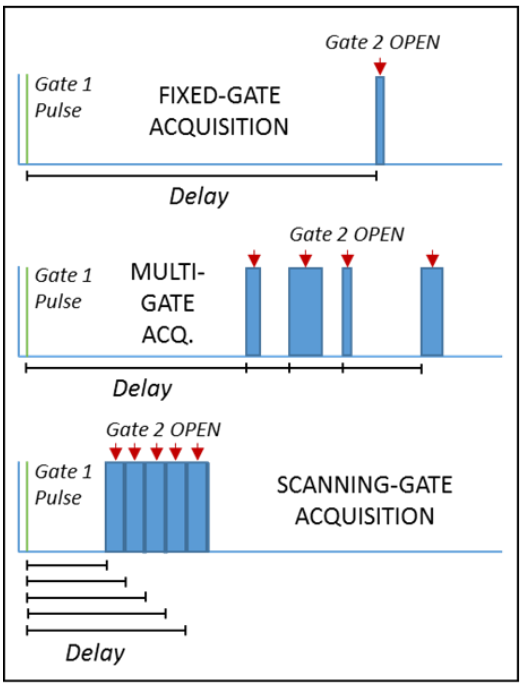

Table 5.2: DTIMS ion gate settings

Scan Period (ms)	20.3
Gate #1 Pulse Width (µs)	50-800 (100 std.)
Gate #2 Pulse Width (µs)	25-400 (100 std.)
Scan Step (µs)	25-250 (25 std.)
Dwell Time (ms)	1015 (or 50 scans)

5.4. Results and Discussion

5.4.1. DTIMS Characterization: General Physical Parameters

Before AP-DTIMS-Orbitrap MS performance could be evaluated effectively, it was necessary to gauge basic IMS functionality and optimize the physical parameters known to have the greatest impact on time-dispersive mobility resolution and sensitivity – drift gas temperature, drift potential/electric field strength, and drift gas flow rate. During this assessment, each parameter was systematically adjusted while the DTIMS was operated in single-gate acquisition or Faraday analysis mode using a gate pulse width of 100 µs. A 25 ppm w/v mixture of standard DTIMS calibration compounds comprising nicotinamide (K_0 = 1.85 cm^2 V^{-1} s^{-1}), 2,6-ditertbutyl pyridine (K_0 = 1.42 cm^2 V^{-1} s^{-1}), and trihexylamine (K_0 = 1.06 cm^2 V^{-1} s^{-1}), was used for analysis. The mobility values reported are from the literature[135], but experimental values were verified through a drift time calibration calculation [$K_{0\text{unknown}} = (t_{d\text{unkown}}/t_{d\text{standard}})*K_{0\text{standard}}$] to be within ±2%.

Drift Gas Flow Rate

Drift gas flow dynamics are the principal determinant affecting resolving power and sensitivity. The MA3100 AP-DTIMS module is partially enclosed with the ESI source equipped. At a standard drift gas temperature (180 ˚C) and operation voltage (nominal entrance electrode potential: +8500 V, effective drift potential: +5750 V), the drift gas flow rate was found to have the most immediate effect on signal appearance. On its own, the volume and rate of gas withdrawn by the spectrometer vacuum near the anode did not appear to significantly disrupt signal. Rather, it was obvious that drift gas uniformity was influenced not just by the drift gas flow rate, but the rate of gas evacuated by the anterior exhaust pump.

Figure 5.2A-C shows Faraday responses for drift air flow rates set between 1.0-3.0 L min^{-1} and different exhaust pumping rates (± ~1.0 L min^{-1} from the drift gas rate). For a low drift gas flow rate of 1.0 L min^{-1}, all analyte peaks remained clustered to some extent, as indicated by the broader shoulders detected following each peak. When selecting for these shoulders with the second DTIMS gate function, the protonated and/or adduct analyte ion masses associated with the adjacent peak drift times (or K_0) were not observed, only spectrum noise, suggesting these shoulders were solvent-based ions with low m/z falling below the targeted mass range. Declustering and peak shape improved with drift gas held at 2.0 L min^{-1}, where only a small shoulder remained for the first nicotinamide analyte peak. (This result may be explained by considering the superior volatility of the other 2,6-dtBP and trihexylamine analytes.) At 2.0 L min^{-1}, if the exhaust pump rate was set higher than the drift gas flow rate, signal was observed to decrease, particularly for the most volatile 2,6-dtBP species. With the drift gas at 3.0 L min^{-1}, solvent declustering was most effective and signal peaks were clearly resolved. Increasing the exhaust flow rate had an inconsistent outcome, again, almost singularly affecting signal for 2,6-dtBP. The Faraday response for the 2,6-dtBP analyte largely

disappeared with exhaust flow rates between 1-2 L min^{-1}, but was slowly recovered with increasing pump flow rates.

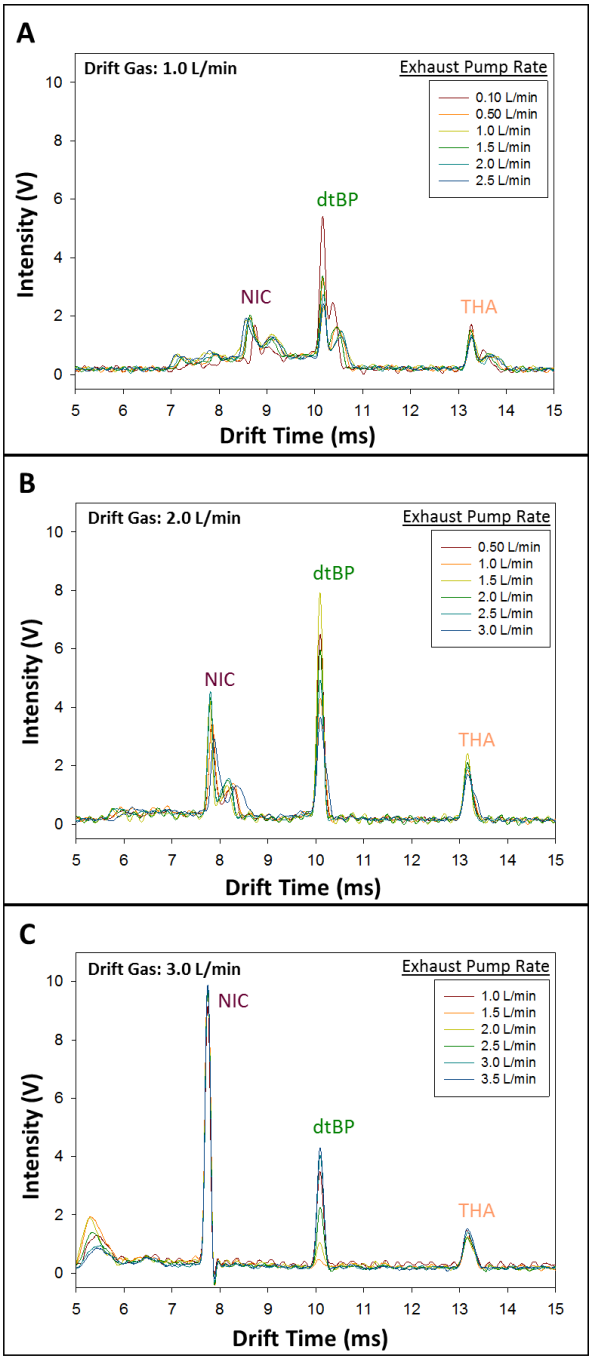

Figure 5.2: DTIMS Faraday responses for a standard solution of nicotinamide (NIC), 2,6-dtBP (dtBP), and trihexylamine (THA) 25 ppm w/v in 50:50 methanol/water as a function of drift gas (air) flow rate and exhaust pump rate. Drift gas flow rates were 1.0 L min^{-1} (**A**), 2.0 L min^{-1} (**B**), and 3.0 L min^{-1} (**C**). DTIMS operation potential was set to +8,500 V and drift gas temperature was held at 180 ℃.

The causes for this behavior can be rationalized based on a variety of factors, but mainly, it is suspected that the exhaust pump is either destabilizing the electrospray to circumstantially disfavor ionization of specific analytes, or perhaps more probable, it is assumed that rapidly volatilized analytes like 2,6-dtBP were influenced to diffuse along the periphery of the desolvation/drift region and were thus most negatively impacted by an imbalance between drift gas and exhaust pump flow rates aggravating the laminar flow profile. Comparatively, the steric bulk of trihexylamine's hydrocarbon chains correlate with a larger collisional cross-section and reduced accessibility for protonation, but also likely contributed drift properties affected by partial concentration/aggregation and confinement along the central drift axis that translated to the lowest analyte intensity measured on the hollow-core Faraday plate. Signal was arguably greatest for nicotinamide at higher drift gas flow rates; however, due to delayed ion volatilization and longer survivability of the analyte in spray droplets passing the initial turbulent flow region. Overall, the influence of drift gas flow rate on arrival time distribution was negligible, and once declustered, resolving power for each peak remained constant regardless of the drift gas flow rate.

Drift Gas Temperature

As with drift gas flow rate, the drift gas temperature is a critical parameter affecting the gas uniformity and ion-droplet solvation in the drift region which govern resolving power and sensitivity. The MA3100 drift and exhaust gas flow rates were set to intermediate values (2.0 L min^{-1} and 0.5 L min^{-1}, respectively) and the operation voltage was maintained (+8500 V). At temperatures below 100℃, Faraday signal was poor to nonexistent for all three analytes, which is likely the consequence of inadequate droplet desolvation and incomplete transmission for clustered ions in the drift region. Ramping drift tube temperatures from 100 °C to 240 °C, clear signal trends included an increase in

all three analyte responses and a concerted peak shift of ~3 ms to earlier arrival times, as seen in Figure 5.3.

Additionally, the nicotinamide clustered solvent-shoulder peak was seen to subside as temperature was raised. These findings are congruent with the arguments made for the analytes concerning drift gas flow rate, where 2,6-dtBP was the most volatile and persistent signal even at lower drift gas temperatures, and the nicotinamide peak grew to dominate the spectrum with increasing temperature. It is important to note that above ~200 °C, the spectrum baseline was elevated up to ~2 V due to an artificial current induced on the warmed Faraday plate. Interestingly, resolving power (2,6-dtBP, R_p~70) did not vary appreciably across the temperature range due to increased band broadening with higher temperatures, although a favorable declustering of nicotinamide above 180 °C was observed. Also, peak-to-peak separation for 2,6-dtBP and trihexylamine showed only a minor decrease between 100-240 °C, with peak spacing reduced by ~0.6 ms. Estimating for a Gaussian distribution, the FWHM resolution at 240 ˚C was $R_{p\text{-}p}$~10.1 and the separation factor (α ~1.29-1.31) was not seen to vary significantly across temperatures.

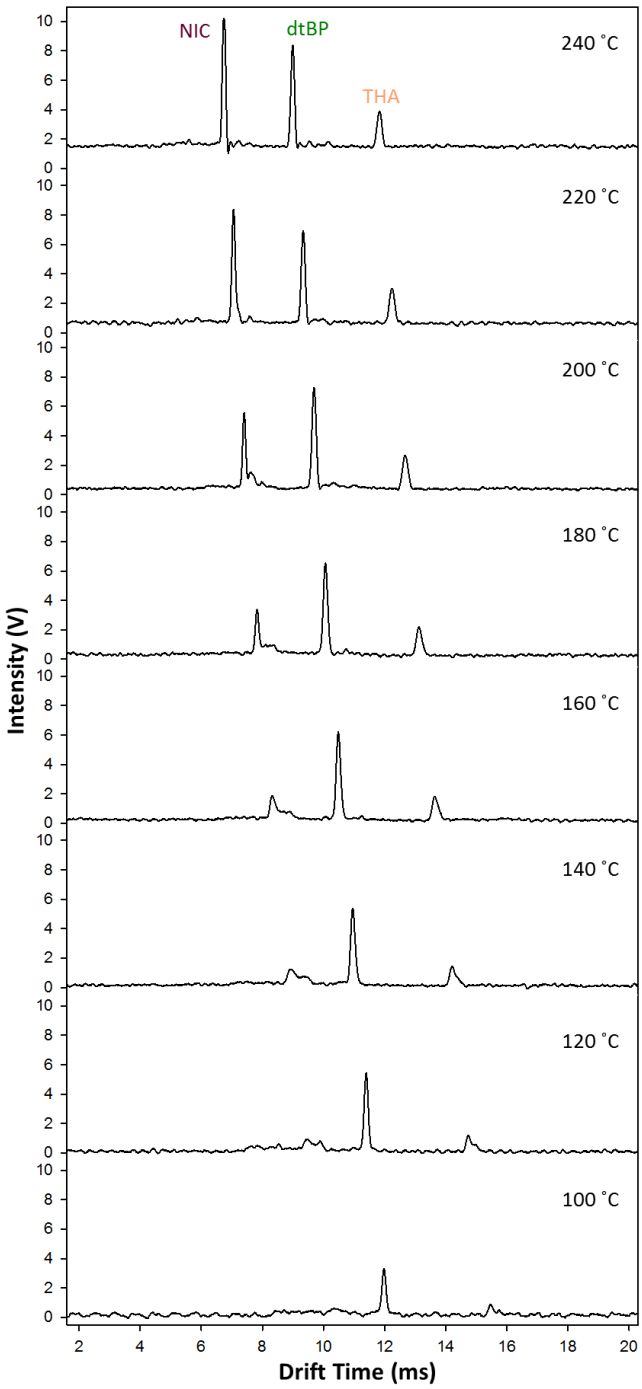

Figure 5.3: DTIMS Faraday responses for a standard solution of nicotinamide (NIC), 2,6-dtBP (dtBP), and trihexylamine (THA) 25 ppm w/v in 50:50 methanol/water as a function of drift gas temperature. DTIMS operation potential was set to +8,500 V, and drift gas flow rate and exhaust pump rate were 2.0 L min^{-1} and 0.5 L min^{-1}, respectively.

Drift Tube Potential

The IMS electric field strength defined by the applied drift tube potential was the last parameter examined having a significant impact on signal intensity and resolution. The DTIMS temperature was fixed (180 °C) and the drift/exhaust gas flow rates were set again to a convenient optimum (2.0 L min-1 and 0.5 L min-1, respectively). In positive mode, Faraday signal was essentially absent for analytes below an operation potential of +6000 V (approximate drift potential: +3775 V). Shown in Figure 5.4, as the operation potential was raised from +6500 V to a maximum of +10,000 V (max effective drift potential: +6300 V), signal for all three analytes was seen to increase owing to sufficient electric field strength (max: ~600 V cm^{-1}) improving transmission. Concomitant with the signal increase for all analytes was an expected shift to lower drift times for the +4000 V potential escalation, totaling ~3.5 ms. Unlike what was seen for drift gas flow rate and gas temperature, the degree of solvent clustering did not appear much affected by increasing drift potentials, as evidenced by the remaining solvent shoulder on the nicotinamide peak. Resolving power improvement was minimal, only rising from R_p~61 to R_p~66 for 2,6-dtBP across the potential range shown, but the change in peak-to-peak separation was greater. Drift time spacing was decreased by 1.1-1.3 ms between adjacent peaks, while the α term again remained constant at ~1.3, translating to FWHM $R_{p\text{-}p}$~9.4 at 10 kV.

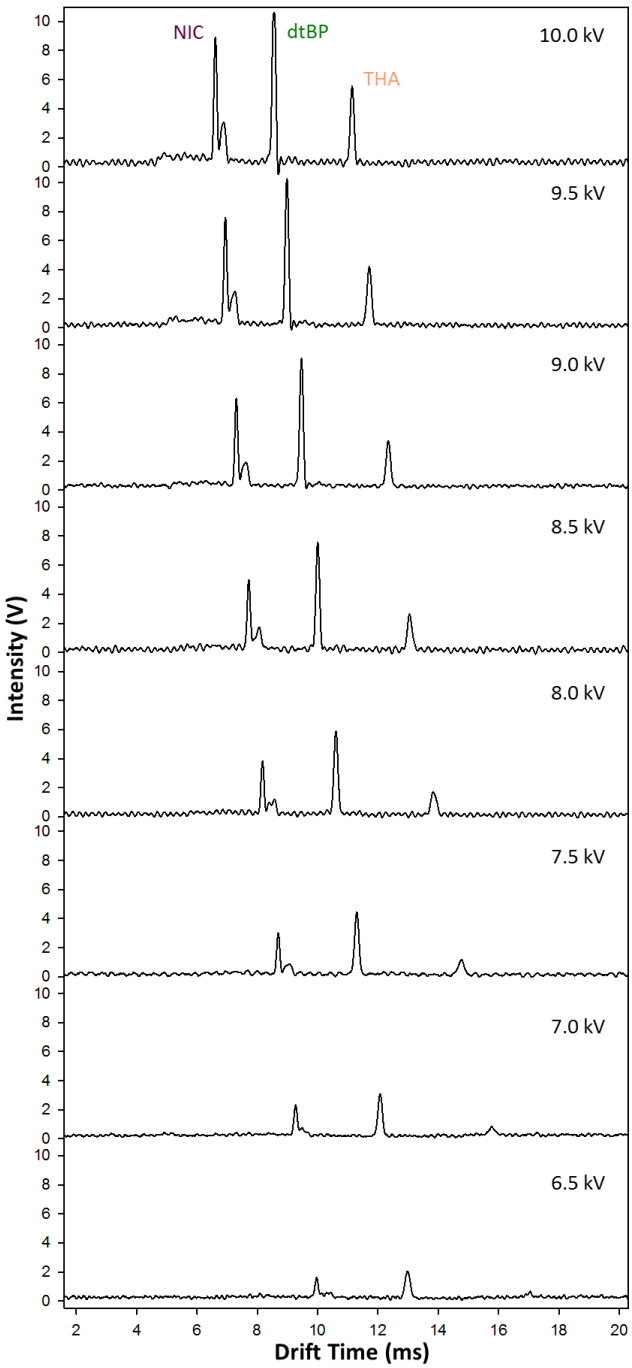

Figure 5.4: DTIMS Faraday responses for a standard solution of nicotinamide (NIC), 2,6-dtBP (dtBP), and trihexylamine (THA) 25 ppm w/v in 50:50 methanol/water as a function of DTIMS operation potential. Drift gas temperature was set to 180 ˚C, and drift gas flow rate and exhaust pump rate were 2.0 L min^{-1} and 0.5 L min^{-1}, respectively.

5.4.2. DTIMS-Orbitrap MS Characterization: Sensitivity and Resolving Power

DTIMS Ion Gate Operations and Orbitrap Detector Function

General observations pertaining to the Orbitrap scan behavior were made during DTIMS characterization of the positive mode standards. Figure 5.5A-B depicts mass spectra recorded for the analytes in "open mode," with continuous ion passage through the DTIMS, and in "gated mode," where the ions were pulsed conventionally using the first ion gate (pulse width: 100 us) and selected for in a wide window using the second ion gate (pulse width: 12 ms). Immediately noticeable is the different distribution of intensities for the analytes between these analysis modes, which are also distinct from the distribution observed in the Faraday mode response. When compared with the Faraday arrival time trace, the relative peak intensity profiles observed in the open mode mass spectrum (Figure 5.5A) are attributed to a combination of weighted influences, including the radial dispersion of analyte ions in the drift cell and their relative proton affinities. It is possible the mass analyzer favored the tertiary amine being confined along the drift central axis in line with the spectrometer capillary inlet, or it is feasible the Orbitrap detector automatically prioritized gain for the lowest intensity species. Radial ion density measurements correcting for anode area are needed to verify this rationale. The biasing nature of the Orbitrap gain parameter, set here to the lowest value of 2.0E+04 counts, became more transparent for a DTIMS fixed-gate acquisition (Figure 5.5B) versus a continuous ion flux, where the peak distribution shifted to the inverse intensity profile seen in open mode. It is speculated that the Orbitrap was preferentially gaining for the first mobility peak eluted to the analyzer, in this instance, nicotinamide. Upon nearing the nominal gain value, the intensities for the lower mobility analytes 2,6-dtBP and trihexylamine became slightly suppressed.

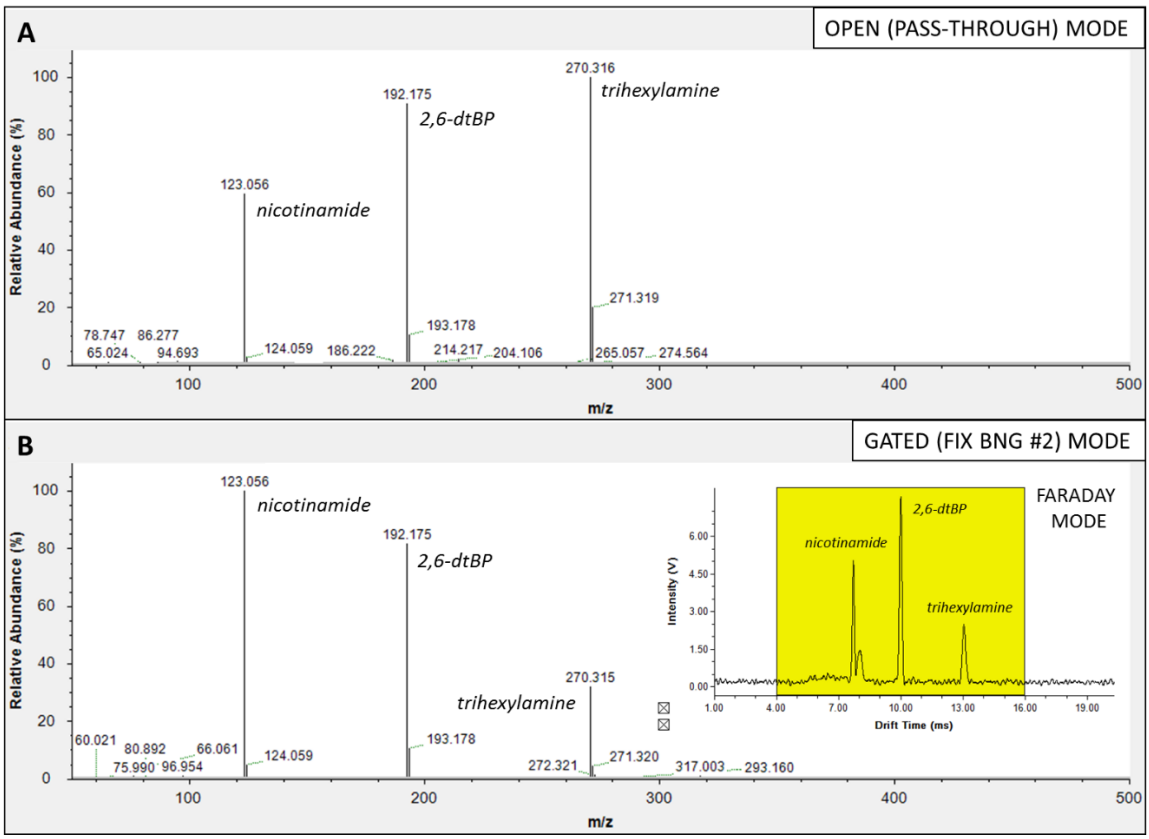

Figure 5.5: Comparison of the peak intensity distribution in mass spectra acquired for a 25 ppm w/v solution of mobility standards setting both DTIMS gates open (**A**) or fixing BNG #2 open for 12 ms (**B**). The inset in (**B**) shows the Faraday image for the gated-mode acquisition.

This trend was not observed to be skewed the same way when conducting DTIMS scanned-gate acquisitions, where the second BNG was pulsed open over fractions of each peak in sequentially processing bins of time. Data shown in Figure 5.6A-C were obtained scanning BNG #2 over a 12 ms window of the IMS drift period, where the Faraday response, MS TIC, and MS spectrum all exhibit the same peak profiles. The nicotinamide signal was approaching anode saturation, while the diminished intensity of the 2,6-dtBP and trihexylamine signals in the MS spectra relative to the Faraday image may again be a symptom of the uneven radial ion distribution. A higher drift tube temperature (≥200 ℃) and operation potential (+9000 V) were used in this analysis, perhaps better facilitating analyte desolvation and lateral (over axial) diffusion.

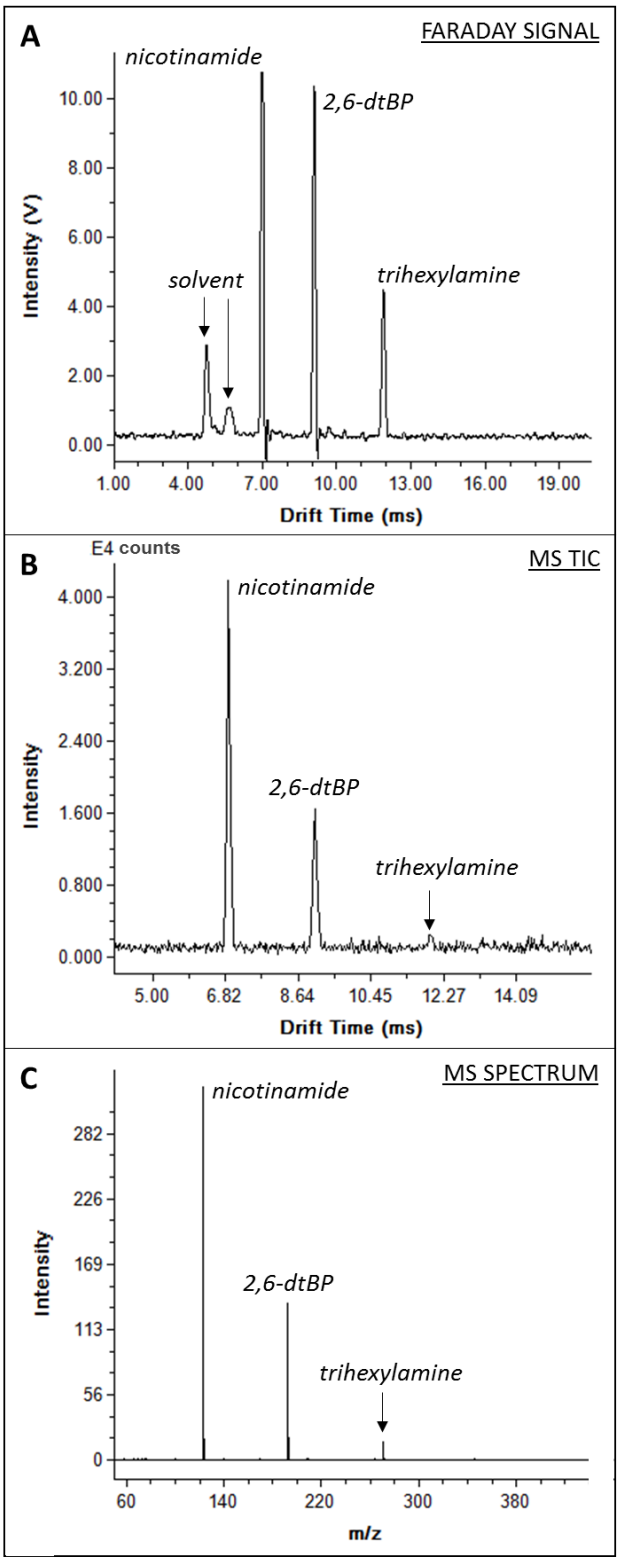

Figure 5.6: Faraday response (**A**), "scan mode" MS TIC (**B**), and total mass spectrum (**C**) acquired for a 25 ppm w/v solution of mobility standards scanning BNG #2 between 4-16 ms in the drift window using a 100 µs gate pulse width and a 25 µs scan step.

DTIMS Gate Pulse Width and Scan Step Functions

The contribution of gate pulse width on DTIMS-Orbitrap MS sensitivity and resolving power was gauged to better understand the effect of scanning gate operations on MS signal fidelity. In negative mode, analysis of a citric acid standard was performed using different BNG #1 and #2 pulse width ratios, and different scan step increments to control over- or under-sampling. Firstly, Figure 5.7 shows the Faraday responses for 4 ppm w/v (~21 pmol/µL) citric acid with gradually increasing gate #1 pulse widths.

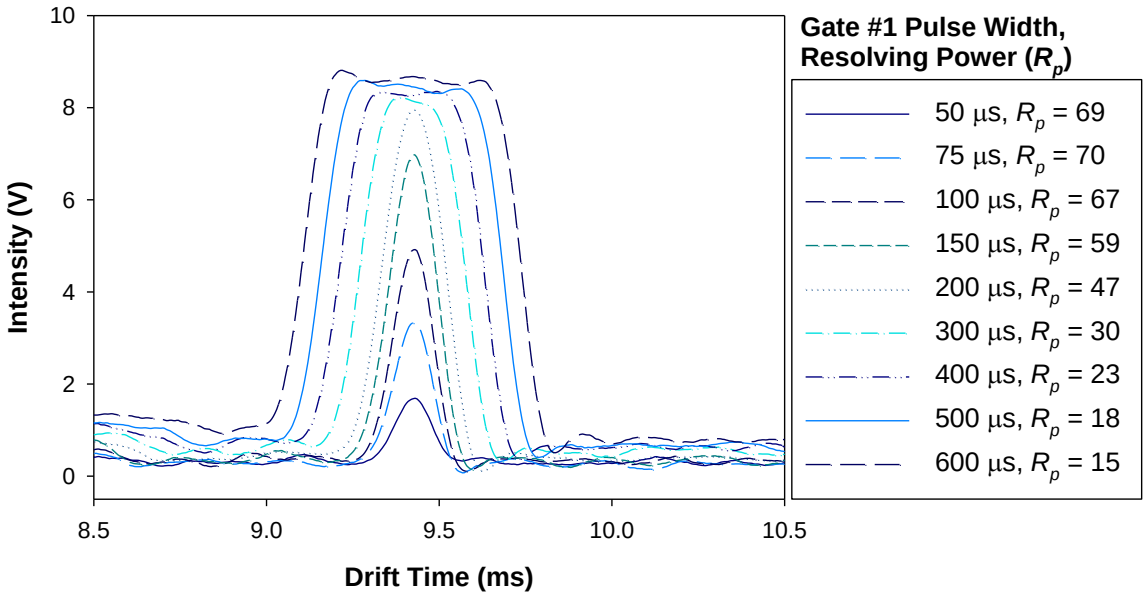

Figure 5.7: Faraday signal response for 4 ppm w/v citric acid in 80:20 methanol/water using increasing DTIMS BNG #1 pulse widths. DTIMS operation potential was -7000 V, drift gas temperature was 200 ˚C, and drift gas flow rate and exhaust pump rate were 2.0 L min^{-1} and 0.5 L min^{-1}, respectively.

The Gaussian peaks showed increasing intensities with near linearity until a pulse width of approximately 300 µs. Beyond this value the Faraday signal remained below saturation, but the peaks plateaued and broadened, further diminishing mobility resolving power. This effect was a consequence of longer gate pulse widths collecting ions over a greater span of time, but for a stable ion density regulated by the ESI source ion current and analyte concentration. In practice, increasing the gate #1 pulse width also extends the

drift time by a commensurate amount on the falling edge of the widening peak, so conventionally, the peaks in Figure 5.7 were aligned to a centroid by subtracting ½ pulse width from the drift time. For Faraday mode, gate #1 pulse widths of 75-150 µs were determined to provide the best balance between sensitivity and resolving power.

The signal effect of gate #2 pulse operations relative to gate #1 were evaluated in scan mode. Orbitrap parameters, elaborated on in the next section, were set (resolution: 17,500 [12 Hz], AGC: 5.0E+06, IT: 1000 ms) to preclude signal artifacts from erratic detector cycle times. Gate #1 pulse width was set to 100 µs, while gate #2 pulse widths were varied from 25-400 µs over a drift time scan window of 2.5 ms centered on the citric acid Faraday response. Figure 5.8 shows the same trend seen with Faraday mode depicted for Orbitrap total ion chronograms. For the shortest gate #2 pulse width (25 µs), no signal was detected since the programmed pulse width was below the rated cut-off of the ion shutter.

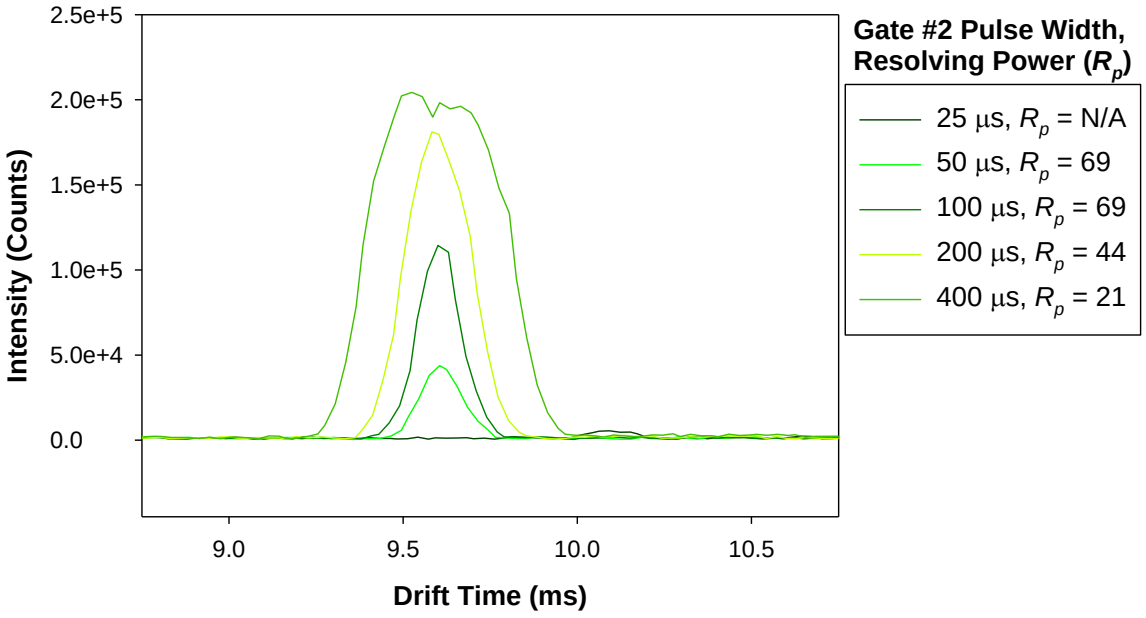

Figure 5.8: MS TIC signal for 10 ppm w/v citric acid in 80:20 methanol/water using increasing DTIMS BNG #2 pulse widths over a 2.5 ms scan window. The BNG #1 pulse width was 100 µs and the scan step was 25 µs. DTIMS operation potential was -7000 V, drift gas temperature was 200 ˚C, and drift gas flow rate and exhaust pump rate were 2.0 L min^{-1} and 0.5 L min^{-1}, respectively.

Peak area was observed to increase as resolution decreased, and for a given gate pulse width, resolving power did not appear worse than the Faraday response (BNG #1 and #2 at 100 µs: R_p ~60-70). For alignment, the citric acid signal peaks were corrected for gate pulse width by subtracting ½ of the first BNG pulse width and adding ½ of the second BNG pulse width. Improved timing correction for instances where the pulse width of gate #2 was larger than gate #1 required addition of an extra adjustment factor equal to $(1/16)t_{gate\#2}$, which is thought to be related with the scan step. Not obvious due to realignment, peak broadening in the MS TIC occurred opposite to Faraday mode, with signals extending on the rising peak edge to earlier drift times as gate #2 pulse width increased. Consistent with expectation, shorter gate #2 pulse widths relative to gate #1 resulted in lower intensity TIC signals due to gate shutter "clipping" of complete ion mobility packets, with modest or no improvement to resolving power. Interestingly for gate #2 pulse widths exceeding the initial gate #1 pulse duration, rather than level off the TIC signal continued to increase despite a finite ion density defined by the first gating event. Importantly, this behavior is attributed again to the designated scan step value (25 µs). The ratio of the scan step to BNG #1 pulse width (100 µs) was 4:1 during these measurements, which translated to wider gate #2 bin widths effectively acquiring multiple slices of the entire target mobility region leading to augmented signal intensity.

The impact of the scan step function on signal was investigated independently, setting gate #1 and gate #2 pulse widths equal (100 µs). Gate scan steps were varied from 12.5 µs up to 200 µs for an IMS dwell time of 1015 ms, equating to 50 spectral acquisitions per scan step over the 20.3 ms drift period. Orbitrap parameters were fixed as before (resolution: 17,500 [12 Hz], AGC: 5.0E+06, IT: 1000 ms). Figure 5.9 shows the citric acid MS TIC signal using these scan steps, which correspond to oversampled ratios of 8:1 (12.5 µs), 4:1 (25 µs), and 2:1 (50 µs); a matched sampling ratio of 1:1 (100 µs); and an undersampled ratio of 1:2.5 (250 µs). There was minor drift time variance across peak apexes for different scan steps, which may be correlated with minute fluctuations in

measured ion intensity over the different mobility time bins or the number of sample points acquired per peak. Obviously, undersampling resulted in a more dramatic loss of resolution. Oversampling with the scan step function was critical to refine peak shape for cleaner peak profiles using larger gate bin widths (>100 µs), as fewer points were acquired across mobility peaks with an average resolution of ~0.5-1 ms. Although not shown, scaling the gate pulse widths and scan step within an proportionately sized drift window is also an important consideration, as larger gate bin widths together with larger scan steps (*e.g.* BNG #1 & #2: 400 µs, scan step: 200 µs) resulted in data loss from incomplete or clipped signal peak edges in a narrow ~2 ms scan window.

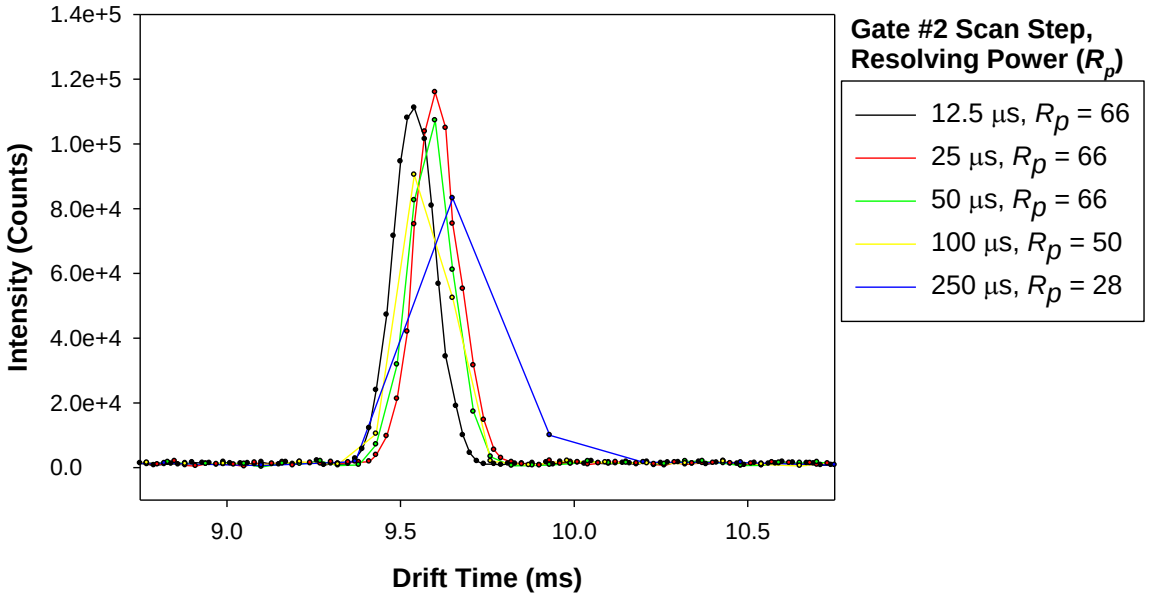

Figure 5.9: MS TIC signal for 10 ppm w/v citric acid in 80:20 methanol/water using increasing DTIMS BNG #2 scan step ratios over a 2.5 ms scan window. BNG #1 and #2 pulse widths were set equal at 100 µs. DTIMS operation potential was -7000 V, drift gas temperature was 200 ˚C, and drift gas flow rate and exhaust pump rate were 2.0 L min^{-1} and 0.5 L min^{-1}, respectively. The number of data points per peak are plotted with each curve trace.

Orbitrap Automatic Gain Control and Injection Time

Apart from DTIMS gate pulsing operations affecting throughput, the Orbitrap detector scan functions were the other principal determinants of performance, as they had

a potentially substantial influence on system sensitivity, resolution and the analytical cycle time. Thermo Xcalibur software provided limited tune capabilities for the key parameters effecting detector scan rate, including analyzer resolution, injection time, and automatic gain control. These variables were inspected in depth while assessing limits of detection using the DTIMS in both fixed-gate and scan mode acquisitions. The lowest available analyzer resolution (17,500) was chosen for all characterization experiments in order to permit the fastest allowable trap scan rate (~12 Hz) for the selected mass range (m/z = 50-500). The automatic gain control, which defined the threshold for the target ion flux, was set initially to the highest available value (5.0E+06 counts) in order to stabilize the injection time. The maximum injection time, or the nominal duration of ion accumulation and the rate-limiting cycle step governing sensitivity, was adjusted between 100-2000 ms, which were fairly forgiving values for the lower analyte concentrations anticipated based on DTIMS transmission.

Conducting a fixed-gate acquisition (BNG #1 pulse width: 100 µs, BNG #2 pulse width: 2.5 ms), Figure 5.10 shows a calibration curve for a citric acid concentration series as a function of injection time. Interestingly, no observable trend was forecast based on the injection time, as the average signal intensities for a given concentration and variable injection times remained clustered (RSD ~3.6% excluding 100 ppb). Based on the linear dynamic range of the curve (0.1-10 ppm citric acid), the limit of detection for these settings was estimated to be approximately ~800 ppb w/v (~4 pmol/µL). Fixing the injection time (IT: 1000 ms), the same trend in the concentration curve was observed for a scan mode acquisition (BNG #1 & #2 pulse widths: 100 µs, scan step: 25 µs), but overall intensities were lower by 2-3 orders of magnitude. The loss in sensitivity for a scanning acquisition is expected, as the mass analyzer measures smaller time bin divisions for a single mobility peak. The limit of detection in scan mode was on par with the previous figure, but slightly lower at ~600 ppb w/v (~3 pmol/µL), justified by the narrower degrees of variance in smaller sample time bins.

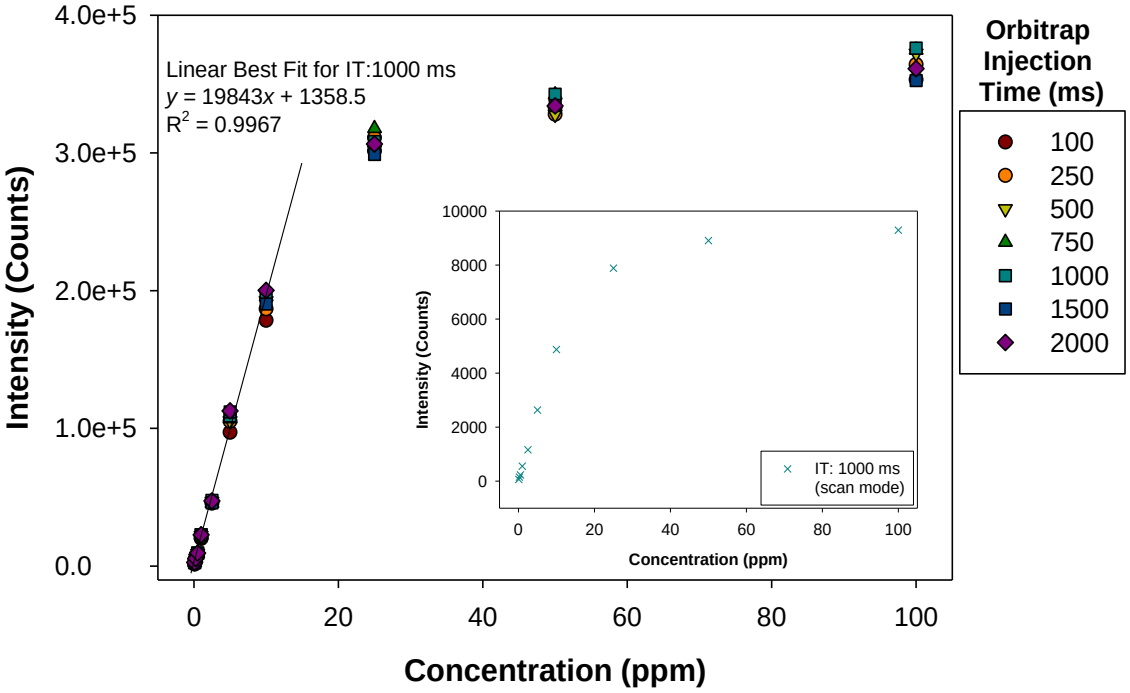

Figure 5.10: Citric acid concentration curve for dual-gate AP-DTIMS-Orbitrap MS as a function of Orbitrap maximum injection time (IT). DTIMS BNG #1 pulse width was set to 100 µs and BNG #2 was fixed open from 8.5-11 ms (2.5 ms window). MS automatic gain control was held at 5.0E+06. Each point is the average of over ~110 Orbitrap acquisition scans. A trend-line is drawn for the linear dynamic range (0.1-10 ppm). The inset shows a similar curve trend for a scanned-gate acquisition over the 2.5 ms window (BNG #1 and #2: 100 µs, scan step: 25 µs).

The AGC function became relevant at higher sample concentrations when selecting the appropriate injection times. Figure 5.11 shows overlaid MS TIC spectra for a scan mode acquisition of 25 ppm w/v citric acid using low (2.0E+04) and high (5.0E+06) AGC values. Using the high AGC setting, an injection time of 1000 ms was fixed, as the total measured intensity always remained below the target ion count threshold for the given analyte concentration. However, the low gain ion count threshold was achieved much faster, resulting in injection time fluctuations from the maximum IT of 1000 ms down to several hundred milliseconds. These injection time variations corresponded to an increase in the number of detector scan cycles and acquisition events

with a measured analyte intensity. It is significant to note that the EXCELLIMS VisIon software generated the MS spectrum by averaging over the entire scan acquisition window (*e.g.* 2.5 ms), where the signal peak was absent a percentage of the time leaving only baseline. Consequently, the *reported* ion intensity was ultimately lower for the higher gain acquisition, containing fewer signal data, despite identical peak areas.

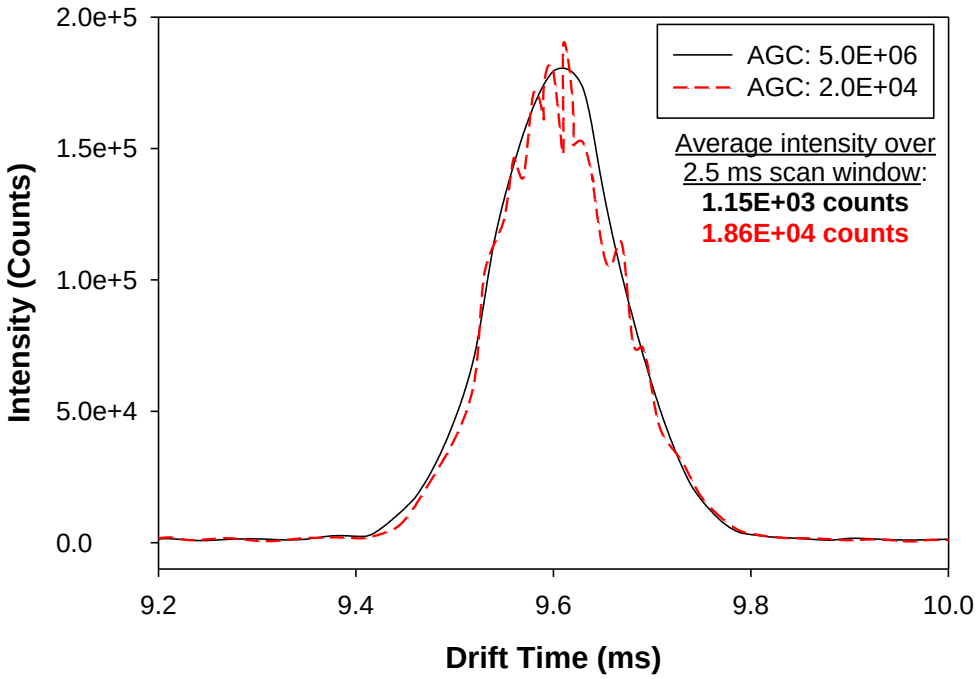

Figure 5.11: Scan mode analysis signal for 25 ppm w/v citric acid using high AGC (5.0E+06) and low AGC (2.0E+04) and a maximum injection time set to 1000 ms. (BNG #1 & #2: 100 µs, scan step: 25 µs).

5.4.3. DTIMS-Orbitrap MS: Benchmark Applications

With a firmer understanding of the dual-gate AP-DTIMS performance capabilities coupled to Orbitrap MS, benchmark sample sets were analyzed to showcase system qualifications in routine applications involving isomer separation and identification. Figure 5.12A shows the Faraday response and associated mass spectrum for a 100 ppm w/v mixture of two reverse peptide sequences (Ser-Asp-Gly-Arg-Gly and Gly-Arg-Gly-Asp-Ser) collected using optimized mobility parameters with a fixed-gate acquisition (8-

10 ms BNG #2 pulse width). Three essential peaks were present in the Faraday image, representing the singly charged peptide monomers (m/z = 491.221) co-eluted at t_d = 12.25 ms and the doubly protonated monomers (m/z = 246.114, m+1/z = 246.616) of GRGDS and SDGRG at t_d = 7.12 ms and 7.45 ms, respectively.

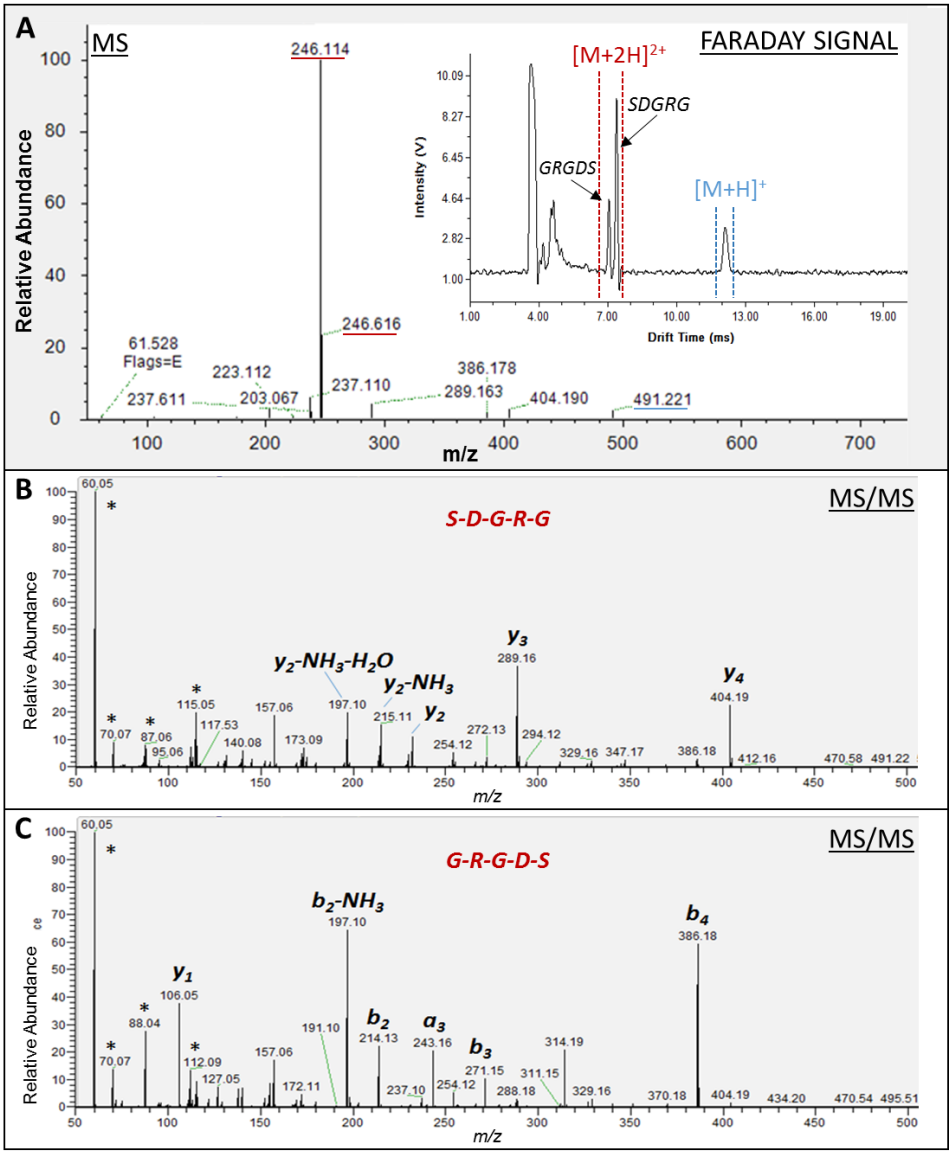

Figure 5.12: Mass spectrum and Faraday response (*inset*) for 100 ppm w/v of mixture of [Ser-Asp-Gly-Arg-Gly] and [Gly-Arg-Gly-Asp-Ser] peptide isomers in 50:50 acetonitrile/water with 0.1% formic acid (**A**). All ion fragmentation HCD using a normalized collision energy of 20 V of the independent peptide isomers separated by ion mobility (**B** and **C**). (DTIMS operation potential: 10,000 V, drift gas temperature: 220 ˚C, drift gas flow rate: 3.0 L min^{-1}, exhaust pump rate: 1.5 L min^{-1}). Asterisks (*) denote identified sidechain fragments of serine, aspartic acid, and arginine.

The $[M+2H]^{2+}$ species, having reported collision cross-section areas of Ω = 222.7 $Å^2$ and Ω = 211.7 $Å^2$[153], were clearly resolved to baseline by AP-DTIMS (R_p~72) with roughly double the resolving power possible for these ions using TWIMS (R_p>36). Isomer identities were verified by drift time measurements for single-component peptide standards, and were further confirmed by high energy collision dissociation (HCD) MS/MS analysis of the isolated isomer peaks separated by ion mobility. Figure 5.12B-C show the characteristic HCD MS/MS spectra for the peptide sequences with unique fragment assignments determined for each isomer using open-source ProteinProspector software version 5.17.1 (University of California, San Francisco, USA).

In addition to the reverse peptide sequences, a simple carbohydrate mixture of sugar isomers and structural homologues were analyzed. Analyte solutions were concentrated at 100 ppm w/v with a 2.5x excess of NaCl salt to facilitate positive mode ionization via sodium adduct formation. Figure 5.13A-D depicts a VisIon data quadrant for Faraday and MS spectra obtained using DTIMS scan mode over a 4 ms scan acquisition window. The 200 µs gate pulse widths used resulted in a small reduction in R_p to benefit sensitivity, and also a large Faraday solvent signal. Within the drift time zone of 9-13 ms, four distinct peaks can still be observed. In order of elution, the carbohydrate peaks are correlated with $[M+Na]^+$ for the disaccharide D-(+)-melebiose (m/z = 365.105) at t_d = 9.94 ms, and trisaccharide isomers D-(+)-melebiose (m/z = 527.158) and D-(+)-raffinose (m/z = 527.158) a t_d = 11.70 ms and t_d = 12.19 ms, respectively. The peak order is consistent with mobility distribution reports from the literature, and was verified again by analyzing single-component solutions of the standards. The one peak not assigned to a sugar at t_d = 10.70 ms is a suspected contaminant tentatively identified as the sodiated adduct of decamethylcyclopentasiloxane (m/z = 393.082), a common ESI background ion, presumed to exhibit enhanced ionization here owing to ready accommodation of Na^+ in the compound's ring-cavity. Again, the Faraday and MS TIC peak profiles echo one another, and corroborate the MS spectrum intensity for isobaric sugars. The plot of m/z as

a function of drift time conveys an additional visual analysis element, portraying the nested IM-MS distribution and precursor trend-lines. The ellipses drawn on the plot demark peaks for the carbohydrates and contaminant ion, while filtering any other background signal overlapping in the same mass/mobility region. This data show the power of AP-DTIMS-Orbitrap MS for discriminating even lower intensity analytes from potentially convoluted chemical systems.

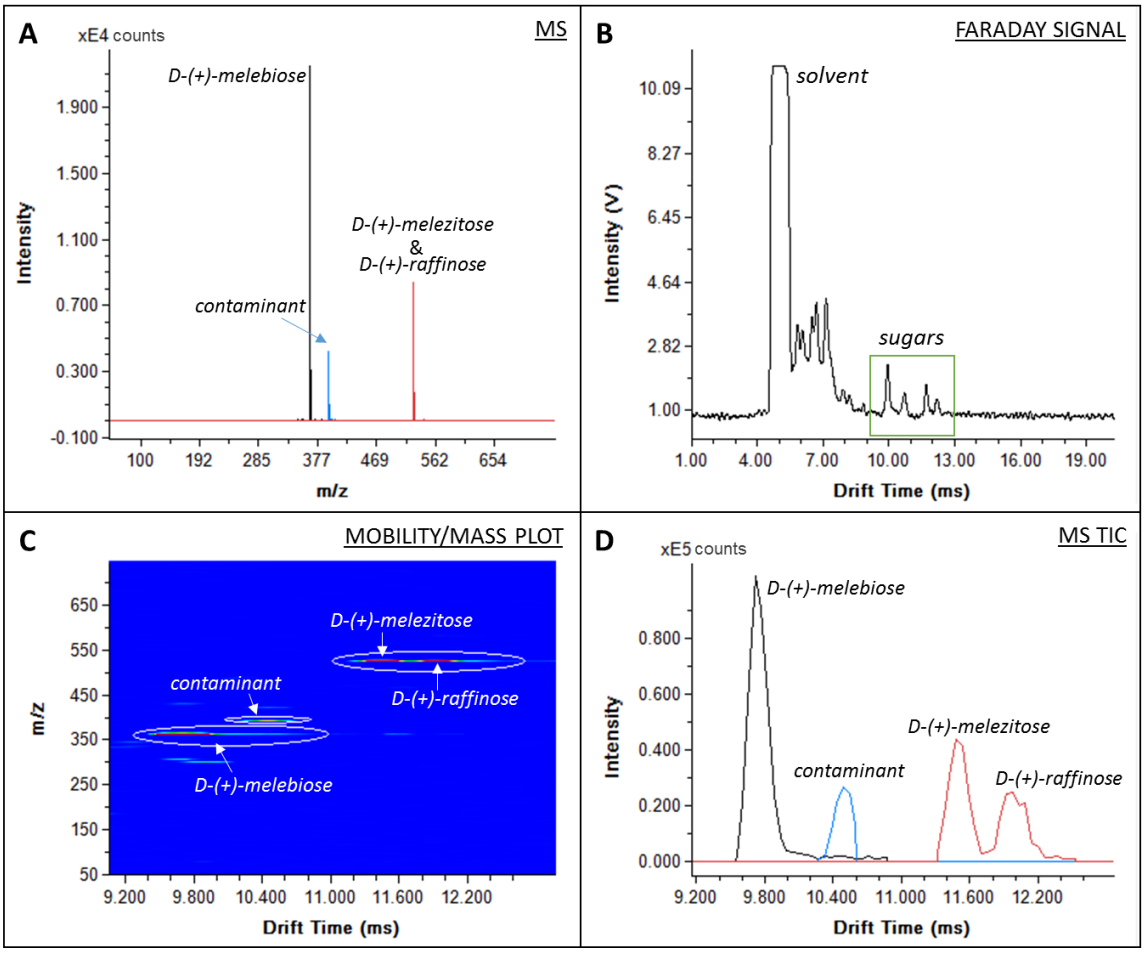

Figure 5.13: AP-DTIMS-Orbitrap MS analysis for 100 ppm solution (w/v in 50:50 methanol/water) of 3 saccharides: D-(+)-melebiose, D-(+)-melezitose, and D-(+)-raffinose. Panels show the extracted mass spectra for each mixture component (**A**), the corresponding Faraday response (**B**), a map of the chemical space with m/z plotted as a function of drift time (**C**), and the extracted MS total ion chronograms (**D**). (BNG#1 & #2: 200 µs, scan step: 50 µs; AGC: 5.0E+06, IT: 1000 ms, Resolution: 35,000).

5.5. Conclusion

This work involved preliminary characterization of a dual-gate AP-DTIMS-Orbitrap system, showcasing its performance capabilities. The DTIMS unit afforded the greatest separation efficiency near the maximum operation potential of 10,000 V while using gas temperatures ≥200 ˚C and high drift gas flow rates of 2.0-3.0 L min^{-1} balanced with lower exhaust pump rates of 0.5-1.5 L min^{-1}. The effect of different ion mobility gating schemes on sensitivity and resolving power were thoroughly investigated. It was found that resolving power (R_p≤75, BNG pulse width: 50-150 µs) was mostly delimited by the initial DTIMS gate pulse width, and during scan mode analysis, the scan step bin width for the second ion gate if pulse width was set equal to the first gate. Likewise, sensitivity and throughput were primarily dictated by DTIMS gate pulse width, while Orbitrap parameters governing analytical cycle had a subtler influence. Once set to obtain measureable signal, Orbitrap variable injection times did not appear to significantly alter intensity levels at high gain settings, but had a more pronounced impact on the average signal intensity at the lowest gain settings and higher analyte concentrations depending on the size of the mobility acquisition window. Peak intensity profiles presumably reflected the radial ion density in the drift region, and were subject to change when conducting MS analysis with the DTIMS operating in open mode or fixed-gate mobility mode on account of the analyzer trapping preferences. The optimized AP-DTIMS-Orbitrap MS configuration was used successfully to resolve simple mixtures of peptide and sugar isomers, and HCD MS/MS was performed to further validate peptide identities based on characteristic fragmentation spectra. Future experiments will include collision cross-section measurements together with IM-MS platform peak capacity estimations. Lastly, the system is being developed to implement time-based digitally-multiplexed ion gating schemes using Hadamard Transforms to dramatically enhance DTIMS-MS sensitivity and throughput. An additional complement to these experiments will involve testing a homebuilt dual-gate AP-DTIMS prototype constructed with resistive glass rather

than stacked ring electrodes (Appendix C), coupling the unit with Orbitrap MS for comparison studies regarding resolving power and sensitivity.

CHAPTER 6. CONCLUSIONS AND OUTLOOK

6.1 Abstract

A summary of the research results gathered throughout this body of work are culminated in this chapter and shared with newly learned insights. Attention is given to the advancements made in plasma ion source development for ambient desorption/ionization, and to the separation and accurate detection capabilities demonstrated by a new combination of high-resolution ion mobility/mass spectrometry instrumentation. Future experimental directions for these original projects are also discussed, adding perspective to the current MS field framework.

6.2 Progress with Plasma-based Ambient Sampling Strategies: Understanding and Implementation

The number and diversity of plasma discharge ion sources that have emerged in the past decade have prompted a breadth of studies aimed at diagnosing and distinguishing performance between sources, and also refining ambient desorption/ionization sampling efficiency for MS. In parallel with the widespread commercial dissemination of the DART ion source, several early characterization studies were conducted by our group. This research principally involved source fluid dynamics simulations using different sample tablet geometries[39], discovery of sensitivity "hotspots" in the sample region at the spectrometer interface[38], and comparison with standard ESI regarding internal energy deposition during analyte ionization[100]. These pioneering studies were soon followed by other rigorous investigations determined to better comprehend plasma ionization and mass transport mechanisms. Such reports have detailed solvent microenvironment charge-transfer interactions[34], spectroscopically probed active metastable reagent populations[33], assessed ionization efficiency and signal intensities for different plasma device architectures[31], and visualized discharge source

fluid dynamics in real-time[40]. In this dissertation, Chapters 2-4 (and Appendices A-B) have provided new research expanding off these fundamental explorative works with ambient plasma sources.

6.2.1. Physiochemical Variables Determining Plasma Discharge Source Performance

Although DART is now widely utilized by clinical, industrial, and security sectors, a consistent standard sampling practice informed by real-time interpretation of fluid dynamic effects has not been established, which has led to imperfect and often poor reproducibility and signal stability. The Schlieren visualizations of the DART gas stream have served to rectify the misconceptions about source gas flow profiles while instructing proper sample probe placement for improved sampling efficiency. Specifically, insertion of capillary, swab, and drug tablet sample formats along the periphery of the highly-collimated helium stream was seen to preserve flow fidelity and potentially maximize sample exposure to the heated metastable gas for adequate desorption without complete disruption of fluid mass transport. In addition, gas flow patterns were also visualized for a newly adopted DART sampling procedure using sample-coated transmission screens and auxiliary vacuum draw at the spectrometer inlet, a configuration intended to better focus gas flow and improve quantitation. For such scenarios, the observed partial gas transmission through the sample screens was offset by significant gas deflection off the meshes and errant gas flows entrained around the mesh holder perimeter by the auxiliary vacuum. For every sampling arrangement explored, tighter source-instrument interface proximities (≤2 cm) were expected to mitigate the impact of gas flow diversion and turbulence effects induced by auxiliary pump pulsation. Since the interface spacing in the arrangements studied was exaggerated to facilitate clearer Schlieren visualizations, future experiments are required to further validate our fluid dynamics interpretations with MS sensitivity measurements under these conditions and also when employing alternative argon or nitrogen DART plasma gases.

As shown, the source gas fluid dynamics governing mass transport at the AP interface are a significant factor impacting ambient plasma source sampling efficiency. The other main determinants not surveyed during Schlieren visualization were the plasma support gas composition and discharge power (ion current). These variables dictate plasma gas temperature, and the energy and density of the active reagent population. A collaborative study (Appendix A) was dedicated to measuring the density of metastable helium atoms, understood to be the active species that initiate atmospheric pressure chemical ionization, in a variety of ambient discharge sources using absorbance spectroscopy. Results indicated that higher power, RF-driven plasma devices generated greater densities of helium metastable atoms (≥6x) than their DC counterparts, promising potentially greater ionization efficiencies. Our TM-VaPI source, reviewed again here shortly, was an ideal platform to test this hypothesis. The plasma source was operated at equivalent discharge powers (~20 W) using both high-frequency AC and DC modes of excitation in order to correlate the spectroscopy findings with MS signal intensities. Interestingly, the reactant ion populations and net analyte signal intensities were nearly equivalent for both excitation modes. Differences in performance between AC and DC regimes were more overtly linked to gas temperature variations affecting sample desorption and vacuum pressure. Although helium metastable atoms were empirically predicted in the aforementioned study to be the limiting reagents in the AP chemical ionization cascade, our MS results implied that alternate mechanisms less dependent on metastable density are likely involved, perhaps including unrevealed radical dissociation pathways. Further experiments are needed to reconcile the incongruence between measured helium metastable densities and ion abundance, such as more highly localized absorbance/emission spectroscopy measurements of downstream plasma species, even in the presence of analyte. These experiments could be expanded to nitrogen and argon support gases as well, for which mechanisms are not as well understood.

6.2.2. Development of New Ambient Plasma Sources for Mass Spectrometry: Versatility and Portability

Findings from the DART Schlieren visualization studies inspired a new source assembly with a more controlled ambient sampling scheme to minimize material losses for better quantitation and reproducibility, while at the same time enabling more versatile sampling strategies. The VaPI source was constructed featuring a cross union enclosure that bridged the plasma discharge and spectrometer AP inlet, with the merits of the design including conserved gas transport, confined plasma reagent/volatilized analyte mixing, and partial vacuum pressures assisting sample collection. This vessel was readily adapted to different modes of sample introduction, via thermal desorption from transmission sample meshes or laser ablation from sample substrates. TM-VaPI signal stability and sensitivity relied on balancing source helium flow rate and plasma power/gas temperature to maintain the vacuum pressure that aided sample uptake. With optimized settings, volatile solutions spotted to the sample meshes produced highly repeatable peak traces (RSD ± 8%). Even solid drug tablets could be effectively sampled directly on the mesh without dissolution steps by regulating plasma power and cross union temperature.

When modified for IR laser desorption/plasma ionization, it was found that the LA-VaPI apparatus permitted greater reactant ion consumption and higher amino acid analyte signal intensities than the conventional “open” AP interface configuration. Laser ablation was performed from liquid matrices, and it was found that a mixed aqueous/organic matrix afforded better intensity and a more even distribution of PEG analytes than a purely aqueous matrix, suggesting enhanced volatilization. This concept is now being carried forward in a new hybrid ambient sampling platform employing surface acoustic wave nebulization (SAWN) with VaPI for controlled micro-droplet formation/introduction. In addition, when high concentrations of salt were added to the sample solution or when analyzing unpurified model prebiotic reaction mixtures, LA-

VaPI was seemingly resilient to suppressive matrix effects that would otherwise be detrimental to ESI. Unlike what has been suggested for similar IR-LAMICI setups, a heated plasma gas was still required to help declustering of ablated material; and moreover, VaPI still appeared restricted to the upper mass limits imposed by thermal desorption threshold (800-1000 Da) seen with DART. Changes to either the sample chemistry or delivery method may help overcome this limitation, and these two aspects will be revisited when proposing future directions for the technique, with particular consideration of solid substrates/matrices in chemical imaging applications.

While developed as a multipurpose source to manage sampling in diverse formats or from complex matrices, the current VaPI construct is best suited for stationary benchtop instrumentation. But there remains growing demand for field-ready tools enabling mobile, on-site analysis with ion mobility detectors and miniature mass spectrometers. DART has nearly cornered the market in this regard, but the source still carries unnecessary bulk and is not conservative with power/gas resources. Our lab, in collaboration with the Orlando group (GT), has continued development of an MHCD microplasma device (Appendix B) as an ultra-portable, resource efficient ion source intended for environmental monitoring of air/water aboard the International Space Station. Compared with standard DART operation parameters, this compact planar dielectric barrier discharge source consumed far less gas ($\leq$1 L min^{-1}) and power ($\leq$1 W) while producing nearly equivalent ion populations and intensities for target volatiles. The MHCD source was also found to work well with cheaper alternative gases like nitrogen and argon in place of helium, which increased device longevity. With nitrogen working gas, the MHCD produced more unique fingerprint spectra for analytes than DART, leveraging ratios of protonated clusters and ammoniated adduct species to potentially aid identification on lower resolution detectors. The next stages of development with the MHCD source involves spatially-dense microcavity arrays to amplify ion generation and sensitivity, automated microfluidic sampling for greater control and quantitative ability,

and operation of the (helium) discharge with AC excitation to prolong device lifetime, further conserve resources, and enhance ionization efficiency. In addition, fluid dynamics studies of the microplasma, much like the Schlieren visualizations for DART, could prove critically informative.

6.2.3. Coupling Plasma Ion Sources with Ion Mobility Spectrometry

It has been a substantial challenge to couple ambient plasma discharge sources like DART, which operate at potentials near ground, with atmospheric pressure drift tube IMS detectors. The electric field gradients required to propel ions through such pressures result in excessively large inlet potential barriers on these instruments and the fluid dynamics of a counter-flowing buffer gas are not conducive to efficient ion injection. We endeavored to couple a DART plasma source with standalone resistive-glass DTIMS using a repeller point electrode as a field-focusing element. The effect was illustrated with PE contours modeled using SIMION 8.1. The point electrode, when elevated to a potential above the IMS entrance but below the threshold for corona discharge, worked to favorably shape the electric field gradient at the spectrometer inlet and facilitate ion transmission. This new ion source motif retained the advantage of ambient plasma sampling by not restricting source accessibility or the sample introduction format, which were the shortfalls of previously reported coupling tactics.

Parameter space experiments determined maximum sensitivity was achieved when partially inserting the point electrode, centered and on-axis, into the IMS inlet while also keeping the DART source orthogonal to the DTIMS inlet to minimize gas turbulence within the IMS entrance. Analysis of a solid drug tablet without extra preparation was successfully demonstrated. Adjusting the electrode potential 1-2 kV above the DTIMS inlet, ion mobility signal could be tuned to produce N_2 DART-specific or corona-specific responses, with different mobility peaks tentatively assigned by MS as ammoniated or protonated adducts corresponding to the different modes of ionization.

Observation of an electrode current (μA) and intermittent electrode "glow" suggested that a simultaneous secondary ionization/stimulated electrode emission mechanism was possibly involved. Future experiments using a highly-insulated repeller electrode together with ion flight simulations modeling the positive ion and negative counter-ion trajectories could corroborate this hypothesis. New directions for this work are being continued on an identical DTIMS prototype possessing a more "user-friendly" grounded inlet and inverse potential gradient bias.

6.3 Development of a High-Resolution Ion Mobility-Mass Spectrometry Platform for Multidimensional Analysis

Since ion generation and transport are essential for MS, the majority of this dissertation research has been dedicated to method development at the front-end of the instrument, attempting to optimize ambient source ionization and transmission efficiency to maximize selectivity and sensitivity. Rather than continue perfecting the ion source performance alone, the last segment of research presented Chapter 5 was focused on improving instrument peak capacity and sensitivity by incorporating an additional analytical dimension for ion separation and selection at the AP interface.

An unprecedented arrangement of high-resolution AP-DTIMS coupled with an ultra-accurate mass FT Orbitrap mass analyzer was extensively characterized. General DTIMS performance was optimized using drift cell voltages of 9,000-10,000 V, drift gas temperatures of 180-220℃, drift gas flow rates of 2.0-3.0 L min^{-1}, and exhaust pump rates of 0.5-1.5 L min^{-1}. The ratio of drift gas flow rate to exhaust pump rate was critical to maintaining drift gas uniformity and resolvable signal responses. Narrow ion gate pulse widths of 75-150 μs offered the best balance between DTIMS sensitivity and resolving power, with R_p ~70 achieved on average for mobility calibration standards, double the routine R_p of reduced-pressure IM-MS instruments. The DTIMS dual-gate functionality was evaluated for fixed-gate and scanned-gate operations in association with the main Orbitrap parameters effecting detector scan speed – resolution, injection

time, and automatic gain control. With the second gate pulsed open across 75% of the IMS drift period, it was observed that the added mobility component caused a shift in MS spectral intensities as the Orbitrap gain preferentially targeted the first mobility peak. Accordingly, MS intensity for more trace analytes or compounds with lower ion mobilities must be restored by exclusively tailoring the mobility window. When scanning the second ion gate, overall MS sensitivity was diminished by ~10^2-10^3 compared to fixed-gate operation (depending on the pulse width), while oversampling the second gate scan-step function helped prevent MS TIC peak distortion and broadening. Surprisingly, it was found that varying the Orbitrap injection time did not significantly impact sensitivity regardless of the gain setting for fixed-gate acquisitions, but only when scanning the second ion gate, greater average signal intensity was achieved with a lower gain threshold for a given acquisition period. The important implications from these experiments concern how the size of the fixed-gate mobility window(s) or mobility scan period appear to have a more pronounced influence on sensitivity than the detector scan parameters, and that acquiring greater peak density in both the mobility and m/z dimensions can compromise or skew sensitivity.

Following system diagnosis, benchmark samples were analyzed to qualitatively demonstrate the performance advantages of AP-DTIMS-Orbitrap MS compared to TWIMS-ToF and FAIMS-ToF systems. Selected sugar isomers and reverse peptide sequences were shown to be successfully resolved from one another in the mobility dimension, and their identities were verified by accurate mass and/or characteristic HCD MS/MS fragmentation spectra on the Orbitrap. Immediate ongoing characterization experiments include accurate determination of polymer collision cross-sections using the AP-DTIMS and estimation of ion transmission efficiency at the drift tube exit with radial ion density measurements. The next phases of system development described in the future directions section will involve digital multiplexing and a custom DTIMS prototype with alternative materials to further enhance throughput, sensitivity, and resolving power.

6.4 Proposed Future Directions

6.4.1. Hybrid Ambient Source Development and Enhanced Sampling Approaches

Ambient plasma desorption/ionization technologies will continue to mature and progress toward the extremes of miniaturization and versatility. The MHCD microplasma represents one angle in pursuit of this goal, while the hybrid sampling strategies capable with VaPI offer another. For instance, taking the MHCD concept much further, an ideal next-generation device would embody a compact, portable plasma discharge that is tunable across a broad power range. This might be accomplished through some combination of modulating discharge gas composition and ion current using a modified ICP device architecture. The adjustable power envelope would enable a gradual transition from soft, chemically-selective molecular ionization to atomic ionization for elemental analysis, thus providing an expanded spectrum of information and all using a single source.

However, the present and immediate future for current plasma sources is in mass spectrometry imaging applications, which popularly include forensic analysis of residues and bioorganic tissue surveys in clinical disease studies. For typical plasma device dimensions and source gas requirements, spatial resolution continues to be corrupted by dispersion of the impinging plasma/gas stream when directly probing a surface. Reduction of source dimensions and gas volumes to alleviate this complication has resulted in proportionally decreased source power and ultimately lower sensitivity. Hence, corona, DART, and other DBD-type plasma sources have been paired most frequently with AP photoacoustic (laser) ablation schemes to afford higher spatial resolution while also overcoming the plasma thermal desorption limits.

The advantage of such a configuration was shown for VaPI in this text, but MS imaging for this source was not explicitly demonstrated. In fact, the LA-VaPI source design was original envisioned for imaging 2-D TLC substrates, where the combination

of vacuum suction and high plasma power were desired to facilitate collection of heavier ablated particles and aid thermal declustering. In preliminary experiments, several TLC chemistries were tested for their matrix efficacy in terms of IR absorption efficiency and background matrix ion intensity; however, even for the best silica-based matrix, signal was inconsistent and sensitivity was underwhelming for analytes that possessed a high affinity for the TLC stationary phase. Attempting to overcome these issues by tuning laser and plasma parameters to extremes would likely incur unwanted effects such as excessive fragmentation and degradation and/or unmanageable ablation plume dynamics together with oversized particulates too heavy and clustered to be properly sampled.

Extending such considerations to the future of plasma sources in MS imaging motifs, more creative preparation of the sample chemistry or new delivery methods should be explored. Specifically for the intended use of IR LA-VaPI with TLC plate imaging, factors like particle size, functionalized phase chemistry (that can distort absorption efficiency as well as analyte affinity), and packing density or binding agents used should be contemplated. Similar to nanoparticle-enhanced absorption with MALDI-MS, one approach may be as simple as doping the TLC coating with highly absorptive graphite particles. Alternatively, the substrate chemistry may undergo an activation or selective chemical derivatization step before analysis. If tampering with the sample chemistry would be too deleterious or compromise the spatial resolution, yet another possibility could involve plasma gas dopants used to assist analyte extraction from ablated material or to activate selective ionization pathways for different classes of compounds while suppressing unfavorable ones, reminiscent of AP photoionization source mechanisms.

MS imaging of TLC plates is only one example application, but the same principles learned are relevant to other sample types. Where laser ablation fails, the VaPI source construct is also amenable to coupling with imaging-compatible desorption sprays, like DESI, which offer the benefits of dynamic solvent/liquid extraction prior to

ionization. Moreover, MS imaging with these sources is no longer restricted to 2-D substrates using laser or spray desorption. A new robotic plasma probe ionization (RoPPI) technique, which uses a high-precision automated robotic arm to probe areas of a digitally-mapped object surface and serially position sample for DART-MS, is being developed in our lab for MS imaging of irregular 3-D surfaces[154]. Emerging applications include RoPPI-MS imaging of meteorites for prebiotic chemistries and cell signaling networks of bacterial colonies grown on agar plates.

6.4.2. Digitally-Multiplexed AP-DTIMS-FT-MS and Alternative DTIMS Architectures

For now, the AP-DTIMS-Orbitrap MS performance in terms of peak capacity and throughput continues to be partly compromised by the low duty cycles associated with pulsed DTIMS ion sampling and signal averaging during scanned-gate acquisitions. The next priority in method development involves implementation of a time-based multiplexing approach for DTIMS analysis to improve total IM-MS throughput and sensitivity, thereby helping to increase peak coverage in the m/z and mobility dimensions. This process entails pulsing the initial IMS ion gate open several times in a pseudo-random sequence during a single acquisition, with the second ion gate mirroring the sequence on a scanned delay from the first ion gate. A Fourier Transform algorithm is then used to deconvolute the time-binned signal responses after detection/acquisition. This multiplexed gating scheme will effectively augment the duty cycle to bolster sensitivity while maintaining the resolving power afforded by narrower gate pulse widths. Our lab has previous experience with and will continue multiplexing using Hadamard matrix sequences, for which a DTIMS signal-to-noise enhancement of 9-fold over conventional signal averaging was observed for a 50% gating duty cycle[88]. In our IM-MS arrangement, these Hadamard sequences will be software triggered and run using linked arbitrary waveform generators and a synchronized DAQ card that feed directly into the external inputs controlling the internal MA3100 gate scan timing hardware. The

underlying concern that remains to be solved is synchronization of the digitally-multiplexed gate functions with the variable scan speeds of the Orbitrap detector, so a method to extract/modulate the Orbitrap detector scan pulse to be used as a trigger for the DTIMS is being thoroughly investigated.

While time-based multiplexing provides one means to increase sensitivity, other instrumental measures related to the DTIMS build design can help increase separation power and resolution. For example, drift tube spectrometers using stacked-ring electrodes have started implementing RF-confining fields to reduce diffusion-based band broadening and transmission losses within the drift cell. Recalling Chapter 4, more of our future work will involve modification of the standalone DTIM detector into a dual-gate AP-DTIMS prototype for coupling to our Orbitrap MS. The modified DTIMS variant offers a few select advantages over the current EXCELLIMS discrete electrode model that we have characterized. In theory, the resistive glass elements eliminate the fringe electric field inhomogeneities between stacked electrode rings to produce more stable and uniform electric field gradients. Additionally, the resistive glass DTIMS we are adapting features a drift region 2.5x longer and capable of R_p>100. Appendix C briefly highlights the progress toward completing this new resistive glass dual-gate prototype, detailing the design and demonstrating functionality for an operational unit before coupling with MS.

Projecting further into the future, we can envisage enhancing performance for resistive glass IM spectrometers by implementing a spatial multiplexing approach to also achieve greater sensitivity gains. This could readily done by fabricating the glass tube drift space into a rounded “honeycomb” array, possibly with a matching electrospray source array and detector capillary array unified at a single MS inlet or Faraday amplifier. As low mobility sensitivities necessitate fairly concentrated samples that inevitably lead to instrument contamination and decreased resolving power, we are planning to passivate active sites on the semi-permeable glass surface of the drift tube using sialylation reagents in order to reinforce chemical stability and improve drift gas purity.

APPENDIX A. Absolute Number Density of Helium Metastable Atoms Determined by Atomic Absorption Spectroscopy in Helium Plasma-based Discharges Used as Ambient Desorption/Ionization Sources for Mass Spectrometry

Adapted from

Reininger, C.; Woodfield, K.; Keelor, J. D.; Kaylor, A.; Fernández, F. M.; Farnsworth, P. B. *Spectrochim. Acta B.* **2014**, *100*, 98-104.

A.1. Abstract

The absolute number densities of helium metastable atoms in the 2s $^3S_1$ state were obtained for different ambient desorption/ionization plasma-discharge device architectures by atomic absorption spectroscopy. The ion sources examined included a high frequency dielectric barrier discharge (HF-DBD), a low temperature plasma (LTP), and a point-to-plane glow discharge motif that was operated using both continuous DC excitation or sine-waveform AC excitation. Peak densities measured in the downstream luminous plasma plume emanating from the LTP and HF-DBD exit capillaries were found to be 1.39 x 10^{12} cm^{-3} and 0.011 x 10^{12} cm^{-3}, respectively. The point-to-plane glow discharges did not generate a visible afterglow, and the metastable absorbance beyond the exit electrode were below detection limits. However, the peak densities for the metastable atom population produced in the active plasma region between electrodes for the AC-driven and DC-driven discharges were 0.58 x 10^{12} cm^{-3} and 0.097 x 10^{12} cm^{-3}, respectively. Time-resolved measurements for the metastable atom concentrations in the AC power regime showed variable pulsed absorbance patterns which deviated from the applied voltage waveforms.

A.2. Introduction

A multitude of ambient desorption/ionization constructs have continued to emerge over the past decade for mass spectrometry. The most diverse assortment of techniques have involved plasma discharge devices, namely the commercially-popularized direct analysis in real time (DART)[2] and versatile flowing atmospheric pressure afterglow (FAPA)[29] sources, but also LTP[24] and other variants of DBD probe in portable instrumentation and hybrid source assemblies[10, 155]. Most of these plasma sources employ helium support gas, for which a stable, tunable-power discharge is easy to maintain in either DC or AC modes of operation. Importantly, helium provides superior thermal conductivity to facilitate desorption and helium-based discharges generate highly-excited energy states with exceptional lifetimes. These high energy metastable atoms are able to ionize molecules from sample substrates via direct energy transfer, or as the mechanism is more commonly understood, incite a cascade of reactions through atmospheric primary ions that lead to solvent-mediated proton exchanges with analytes[32, 34]. Since these metastables are considered the active species and limiting reagents for analyte ion formation, source efficiency is associated with the concentration of helium metastables generated by the plasma source. Furthermore, effectiveness of these sources is then susceptible to sample matrix effects and ion suppression if metastable number densities are low and there is poor chemical selectivity for target analytes in the downstream ionization mechanism[156].

In addition to the fluid dynamics governing mass transport at the spectrometer interface, and source gas temperatures affecting thermal desorption capacity, it follows that a significant metric to classify plasma source capability is related to the abundance of helium metastable atoms. The absolute number density of the metastable reagent species He (2s) $^3S_1$, or He_m, was thus measured by atomic absorption spectroscopy for HF-DBD, LTP, and AC/DC point-to-plane glow discharge source designs to infer more about their efficiencies. The measured He_m densities were also compared with estimated

concentrations of atmospheric H_2O and N_2, confirming the likelihood of He_m as the limiting reagents in the theorized ambient ionization pathway.

A.3. Experimental

A.3.1. Helium Plasma-discharge Sources

Ultra-high purity helium gas (99.999%) was acquired from Airgas (Radnor, PA, USA) and used for all experiments. Helium flow rates were regulated using MKS 1170A mass flow controller and an MKS 246C power unit/display (MKS Instruments, Andover, MA, USA).

High-frequency Dielectric Barrier Discharge

The HF-DBD device construction was similar to another type characterized previously[157], with this source featuring capillary dimensions able to produce a fine, protrusive afterglow extending ~30 mm. An image of the operating source and a detailed schematic of the assembly can be found in Figure A.1. The HF-DBD discharge was powered by an ENI HPG-2 radiofrequency power supply (MKS Instruments), and the optimized power and frequency parameters used were 31 W and 350 kHz, respectively, and were determined by matching the forward and load powers reported by the AC supply as closely as possible. The applied voltage waveform was monitored on a 500 MHz digital oscilloscope (LeCroy Corporation, Chestnut Ridge, NY, USA).

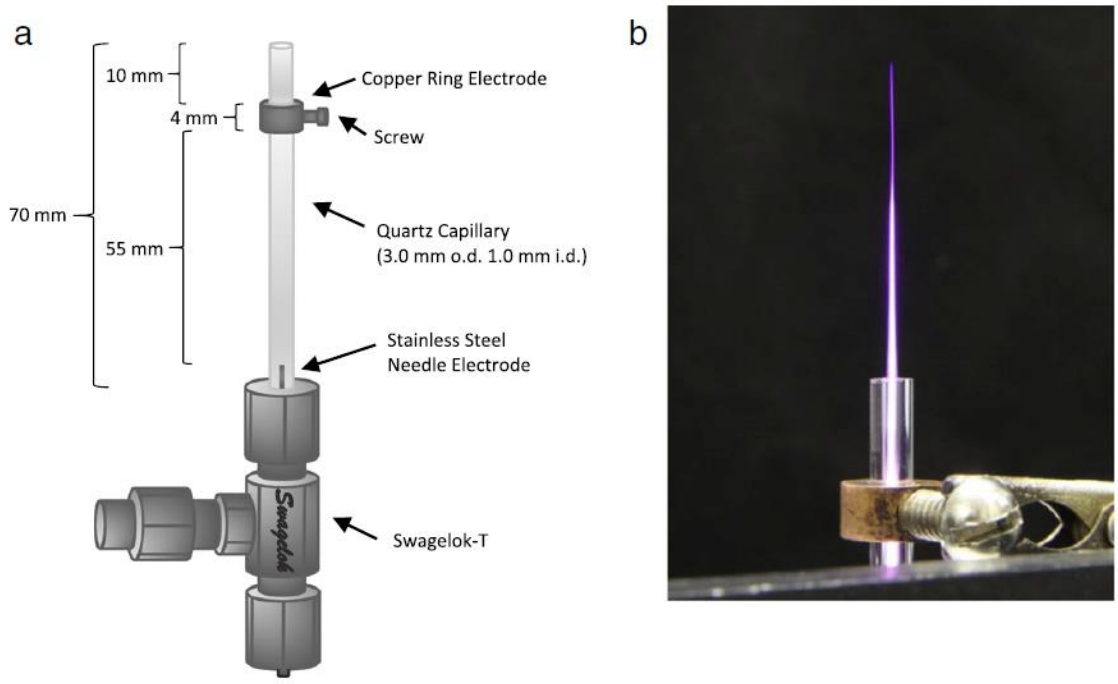

Figure A.1: Schematic (**a**) and photograph (**b**) of active HF-DBD.

Low Temperature Plasma

The LTP source used was modeled after an original design described by the Cooks group[24]. An image of the LTP in operation and a schematic depicting details for the source construction are shown in Figure A.2. A custom-built power supply approximating an automotive ignition coil was used to deliver a 9.7 kV p-p voltage to the LTP with a frequency of 4.5 kHz. The helium source gas flow rate was set to 1 L min^{-1}.

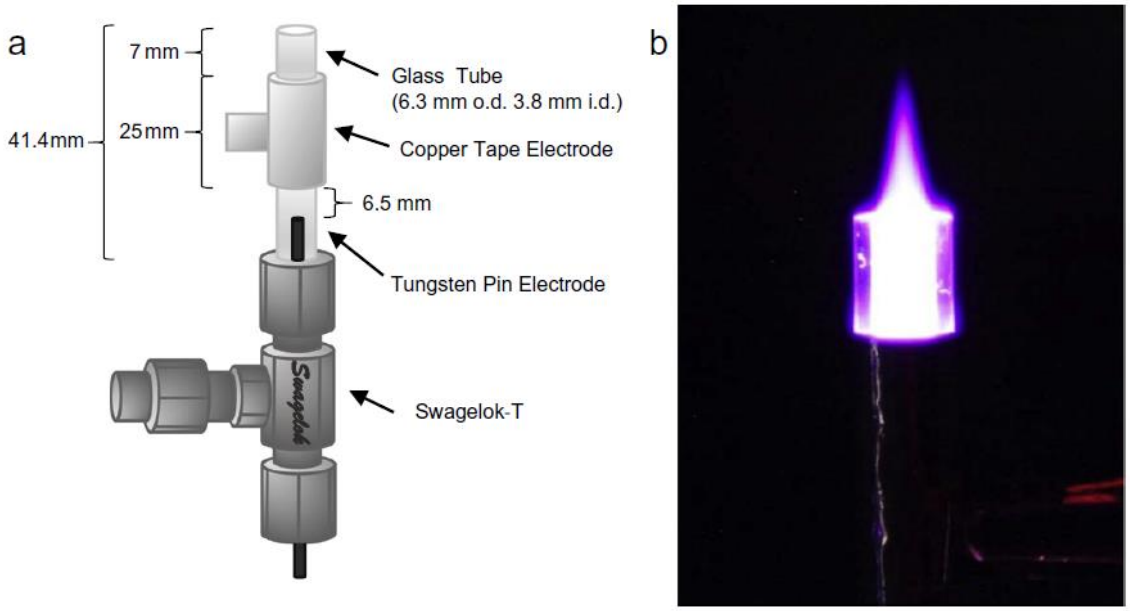

Figure A.2: Schematic (**a**) and photograph (**b**) of active LTP.

Point-to-Plane Atmospheric Pressure Glow Discharges

The point-to-plane glow discharge source motif is depicted in Figure A.3, which shows a detailed schematic of the device electrode geometry and dimensions together with pictures of its operation in both DC and AC power regimes. The discharge quartz capillary was capped with a grounded aluminum disk electrode (*i.d.* = 1 mm). Helium was passed through the source cell at 2 L min^{-1} for both modes of excitation. DC power was provided to the enclosed tungsten cathode needle from a BHK 1000-0.2 MG high voltage power supply. The HV supply operated in current-limited mode, delivering a 25 mA current through a 2.24 kΩ ballast resistor in series with the plasma for a discharge potential of -494 V. In AC mode, the ENI HPG-2 unit supplied a high voltage to the tungsten pin using a frequency of 325 kHz and an approximate power of 4 W.

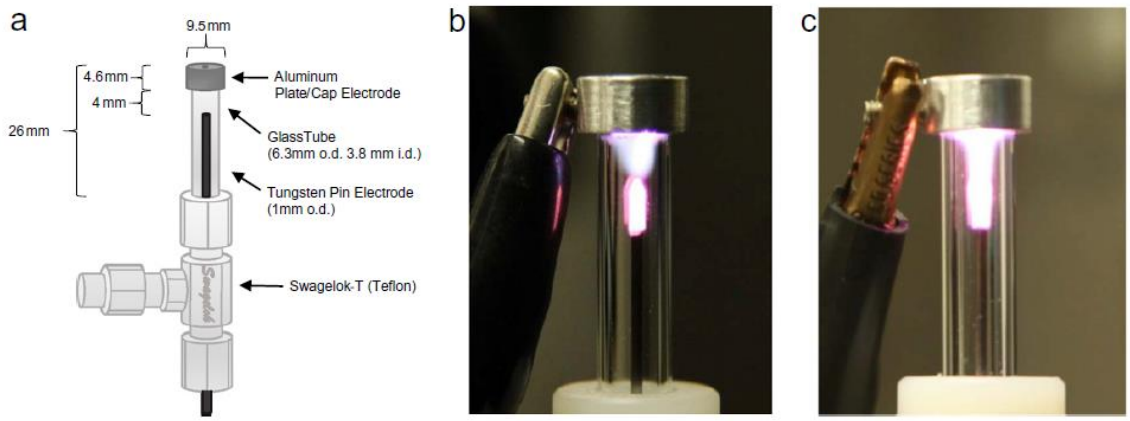

Figure A.3: Schematic (**a**) and photographs of active glow discharge using DC excitation (**b**) and AC excitation (**c**).

Low-pressure Reference Discharge Cell

The absorbance transitions for atomic helium states 2s $^3S_1$ – 2p $^3P_0$, 2s $^3S_1$ – 2p $^3P_1$, and 2s $^3S_1$ – 2p $^3P_2$ occur at well-known wavelengths of 1082.9091140 nm, 1083.0250105 nm, and 1083.0339773 nm, respectively[158]. At low pressures, the collisional broadening that diminishes the resolution of absorbance peaks for each transition is greatly reduced, so that the discrete transitions may be resolved from one another with high accuracy. Accordingly, a low-pressure discharge reference cell was constructed for the purpose of accurately measuring helium metastable atom densities based on the transitions listed with excellent signal-to-noise ratios. The reference discharge cell built for accurate frequency calibration during atomic absorbance measurements bore resemblance to the LTP source, and the design adapted from Weijan Lu *et al.*[159] is illustrated in Figure A.4 schematic. A metal-to-glass (stainless steel-to-7740 Pyrex-UHV series) adaptor fitting with 12.7 mm outer diameter served at the cathode housing (MDC Vacuum Products LLC, Hayward, CA, USA). A tungsten pin (*dia.* = 2 mm) inserted within the glass tube acted as the anode. Two quartz windows fashioned into the Pyrex body near the anode afforded a clear optical path through the positive column of the discharge. This assembly was mounted on a six-way stainless steel

cross union (MDC Vacuum Products), for which spare joints were used to connect a helium gas line, a pressure gauge (Granville Philips convection gauge, Longmont, CO, USA), a roughing vacuum pump, and a 1.7 L stainless steel gas buffer reservoir. The reference cell was baked for several hours and purged before measurements, then pressurized to 0.5 torr helium, which sustained a discharge of 6 mA and 350 V during operation. Peak absorbance under these conditions maxed out at 0.7 a.u.

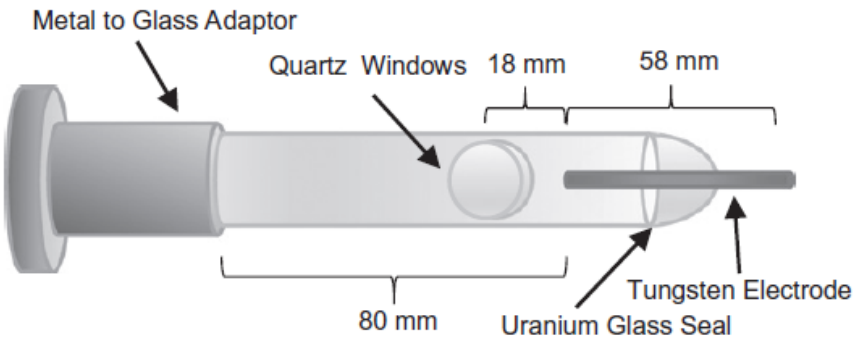

Figure A.4: Schematic of low-pressure reference discharge cell.

A.3.2. Atomic Absorbance Spectroscopy

Absorbance Spectrometer

The apparatus devised for absorbance spectroscopy is illustrated in Figure A.5, and is configured similarly to a setup used by Urabe *et al.* in a mechanistic DBD excitation study[160]. A TLB-6900 VortexTM II laser (New Focus, Santa Clara, CA, USA) was used as the light source, producing a nominal wavelength light beam at 1083 nm with sufficient mop hop to be modulated across the three aforementioned helium transitions. The laser beam, with a specified line width of 300 kHz, was passed through an optical isolator (I-106 T-4 L, Isowave, Dover, NJ) and then divided with beam splitters into sample and reference beams. The remaining beam transmitted through the splitters was directed into a confocal Fabry-Perot interferometer, which was used as a frequency comb.

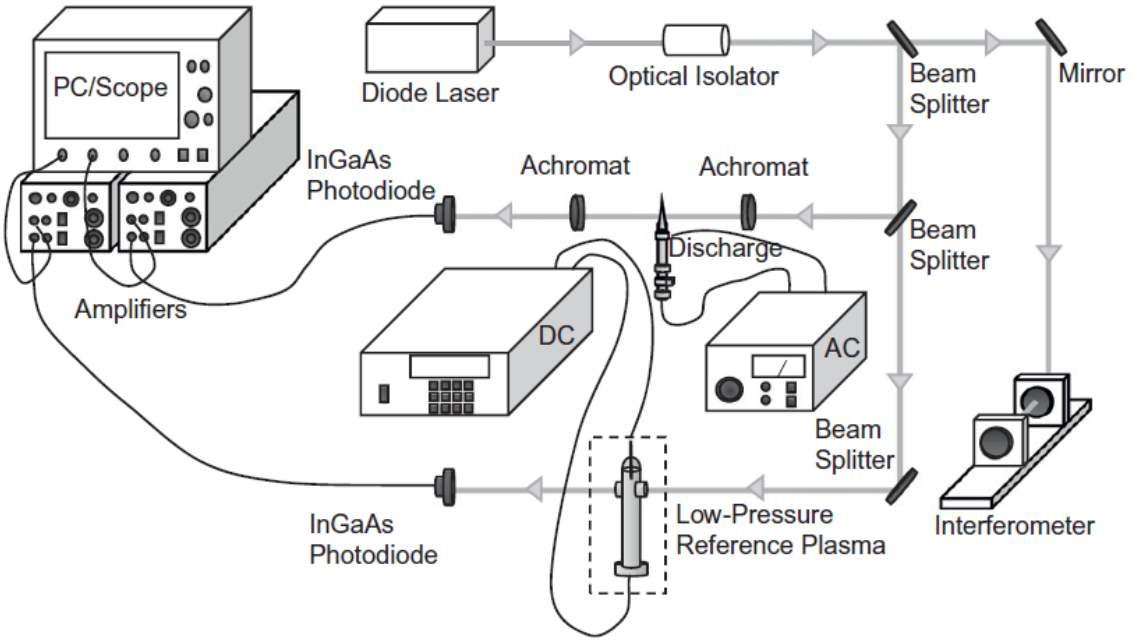

Figure A.5: Diagrammatic illustration of the atomic absorption instrument. The low-pressure discharge cell was only in place during wavelength calibration measurements.

The sample beam was recollimated through two aligned achromats (50 mm f.l.), with the source plasma being examined positioned at the focal waist between the lenses. Along a separate channel, the reference beam was passed through the low pressure discharge cell. Both sample and reference beams were monitored using matched InGaAs photodiode detectors (SM05PD5A, Thorlabs, Newton, NJ) connected to a differential amplifier (AM501, Tektronix, Beaverton, OR). The amplifier output signals simultaneously to a digital I/O adapter (DAQ-PCI-6110, National Instruments, Austin, TX) and a digital oscilloscope (Wavesurfer, LeCroy). When averaging absorbance over time, the laser was scanned back and forth across the narrow range of wavelengths corresponding to each helium transition using a triangle waveform and a scanning frequency of 40 mHz. For time-resolved measurements, the laser was lock-tuned to the blended peak of the two most intense helium transitions, and the sample and reference signals were recorded as a function of time. Photodiode response speed was mediated using a 50 Ohm termination, and the amplifier bandwidths were set to maximum at 1

Mhz. System responses were cross-checked using neutral density filters during experiments to verify the electronics and optical transitions were not being saturated by the laser.

Since accurate metastable atom number density calculations were frequency-dependent, the laser frequency axis was calibrated from the simultaneous outputs recorded for the reference discharge cell and the Fabry-Perot interferometer. Comparing the spacing between the atomic helium lines and number of fringes between peaks, the free spectral range ($\Delta\lambda$) of the interferometer was found to be 730.1 MHz. When measuring absorbance for the different plasma sources, this interferometer worked as a precise optical ruler.

Absolute Number Density Calculations

In the case of these experiments, the spectral bandwidth of the source was far narrower than the absorption transitions of interest. For these instances, the absorbance for an individual transition can be expressed as

$$A_{v\alpha} = \frac{A_{21} c^2 g_{2\alpha} S_{v\alpha} n_1}{v_\alpha^2 g_1 8\pi} \cdot \frac{x}{\ln(10)} \qquad (1)$$

where $A_{v\alpha}$ represents the frequency-dependent absorbance, A_{21} is the Einstein A coefficient, c is the speed of light, the degeneracies of the upper and lower levels are assigned as g_1 and g_2, S_v is the normalized line shape function, n_1 defines the number density of absorbing atoms, and the absorbance path-length is given as x. The subscript α in this equation designates a specific absorbance transition. Measurements were done in this work over a very narrow frequency range wide enough to encompass the three partially-resolved helium transitions. The equation[161] for these absorbance values can expanded as

$$A_{v\,\text{total}} = \frac{A_{21} c^2 n_1}{g_1 8\pi} \cdot \frac{x}{\ln(10)} \left(\frac{g_{2\alpha} S_{v\alpha}}{v_\alpha^2} + \frac{g_{2\beta} S_{v\beta}}{v_\beta^2} + \frac{g_{2\gamma} S_{v\gamma}}{v_\gamma^2} \right) \qquad (2)$$

where now the subscripts α, β, and γ represent the three discrete helium transitions being probed. The Einstein coefficients remain identical for all transitions in this circumstance, and are reported within an accuracy tolerance of 0.3%[162]. When integrating over the scanned frequency range of the laser, considering the frequency terms constant, than the absorbance equation becomes

$$A_{int} = \frac{A_{21} c^2 n_1}{g_1 8\pi} \cdot \frac{x}{\ln(10)} \left(\frac{g_{2\alpha}}{v_\alpha^2} + \frac{g_{2\beta}}{v_\beta^2} + \frac{g_{2\gamma}}{v_\gamma^2} \right) \quad (3)$$

And finally solving for the number density, n_1, gives the final expression

$$n_1 = \frac{A_{int} g_1 8\pi}{A_{21} c^2} \cdot \frac{\ln(10)}{x} \left(\frac{g_{2\alpha} S_{v\alpha}}{v_\alpha^2} + \frac{g_{2\beta} S_{v\beta}}{v_\beta^2} + \frac{g_{2\gamma} S_{v\gamma}}{v_\gamma^2} \right)^{-1} \quad (4)$$

The helium metastable atom number densities were calculated from Eq. (4) using the numerically-integrated absorbance values and path lengths equal to the diameter of the plasma plume or discharge cell beam-intercept region. Inhomogeneity of the sample zone was not factored, as radially-resolved density measurements were not conducted[160]. Only light-of-sight absorbance values are reported.

A.4. Results and Discussion

A.4.1. Time-averaged Density Measurements

HF-DBD Results

The HF-DBD was the most familiar source design for the investigators and was selected as the benchmark system for this study. Representative absorbance scan traces for the three helium transitions being monitored are shown in Figure A.6. Three peaks can be clearly distinguished looking at the light gray trace corresponding to the time-averaged transitions of the low pressure discharge. The Gaussian profiles for the reference cell discharge here revealed primarily Doppler broadening effects. In contrast, the bold trace superimposed on top of the lighter trace is the time-averaged absorbance for the HF-DBD, where at atmospheric pressure the Voight profiles were dominated by

collisional broadening. For a limited experimental data set, the results were fit to Voigt profiles, for which the integrated absorbances were found to exhibit broader limits than the fitted curves. This practice skewed number density calculations on average 2.5% higher than predicted by straight numerical integration of the data. To compensate, values reported in this work are systematically 2-3% low, and include only integrated experimental data that ignores contributions from the extreme line wings beyond the laser scan limits. Likewise, no larger error contributions were assumed from incongruences between absorbance path length and plasma capillary internal diameters.

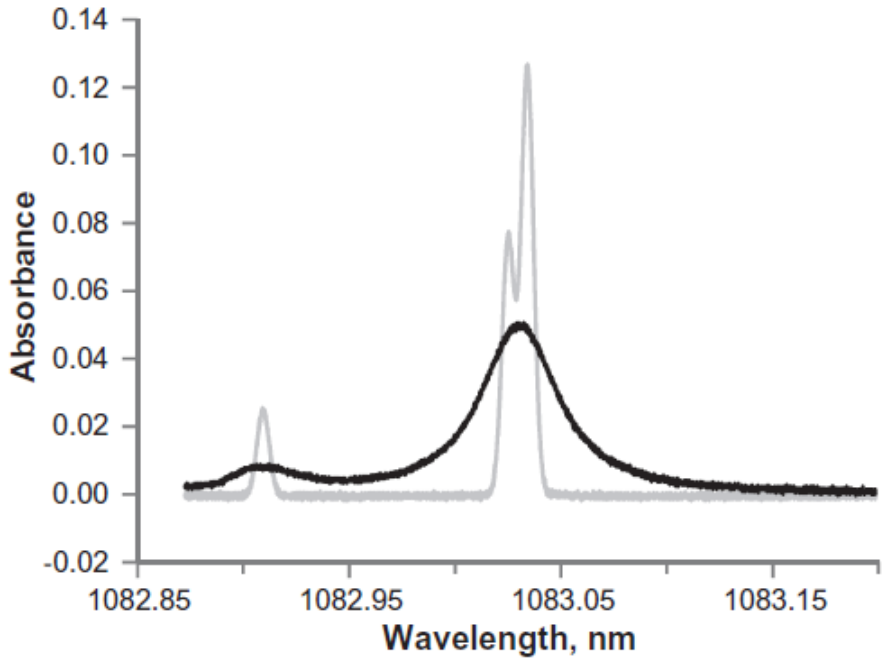

Figure A.6: Absorbance spectra for low-pressure reference discharge (gray trace) and HF-DBD (bold trace).

Metastable helium number densities were measured as a function of plasma plume position downstream from the HF-DBD capillary exit and plotted in Figure A.7. The number density distribution along this plot is in good agreement with the relative densities of He_m obtained by laser-induced florescence and reported previously[157]. Although, the time-averaged maximum value observed at position 1.5 mm beyond the capillary tip (1.4×10^{12} cm^{-3}) was considerably higher, by at least an order of magnitude,

than the values determined for other atmospheric pressure helium DBD[160] and RF microplasmas [163]. For these results, the number density limit of detection within a 1 mm pathlength was estimated to be 3 x 10^9 cm^{-3}. This value was derived from time-averaging 24 absorbance scans where the signal was equal to 3 times the baseline noise level.

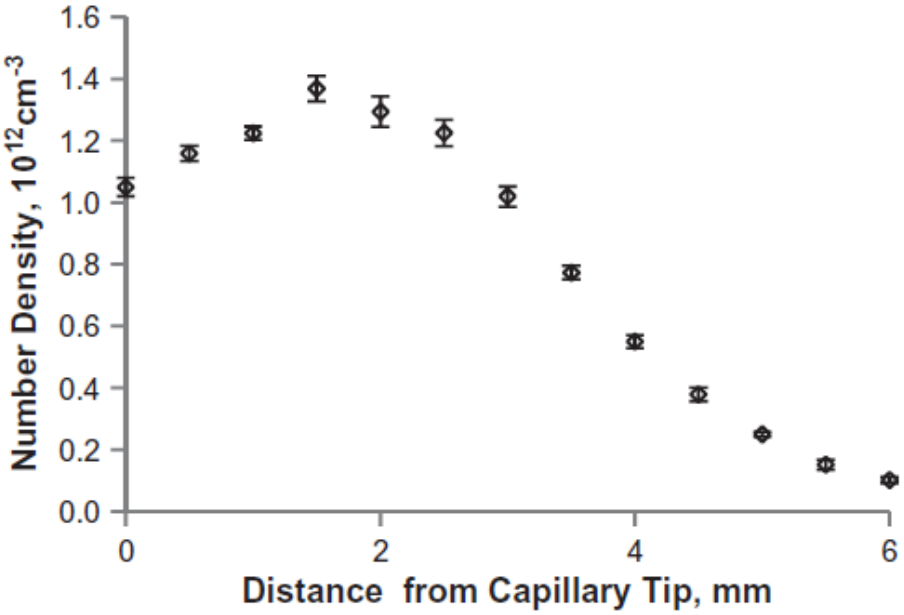

Figure A.7: Absolute number densities of He_m in the HF-DBD as a function position in the luminous plasma plume downstream from the capillary exit. The error bars represent the standard deviation of 24 replicate determinations made in rapid succession.

Comparison with LTP and Glow Discharge Plasmas

The time-average number densities of helium metastable atoms calculated for each plasma device are laid out in Table A.1. Of the four plasma source architectures evaluated, the HF-DBD produced the highest He_m number densities. This result was not unexpected, as HF-DBD was the highest power discharge with the smallest source dimensions to locally concentrate the species. Calculated He_m densities for the LTP source were quite a bit lower than the HF-DBD. This observation was justified given the larger LTP source dimensions which permit a more diffuse plasma, but also the poorer discharge duty cycle inferred from time-resolved measurements that will be explained

shortly. For both the DC-powered and AC-driven glow discharges, a sufficiently large metastable densities were generated in the source inter-electrode region, but He_m absorbance downstream from the cap electrode was below detection limits and densities could not be determined. This result suggests an efficient excited-state quenching mechanism once the metastable-enriched gas was transported beyond the grounded disk counter-electrode, possibly from direct Penning ionization of He_m with N_2 to initiate the atmospheric pressure chemical ionization cascade. Further analysis of the downstream reaction products, perhaps by emission spectroscopy, could provide more insight to confirm this hypothesis. Significantly, the difference in number densities calculated for the AC or DC discharge modes is in agreement with another simulation study by Boegaerts and Gijbels, which reported a higher density of metastable argon atoms in the inter-electrode cavity of low-pressure DBD when employing RF excitation versus DC excitation[164].

Table A.1: Time-averaged number densities of He_m for four plasma sources

Plasma source	Excitation mode	Location	Path length (mm)	Density of He (2 s) $^3S_1$ atoms (10^{12} cm^{-3})
HF-DBD	AC, 350 kHz	1 mm downstream from capillary exit	1	1.39 ± 0.03
LTP	AC, 4.5 kHz	1 mm downstream from capillary exit	4	0.01111 ± 0.0007
Glow discharge	AC, 325 kHz	1 mm downstream from end cap	~1	<0.003
Glow discharge	AC, 325 kHz	Midway between pin and end cap electrodes	4	0.585 ± 0.006
Glow discharge	DC	1 mm downstream from end cap	~1	<0.003
Glow discharge	DC	Midway between pin and end cap electrodes	4	0.097 ± 0.002

It is important to note that the quantity of He_m produced with a plasma discharge is only one aspect by which to judge the potential performance of an ambient desorption/ionization source. Sampling efficiency with these devices is contingent on not simply the concentration of reactant ions generated by the limiting He_m reagent, but also the total flux of those reactant ions delivered to a sample, the accessibility and rate or degree of interaction with the analyte, and finally the volume of gas collected by the spectrometer. Based on He_m abundance alone, the RF glow discharge appears to be a more promising candidate than the DC glow discharge. Under conditions where not just the quantity but the flux of reagent ions decides source performance, the glow discharge

is also predicted to compete favorably with the higher power HF-DBD. Despite a 40% lower He_m number density, the RF glow discharge possesses a plasma cross-sectional area 16 times larger than that of the HF-DBD. Ultimately, source efficiency depends on the density of reactant ions produced by the He_m supply, and the quantities of He_m measured for each source here is only one facet of the full characterization.

A.4.2. Time-resolved Density Measurements

The potential performance of different plasma sources for ambient desorption/ionization may be related to time-averaged number density calculations. But more information regarding the discharge mechanisms of each plasma design was obtained from time-resolved absorbance measurements. For instance, three of the four plasmas investigated were operated using AC excitation, known in DBD devices to periodically generate plasma discharge "bullets" synchronous the applied voltage waveform [165-168]. As it was not practical to scan over all three transitions to study this behavior as done for time-averaged mode, time-resolved measurements were conducted by tuning the laser to excite only the largest transition peak while transmitted signal intensity was monitored as a function of time.

HF-DBD Results

Signal was recorded at a site 0.5 mm downstream from the capillary exit in the HF-DBD plasma plume. Seen in Figure A.8, the bold absorbance traces are overlaid on the AC voltage waveform. The absorbance signal cycle indicates that plasma "bullets" were being generated at half the frequency of the voltage waveform. This particular phenomenon has not been reported before, and the pattern may be an outcome specific for the HF-DBD source electrode geometry and operating frequency. Previous measurements have suffered an artifact[157] produced by the occasional single-cycle gap between bullets, in which averaging synchronized with the voltage waveform convolutes

signal modulation with the voltage frequency to half the full depth of modulation. In Figure A.8, the signal rise times were limited by the bandwidth of the amplifier, while the peak fall times were close the voltage waveform period (3-4 µs). These results are for an HF-DBD with maximum power coupling between the discharge and supply. Detuning the frequency produced more erratic signal patterns until the plasma was extinguished at half the optimum RF frequency. No settings afforded an absorbance maximum cyclically-aligned with the voltage waveform. At this stage of understanding, the time-resolved behavior observed is simply a curiosity that does not markedly impact the efficacy of the HF-DBD as a stable discharge ion source for mass spectrometry.

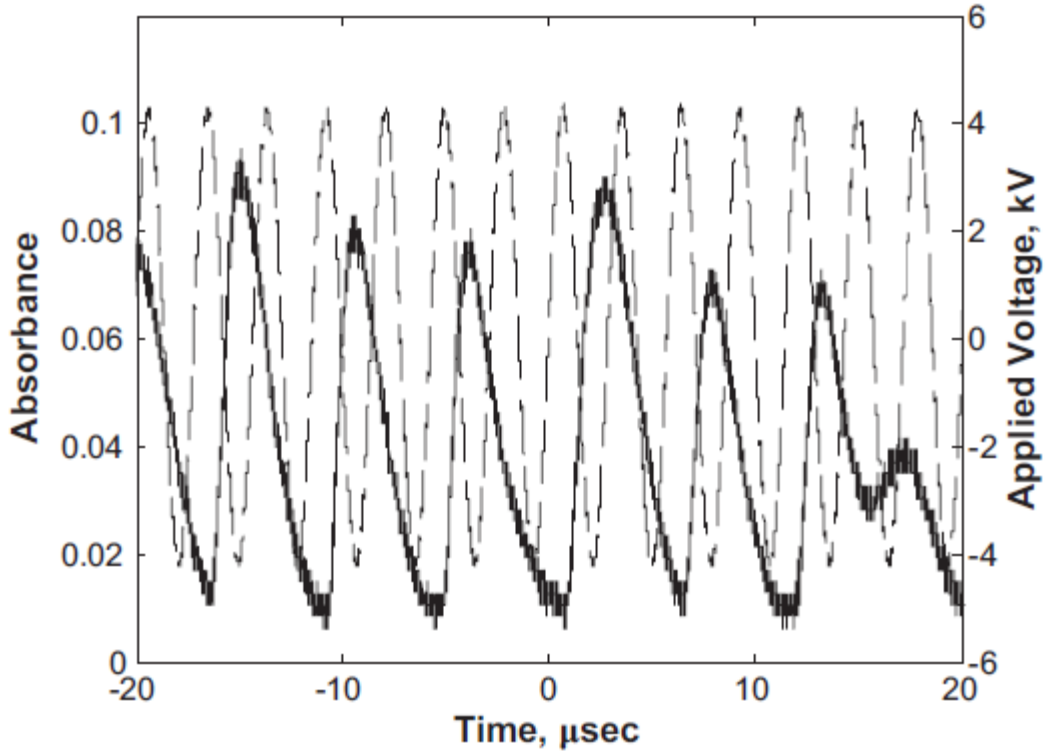

Figure A.8: Time-resolved absorbance measured in the HF-DBD afterglow 0.5 mm downstream from the capillary exit. The dashed trace is the applied voltage waveform from the power supply and the bold signal trace is the HF-DBD absorbance.

LTP Results

The time-resolved absorbance trends observed for an LTP are presented in Figure A.9. As with the HF-DBD, signal pulses for the metastable transitions were not

synchronous with the voltage waveform, and were highly imperfect. A regular absorbance peak was seen during the rising slope of the negative half cycle, while 1-3 peaks with varying intensities emerged inconsistently on the falling edge of the positive half cycle. The pulse rise times were again limited by amplifier bandwidth, and the fall times (6 µs) were longer than those for the HF-DBD signals. This subtle difference in pulse width may be related to the larger dimensions of the LTP discharge. More significant is the difference in duty cycle between the HF-DBD and LTP, with the much lower duty cycle of the LTP reflected by the comparatively low time-averaged He_m number densities. While this is not a direct performance indicator, the higher powers and frequencies used in DBD sources are suspected to benefit ionization efficiency relative to LTP.

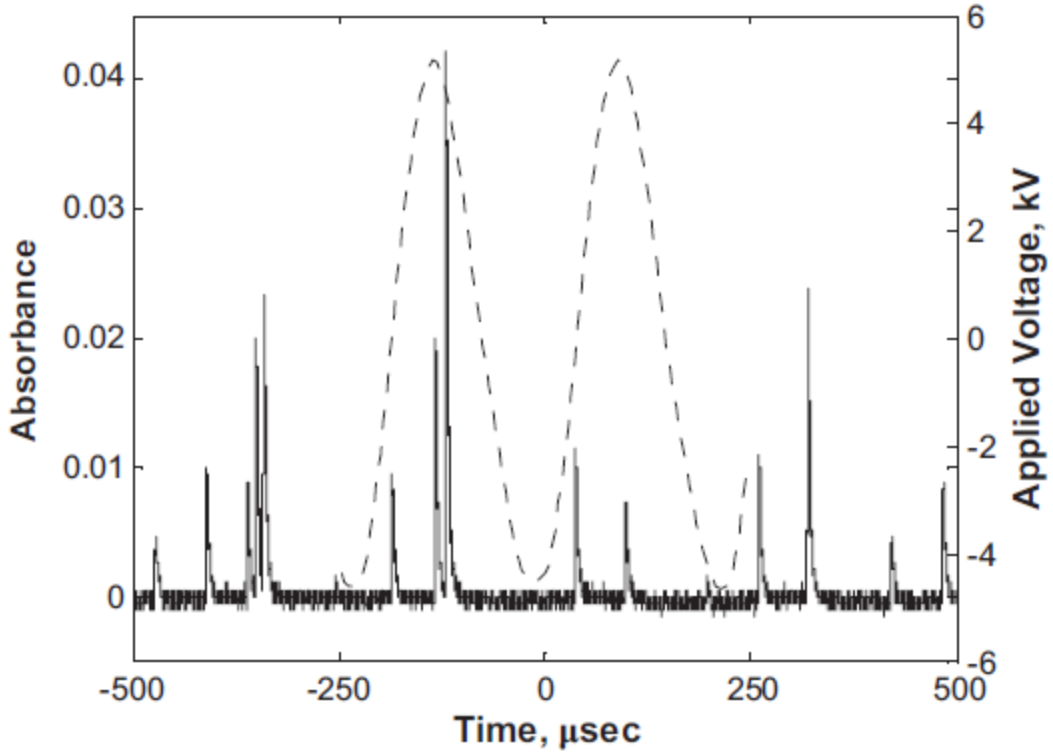

Figure A.9: Time-resolved absorbance measured for the LTP plasma plume 0.5 mm downstream from the capillary exit. The dashed trace is the applied voltage waveform from the power supply and the bold signal trace is the LTP absorbance.

Glow Discharge Results

The DC glow discharge generated a low, but constant density of He_m when measuring at the midpoint of the positive discharge column between electrodes, and the signal absorbance relative to a continuous DC potential was unexceptional. The absorbance profile observed for the AC-driven glow discharge inter-electrode region is shown in Figure A.10. The signal trace conveys a steady-state density of metastable helium atoms, resembling the stable DC excitation, but with frequency fluctuations of the applied voltage waveform superimposed. The uncharacteristic absorbance behaviors discovered for DBD and LTP plasmas were not observed for the glow discharges.

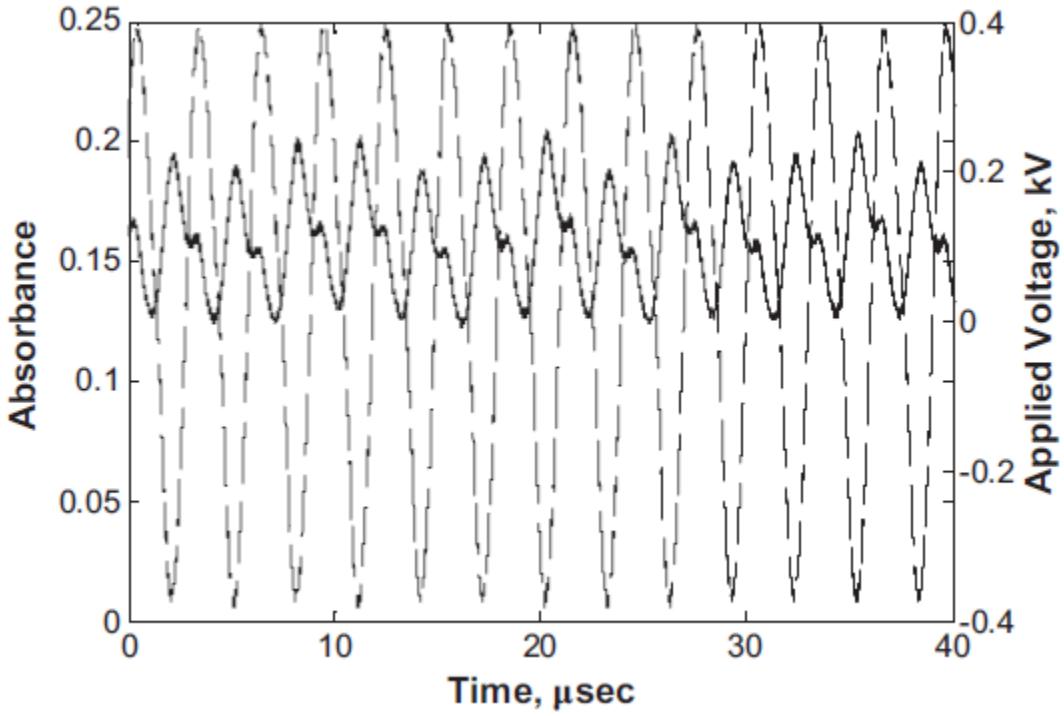

Figure A.10: Time-resolved absorbance measured for the AC-excited glow discharge midway between electrodes. The dashed trace is the applied voltage waveform from the power supply and the bold signal trace is the plasma absorbance.

A.4.3. Limiting Reagent Determination

The ambient ionization pathway proposed for plasma discharge sources encompasses a chain of reactions involving several atmospheric constituents[34]. By its

very nature, the term “ambient” suggests environmental conditions that are uncontrolled, and variations in the concentration and reactivity of atmospheric molecules essential to the mechanism is a cause for concern, especially if reproducible analysis is desired. For example, protonated water clusters are assumed to be primary charge transfer reagents during ionization, but the density of water vapor can vary by an order of magnitude depending on location and day-to-day weather conditions. If too few reactant molecules are available in the atmosphere, enhancing ionization by increasing the He_m number density becomes moot.

Therefore, to quickly validate the conjecture that He_m are limiting reagents under ambient conditions, the concentrations of atmospheric N_2 and H_2O were estimated using the ideal gas law with experimental and reported values. At 1 atmosphere of pressure and for the relatively low plasma rotational temperatures between 250 K and 550 K [33], discharge gas densities are on the order of 10^{19} cm^{-3}. Helium metastable concentrations are present under these conditions in the ppm range, on par with the typical level of impurities in the ultra-high purity helium source gas. Both N_2 and H_2O (at 30% humidity) at room temperature are expected to be present in densities of ~2 x 10^{19} cm^{-3} and ~2 x 10^{17} cm^{-3}, respectively, which are in huge excess over the predicted He_m population. Clearly, helium metastable atoms are the limiting reagents for the proposed ionization mechanisms, but other factors affecting this claim are purity of the support gas and effectiveness of gas mixing/residence time for reactions. Some of these fluid dynamics aspects were investigated in Chapter 2 of this dissertation.

A.5. Conclusion

Four common constructs for helium-based plasma discharge devices were studied. Atomic absorbance spectroscopy was used to ascertain the number densities of helium metastable atoms generated by each discharge and these values were qualitatively correlated with their potential performance capabilities as ambient desorption/ionization

sources for mass spectrometry. The HF-DBD was found to produce the largest He_m density in the afterglow plume, owing to higher operating powers and smaller device dimensions. Although similar to the HF-DBD, the LTP operated with a lower frequency and duty cycle than the HF-DBD, resulting in lower metastable number densities. The point-to-plane glow discharge generated a He_m concentration ~6 times higher using RF excitation versus continuous DC excitation, but densities were still less than half that of the HF-DBD. Number densities could only be measured in the inter-electrode plasma region for the glow discharges, as low absorbances in source gas beyond the capillary electrode suggested highly efficient metastable quenching. These findings beget more questions regarding the fate of the helium metastable atom in the downstream afterglow which can be answered by spectrometric analysis of product species formed later in the ambient ionization cascade. Lastly, the metastable abundances reported here are only one determinant of source performance, and a truer measure of capability should include ion flux and analyte sensitivity measurements confirmed by mass spectrometry.

APPENDIX B. Microplasma Ionization of Volatile Organics for Air/Water Contaminant Analysis Aboard the International Space Station

Adapted from

Bernier, M. C.; Alberici, R. M.; Keelor, J. D.; Dwivedi, P.; Zambrzycki, S. C.; Wallace, W. T.; Gazda, D. B.; Limero, T. F.; Symonds, J. M.; Orlando, T. M.; Macatangay, A. Fernández, F. M. *J. Am. Soc. Mass Spectrom.* **2016**, *27*(7), 1203-10.

B.1. Abstract

A microhollow cathode discharge (MHCD) device was developed as an ultra-portable, high-efficiency ion source alternative for MS-based environmental monitoring on board the International Space Station (ISS). MHCD performance was characterized for different working gas compositions and flow rates, the source power requirements, and device longevity while sampling target volatile organics. Sensitivity and specificity for analytes using the MHCD prototype were compared with results obtained using a standard commercial DART plasma source.

B.2. Introduction

There is growing incentive to design not only more powerful MS instruments, but also more compact and versatile systems to allow new and broader applications. The advent of both ambient plasma ionization techniques and miniaturized MS detector technologies has increased the utility of MS for *in situ* environmental monitoring, with one outstanding example being contaminant analysis aboard manned spacecraft. The International Space Station is a hyper-enclosed, highly-regulated environment with strict standards for the concentration of low-molecular-weight polar organics which can accumulate over time and endanger health of personnel. Part-per-million (ppm) level

detection of toxins in cabin air has been routinely performed using gas chromatography and differential mobility spectrometry[169], Fourier-transform infrared spectroscopy[170], or miniaturized mass spectrometry[171], while water analysis for total carbon and biocide concentrations has relied on a separate suite of methods involving heated UV/persulfate oxidation[172] and solid-phase extraction/colorimetric spectroscopy[173]. Problematically, comprehensive air/water analysis has required a return to atmosphere as the gamut of these specialized laboratory techniques are not yet sustainable in-flight and are limited by weight, power, cost, safety, etc. The desire remains to consolidate platforms for simultaneous air and water analysis and/or increase the specificity and sensitivity of current analyzer technologies to facilitate real-time interpretation.

Modern MS interfaces have become more accessible to accommodate ambient desorption/ionization sources, simplifying introduction for a diversity of sample formats. In a previous companion study, a new sampling strategy was reported which implemented a novel ETV (electrothermal vaporization) module paired with a DART plasma discharge source coupled to a time-of-flight mass analyzer[110]. This technique was shown to enhance sensitivity and reproducibility during screening of ISS volatile organics, but suffered from disadvantages related to power and bulk. Presented here, the next phase of ion source modification/development was focused on minimizing spatial requirements and lowering power/gas resource consumption using a MHCD microplasma discharge. These sub-millimeter scale "cold" plasmas[174] have a history of use as sources for emission spectroscopy[175, 176] and have been employed recently as discharge ionization and vacuum ultraviolet (VUV) photoionization sources with MS[177-179]. Advantageously, microplasma devices can be fabricated with greatly reduced dimensions and power requirements over conventional ambient plasma techniques[180, 181] for increased fieldability in sensing applications[182-186] without sacrificing functionality. The MHCD source performance for screening volatile organics was compared with the performance of a DART ion source using conventional ambient plasma sampling

practices. To the best of our knowledge, this study marks the first attempt to evaluate the efficacy of an MHCD device for environmental analysis important to space exploration.

B.3. Experimental

B.3.1. MHCD Microplasma

Figure B.1 depicts the components and dimensions of our MHCD device along with illustration of microplasma operation. The MHCD prototype was constructed using a metal-insulator-metal dielectric barrier configuration, with molybdenum foil disk electrodes (*dia.* = 8 mm, *h* = 100 µm) separated by a mica insulating disk (*dia.* = 10 mm, *h* = 100 µm). Each disk was perforated at the center by laser etching, forming a 300 µm cylindrical-volume discharge cavity when aligned and stacked. The disks were secured inside an aluminum and PEEK screw-capsule housing, with a ¼" gas input connection on the back half capsule and a threaded electrode contact to the front electrode below the cavity exit orifice on the front half capsule. The MHCD discharge was powered using a PS350/5000V V-25 W high voltage DC supply (Standford Research Systems, Inc., Sunnyvale, CA, USA). Depending on the source gas used, potentials between +600-2400 V were applied to the front Mo electrode. The electrode was connected in series with a 20 MΩ ballast resistor, which helped to sustain the discharge with a current of 30-120 µA. Device power was estimated at 0.1 W when using nitrogen gas, and far less when using alternative argon and helium source gases (0.100-1.0 L min^{-1}). In all experiments, the source was placed at an interface distance of 4 mm apart and on axis with spectrometer inlet, where the maximum population of protonated reactant ion clusters $(H_2O)_nH^+$ were observed.

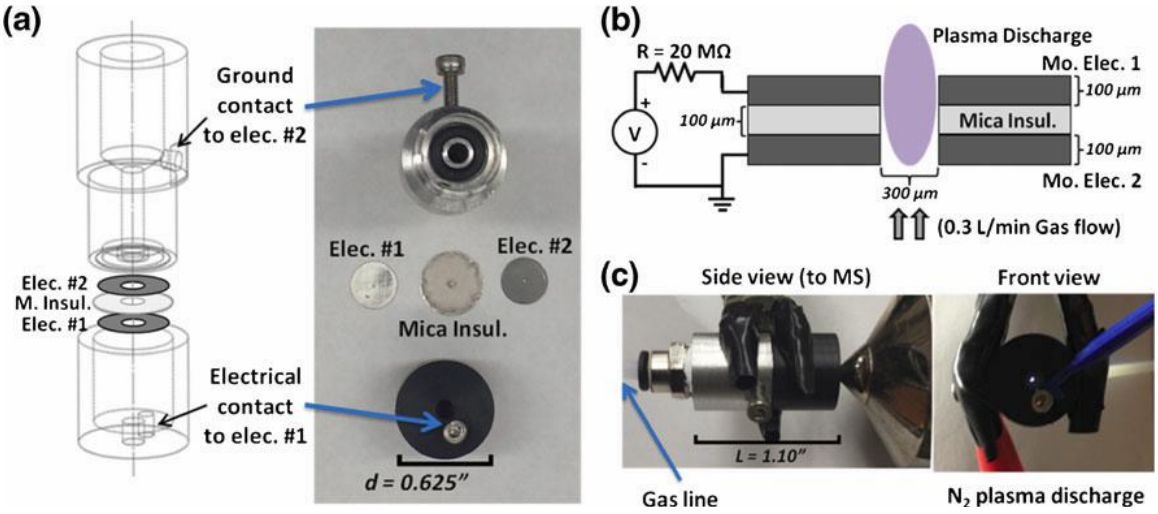

Figure B.1: Schematics and images of the metal-insulator-metal (MIM) microhollow cathode discharge (MHCD) microplasma device. Detailed component breakdown of the MHCD assembly (**a**). Side-view (**b**) and front-view (**c**) of the source showing an active discharge plasma in operation using 0.3 L min^{-1} nitrogen gas.

B.3.2. Direct Analysis in Real Time

The DART-SVP ion source (IonSense Inc., Saugus, MA, USA) has been described in detail previously. In short, the DART source uses a point-to-plane discharge motif, with a negatively-biased point electrode spaced ≤1 mm from a grounded disk electrode. A DC potential of several kV is applied to the point electrode through a ballast resistor (500 kΩ-1 MΩ) to produce a glow discharge ranging from 0.5-10 mA depending on the working gas used, helium or nitrogen. Effective electrode potentials measured with a HV probe (Fluke 179 True RMS multimeter) for different source gases were approximately -400 V for helium/argon and -1850 V for nitrogen, affording a range of possible plasma powers (0.1-10 W). The DART discharge chamber is recessed several centimeters from the source exit by a ceramic heating element, which is capped at the outlet by a Mo grid electrode (+200 V). The grid serves to filter primary ions from the discharge ensuring metastable atoms are the active reagents in the expelled afterglow gas. When operating DART in this work, the ceramic heater was left off for a truer measure of plasma efficiency compared to the MHCD. Additionally, thermal desorption was also not

a priority for volatile analytes of interest and would only contribute to power requirements. DART gas flow rates were varied from 0.15 L min^{-1}, comparable to MHCD settings, up to a more standard DART flow rate of 2.0 L min^{-1}. The DART exit nozzle was positioned on-axis 5-8 mm away from the MS skimmer orifice during experiments, where the maximum reactant ion intensity was again observed.

B.3.3. TOF MS Instrumentation

All mass spectra were collected on a JMS-T100LC AccuTOF orthogonal time-of-flight mass spectrometer (JEOL, Inc., Peabody, MA, USA). The instrument was tuned to detect a low mass range of 10-300 Da. The orifice temperature was maintained at 100℃ and inlet ion optics settings were optimized to minimize in-source fragmentation (Orifice #1: 10 V; Ring Lens: 6 V; Orifice #2: 2 V). The ion guide RF voltage was fixed at 200 V, with the guide reference voltage set to -29 V, the pusher bias voltage at -0.28 V, and MCP detector at 2650 V. Mass resolutions between 1700 and 4100 (FWHM) were possible for the target analytes measured with the 18-121 Da mass range.

B.4. Results and Discussion

B.4.1. General MHCD Performance and Comparison with DART

DART and MHCD source capabilities were quickly assessed from the qualitative survey of spectra presented in Figure B.2, showing the reactant ion populations and distribution of analyte ion species produced by each device using nitrogen source gas. Evident in spectrum panel (a) of Figure B.2, the only background ions observed for either source were protonated water clusters, with $[(H_2O)_2H]^+$ seen as the most intense species for both sources followed by the protonated water trimer. Analytes were introduced via glass capillary probes that were wetted from neat volatile solutions and inserted into the sample gap ~2 mm from the exit orifice of each source. Not surprisingly, protonated analyte clusters were the main ions observed for each of the alcohols and acetone.

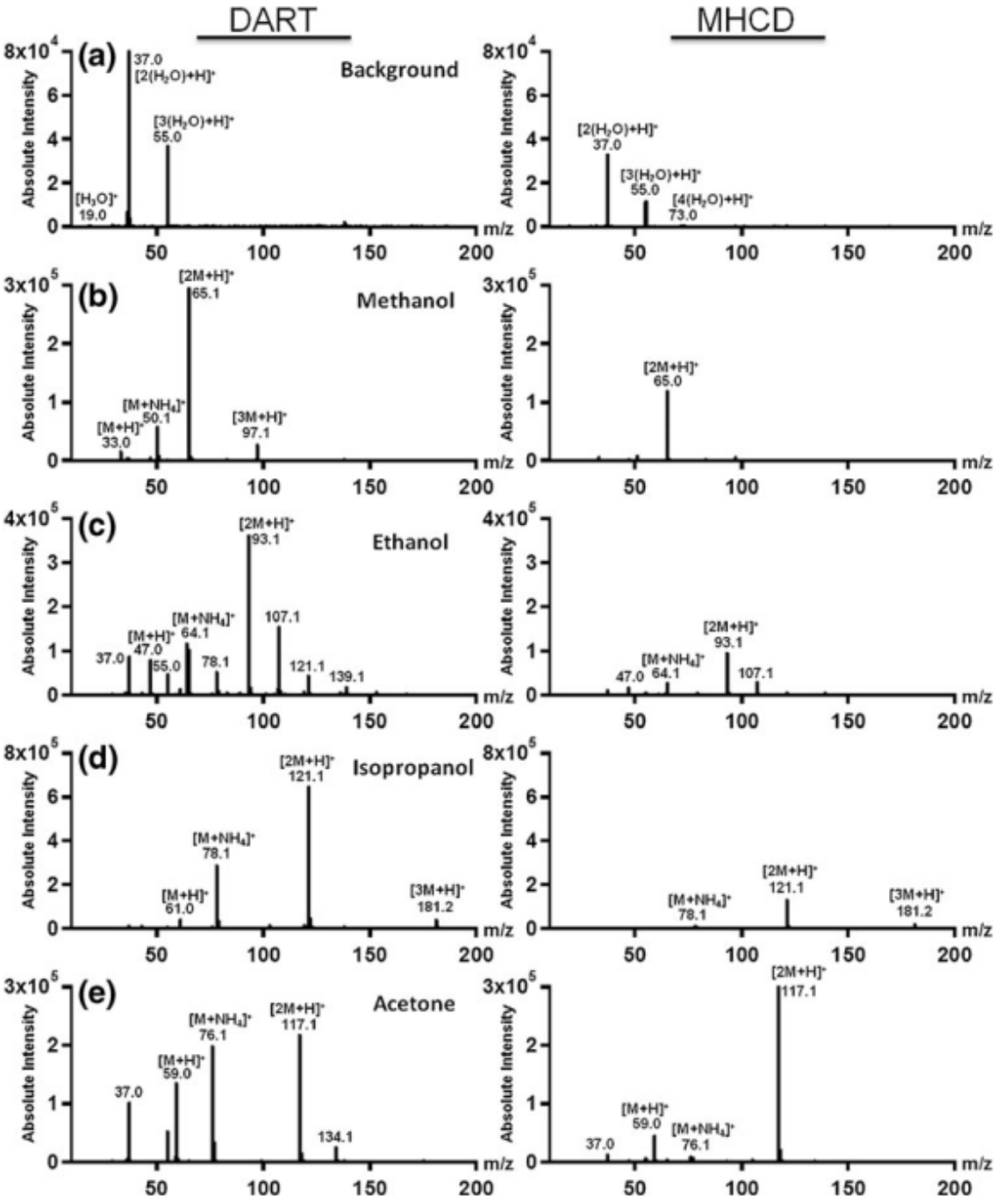

Figure B.2: Mass spectra of target ISS test analytes acquired using DART and MHCD microplasma ion sources with nitrogen source gas at 2.2 L min^{-1} and 0.5 L min^{-1}, respectively. Spectra for DART (left column) and MHCD (right column) are shown for background ions (**a**), methanol (**b**), ethanol w/ 0.5% IPA (**c**), isopropanol (**d**), and acetone (**e**).

The dominant species detected for each analyte in spectrum panels (b-e) of Figure B.2 was the protonated dimer, but in many cases, the trimers were seen as well. Interestingly, a measurable abundance of analyte adducts with ammonium were also observed, primarily with DART versus the MHCD. Given the lower ionization potential, IP (10.02 eV) and higher proton affinity, PA (~850 kJ mol^{-1}) of ammonium relative to the IP (12.62 eV) and PA (~690 kJ mol^{-1}) of water, the probability of ammonium formation is high[187]. Ammonium adducts were detected in the largest proportion relative to protonated dimers for acetone, whose ketone functionality may have helped to stabilize the adduct[188]. It is possible that the ammonium constituent was atmospheric in origin, but it is also suspected to be a downstream product generated by N_2 plasma discharges. For every sample, the highly clustered analyte moieties and survival of ammoniated adducts are attributed to the pure concentration of the samples and the low-energy spectrometer orifice settings used which reduced ion-adduct activation over the dissociation energy barrier.

To some advantage, the presence of several ion species for each volatile with characteristic or source specific distributions, e.g. protonated $[M+H]^+$, clustered $[nM+H]^+$, and adduct $[M+NH_4]^+$, could also facilitate analyte identification based on unique spectral fingerprints when using low mass resolution analyzers. Overall, all analyte signals appeared more intense for the DART source. This finding can be rationalized by the larger ion current of the DART glow discharge (mA) compared to the MHCD (µA), which should theoretically generate a larger number of active metastables. However, this claim requires spectroscopic validation to be certain. The higher volumetric flow rate of DART gas (2.2 L min^{-1}) into the sample region versus the MHCD (0.5 L min^{-1}) is also a consideration for the difference between sources. Furthermore, the greater linear velocity of the MHCD gas expelled from the 300 µm cavity produced a more turbulent jet that could corrupt some ion transport compared to the more laminar source gas profiles predicted for DART.

Despite a somewhat lower average signal intensity relative to DART, the estimated limits of detection for the MHCD device were on par with designated expectations for the ISS. Using a low source gas flow rate (0.100 L min^{-1}), and defining LODs as the minimum amount of material deposited on a borosilicate capillary probe, the values were found to be 3000 pmol (100 ppm) for methanol, 2000 pmol (100 ppm) for ethanol, 170 pmol (10 ppm) for isopropanol, and 430 pmol (25 ppm) for acetone. The Spacecraft Water Exposure Guideline (SWEG) specifies 100-day exposure limits of 40 ppm and 150 ppm for methanol and acetone[189, 190]. The condition for acetone was easily met, but the 2.5 times greater LOD for methanol from our experiments with the MHCD suggest that too much sample material can be lost using routine ambient sampling practices with capillary probes. To this effect, more controlled, standardized methods for sample introduction that will minimize fluid dynamic losses while enhancing residence time and sample/metastable gas interaction are being developed, similar to DART-ETV, in order to refine and satisfy the SWEG value LODs.

B.4.2. Effect of Gas Composition and Flow Rate

To qualify the viability of the MHCD as a suitable ion source for ISS applications, the device was tested using a select variety of operating gases at different flow rates to gauge what gains could be made regarding ionization efficiency, power/gas consumption, and source longevity. Figure B.3 shows mass spectra for the previous set of target volatiles using the nitrogen, argon, and helium MHCD gases. The optimal argon and nitrogen flow rates used (0.3 L min^{-1} and 0.5 L min^{-1}, respectively) were substantially lower compared to the optimal helium flow rate (1.0 L min^{-1}). It is suspected that the larger gas densities for argon and nitrogen worked to destabilize the MHCD discharge at higher flow rates, likely as a result of fluctuating cavity pressures altering the breakdown potential. The MHCD plasma current was fixed at 0.050 mA in this scenario to ensure

similar power discharges for each gas, and the mass spectrometer orifice voltages were kept low as before to minimize the likelihood of in-source fragmentation.

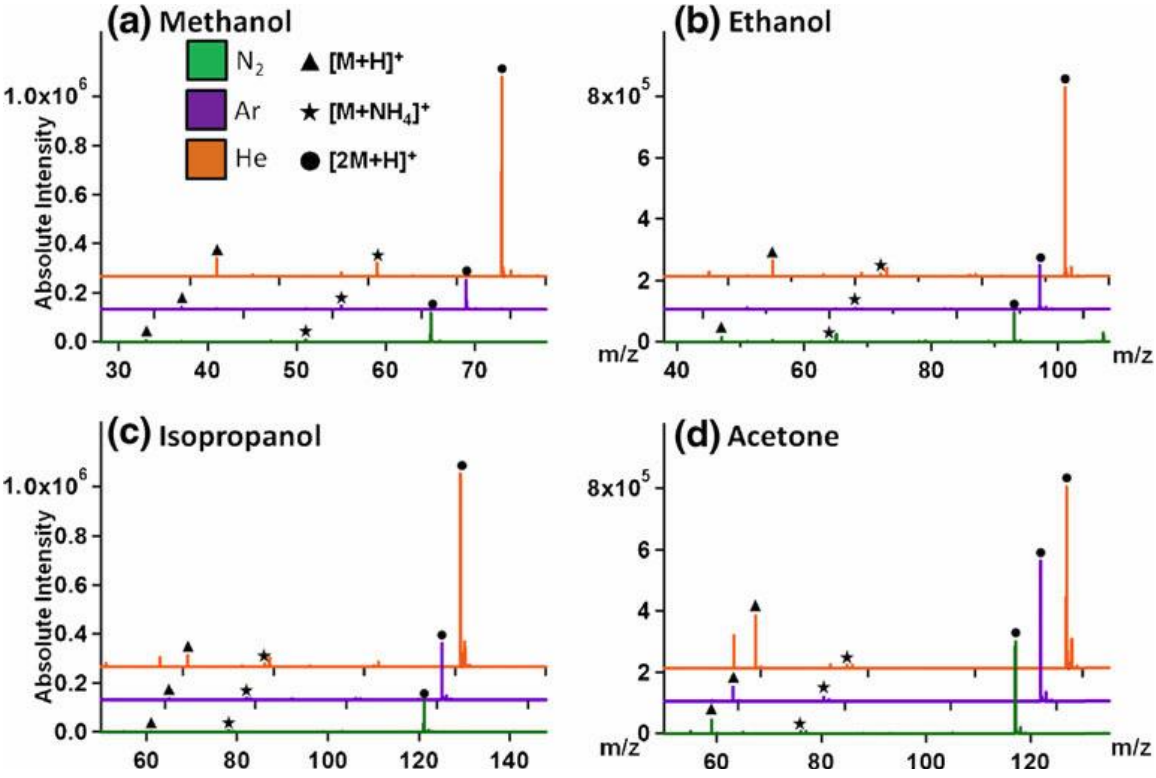

Figure B.3: Microplasma mass spectra for volatile analytes methanol (**a**), ethanol (**b**), isopropanol (**c**), and acetone (**d**). Spectra were acquired using nitrogen (green), Ar (purple), and He (orange) discharge gases at optimized flow rates of 1.0, 0.3, and 0.5 L min^{-1}, respectively, and plasma currents of 0.050 mA for all gases. Identified species are indicated by markers, showing $[M+H]^+$ (black triangles), $[M+NH_4]^+$ (black stars), and $[2M+H]^+$ (black circles). Spectra are an average of three trials collected from one total ion chronogram taken over multiple insertions of capillary probes carrying volatile sample.

Consistent with the results in Figure B.2 and also between all gas types used, the most abundant species observed for each analyte was the protonated dimer $[2M+H]^+$, followed by much lower signals for the protonated monomer $[M+H]^+$ and ammonium adduct $[M+NH_4]^+$. As anticipated, the largest signal intensities in Figure B.3 spectra (a)-(d) were seen for the helium plasma. Helium generates much higher energy metastables (19.8-20.6 eV) compared to nitrogen and argon (≤11.6 eV for both), and was also used at a higher flow rate relative to the other gases[33, 140, 143]. Also partially significant is the

higher heat capacity and thermal conductivity of helium, which could contribute to a hotter plasma gas assisting thermal desorption of the analytes. The dimer intensities were most similar between source gases in spectrum (d) of Figure B.3, which can be reasoned to some extent by the much higher partial pressure for acetone (0.53 atm) over the alcohols (≤0.17 atm), which could have more effectively saturated the ionization region.

The MHCD and DART gas flow rates had a significant impact on the ionization and transport efficiency for either source, particularly in the case of DART where the plasma discharge is remote from the mass spectrometer inlet compared to the proximate placement of the MHCD. Figure B.4 highlights the changes in signal intensity for the majority protonated dimer species observed for every analyte using a range of flow rates for nitrogen, argon, and helium support gases. In all examples, dimer signal intensities were highest for helium plasmas considering the reasons proposed above with Figure B.3.

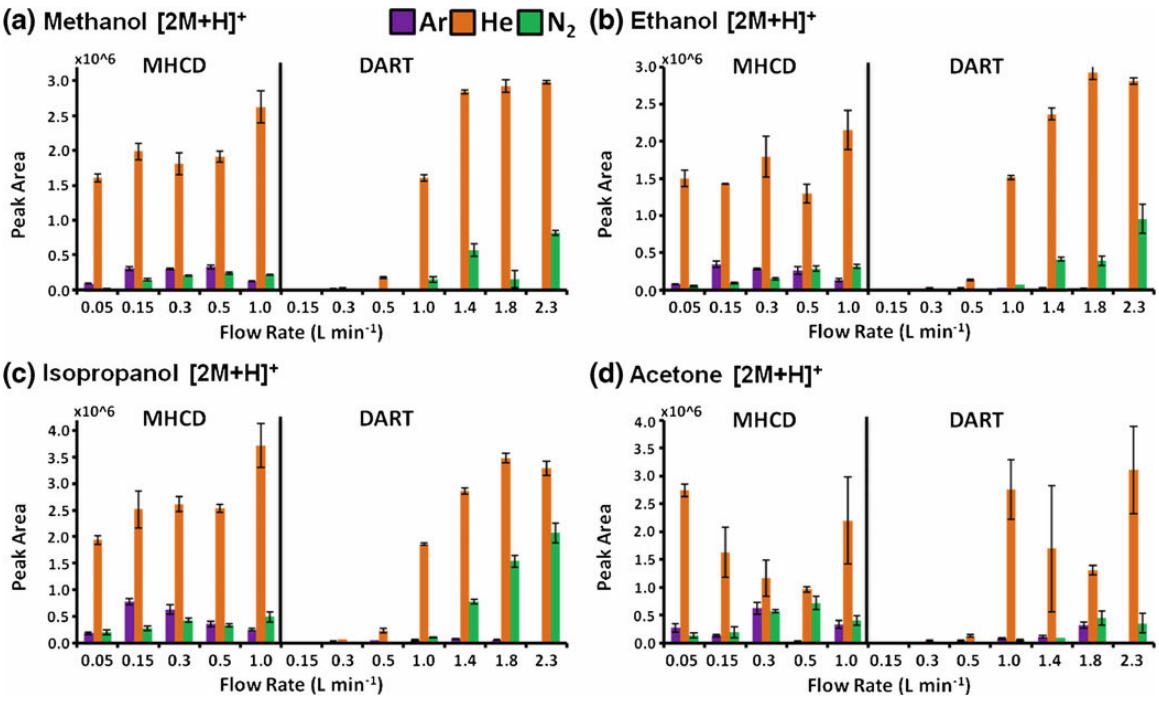

Figure B.4: Peak areas of the $[2M+H]^+$ species detected for methanol (**a**), ethanol (**b**), isopropanol (**c**), and acetone (**d**) using argon (purple), helium (orange), and nitrogen (green) gases with the MHCD (left) and DART (right) source. Flow rates were 0.05, 0.15, 0.3, 0.5, and 1.0 L min^{-1} for the MHCD and 0.15, 0.3, 0.5, 1.0, 1.4, 1.8, and 2.2 L min^{-1} for DART. Error bars were derived from the standard deviation of three trials.

The results for the alcohol analytes in Figure B.4 spectra (a)-(c) are very similar, with signal for the MHCD seen to gradually improve as helium flow rates were increased from 0.05 L min^{-1} up to 1.0 L min^{-1}. Meanwhile, the signal intensities using argon and nitrogen were not only far lower than helium as predicted, but also fairly constant regardless of flow rate, and more or less equal between the two gases. The effect of gas flow rate was much more obvious looking at the alcohol signal intensities for the DART source. For helium and nitrogen, measureable signal intensities increased rapidly above 0.5 L min^{-1} and began to plateau around 1.5 L min^{-1}, again with signal for helium gas superior to signal for nitrogen. However, higher intensities were achieved for nitrogen discharges with DART compared to the MHCD using higher gas flow rates, while regardless of argon flow rate, the DART signal was largely undetectable. This observation is largely explained by the additional distance of the DART discharge chamber from the AP interface, where at flow rates used for the MHCD, the afterglow was susceptible to metastable depletion prior to being expelled into the sample gap. This phenomenon was particularly true for denser argon gas, and diatomic nitrogen, which has available modes of electronic-vibrational relaxation.

While the arguments for MHCD and DART source performance hold true, the signal trend seen for acetone in Figure B.4 spectrum (d) using helium was notably different than the trend seen for the alcohols. Interestingly, signal intensity for acetone was largest for either the lowest or highest MHCD flow rates used (0.05 L min^{-1} and 1.0 L min^{-1}), similar to DART for flow rates between 1.0 L min^{-1} and 2.3 L min^{-1}. This swing in signal may be due to a shift between vacuum-governed mass transport at the spectrometer inlet at low flow rates and transmission dictated by the source gas flow profile with higher flow rates. Sensitivity for acetone using nitrogen and argon source gases was greater and also more consistent with MHCD versus DART. Summarily, the MHCD is able to provide nearly equivalent signal to DART at a fraction of the gas cost, making the device and attractive alternative in resource-limited circumstances.

B.4.3. Device Power and Lifetime

An ideal source for dependable and routine analysis aboard the ISS would not only balance resource cost and operation efficiency, but remain durable over continuous or long term use. MHCD longevity was mainly influenced by the device *I/V* characteristics, plasma support gas type and flow rate, and the electrode materials. Figure B.5 depicts the power curves for the MHCD plasma using nitrogen, helium, and argon discharge gases. The onset potentials necessary to sustain a plasma were much higher for nitrogen than for helium and argon, which exhibited nearly identical breakdown behavior. While the power requirements were higher for nitrogen, the device lifetimes were atypically longer than for the lower power helium discharge. At device currents above 0.120 mA, the MHCD helium plasma could be maintained for only 2-4 hours before electrode deterioration and irreversible performance degradation. The advanced deterioration rate with helium is likely a symptom of electrode sputtering incited by higher energy metastables and a "hotter" plasma discharge owing the gas thermal conductivity. Constant operation at the same current using nitrogen or argon could be accomplished for over 24 hours with no evidence of wear. Moreover, MHCD lifetimes could be extended over 100 hours for all plasma gas types if the device was operated at lower powers ($\leq$50 μA) or the plasma activity was not continuous. Future experiments will attempt to drive the MHCD source using AC waveforms instead of a DC potential to reduce sputtering and prolong lifetimes[191]. A nitrogen-based MHCD plasma would provide the best balance between reliability, cost, and efficiency, notwithstanding the slightly higher power draw.

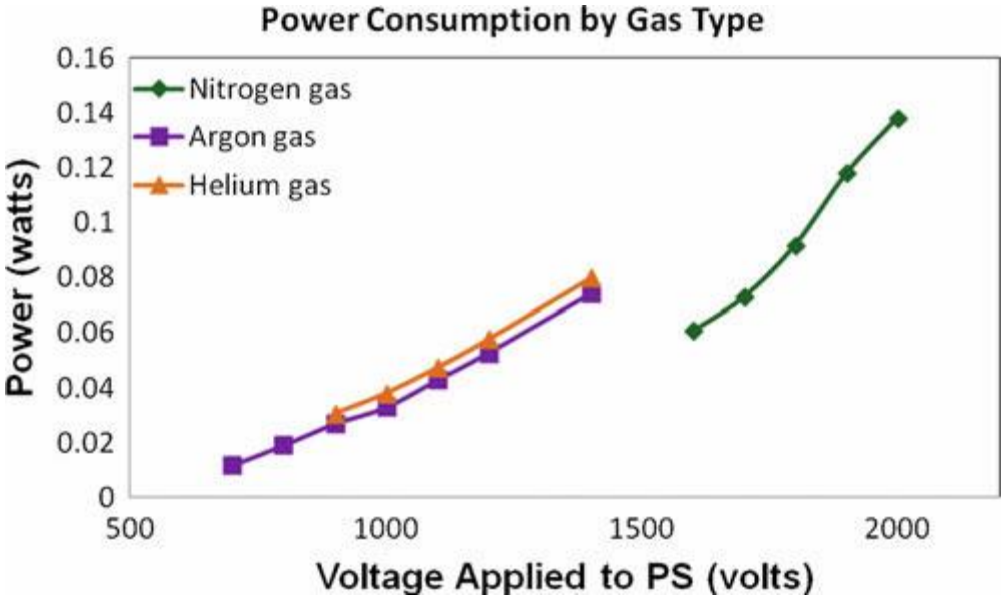

Figure B.5: MHCD microplasma power consumption as a function of plasma gas type for a constant gas flow rate (0.100 L min^{-1}) using nitrogen highlighted in green (diamonds), argon highlighted in purple (squares), and helium highlighted in orange (triangles).

B.5. Conclusion

The feasibility of a compact, field-ready MHCD ion source prototype for monitoring of low molecular weight organics via mass spectrometry was demonstrated. Device efficiency was evaluated based on the resource requirements and measured analyte abundances compared to a commercial DART ion source. The main detected species for every analyte was the protonated dimer $[2M+H]^+$, but the protonated monomer $[M+H]^+$, protonated timer $[3M+H]^+$, and ammonium adduct $[M+NH_4]^+$ were also seen in some instances. Operation with helium gas produced the greatest signal intensities for either source; however, the MHCD was prone to degradation using helium even at lower discharge powers. Although less intense, MHCD signal with nitrogen or argon plasma gas was nearly equivalent between gases. Even with the slightly elevated breakdown potential, nitrogen appeared to offer the best balance between gas flow rate and ionization efficiency, and was also capable of producing spectra with the greatest diversity of analytes for fingerprinting. Overall, sensitivity for the examined volatiles was

very similar between the MHCD and DART sources following optimization, and the conservative power/gas consumption with the MHCD for equivalent performance makes it an attractive alternative for portable applications.

APPENDIX C. Design and Construction of a Resistive Glass Dual-Gate AP-DTIMS Prototype

C.1 Abstract

This chapter provides a summary of the progress toward development of a monolithic resistive glass AP-DTIMS. It highlights changes made to a prototype commercial DTIMS detector modeled after the unit described previously in Chapter 4, involving addition of a second ion gate and anode/amplifier modifications to reduce Faraday noise and permit coupling with Orbitrap MS. Preliminary performance and operational characteristics of the dual-gate prototype in fixed-gate mode is showcased.

C.2. Introduction

The qualities of resistive glass elements for ion containment and transport have already been introduced in Chapter 4 when describing a standalone DTIM detector. Traditionally employed in photodiodes, these resistive glass materials are now used as MS ion optic components like inlet transfer capillaries[192], ion guides, drift tube ion mobility cells, collision gas stages, and ToF reflectron lenses[193]. The lead silicates, reduced in a hydrogen atmosphere to produce semiconductive layers[194], can be manufactured in a range of custom sizes and dimensions, are fairly robust to high temperatures (400℃) and mechanical abrasion, possess long-term stability in vacuum or nitrogen atmospheres, and can be tuned during fabrication to low (10^5-10^9 Ω) or high (10^9-10^{11} Ω) resistances[195]. Although, the most desirable attribute as it pertains to ion transmission for ion mobility applications is the electric field homogeneity offered by the monolithic glass body, confirmed by Kelvin probe measurements of the interior surface layer resistance uniformity (1-2.5% variation) and conductivity showing negligible surface charging[196, 197]. Compared to the more common stacked-ring electrode drift tube

motifs, the radial electric field homogeneity of the resistive glass potentially translates to improved ion mobility resolving power by mitigating uneven electric field influences on ion internal energies and minimizing diffusion broadening effects on the ion packet fringes. A further advantage, when serving as mobility cells, the glass tubes are self-contained and do not require secondary sealed enclosures to retain buffer gases like older stacked-ring models. Here, work has begun on assembly of a dual-gate resistive glass AP-DTIMS as a potentially higher resolution alternative to the commercial EXCELLIMS unit characterized for DTIMS-Orbitrap MS in Chapter 5, with over twice the drift length and very good axial confinement of the radial ion density within ~1 cm. The steps taken toward constructing the prototype are outlined regarding the second gate and anode modifications required for MS compatibility, and AP-DTIMS operation for a fixed-gate Faraday acquisition is quickly demonstrated.

C.3. Experimental

The base construction for the dual-gate DTIMS comprised a commercial prototype unit manufactured by PHOTONIS, USA (Sturbridge, MA). The dimensions of the resistive glass desolvation and drift cells were nearly identical to those detailed for the older standalone DTIMS in Chapter 4, possessing lengths of 11 cm and 25 cm, respectively, and an *i.d.* = 3 cm. Both cells were aligned in PEEK block mounts with support rails. The first photo-etched Bradbury-Nielsen gate (wire spacing: ~500 μm) was positioned between the desolvation and drift cells as before. The drift cell terminus was modified to include a custom-designed PEEK assembly that housed the second identical BN gate and an aperture mesh screen spaced ~1 mm behind. The small collection of new pieces designed and machined are shown in Figure C.1, comprising a PEEK block mount for the end of the drift cell, a PEEK adapter ring to hold the second gate and fasten the detector amplifier unit, PEEK spacers to brace the new hollow-core Faraday plate, and a

new cylindrical aluminum anode casing. PEEK pieces were fashioned to dimensions matching the first ion gate and original anode adapter mounts.

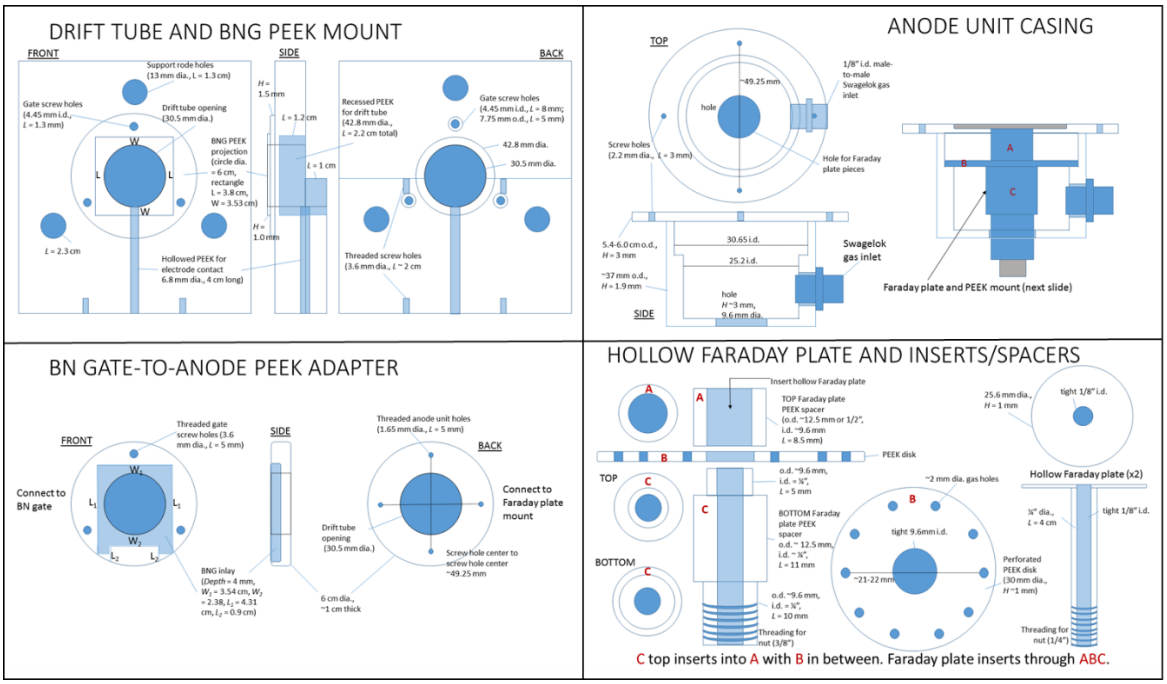

Figure C.1: Showcase of newly machined parts for dual-gate resistive glass AP-DTIMS.

The Faraday detector/amplifier module was reattached directly behind the second ion gate. The center of the aluminum Faraday plate (*o.d.* ~2.5 cm) was bored hollow (*i.d.*. ~1/8”) to allow insertion of an extended MS capillary, which can be passed through a machined opening made level with the Faraday plate central axis located on the back of the amplifier’s stainless steel shielding enclosure. Two E3630A 20 V DC power supplies (Agilent/Hewlett Packard) were used to provide voltage in CV mode (~12 V each) to the DTIMS internal Ultravolt 15FL12 HV biasing power supply, drift tube polyimide heating elements (Minco Products, Inc.), main voltage divider, first ion gate pulsing electronics, and optional high gain Faraday amplifier. Electrode contacts from the PHOTONIS voltage divider were connected at the entrance and exit openings of each glass cell, and to the pulsing electronics for each set of BNG wires on the first ion gate. In addition to grounding the amplifier casing, noise filtering capacitors (1 µF, 500-630 V) connecting to ground (0 V) were attached at the drift cell terminus and the aperture mesh to prevent

induced current saturation of the detector by electric field fluctuations during ion gate pulses. A pot tuner regulating the HV output voltage to the PHOTONIS divider was used to adjust DTIMS potential between 0-12.5 kV, while the aperture mesh was held at ~150 V using a PS3525/2500V-25W unit (Sandford Research Systems).

A secondary voltage divider with integrated gate pulsing electronics built by TOFWERK AG (Thun, Switzerland) was used to power and operate the second ion gate. The divider voltage was generated by a 20 kV HCL 14-20000 HV supply (FUG Elektronik GmbH) plugged into the 15 kV input, and the gate switch electronics were powered by an additional 24 V, 2.4 A custom DC power unit driving another internal 15FL24 HV biasing supply (Ultravolt). Separate output leads from gate ports #1 and #2 on the divider were connected to each of the second ion gate wire sets using shielded coaxial cables. An asymmetric potential was applied to each gate when "closed" (±70 for gate #1, ±35 for gate #2) and gates were floated at the divider potential when "open." TTL gate trigger pulses were delivered to each gate switch from a DG535 signal delay/pulse generator (Stanford Research Systems), using BNC channel A-B for gate #1 and BNC channel C-D for gate #2. Gate pulse widths were set to 200 µs for each gate at a frequency of ~10 Hz during fixed-gate Faraday acquisition. The custom TOFWERK amplifier used had a 250 µs rise time (10-90%), 0.1 pA mV^{-1} gain, and 2 pA noise level. Signal for 128 spectral averages was monitored on a TDS 2024 200 MHz oscilloscope (Tektronix). Dimethyl methylphosphonate (DMMP) acquired from Sigma-Aldrich (St. Louis, USA) was sampled as a vapor from neat (97%) solution. Ions were generated using a Tungsten point electrode as a corona discharge, elevated to a positive potential of ~15 kV in front of the IMS inlet with a 20 kV HCP 14-20000 HV supply (FUG Elektronik GmbH). The DTIMS was operated at ambient temperature and pressure. Setup and design details for the prototype are illustrated in Figure C.2.

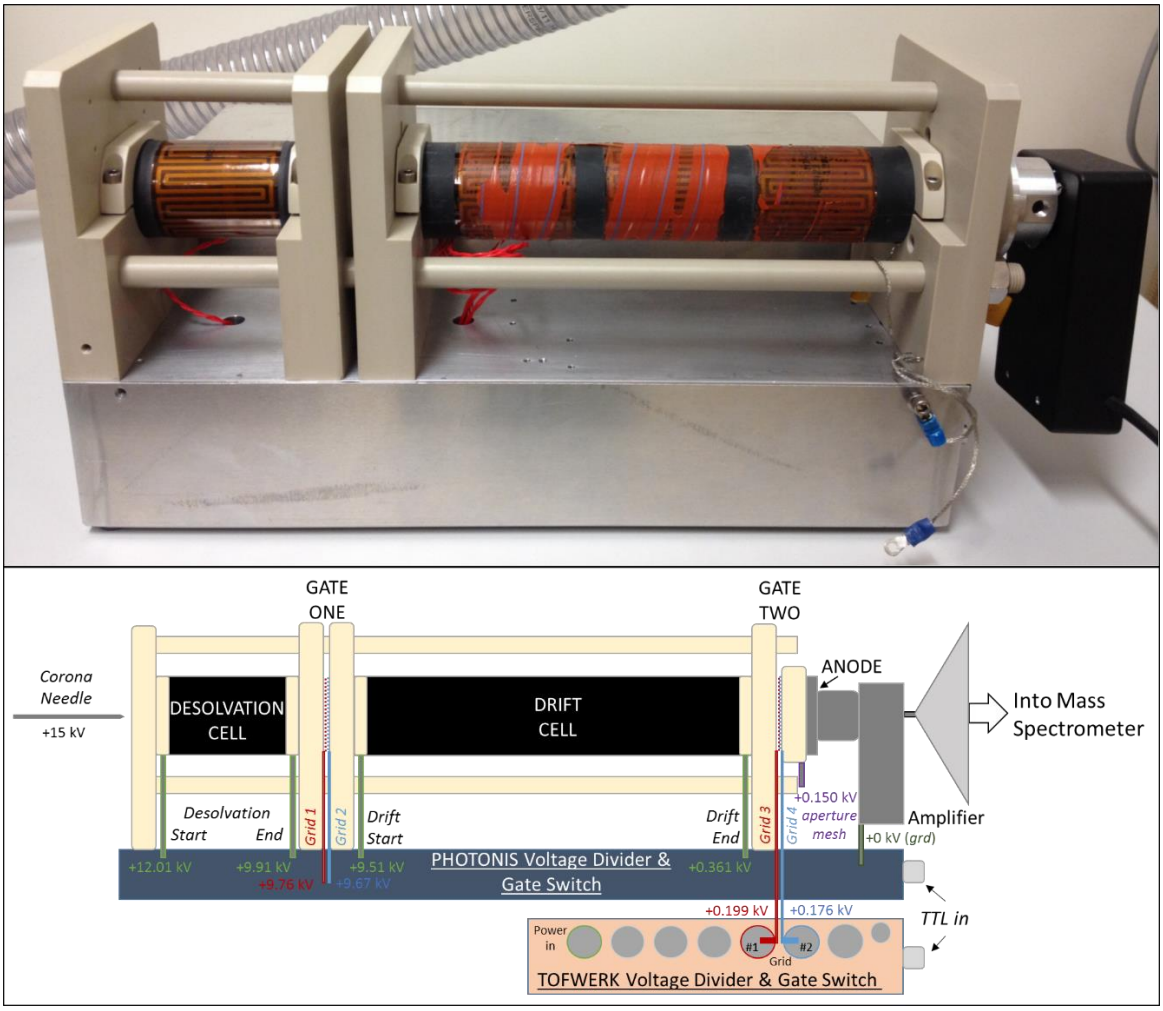

Figure C.2: Photograph (top) and cartoon schematic (bottom) of assembled dual-gate resistive glass AP-DTIMS prototype.

C.4. Preliminary Results

So far, most of the effort toward developing a dual-gate resistive glass AP-DTIMS has been dedicated to the design of new parts, construction of the instrument, and assessment of basic functionality. Following assembly, the DTIMS was operated in conventional (single gate) mode while a range of fixed potentials were applied to the second BNG to determine the window of voltages permitting ion transmission to the detector. Figure C.3 shows the Faraday responses for a corona discharge RIP (detected with the aperture mesh removed). The peak is abnormally broad and featureless since drift gas was not flowing the drift region was not heated to facilitate declustering. With

the gate wires held between 100 V and 300 V, Faraday signal intensity was the greatest. When applying no potential (0 V), a small signal hump appeared from partial ion transmission and a shadow voltage displayed on the power supply readout was induced by the ion current. Above +350 V, the ions were completely scattered and no signal was observed. The sinusoidal oscillations in the baseline are attributed to the gate acting as an antenna to amplify ambient periodic noise, which can be abated by extensive shielding and proper grounding of the whole gate switch circuit.

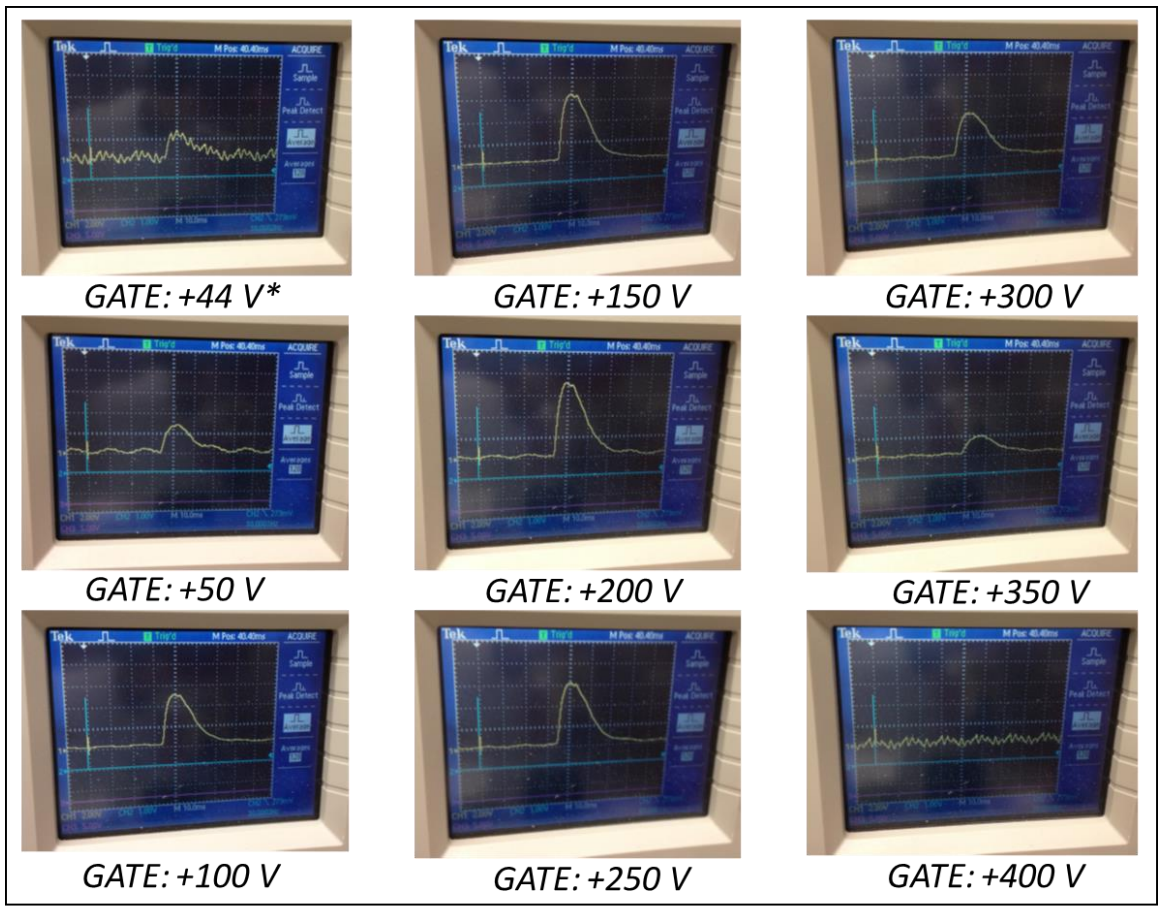

Figure C.3: Corona discharge RIP signal transmission with different fixed voltages applied to the second BNG. Faraday response observed without drift gas or heating.

In order to test the gate switch function, the second BNG was then configured to operate in fixed-gate acquisition mode by pulsing open over a window centered on the drift time of the RIP peak (t~40 ms). Upon triggering the second ion gate using a narrow

pulse width of 200 µs to sample only a fraction of the RIP, a peak shape very distinct from the RIP signal hump was visible from the Faraday response in Figure C.4, with a baseline resolution of several milliseconds. Notably, this peak remained present even in the absence of an ion source, and so was not chemical but rather electronic in origin. The peak trace initiated with an inverse square-wave step (Δt~200 µs) pulsing open, mirrored by a sharp rise to an amplifier saturation level (Δt~600 µs) pulsing closed, followed by a gradual falling slope to baseline (Δt~10 ms) as the induced charge dissipated. This characteristic response shape is correlated with electric field fluctuations inducing a shadow current on the anode when the gate pulse was triggered. To mute this symptom, an aperture grid (>2 mm wire spacing) was installed between the second gate and the Faraday plate connected to a 1 µF filtering capacitor. Ion transmission was maintained with the aperture grid held at potentials of 100-200 V.

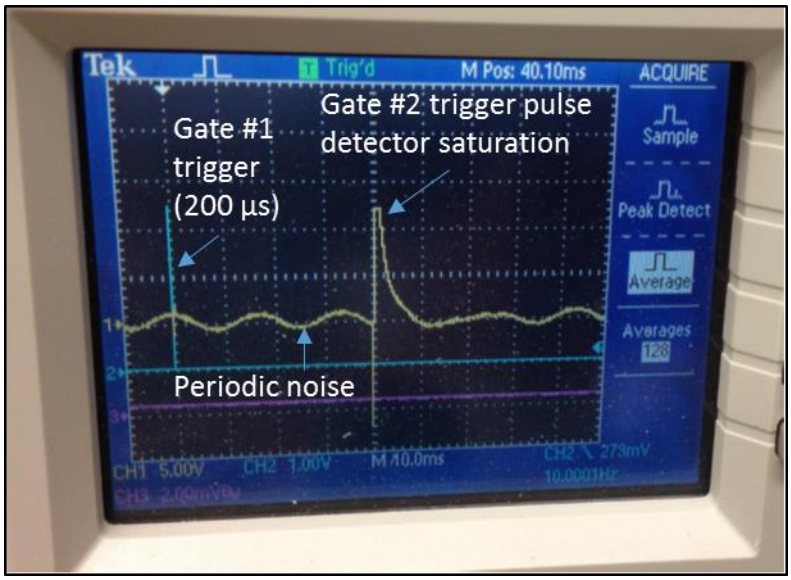

Figure C.4: Example of periodic noise and the Faraday response induced by the second gate trigger pulse. No ion source or aperture grid present.

Neat DMMP vapor was ionized by corona discharge and measured using fixed-gate acquisition as a proof of basic dual-gate DTIMS operation. Pulsing the second gate open ~80 ms after a 10 ms delay from the first gate trigger pulse (200 µs), signal peaks

for DMMP were observed starting at *t*~39 ms, slowly disappearing when the DMMP was removed from the inlet. Evident at the extremes of the 80 ms drift time window are the familiar "open-close" gate pulse-induced Faraday traces. At the fringes of the mobility time window sampled, these artifacts should not interfere with resolution or sensitivity for peaks centered in the selected drift region. The induced current response for the open pulse event showed a more gradual falling edge than seen before in Figure C.4 given the longer duration of the pulse (ms vs. µs). Although cut off on the oscilloscope image in Figure C.5, it did not appear that the induced current reached detector saturation owing to the presence of the aperture grid and the partial dampening effect of the filtering capacitor.

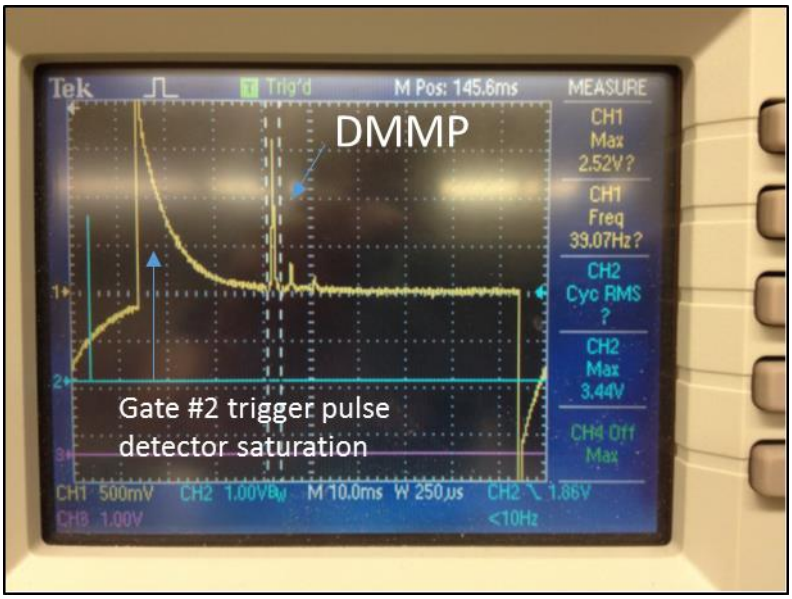

Figure C.5: Faraday signal for corona discharge of neat DMMP vapor and the residual trigger pulse response at the fringes of the 80 ms drift time window using a low grid density aperture.

This induced current behavior, at some cost to sensitivity, has since been eliminated by replacing the wide-spaced grid with a denser aperture mesh. The effects might also be mitigated using different (lower) asymmetric BNG pulse ± bias amplitudes, or possibly only biasing one set of gate wires at a higher (positive) potential while floating the second set. Hoping to generate a cleaner shutter pulse, a second gate #2

trigger relay was assembled from additional PHOTONIS prototype parts. However, the gate switching electronics could only sustain an "open" pulse for ~4 ms. Since a wider ion mobility selection window with greater tunability is desirable, the older TOFWERK gate switch and divider continue to be used.

C.5. Conclusion

Now that successful operation of the dual-gate resistive glass AP-DTIMS prototype has been demonstrated, it is nearly ready to be coupled with the Orbitrap MS for comparison studies with the EXCELLIMS unit. The prototype will be mounted level with the spectrometer AP inlet, and an extended Orbitrap transfer capillary (*o.d.* = 1/16") insulated in a macor sleeve (*o.d.* ~ 1/8") will be inserted through the anode/Faraday axis. The initial concern with this arrangement will relate to potential vibrational sources of noise for the Faraday detector. When heating the drift tube, a source enclosure with diaphragm pump connections may be designed and implemented to assist with laminar buffer gas flow and prevent losses of resolution. Currently, the hardware only allows for fixed-gate DTIMS acquisitions, but another objective is to develop integrated IMS-MS software. Early phases of development will involve modification of the gate timing scheme outlined by Kwasnik *et al.*[133] to perform conventional mobility scans using Labview virtual instruments and synchronized waveform generators to trigger each gate.

REFERENCES

[1] Z. Takáts, J. M. Wiseman, B. Gologan, R. G. Cooks. Mass Spectrometry Sampling Under Ambient Conditions with Desorption Electrospray Ionization. *Science* **2004**, *306*, 471.

[2] R. B. Cody, J. A. Laramée, H. D. Durst. Versatile New Ion Source for the Analysis of Materials in Open Air under Ambient Conditions. *Anal Chem* **2005**, *77*, 2297.

[3] L. A. McDonnell, R. M. A. Heeren. Imaging mass spectrometry. *Mass Spectrom Rev* **2007**, *26*, 606.

[4] J. M. Wiseman, D. R. Ifa, A. Venter, R. G. Cooks. Ambient molecular imaging by desorption electrospray ionization mass spectrometry. *Nat Protoc* **2008**, *3*, 517.

[5] O. S. Ovchinnikova, K. Kjoller, G. B. Hurst, D. A. Pelletier, G. J. Van Berkel. Atomic Force Microscope Controlled Topographical Imaging and Proximal Probe Thermal Desorption/Ionization Mass Spectrometry Imaging. *Anal Chem* **2014**, *86*, 1083.

[6] K. Chughtai, R. M. A. Heeren. Mass Spectrometric Imaging for Biomedical Tissue Analysis. *Chem Rev* **2010**, *110*, 3237.

[7] M. Haapala, J. Pól, V. Saarela, V. Arvola, T. Kotiaho, R. A. Ketola, S. Franssila, T. J. Kauppila, R. Kostiainen. Desorption Atmospheric Pressure Photoionization. *Anal Chem* **2007**, *79*, 7867.

[8] P. Nemes, A. Vertes. Laser Ablation Electrospray Ionization for Atmospheric Pressure, in Vivo, and Imaging Mass Spectrometry. *Anal Chem* **2007**, *79*, 8098.

[9] J. J. Coon, K. J. McHale, W. W. Harrison. Atmospheric pressure laser desorption/chemical ionization mass spectrometry: a new ionization method based on existing themes. *Rapid Commun Mass Spectrom* **2002**, *16*, 681.

[10] M. E. Monge, G. A. Harris, P. Dwivedi, F. M. Fernández. Mass Spectrometry: Recent Advances in Direct Open Air Surface Sampling/Ionization. *Chem Rev* **2013**, *113*, 2269.

[11] W. W. Harrison, C. Yang, E. Oxley. Peer Reviewed: Pulsed Glow Discharge: Temporal Resolution in Analytical Spectroscopy. *Anal Chem* **2001**, *73*, 480 A.

[12] A. P. Napartovich. Overview of Atmospheric Pressure Discharges Producing Nonthermal Plasma. *Plasmas Polym* **2001**, *6*, 1.

[13] N. Na, C. Zhang, M. Zhao, S. Zhang, C. Yang, X. Fang, X. Zhang. Direct detection of explosives on solid surfaces by mass spectrometry with an ambient ion source based on dielectric barrier discharge. *J Mass Spectrom* **2007**, *42*, 1079.

[14] J. M. Nilles, T. R. Connell, S. T. Stokes, H. Dupont Durst. Explosives Detection Using Direct Analysis in Real Time (DART) Mass Spectrometry. *Propell Explos Pyrot* **2010**, *35*, 446.

[15] B. Gilbert-Lopez, J. F. Garcia-Reyes, C. Meyer, A. Michels, J. Franzke, A. Molina-Diaz, H. Hayen. Simultaneous testing of multiclass organic contaminants in food and environment by liquid chromatography/dielectric barrier discharge ionization-mass spectrometry. *Analyst* **2012**, *137*, 5403.

[16] A. H. Grange. Semi-quantitative analysis of contaminants in soils by direct analysis in real time (DART) mass spectrometry. *Rapid Commun Mass Spectrom* **2013**, *27*, 305.

[17] X. Ma, S. Zhang, Z. Lin, Y. Liu, Z. Xing, C. Yang, X. Zhang. Real-time monitoring of chemical reactions by mass spectrometry utilizing a low-temperature plasma probe. *Analyst* **2009**, *134*, 1863.

[18] J. Hajslova, T. Cajka, L. Vaclavik. Challenging applications offered by direct analysis in real time (DART) in food-quality and safety analysis. *TrAC-Trend Anal Chem* **2011**, *30*, 204.

[19] F. M. Fernandez, R. B. Cody, M. D. Green, C. Y. Hampton, R. McGready, S. Sengaloundeth, N. J. White, P. N. Newton. Characterization of solid counterfeit drug samples by desorption electrospray ionization and direct-analysis-in-real-time coupled to time-of-flight mass spectrometry. *ChemMedChem* **2006**, *1*, 702.

[20] Y. Liu, Z. Lin, S. Zhang, C. Yang, X. Zhang. Rapid screening of active ingredients in drugs by mass spectrometry with low-temperature plasma probe. *Anal Bioanal Chem* **2009**, *395*, 591.

[21] T. M. Brewer, J. R. Verkouteren. Atmospheric identification of active ingredients in over-the-counter pharmaceuticals and drugs of abuse by atmospheric pressure glow discharge mass spectrometry (APGD-MS). *Rapid Commun Mass Spectrom* **2011**, *25*, 2407.

[22] M. Zhou, J. F. McDonald, F. M. Fernandez. Optimization of a direct analysis in real time/time-of-flight mass spectrometry method for rapid serum metabolomic fingerprinting. *J Am Soc Mass Spectrom* **2010**, *21*, 68.

[23] C. M. Jones, F. M. Fernandez. Transmission mode direct analysis in real time mass spectrometry for fast untargeted metabolic fingerprinting. *Rapid Commun Mass Spectrom* **2013**, *27*, 1311.

[24] J. D. Harper, N. A. Charipar, C. C. Mulligan, X. Zhang, R. G. Cooks, Z. Ouyang. Low-Temperature Plasma Probe for Ambient Desorption Ionization. *Anal Chem* **2008**, *80*, 9097.

[25] L. C. Chen, Z. Yu, H. Furuya, Y. Hashimoto, K. Takekawa, H. Suzuki, O. Ariyada, K. Hiraoka. Development of ambient sampling chemi/chemical ion source with dielectric barrier discharge. *J Mass Spectrom* **2010**, *45*, 861.

[26] L. V. Ratcliffe, F. J. M. Rutten, D. A. Barrett, T. Whitmore, D. Seymour, C. Greenwood, Y. Aranda-Gonzalvo, S. Robinson, M. McCoustra. Surface Analysis under Ambient Conditions Using Plasma-Assisted Desorption/Ionization Mass Spectrometry. *Anal Chem* **2007**, *79*, 6094.

[27] T. L. Salter, I. S. Gilmore, A. Bowfield, O. T. Olabanji, J. W. Bradley. Ambient Surface Mass Spectrometry Using Plasma-Assisted Desorption Ionization: Effects and Optimization of Analytical Parameters for Signal Intensities of Molecules and Polymers. *Anal Chem* **2013**, *85*, 1675.

[28] F. J. Andrade, J. T. Shelley, W. C. Wetzel, M. R. Webb, G. Gamez, S. J. Ray, G. M. Hieftje. Atmospheric Pressure Chemical Ionization Source. 2. Desorption−Ionization for the Direct Analysis of Solid Compounds. *Anal Chem* **2008**, *80*, 2654.

[29] F. J. Andrade, J. T. Shelley, W. C. Wetzel, M. R. Webb, G. Gamez, S. J. Ray, G. M. Hieftje. Atmospheric Pressure Chemical Ionization Source. 1. Ionization of Compounds in the Gas Phase. *Anal Chem* **2008**, *80*, 2646.

[30] J. Kratzer, Z. Mester, R. E. Sturgeon. Comparison of dielectric barrier discharge, atmospheric pressure radiofrequency-driven glow discharge and direct analysis in real time sources for ambient mass spectrometry of acetaminophen. *Spectrochim Acta B* **2011**, *66*, 594.

[31] K. McKay, T. L. Salter, A. Bowfield, J. L. Walsh, I. S. Gilmore, J. W. Bradley. Comparison of Three Plasma Sources for Ambient Desorption/Ionization Mass Spectrometry. *J Am Soc Mass Spectrom* **2014**.

[32] I. Dzidic, D. I. Carroll, R. N. Stillwell, E. C. Horning. Comparison of positive ions formed in nickel-63 and corona discharge ion sources using nitrogen, argon, isobutane, ammonia and nitric oxide as reagents in atmospheric pressure ionization mass spectrometry. *Anal Chem* **1976**, *48*, 1763.

[33] G. C. Y. Chan, J. T. Shelley, J. S. Wiley, C. Engelhard, A. U. Jackson, R. G. Cooks, G. M. Hieftje. Elucidation of Reaction Mechanisms Responsible for Afterglow and Reagent-Ion Formation in the Low-Temperature Plasma Probe Ambient Ionization Source. *Anal Chem* **2011**, *83*, 3675.

[34] L. Song, S. C. Gibson, D. Bhandari, K. D. Cook, J. E. Bartmess. Ionization Mechanism of Positive-Ion Direct Analysis in Real Time: A Transient Microenvironment Concept. *Anal Chem* **2009**, *81*, 10080.

[35] Y. Zhao, M. Lam, D. Wu, R. Mak. Quantification of small molecules in plasma with direct analysis in real time tandem mass spectrometry, without sample preparation and liquid chromatographic separation. *Rapid Commun Mass Spectrom* **2008**, *22*, 3217.

[36] H. Danhelova, J. Hradecky, S. Prinosilova, T. Cajka, K. Riddellova, L. Vaclavik, J. Hajslova. Rapid analysis of caffeine in various coffee samples employing direct analysis in real-time ionization-high-resolution mass spectrometry. *Anal Bioanal Chem* **2012**, *403*, 2883.

[37] B. Gilbert-Lopez, H. Geltenpoth, C. Meyer, A. Michels, H. Hayen, A. Molina-Diaz, J. F. Garcia-Reyes, J. Franzke. Performance of dielectric barrier discharge ionization mass spectrometry for pesticide testing: a comparison with atmospheric pressure chemical ionization and electrospray ionization. *Rapid Commun Mass Spectrom* **2013**, *27*, 419.

[38] G. Harris, C. Falcone, F. Fernández. Sensitivity “Hot Spots” in the Direct Analysis in Real Time Mass Spectrometry of Nerve Agent Simulants. *J Am Soc Mass Spectrom* **2012**, *23*, 153.

[39] G. A. Harris, F. M. Fernandez. Simulations and Experimental Investigation of Atmospheric Transport in an Ambient Metastable-Induced Chemical Ionization Source. *Anal Chem* **2009**, *81*, 322.

[40] K. P. Pfeuffer, S. J. Ray, G. M. Hieftje. Measurement and visualization of mass transport for the flowing atmospheric pressure afterglow (FAPA) ambient mass-spectrometry source. *J Am Soc Mass Spectrom* **2014**, *25*, 800.

[41] K. P. Pfeuffer, J. T. Shelley, S. J. Ray, G. M. Hieftje. Visualization of mass transport and heat transfer in the FAPA ambient ionization source. *J Anal At Spectrom* **2013**, *28*, 379.

[42] S. Yu, E. Crawford, J. Tice, B. Musselman, J.-T. Wu. Bioanalysis without Sample Cleanup or Chromatography: The Evaluation and Initial Implementation of Direct Analysis in Real Time Ionization Mass Spectrometry for the Quantification of Drugs in Biological Matrixes. *Anal Chem* **2009**, *81*, 193.

[43] T. T. Häbe, G. E. Morlock. Quantitative surface scanning by Direct Analysis in Real Time mass spectrometry. *Rapid Commun Mass Spectrom* **2015**, *29*, 474.

[44] Y. Liu, X. Ma, Z. Lin, M. He, G. Han, C. Yang, Z. Xing, S. Zhang, X. Zhang. Imaging Mass Spectrometry with a Low-Temperature Plasma Probe for the Analysis of Works of Art. *Angew Chem Int Edit* **2010**, *49*, 4435.

[45] J. T. Shelley, S. J. Ray, G. M. Hieftje. Laser Ablation Coupled to a Flowing Atmospheric Pressure Afterglow for Ambient Mass Spectral Imaging. *Anal Chem* **2008**, *80*, 8308.

[46] J. Zhang, Z. Zhou, J. Yang, W. Zhang, Y. Bai, H. Liu. Thin Layer Chromatography/Plasma Assisted Multiwavelength Laser Desorption Ionization Mass Spectrometry for Facile Separation and Selective Identification of Low Molecular Weight Compounds. *Anal Chem* **2012**, *84*, 1496.

[47] J. C. May, J. A. McLean. Ion Mobility-Mass Spectrometry: Time-Dispersive Instrumentation. *Anal Chem* **2015**, *87*, 1422.

[48] M. A. Mäkinen, O. A. Anttalainen, M. E. T. Sillanpää. Ion Mobility Spectrometry and Its Applications in Detection of Chemical Warfare Agents. *Anal Chem* **2010**, *82*, 9594.

[49] R. G. Ewing, D. A. Atkinson, G. A. Eiceman, G. J. Ewing. A critical review of ion mobility spectrometry for the detection of explosives and explosive related compounds. *Talanta* **2001**, *54*, 515.

[50] I. A. Buryakov, Y. N. Kolomiets. Rapid Determination of Explosives and Narcotics Using a Multicapillary-Column Gas Chromatograph and an Ion-Mobility Spectrometer. *J Anal Chem* **2003**, *58*, 944.

[51] I. Márquez-Sillero, E. Aguilera-Herrador, S. Cárdenas, M. Valcárcel. Ion-mobility spectrometry for environmental analysis. *TrAC-Trend Anal Chem* **2011**, *30*, 677.

[52] W. Vautz, D. Zimmermann, M. Hartmann, J. I. Baumbach, J. Nolte, J. Jung. Ion mobility spectrometry for food quality and safety. *Food Addit Contam* **2006**, *23*, 1064.

[53] G. A. Eiceman, D. A. Blyth, D. B. Shoff, A. P. Snyder. Screening of solid commercial pharmaceuticals using ion mobility spectrometry. *Anal Chem* **1990**, *62*, 1374.

[54] R. Fernández-Maestre, H. Hill, Jr. Ion mobility spectrometry for the rapid analysis of over-the-counter drugs and beverages. *Int J Ion Mobil Spectrom* **2009**, *12*, 91.

[55] H. Borsdorf, G. A. Eiceman. Ion Mobility Spectrometry: Principles and Applications. *Appl Spectrosc Rev* **2006**, *41*, 323.

[56] S. Rokushika, H. Hatano, M. A. Baim, H. H. Hill. Resolution measurement for ion mobility spectrometry. *Anal Chem* **1985**, *57*, 1902.

[57] G. R. Asbury, H. H. Hill. Evaluation of ultrahigh resolution ion mobility spectrometry as an analytical separation device in chromatographic terms. *J Microcolumn Sep* **2000**, *12*, 172.

[58] W. F. Siems, C. Wu, E. E. Tarver, H. H. Hill, Jr., P. R. Larsen, D. G. McMinn. Measuring the Resolving Power of Ion Mobility Spectrometers. *Anal Chem* **1994**, *66*, 4195.

[59] G. E. Spangler, C. I. Collins. Peak shape analysis and plate theory for plasma chromatography. *Anal Chem* **1975**, *47*, 403.

[60] G. E. Spangler. Expanded theory for the resolving power of a linear ion mobility spectrometer. *Int J Mass Spectrom* **2002**, *220*, 399.

[61] M. Tabrizchi, F. Rouholahnejad. Comparing the effect of pressure and temperature on ion mobilities. *J Phys D Appl Phys* **2005**, *38*, 857.

[62] M. Tabrizchi. Temperature effects on resolution in ion mobility spectrometry. *Talanta* **2004**, *62*, 65.

[63] M. Tabrizchi, F. Rouholahnejad. Pressure effects on resolution in ion mobility spectrometry. *Talanta* **2006**, *69*, 87.

[64] K. Giles, S. D. Pringle, K. R. Worthington, D. Little, J. L. Wildgoose, R. H. Bateman. Applications of a travelling wave-based radio-frequency-only stacked ring ion guide. *Rapid Commun Mass Spectrom* **2004**, *18*, 2401.

[65] S. I. Merenbloom, R. S. Glaskin, Z. B. Henson, D. E. Clemmer. High-Resolution Ion Cyclotron Mobility Spectrometry. *Anal Chem* **2009**, *81*, 1482.

[66] M. E. Ridgeway, J. J. Wolff, J. A. Silveira, C. Lin, C. E. Costello, M. A. Park. Gated trapped ion mobility spectrometry coupled to fourier transform ion cyclotron resonance mass spectrometry. *Int J Ion Mobil Spectrom* **2016**, 1.

[67] M. A. Ewing, S. M. Zucker, S. J. Valentine, D. E. Clemmer. Overtone Mobility Spectrometry: Part 5. Simulations and Analytical Expressions Describing Overtone Limits. *J Am Soc Mass Spectrom* **2013**, *24*, 615.

[68] R. T. Kurulugama, F. M. Nachtigall, S. Lee, S. J. Valentine, D. E. Clemmer. Overtone mobility spectrometry: Part 1. Experimental observations. *J Am Soc Mass Spectrom* **2009**, *20*, 729.

[69] S. J. Valentine, R. T. Kurulugama, E. D. Clemmer. Overtone Mobility Spectrometry: Part 3. On the Origin of Peaks. *J Am Soc Mass Spectrom* **2011**, *22*, 804.

[70] R. Guevremont. High-field asymmetric waveform ion mobility spectrometry: A new tool for mass spectrometry. *J Chromatogr A* **2004**, *1058*, 3.

[71] E. V. Krylov, E. G. Nazarov, R. A. Miller. Differential mobility spectrometer: Model of operation. *Int J Mass Spectrom* **2007**, *266*, 76.

[72] G. P. Reischl. Measurement of Ambient Aerosols by the Differential Mobility Analyzer Method: Concepts and Realization Criteria for the Size Range Between 2 and 500 nm. *Aerosol Sci Tech* **1991**, *14*, 5.

[73] H. Tammet, A. Mirme, E. Tamm. Electrical aerosol spectrometer of Tartu University. *Atmos Res* **2002**, *62*, 315.

[74] D. Guo, Y. Wang, L. Li, X. Wang, J. Luo. Precise determination of nonlinear function of ion mobility for explosives and drugs at high electric fields for microchip FAIMS. *J Mass Spectrom* **2015**, *50*, 198.

[75] K. Michelmann, J. A. Silveira, M. E. Ridgeway, M. A. Park. Fundamentals of Trapped Ion Mobility Spectrometry. *J Am Soc Mass Spectrom* **2015**, *26*, 14.

[76] J. A. Silveira, K. Michelmann, M. E. Ridgeway, M. A. Park. Fundamentals of Trapped Ion Mobility Spectrometry Part II: Fluid Dynamics. *J Am Soc Mass Spectrom* **2016**, *27*, 585.

[77] F. W. Karasek, M. J. Cohen, D. I. Carroll. Trace Studies of Alcohols in the Plasma Chromatograph—Mass Spectrometer. *J Chromatogr Sci* **1971**, *9*, 390.

[78] A. B. Kanu, P. Dwivedi, M. Tam, L. Matz, H. H. Hill. Ion mobility–mass spectrometry. *J Mass Spectrom* **2008**, *43*, 1.

[79] B. T. Ruotolo, K. J. Gillig, E. G. Stone, D. H. Russell. Peak capacity of ion mobility mass spectrometry:: Separation of peptides in helium buffer gas. *J Chromatogr B* **2002**, *782*, 385.

[80] B. H. Clowers, H. H. Hill. Mass Analysis of Mobility-Selected Ion Populations Using Dual Gate, Ion Mobility, Quadrupole Ion Trap Mass Spectrometry. *Anal Chem* **2005**, *77*, 5877.

[81] M. F. Bush, I. D. G. Campuzano, C. V. Robinson. Ion Mobility Mass Spectrometry of Peptide Ions: Effects of Drift Gas and Calibration Strategies. *Anal Chem* **2012**, *84*, 7124.

[82] Z. Hall, A. Politis, M. F. Bush, L. J. Smith, C. V. Robinson. Charge-State Dependent Compaction and Dissociation of Protein Complexes: Insights from Ion Mobility and Molecular Dynamics. *J Am Chem Soc* **2012**, *134*, 3429.

[83] S. D. Pringle, K. Giles, J. L. Wildgoose, J. P. Williams, S. E. Slade, K. Thalassinos, R. H. Bateman, M. T. Bowers, J. H. Scrivens. An investigation of the mobility separation of some peptide and protein ions using a new hybrid quadrupole/travelling wave IMS/oa-ToF instrument. *Int J Mass Spectrom* **2007**, *261*, 1.

[84] B. T. Ruotolo, J. L. P. Benesch, A. M. Sandercock, S.-J. Hyung, C. V. Robinson. Ion mobility-mass spectrometry analysis of large protein complexes. *Nat Protoc* **2008**, *3*, 1139.

[85] W. Hoffmann, J. Hofmann, K. Pagel. Energy-Resolved Ion Mobility-Mass Spectrometry—A Concept to Improve the Separation of Isomeric Carbohydrates. *J Am Soc Mass Spectrom* **2014**, *25*, 471.

[86] B. H. Clowers, W. F. Siems, H. H. Hill, S. M. Massick. Hadamard Transform Ion Mobility Spectrometry. *Anal Chem* **2006**, *78*, 44.

[87] F. J. Knorr, R. L. Eatherton, W. F. Siems, H. H. Hill. Fourier Transform Ion Mobility Spectrometry. *Anal Chem* **1985**, *57*, 402.

[88] M. Kwasnik, J. Caramore, F. M. Fernández. Digitally-Multiplexed Nanoelectrospray Ionization Atmospheric Pressure Drift Tube Ion Mobility Spectrometry. *Anal Chem* **2009**, *81*, 1587.

[89] K. A. Morrison, W. F. Siems, B. H. Clowers. Augmenting Ion Trap Mass Spectrometers Using a Frequency Modulated Drift Tube Ion Mobility Spectrometer. *Anal Chem* **2016**, *88*, 3121.

[90] K. E. Swearingen, J. M. Winget, M. R. Hoopmann, U. Kusebauch, R. L. Moritz. Decreased Gap Width in a Cylindrical High-Field Asymmetric Waveform Ion Mobility Spectrometry Device Improves Protein Discovery. *Anal Chem* **2015**, *87*, 12230.

[91] Y. Seo, A. Andaya, J. A. Leary. Preparation, Separation, and Conformational Analysis of Differentially Sulfated Heparin Octasaccharide Isomers Using Ion Mobility Mass Spectrometry. *Anal Chem* **2012**, *84*, 2416.

[92] A. A. Shvartsburg, G. Isaac, N. Leveque, R. D. Smith, T. O. Metz. Separation and Classification of Lipids Using Differential Ion Mobility Spectrometry. *J Am Soc Mass Spectrom* **2011**, *22*, 1146.

[93] J. L. Kaszycki, A. P. Bowman, A. A. Shvartsburg. Ion Mobility Separation of Peptide Isotopomers. *J Am Soc Mass Spectrom* **2016**, *27*, 795.

[94] R. V. Bennett, C. M. Gamage, A. S. Galhena, F. M. Fernández. Contrast-Enhanced Differential Mobility-Desorption Electrospray Ionization-Mass Spectrometry Imaging of Biological Tissues. *Anal Chem* **2014**, *86*, 3756.

[95] A. A. Shvartsburg, F. Li, K. Tang, R. D. Smith. Characterizing the Structures and Folding of Free Proteins Using 2-D Gas-Phase Separations: Observation of Multiple Unfolded Conformers. *Anal Chem* **2006**, *78*, 3304.

[96] P. Benigni, C. J. Thompson, M. E. Ridgeway, M. A. Park, F. Fernandez-Lima. Targeted High-Resolution Ion Mobility Separation Coupled to Ultrahigh-Resolution Mass Spectrometry of Endocrine Disruptors in Complex Mixtures. *Anal Chem* **2015**, *87*, 4321.

[97] J. A. Silveira, M. E. Ridgeway, F. H. Laukien, M. Mann, M. A. Park. Parallel accumulation for 100% duty cycle trapped ion mobility-mass spectrometry. *Int J Mass Spectrom* **2016**.

[98] Y. J. Li, Z. Z. Wang, Y. A. Bi, G. Ding, L. S. Sheng, J. P. Qin, W. Xiao, J. C. Li, Y. X. Wang, X. Wang. The evaluation and implementation of Direct Analysis in Real Time quadrupole time-of-flight tandem mass spectrometry for characterization and quantification of geniposide in Re Du Ning Injections. *Rapid Commun Mass Spectrom* **2012**, *26*, 1377.

[99] D. Saang'onyo, G. Selby, D. L. Smith. Validation of a Direct Analysis in Real Time Mass Spectrometry (DART-MS) method for the quantitation of six carbon sugars in a saccharification matrix. *Anal Methods* **2012**, *4*, 3460.

[100] G. A. Harris, D. M. Hostetler, C. Y. Hampton, F. M. Fernandez. Comparison of the internal energy deposition of direct analysis in real time and electrospray

ionization time-of-flight mass spectrometry. *J Am Soc Mass Spectrom* **2010**, *21*, 855.

[101] G. S. Settles, E. B. Hackett, J. D. Miller, L. M. Weinstein. *Flow Visualization VII: Full-Scale Schlieren Flow Visualization*, Begell House, NY, New York, **1995**.

[102] J. M. Desse, R. Deron. Shadow, Schlieren, and Color Interferometry. *Aerospace Lab* **2009**, *1*, 1.

[103] G. S. Settles. *Schlieren and Shadowgraph Techniques: Visualizing Phenomena In Transparent Media*, Springer-Verlag, NY, New York, **2001**.

[104] J. J. Perez, G. A. Harris, J. E. Chipuk, J. S. Brodbelt, M. D. Green, C. Y. Hampton, F. M. Fernandez. Transmission-mode direct analysis in real time and desorption electrospray ionization mass spectrometry of insecticide-treated bednets for malaria control. *Analyst* **2010**, *135*, 712.

[105] M. M. Nudnova, L. Zhu, R. Zenobi. Active capillary plasma source for ambient mass spectrometry. *Rapid Commun Mass Spectrom* **2012**, *26*, 1447.

[106] R. G. Ewing, B. H. Clowers, D. A. Atkinson. Direct Real-Time Detection of Vapors from Explosive Compounds. *Anal Chem* **2013**, *85*, 10977.

[107] R. B. Dixon, J. S. Sampson, A. M. Hawkridge, D. C. Muddiman. Ambient Aerodynamic Ionization Source for Remote Analyte Sampling and Mass Spectrometric Analysis. *Anal Chem* **2008**, *80*, 5266.

[108] B. Gilbert-López, M. Schilling, N. Ahlmann, A. Michels, H. Hayen, A. Molina-Díaz, J. F. García-Reyes, J. Franzke. Ambient Diode Laser Desorption Dielectric Barrier Discharge Ionization Mass Spectrometry of Nonvolatile Chemicals. *Anal Chem* **2013**, *85*, 3174.

[109] B. Feng, J. Zhang, C. Chang, L. Li, M. Li, X. Xiong, C. Guo, F. Tang, Y. Bai, H. Liu. Ambient Mass Spectrometry Imaging: Plasma Assisted Laser Desorption Ionization Mass Spectrometry Imaging and Its Applications. *Anal Chem* **2014**, *86*, 4164.

[110] P. Dwivedi, D. B. Gazda, J. D. Keelor, T. F. Limero, W. T. Wallace, A. V. Macatangay, F. M. Fernández. Electro-Thermal Vaporization Direct Analysis in

Real Time-Mass Spectrometry for Water Contaminant Analysis during Space Missions. *Anal Chem* **2013**, *85*, 9898.

[111] J. N. Schaper, K. P. Pfeuffer, J. T. Shelley, N. H. Bings, G. M. Hieftje. Drop-on-Demand Sample Introduction System Coupled with the Flowing Atmospheric-Pressure Afterglow for Direct Molecular Analysis of Complex Liquid Microvolume Samples. *Anal Chem* **2012**, *84*, 9246.

[112] C. Reininger, K. Woodfield, J. D. Keelor, A. Kaylor, F. M. Fernández, P. B. Farnsworth. Absolute number densities of helium metastable atoms determined by atomic absorption spectroscopy in helium plasma-based discharges used as ambient desorption/ionization sources for mass spectrometry. *Spectrochim Acta B* **2014**, *100*, 98.

[113] K. Vandercruyssen, M. D'Hondt, V. Vergote, H. Jansen, C. Burvenich, B. De Spiegeleer. LC–UV/MS quality analytics of paediatric artemether formulations. *J Pharm Anal* **2014**, *4*, 37.

[114] N. Na, M. Zhao, S. Zhang, C. Yang, X. Zhang. Development of a Dielectric Barrier Discharge Ion Source for Ambient Mass Spectrometry. *J Am Soc Mass Spectrom* **2007**, *18*, 1859.

[115] F. M. Green, T. L. Salter, I. S. Gilmore, P. Stokes, G. O'Connor. The effect of electrospray solvent composition on desorption electrospray ionisation (DESI) efficiency and spatial resolution. *Analyst* **2010**, *135*, 731.

[116] M. C. Chen, B. J. Cafferty, I. Mamajanov, I. Gállego, J. Khanam, R. Krishnamurthy, N. V. Hud. Spontaneous Prebiotic Formation of a β-Ribofuranoside That Self-Assembles with a Complementary Heterocycle. *J Am Chem Soc* **2014**, *136*, 5640.

[117] E. T. Parker, M. Zhou, A. S. Burton, D. P. Glavin, J. P. Dworkin, R. Krishnamurthy, F. M. Fernández, J. L. Bada. A Plausible Simultaneous Synthesis of Amino Acids and Simple Peptides on the Primordial Earth. *Angew Chem Int Edit* **2014**, *53*, 8132.

[118] T. M. McCollom. Miller-Urey and Beyond: What Have We Learned About Prebiotic Organic Synthesis Reactions in the Past 60 Years? *Annu Rev Earth Pl Sc* **2013**, *41*, 207.

[119] J. S. Hudson, J. F. Eberle, R. H. Vachhani, L. C. Rogers, J. H. Wade, R. Krishnamurthy, G. Springsteen. A Unified Mechanism for Abiotic Adenine and Purine Synthesis in Formamide. *Angew Chem Int Edit* **2012**, *51*, 5134.

[120] A. W. Schwartz. Intractable Mixtures and the Origin of Life. *Chem Biodivers* **2007**, *4*, 656.

[121] J. Wang, J. Gu, M. T. Nguyen, G. Springsteen, J. Leszczynski. From Formamide to Purine: A Self-Catalyzed Reaction Pathway Provides a Feasible Mechanism for the Entire Process. *J Phys Chem B* **2013**, *117*, 9333.

[122] H. T. Nguyen, Y. A. Jeilani, H. M. Hung, M. T. Nguyen. Radical Pathways for the Prebiotic Formation of Pyrimidine Bases from Formamide. *J Phys Chem A* **2015**, *119*, 8871.

[123] A. L. Weber. Sugar-Driven Prebiotic Synthesis of 3,5(6)-Dimethylpyrazin-2-one: A Possible Nucleobase of a Primitive Replication Process. *Origins Life Evol B* **2008**, *38*, 279.

[124] E. J. Davis, P. Dwivedi, M. Tam, W. F. Siems, H. H. Hill. High-Pressure Ion Mobility Spectrometry. *Anal Chem* **2009**, *81*, 3270.

[125] S. K. Guharay, P. Dwivedi, H. H. Hill. Ion Mobility Spectrometry: Ion Source Development and Applications in Physical and Biological Sciences. *IEEE T Plasma Sci* **2008**, *36*, 1458.

[126] D. J. Weston, R. Bateman, I. D. Wilson, T. R. Wood, C. S. Creaser. Direct Analysis of Pharmaceutical Drug Formulations Using Ion Mobility Spectrometry/Quadrupole-Time-of-Flight Mass Spectrometry Combined with Desorption Electrospray Ionization. *Anal Chem* **2005**, *77*, 7572.

[127] S. Myung, J. M. Wiseman, S. J. Valentine, Z. Takáts, R. G. Cooks, D. E. Clemmer. Coupling Desorption Electrospray Ionization with Ion Mobility/Mass Spectrometry for Analysis of Protein Structure: Evidence for Desorption of Folded and Denatured States. *J Phys Chem B* **2006**, *110*, 5045.

[128] K. M. Roscioli, J. A. Tufariello, X. Zhang, S. X. Li, G. H. Goetz, G. Cheng, W. F. Siems, H. H. Hill. Desorption electrospray ionization (DESI) with atmospheric pressure ion mobility spectrometry for drug detection. *Analyst* **2014**, *139*, 1740.

[129] G. A. Harris, S. Graf, R. Knochenmuss, F. M. Fernandez. Coupling laser ablation/desorption electrospray ionization to atmospheric pressure drift tube ion mobility spectrometry for the screening of antimalarial drug quality. *Analyst* **2012**, *137*, 3039.

[130] M. T. Jafari. Low-Temperature Plasma Ionization Ion Mobility Spectrometry. *Anal Chem* **2010**, *83*, 797.

[131] A. Michels, S. Tombrink, W. Vautz, M. Miclea, J. Franzke. Spectroscopic characterization of a microplasma used as ionization source for ion mobility spectrometry. *Spectrochim Acta B* **2007**, *62*, 1208.

[132] G. A. Harris, M. Kwasnik, F. M. Fernández. Direct Analysis in Real Time Coupled to Multiplexed Drift Tube Ion Mobility Spectrometry for Detecting Toxic Chemicals. *Anal Chem* **2011**, *83*, 1908.

[133] M. Kwasnik, F. M. Fernández. Theoretical and experimental study of the achievable separation power in resistive-glass atmospheric pressure ion mobility spectrometry. *Rapid Commun Mass Spectrom* **2010**, *24*, 1911.

[134] M. Kwasnik, K. Fuhrer, M. Gonin, K. Barbeau, F. M. Fernández. Performance, Resolving Power, and Radial Ion Distributions of a Prototype Nanoelectrospray Ionization Resistive Glass Atmospheric Pressure Ion Mobility Spectrometer. *Anal Chem* **2007**, *79*, 7782.

[135] G. Kaur-Atwal, G. O'Connor, A. Aksenov, V. Bocos-Bintintan, C. L. Paul Thomas, C. Creaser. Chemical standards for ion mobility spectrometry: a review. *Int J Ion Mobil Spectrom* **2009**, *12*, 1.

[136] M. Tabrizchi, T. Khayamian, N. Taj. Design and optimization of a corona discharge ionization source for ion mobility spectrometry. *Rev Sci Instrum* **2000**, *71*, 2321.

[137] K. Sekimoto, M. Takayama. Negative ion formation and evolution in atmospheric pressure corona discharges between point-to-plane electrodes with arbitrary needle angle. *Eur Phys J D* **2010**, *60*, 589.

[138] G. S. Settles, E. B. Hackett, J. D. Miller, L. M. Weinstein. in *Flow Visualaization VII* (Ed.: J. P. Crowder), Begell House, New York, **1995**, pp. 2.

[139] H. Bahrami, M. Tabrizchi, H. Farrokhpour. Protonation of caffeine: A theoretical and experimental study. *Chem Phys* **2013**, *415*, 222.

[140] V. Čermák. Detection of Long-Lived Excited States of Molecules by Penning Ionization. *J Chem Phys* **1966**, *44*, 1318.

[141] R. N. Zare, E. O. Larsson, R. A. Berg. Franck-Condon factors for electronic band systems of molecular nitrogen. *J Mol Spectrosc* **1965**, *15*, 117.

[142] A. G. Borisov, D. Teillet-Billy, J. P. Gauyacq. Singlet-to-triplet conversion in low energy metastable helium-metal surface collisions. *Surf Sci* **1993**, *284*, 337.

[143] S. N. Foner, R. L. Hudson. Mass Spectrometric Studies of Metastable Nitrogen Atoms and Molecules in Active Nitrogen. *J Chem Phys* **1962**, *37*, 1662.

[144] D. J. Burns, D. E. Golden, D. W. Galliardt. Electron excitation of the E 3Σg + state of N2 and subsequent collisional deactivation and energy transfer to the C 3Πu state. *J Chem Phys* **1976**, *65*, 2616.

[145] J. T. Shelley, J. S. Wiley, G. M. Hieftje. Ultrasensitive ambient mass spectrometric analysis with a pin-to-capillary flowing atmospheric-pressure afterglow source. *Anal Chem* **2011**, *83*, 5741.

[146] J. Herron. Modeling Studies of the Formation and Destruction of NO in Pulsed Barrier Discharges in Nitrogen and Air. *Plasma Chem Plasma P* **2001**, *21*, 581.

[147] R. Ono, T. Oda. NO formation in a pulsed spark discharge in N2/O2/Ar mixture at atmospheric pressure. *J Phys D Appl Phys* **2002**, *35*.

[148] D. I. Carroll, I. Dzidic, R. N. Stillwell, E. C. Horning. Identification of positive reactant ions observed for nitrogen carrier gas in plasma chromatograph mobility studies. *Anal Chem* **1975**, *47*, 1956.

[149] Y. Harada, S. Masuda, H. Ozaki. Electron Spectroscopy Using Metastable Atoms as Probes for Solid Surfaces. *Chem Rev* **1997**, *97*, 1897.

[150] S. J. Valentine, R. T. Kurulugama, B. C. Bohrer, S. I. Merenbloom, R. A. Sowell, Y. Mechref, D. E. Clemmer. Developing IMS–IMS–MS for rapid characterization of abundant proteins in human plasma. *Int J Mass Spectrom* **2009**, *283*, 149.

[151] B. T. Ruotolo, J. A. McLean, K. J. Gillig, D. H. Russell. Peak capacity of ion mobility mass spectrometry: the utility of varying drift gas polarizability for the separation of tryptic peptides. *J Mass Spectrom* **2004**, *39*, 361.

[152] S. J. Allen, K. Giles, T. Gilbert, M. F. Bush. Ion mobility mass spectrometry of peptide, protein, and protein complex ions using a radio-frequency confining drift cell. *Analyst* **2016**, *141*, 884.

[153] Reverse peptide kit protocol pamphlet. Waters Corporation, **2014**.

[154] R. V. Bennett, E. M. Morzan, J. O. Huckaby, M. E. Monge, H. I. Christensen, F. M. Fernandez. Robotic plasma probe ionization mass spectrometry (RoPPI-MS) of non-planar surfaces. *Analyst* **2014**, *139*, 2658.

[155] A. Venter, M. Nefliu, R. Graham Cooks. Ambient desorption ionization mass spectrometry. *TrAC-Trend Anal Chem* **2008**, *27*, 284.

[156] A. R. Venter, K. A. Douglass, J. T. Shelley, G. Hasman, E. Honarvar. Mechanisms of Real-Time, Proximal Sample Processing during Ambient Ionization Mass Spectrometry. *Anal Chem* **2014**, *86*, 233.

[157] M. S. Heywood, N. Taylor, P. B. Farnsworth. Measurement of Helium Metastable Atom Densities in a Plasma-Based Ambient Ionization Source. *Anal Chem* **2011**, *83*, 6493.

[158] Y. K. Ralchenko, A. E.; Reader, J.; NIST ASD Team National Institute of Standards and Technology, Gaithersburg, MD, **2011**.

[159] W. Lu, D. Milic, M. D. Hoogerland, M. Jacka, K. G. H. Baldwin, S. J. Buckman. A practical direct current discharge helium absorption cell for laser frequency locking at 1083 nm. *Rev Sci Instrum* **1996**, *67*, 3003.

[160] U. Keiichiro, M. Tadasuke, T. Kunihide, N. G. Biswa. Investigation of discharge mechanisms in helium plasma jet at atmospheric pressure by laser spectroscopic measurements. *J Phys D Appl Phys* **2010**, *43*, 095201.

[161] J. D. a. C. Ingle, S. R. *Spectrochemical Analysis*, Prentice Hall, Englewood Cliffs, N. J., **1988**.

[162] W. L. Wiese, J. R. Fuhr. Accurate Atomic Transition Probabilities for Hydrogen, Helium, and Lithium. *J Phys Chem Ref Data* **2009**, *38*, 565.

[163] B. Niermann, M. Böke, N. Sadeghi, J. Winter. Space resolved density measurements of argon and helium metastable atoms in radio-frequency generated He-Ar micro-plasmas. *Eur Phys J D* **2010**, *60*, 489.

[164] A. Bogaerts, R. Gijbels. Description of the argon-excited levels in a radio-frequency and direct current glow discharge. *Spectrochim Acta B* **2000**, *55*, 263.

[165] J. Julien, L. Mounir, K. Erdinc. Formation and dynamics of plasma bullets in a non-thermal plasma jet: influence of the high-voltage parameters on the plume characteristics. *Plasma Sources Sci T* **2010**, *19*, 065005.

[166] G. V. Naidis. Modelling of plasma bullet propagation along a helium jet in ambient air. *J Phys D Appl Phys* **2011**, *44*, 215203.

[167] J. Shi, F. Zhong, J. Zhang, D. W. Liu, M. G. Kong. A hypersonic plasma bullet train traveling in an atmospheric dielectric-barrier discharge jet. *Phys Plasmas* **2008**, *15*, 013504.

[168] M. Teschke, J. Kedzierski, E. G. Finantu-Dinu, D. Korzec, J. Engemann. High-speed photographs of a dielectric barrier atmospheric pressure plasma jet. *IEEE T Plasma Sci* **2005**, *33*, 310.

[169] T. F. Limero, E. G. Nazarov, M. Menlyadiev, G. A. Eiceman. Characterization of ion processes in a GC/DMS air quality monitor by integration of the instrument to a mass spectrometer. *Analyst* **2015**, *140*, 922.

[170] T. Stuffler, H. Mosebach, D. Kampf, A. Honne, G. Tan. The flight experiment ANITA—a high performance air analyser for manned space cabins. *Acta Astronaut* **2004**, *55*, 573.

[171] P. T. Palmer, T. F. Limero. Mass spectrometry in the U.S. space program: Past, present, and future. *J Am Soc Mass Spectrom* **2001**, *12*, 656.

[172] T. F. Limero, M. Martin, E. Reese. Validation of the volatile organic analyzer (VOA) for ISS operations. *Int J Ion Mobil Spectrom* **2003**, *6*.

[173] D. B. Gazda, R. J. Lipert, J. S. Fritz, M. D. Porter. Investigation of the iodine–poly(vinylpyrrolidone) interaction employed in the determination of biocidal iodine by colorimetric solid-phase extraction. *Anal Chim Acta* **2004**, *510*, 241.

[174] X. Yuan, J. Tang, Y. Duan. Microplasma Technology and Its Applications in Analytical Chemistry. *Appl Spectrosc Rev* **2011**, *46*, 581.

[175] P. Kurunczi, K. E. Martus, K. Becker. Neon excimer emission from pulsed high-pressure microhollow cathode discharge plasmas. *Int J Mass Spectrom* **2003**, *223–224*, 37.

[176] C. Meyer, R. Heming, E. L. Gurevich, U. Marggraf, M. Okruss, S. Florek, J. Franzke. Radiofrequency driven and low cost fabricated microhollow cathode discharge for gaseous atomic emission spectrometry. *J Anal At Spectrom* **2011**, *26*, 505.

[177] O. Kostya, C. Uros, B. M. Anthony. Plasma nanoscience: setting directions, tackling grand challenges. *J Phys D Appl Phys* **2011**, *44*, 174001.

[178] J. M. Symonds, A. S. Galhena, F. M. Fernández, T. M. Orlando. Microplasma Discharge Ionization Source for Ambient Mass Spectrometry. *Anal Chem* **2010**, *82*, 621.

[179] J. M. Symonds, R. N. Gann, F. M. Fernández, T. M. Orlando. Microplasma Discharge Vacuum Ultraviolet Photoionization Source for Atmospheric Pressure Ionization Mass Spectrometry. *J Am Soc Mass Spectrom* **2014**, *25*, 1557.

[180] J. Franzke. The micro-discharge family (dark, corona, and glow-discharge) for analytical applications realized by dielectric barriers. *Anal Bioanal Chem* **2009**, *395*, 549.

[181] V. Karanassios. Microplasmas for chemical analysis: analytical tools or research toys? *Spectrochim Acta B* **2004**, *59*, 909.

[182] T.-C. Chen, Z. Ouyang. Synchronized Discharge Ionization for Analysis of Volatile Organic Compounds Using a Hand-Held Ion Trap Mass Spectrometer. *Anal Chem* **2013**, *85*, 1767.

[183] Y. B. Gianchandani, S. A. Wright, C. K. Eun, C. G. Wilson, B. Mitra. Exploring microdischarges for portable sensing applications. *Anal Bioanal Chem* **2009**, *395*, 559.

[184] S. Kumano, M. Sugiyama, M. Yamada, K. Nishimura, H. Hasegawa, H. Morokuma, H. Inoue, Y. Hashimoto. Development of a Portable Mass Spectrometer Characterized by Discontinuous Sample Gas Introduction, a Low-Pressure Dielectric Barrier Discharge Ionization Source, and a Vacuumed Headspace Technique. *Anal Chem* **2013**, *85*, 5033.

[185] B. Mitra, B. Levey, Y. B. Gianchandani. Hybrid Arc/Glow Microdischarges at Atmospheric Pressure and Their Use in Portable Systems for Liquid and Gas Sensing. *IEEE T Plasma Sci* **2008**, *36*, 1913.

[186] X. Wang, X. Zhou, Z. Ouyang. Direct Analysis of Nonvolatile Chemical Compounds on Surfaces Using a Hand-Held Mass Spectrometer with Synchronized Discharge Ionization Function. *Anal Chem* **2016**, *88*, 826.

[187] S. G. Lias, J. F. Liebman, R. D. Levin. Evaluated Gas Phase Basicities and Proton Affinities of Molecules; Heats of Formation of Protonated Molecules. *J Phys Chem Ref Data* **1984**, *13*, 695.

[188] R. Wu, T. B. McMahon. Stabilization of Zwitterionic Structures of Amino Acids (Gly, Ala, Val, Leu, Ile, Ser and Pro) by Ammonium Ions in the Gas Phase. *J Am Chem Soc* **2008**, *130*, 3065.

[189] H. D. Garcia. *Spacecraft water exposure guidelines for selected contaminants, Vol. 2*, National Research Council, National Academy Press, Washington, DC, **2007**.

[190] H. D. Garcia. *Spacecraft water exposure guidelines for selected contaminants, Vol. 3*, National Research Council, National Academic Press, Washington, DC, **2008**.

[191] M. Hur, K. T. Kim, Y. H. Song. Ac-driven plasma torch with a well-type cathode working in air and CO 2. *J Phys D Appl Phys* **2010**, *43*, 445201.

[192] E. R. Wouters, A. A. Makarov, J. J. Dunyach. *Vol. US20110260048 A1*, Google Patents, **2011**.

[193] B. Laprade. *Vol. US7154086 B2*, Google Patents, **2006**.

[194] K. B. Blodgett. Surface Conductivity of Lead Silicate Glass after Hydrogen Treatment. *J Am Ceram Soc* **1951**, *34*, 14.

[195] FieldmasterTM Resistive Glass Products. *http://connect.physicsworld.com/Journals/2013/04/18/q/u/s/ResistiveGlass.pdf, Accessed: June 14*, 2016

[196] PHOTONIS USA Resistive Glass Capillary Inlet Tubes. *http://slideplayer.com/slide/234572/ Accessed: June 14*, 2016

[197] J. R. Scott, P. L. Tremblay. Noncontact measurement of electrostatic fields: Verification of modeled potentials within ion mobility spectrometer drift tube designs. *Rev Sci Instrum* **2007**, *78*, 035110.

LIST OF PUBLICATIONS

1. Keelor, J. D.; Li, A.; Clowers, B. H.; Fernández, F. M. High-Resolution Atmospheric Pressure Drift Tube Ion Mobility Spectrometry Coupled with Ultra-Accurate Mass High-Resolution Orbitrap Mass Spectrometry. *Queued for submission to Anal. Chem.* **2016**

2. Bernier, M. C.; Alberici, R. M.; **Keelor, J. D.**; Dwivedi, P.; Zambrzycki, S. C.; Wallace, W. T.; Gazda, D. B.; Limero, T. F.; Symonds, J. M.; Orlando, T. M.; Macatangay, A.; Fernández, F. M. Microplasma Ionization of Small Molecules for Air/Water Contaminant Analysis on-board the International Space Station. *J. Am. Soc. Mass Spectrom.* **2016**, *27*(7), 1203-10.

3. **Keelor, J. D.**; Cafferty, B.; Forsythe, J.; Bennett, R. V.; Weber, A.; Farnsworth, P. B.; Fernández, F. M. Multi-modal Ambient Plasma Ionization Source for Vacuum-assisted Transmission Mode and Laser Ablation Sampling Coupled with Mass Spectrometry. *J. Am. Soc. Mass Spectrom.* **2016**, *27*(5), 897-907.

4. Curtis, M.; **Keelor, J. D**.; Jones, C. M.; Pittman, J. J.; Jones, P. R.; Sparkman, O. D.; Fernandez, F. M. Schlieren visualization of fluid dynamics effects in direct analysis in real time mass spectrometry. *Rapid Commun. Mass Spectrom*. **2015**, *29*(5), 431-439.

5. Reininger, C.; Woodfield, K.; **Keelor, J. D.**; Kaylor, A.; Fernandez, F. M.; Farnsworth, P. B. Absolute number densities of helium metastable atoms determined by atomic absorption spectroscopy in helium plasma-based discharges used as ambient desorption/ionization sources for mass spectrometry. *Spectrochim. Acta B.* **2014**, *100*, 98-104.

6. **Keelor, J. D.**; Dwivedi, P.; Fernandez, F. M. An effective approach for Coupling Direct Analysis in Real Time with Atmospheric Pressure Drift Tube Ion Mobility Spectrometry. *J. Am. Soc. Mass Spectrom.* **2014**, *25*(9), 1538-1548.

7. Dwivedi, P.; Gazda, D. B.; **Keelor, J. D.**; Limero, T. F.; Wallace, W. T.; Macatangay, A. V.; Fernandez, F. M. Electro-Thermal Vaporization Direct Analysis in Real Time-Mass Spectrometry for Water Contaminant Analysis During Space Missions. *Anal. Chem.* **2013**, *85*(20), 9898-9906.

VITA

Joel D. Keelor was born in Gaithersburg, Maryland on July 27, 1986. He spent his younger childhood growing up Littleton, Colorado, and his teenage years in Franklin, Tennessee, where he attended Battle Ground Academy from 1998-2004. Post primary education, Joel matriculated to Wooster, OH and received his B.A. in Chemistry at the College of Wooster in 2008, where he was very active in The Wooster Chorus, Don't Throw Shoes improv comedy troupe, and the inaugural service dog program. After college, Joel worked for the Electro-Optical Systems Laboratory at Georgia Tech Research Institute until 2010, when he left to pursue his doctorate in analytical chemistry at Georgia Institute of Technology. When he is not working, or rather perseverating, on his research, Joel enjoys building computers, listening to vinyl records, playing board games with friends, drinking whiskey or beer, and running.